GEOLOGICAL SURVEY OF DENMARK AND GREENLAND BULLETIN 9 · 2006

Scientific results from the deepened Lopra-1 borehole, Faroe Islands

Edited by
James A. Chalmers and Regin Waagstein

GEOLOGICAL SURVEY OF DENMARK AND GREENLAND
DANISH MINISTRY OF THE ENVIRONMENT

Geological Survey of Denmark and Greenland Bulletin 9

Keywords
Faroe Islands, Palaeogene basalts, Lopra-1/1A borehole.

Cover
Maersk Rig 81 on the location of the Lopra-1/1A wells at Suðuroy, Faroe Islands, in August 1996 shortly after the start of drilling. Photo: Regin Waagstein.

Frontispiece: facing page
Maersk Rig 81 on the location of the Lopra-1/1A wells at Suðuroy, Faroe Islands, in August 1996 shortly after the start of drilling. Photo: Regin Waagstein.

Receipt/acceptance dates of manuscripts: see end of individual articles
Printed: 7 July 2006

ISSN 1604-8156
ISBN 87-7871-179-7

Geological Survey of Denmark and Greenland Bulletin
The series *Geological Survey of Denmark and Greenland Bulletin* replaces *Geology of Denmark Survey Bulletin* and *Geology of Greenland Survey Bulletin.*

Citation of the name of this series
It is recommended that the name of this series is cited in full, viz. *Geological Survey of Denmark and Greenland Bulletin.*
If abbreviation of this volume is necessary, the following form is suggested: *Geol. Surv. Den. Green. Bull.* 9, 156 pp.

Available from
Geological Survey of Denmark and Greenland (GEUS)
Øster Voldgade 10, DK-1350 Copenhagen K, Denmark
Phone: +45 38 14 20 00, fax: +45 38 14 20 50, e-mail: geus@geus.dk
or
Geografforlaget ApS
Rugårdsvej 55, DK-5000 Odense C, Denmark
Phone: +45 63 44 16 83, fax: +45 63 44 16 97, e-mail: go@geografforlaget.dk

Contents

Introduction

Martin V. Heinesen, Arne Rosenkrands Larsen and Kai Sørensen

Systematic preparation of the legal framework to govern full-scale hydrocarbon exploration in the Faroe Islands was initiated in 1992, after the Danish government and the Faroese Home Rule government had agreed on the future administrative regime with respect to minerals, including hydrocarbons, in the subsurface of the Faroese area. At about the same time, significant hydrocarbon discoveries were made in the UK offshore area west of the Shetland Islands and close to the UK–Faroese border that led to production starting from the Foinaven and Schiehallion fields later in the decade. For these reasons the petroleum exploration community became interested in the Faroese area.

The stratigraphic section exposed in the islands consists predominantly of a 3000 m thick series of mainly tholeiitic basaltic lavas of late Paleocene age, divided informally into a lower, a middle and an upper series. Until the early 1990s, the only deep wells that had been drilled in the Faroese area were the Vestmanna-1 well, drilled in 1980 in the town of Vestmanna on Streymoy, and the Lopra-1 well drilled on the southernmost part of Suðuroy in 1981, both scientific wells funded mainly by the Faroese government with a contributing grant from the Carlsberg Foundation of Copenhagen (Organising Committee 1984). Vestmanna-1 was a 660 m deep, fully cored, slim well that penetrated the lowermost part of the middle series and the uppermost part of the lower series. Lopra-1 was located near where the stratigraphically lowest basalts are exposed. It was originally drilled to a depth of 2178 m and penetrated approximately 2 km of formerly unknown strata, all of which proved to be a continuation of the subaerially exposed lower basalt series. The well was left open, plugged only by a 10″ gate valve. The uppermost part of the well was cased with a 16 m conductor pipe with a diameter of 14″ and a $9^5/_8$″ casing down to 190 m, whereas the 8½″ diameter main part of the well remained uncased down to terminal depth (TD).

Although the Lopra-1 well did not reach the base of the volcanic pile beneath the Faroe Islands, it revealed some information of significance to the hydrocarbon exploration potential of the area. No strong evidence was seen of any sedimentary section nor hydrocarbon generation in the well, but analysis of tiny amounts of methane-rich gases and oil isolated from the water in the well indicated an origin from marine organic matter beneath the basalt (Jacobsen & Laier 1984). Subsequent seismic experiments, including different vertical seismic profiling (VSP) experiments, indicated a lithological change only *c.* two hundred metres beneath the TD of the well (Kiørboe & Petersen 1995).

After consultation with a number of oil companies, in 1995 the Faroese Petroleum Administration made an arrangement with the Danish state oil company (DONG) to act as operator and coordinator of a joint industry project to deepen the Lopra-1 well. The 19 oil companies that participated in the project are listed in Table 1.The Petroleum Administration was assisted by the Faroese Geological Survey and the Geological Survey of Denmark and Greenland (GEUS). Dansk Operatørselskab i-s (Danop) acted as consultant to DONG with respect to the drilling operation and the Mærsk Rig 81 drilling rig was used. GEUS and the Faroese Geological Survey were responsible for the well site geology and the subsequent geological evaluation of the drilling results.

The primary objective of the deepened well was to ob-

Table 1. The nineteen oil companies that participated in the project

Amerada Hess Ltd.
Amoco DK Exploration Co.
ARCO British Ltd.
BHP Petroleum Inc.
BP Exploration Operation Co. Ltd.
British Gas Exploration & Production Ltd.
Chevron Europe Ltd.
Dansk Olie- og Gasproduktion A/S (DONG)
Deminex UK Oil & Gas Ltd.
Enterprise Oil Exploration Ltd.
Esso Exploration. & Production UK Ltd.
FINA Research S.A.
LASMO (ULX) Ltd.
Mobil North Sea Ltd.
Norsk Hydro A.S.
Phillips Petroleum Co. UK Ltd.
Saga Petroleum International A.S.
Shell Exploration B.V.
Statoil Efterforskning og Produktion A.S.

tain lithological and stratigraphic information about the deepest parts of the Faroe plateau basalt series and their substratum and to acquire information in relation to the hydrocarbon prospectivity of the area. Secondary objectives included: (a) determination of the age and depth to the base of the basalt series, (b) characterisation of the pre-basaltic lithologies, (c) characterisation of the physical properties of the basalt series and their substratum to improve interpretation of regional seismic, gravity and magnetic data and (d) thermal maturity determination of interbasaltic and pre-basaltic organic matter, as well as determination of possible sources for oil and gas shows in the well.

Deepening of the well started on 13 July 1996. It reached its total depth of 3565 m on 3 November 1996. After final wireline logging, it was plugged and abandoned and the rig was released on 13 November 1996. The well penetrated 213 m of subaerially extruded basalt flows of the lower basalt series, a series of pillow lavas 45 m thick and a series of pillow lava debris 41 m thick. Below that was a thick series of volcanic tuffs with some intra-volcanic sandstone and claystone stringers. The only conventional core cut in the well was a 1.5 m (recovered) core from the lowermost basalt flow. Drilling through the base of the volcanics was not achieved.

This book presents a number of research studies carried out in the years following completion of the well. Although no direct information was obtained about prevolcanic rocks, the deepening of the Lopra-1 well has documented the presence on and under the Faroe Islands of the thickest known composite section through the North Atlantic Palaeogene basalt plateau.

References

Jacobsen, O.S. & Laier, T. 1984: Analysis of gas and water samples from the Vestmanna-1 and Lopra-1 wells, Faeroe Islands. In: Berthelsen, O., Noe-Nyegaard, A. & Rasmussen, J. (eds): The Deep Drilling Project 1980–1981 in the Faeroe Islands. Annales Societatis Scientarium Færoensis, Supplementum **IX**, 149–155. Tórshavn: Føroya Fróðskaparfelag.

Kiørboe, L. & Petersen, S.A. 1995: Seismic investigation of the Faeroe basalts and their substratum. Geological Society Special Publication (London) **90**, 111–112.

Organizing Committee 1984: Preface. In: Berthelsen, O., Noe-Nyegaard, A. & Rasmussen, J. (eds): The Deep Drilling Project 1980–1981 in the Faeroe Islands. Annales Societatis Scientarium Færoensis, Supplementum **IX**, 5 only. Tórshavn: Føroya Fróðskaparfelag.

M.V.H., *Jardfrødisavnid (JFS) – Faroese Geological Survey, P.O. Box 3169, FO-110 Tórshavn, Faroe Islands*. Present address: *Jardfeingi – Faroese Earth and Energy Directorate, P.O.Box 3059, FO-110 Tórshavn, Faroe Islands.* E-mail: *martin.v.heinesen@jardfeingi.fo*

A.R.L., *Dansk Olie og Naturgas (DONG) , Agern Alle 24–26, DK-2970 Hørsholm, Denmark*.

K.S., *Geological Survey of Denmark and Greenland, Øster Voldgade 10, DK-1350 Copenhagen K, Denmark.*

Wire-line log-based stratigraphy of flood basalts from the Lopra-1/1A well, Faroe Islands

Lars O. Boldreel

The present study shows that it is possible to use conventional borehole logs to perform a detailed lithological/stratigraphical division of a column of subaerially extruded basalt. A stratigraphical division of the subaerial flood basalts penetrated by the Lopra-1/1A well has been carried out using new wire-line logging data measured in 1996 in the interval 200–2489 m depth. Resistivity data acquired in the interval 200–2178 m depth during 1981 after the initial drilling of the Lopra-1 well have also been incorporated. Eighty-six individual flow units, 18 compound flows and two dolerite dykes have been identified by combining the NPHI porosity, RHOB density, P-, S- and Stonely-sonic transit time, calliper and resistivity logs. Fifty-two sedimentary/tuffaceous layers have also been identified using the CGR and SGR gamma ray and potassium logs in combination with the aforementioned logs. Within the flow units, sonic velocity, density and resistivity are highest in the core where porosity is lowest. This relation is reversed in the uppermost and basal zones of the flow units. The sonic velocity in the core seems to be independent of the thickness of the flow unit. Porous zones seem abundant in some cores and the total section of cores containing porous zones constitutes more than 70% of the thickness of its flow unit, but where porous zones are absent the core makes up only roughly 50% of the thickness of the flow. It is suggested that the flow units with porous cores represent aa flows (88% of the flow units) and the others pahoehoe flows (12% of the flow units).

The log pattern of the flow units (crust, core and basal zone) is similar to log patterns reported from other basalt plateaux. However the patterns in Lopra-1/1A show a larger variation than elsewhere, suggesting that the flow units are more complex vertically than previously thought. Statistical analysis of P-, S- and Stonely-waves, RHOB, NPHI, resistivity, gamma and calliper logs has been carried out. Cross-plots based on the lithological divisions have been produced that show a pronounced reduction in scattering versus P-sonic transit time and P- and S-sonic, RHOB and NPHI logs correlate with depth. The geochemical logs do not reflect the cyclic structure of the flow units and probably represent the primary composition of the basalt. The thorium log especially indicates flow units with high and low radioactivity and it is suggested that a minimum of 36 flow fields form the logged part of the lower basalt series. Dolerite units described in previous works have been confirmed based on the combined interpretation of wire-line logs. The log data suggest that the subaerially extruded basalt has its base at a depth of approximately 2490 m and that a hyaloclastite succession is found below that depth. The transition from subaerially extruded basalt to hyaloclastite produces a negative acoustic impedance and it is found that the transition corresponds to a negative reflection interpreted on VSP surveys from 1988 and 1994.

Keywords: Flood basalts, flood basalt petrophysics, North Atlantic, Faroe Islands, Lopra-1/1A well, Faroese basalt lithology, wire-line logs

---

Geological Institute, University of Copenhagen, Øster Voldgade 10, DK-1350 Copenhagen K, Denmark.
E-mail: *lob@geol.ku.dk*

The Lopra-1 well was deepened in 1996 to drill through a pronounced negative seismic reflection at an estimated depth of 2366 m and an additional reflection at a depth of 3486 m found from the analysis of the data acquired in Vertical Seismic Profiling (VSP) surveys carried out in 1988 (Kiørboe & Petersen 1995) and 1994. Several wire-line logs were run in the upper part of the well (0–2184 m) that had been drilled in 1981 to supplement the previous logging (Nielsen *et al.* 1984). A more extensive logging programme was carried out in the deepened part of Lopra-1/1A and the new wire-line data for the entire well have been analysed.

The wire-line logs were used to investigate the lower basalt series of the Faroe Islands, to construct a lithological and stratigraphical division of the lava sequence and to test whether a subdivision of the basalt column would result in better statistics of its physical properties. The results of the new logging have been both new understanding and results in greater detail than was possible from the data available from the 1981 drilling and logging, and they supplement studies carried out in other basalt covered regions in the world.

It was intended that analysis of the wire-line logs acquired in 1996 should include the logs acquired in 1981, but this turned out to be complicated. It was possible to use the older resistivity data only after they had been corrected manually within individual flow units. Consequently this paper is concerned mainly with interpretation of the wire-line log data measured in 1996 in the subaerially extruded lower basalt series.

Geology of the Faroe Islands

The Faroe Islands consist of subaerially extruded tholeiitic basalt flows erupted in the late Paleocene in connection with the opening of the northern North Atlantic Ocean. The basalts consist of three lava formations called the upper, middle and lower basalt formations (or series). A tuff-agglomerate zone and a coal-bearing horizon separate the lower and the middle formations (e.g. Rasmussen & Noe-Nygaard 1969, 1970; 1990). The three lava formations are all exposed on the islands and the lowest exposed stratigraphical level is found in the southern part of the southernmost island, Suðuroy, where the original Lopra-1 well was drilled. Geological and geophysical investigations based on data from the Lopra-1 well resulted in six papers published in Berthelsen *et al.* (1984). The geology of the well was described by Hald & Waagstein (1984) who found the lava to consist of tholeiitic basalt. A stratigraphical division of the well was established on the basis of drill cuttings collected every 2 m, five cores, the wire-line logs (acquired in 1981) and geochemical rock analysis. This resulted in a division of the sequence into 87 flow units, 27 sedimentary units and two dolerite dykes within the interval 200–2180 m depth plus an additional 10 flow units and five sedimentary beds in the cased interval 0–200 m. The bedding in the well was established using chilled vesicular (amygdaloidal) basalt as a marker of flow tops. The observed transition between vesicular and non-vesicular basalt was afterwards correlated to the neutron-neutron and resistivity logs (Waagstein *et al.* 1982; Nielsen *et al.* 1984). The flow units range in thickness from a few metres to about 50 m with the majority of flows having thicknesses of 5–10 m or 10–15 m. Most of the flows were interpreted as aa type based on the characteristics of the topmost cuttings. Sediments were observed on the top of about one third of the drilled lava flows. Two dolerite dykes were found at 834–738 m and 616–508 m, and Hald & Waagstein (1984) suggested that the real thickness of both dykes is about 9 m assuming an inclination of 85°. The volcaniclastic sediments were distributed more or less randomly throughout the drilled sequence, and no correlation was found either with flow thickness or with chemical composition of the flows. It was concluded that there were no major hiatuses during eruption of the drilled sequence or the overlying 700 m of exposed lower basalt formation.

Data from the Lopra-1 well

The original Lopra-1 stratigraphic well reached a total depth (TD) of 2184 m in 1981. It was deepened in 1996

Table 1. Wire-line log suites 1, 2 and 5 used in this study

Suite 1: 196–2184 m
(in the existing hole drilled in 1981).
Two log runs were carried out:
Run No. 1: LDL-CNL-NGS (recording a maximum hole deviation of 1° from the vertical). GR was run to the surface
Run No. 2 pass 1: DSI-Cross and U&L Dipole
Run No. 2 pass 2: DSI-P&S and Stoneley.
Suite 2: 2185–3158 m
Three runs were carried out:
Run No. 1: LDL-CNL-NGS-DSI.
Run No. 2: SHDT-GR-AMS recording a maximum hole deviation from the vertical of 14°
Run No. 3: GHMT-GR.
Suite 5: 2204–3531 m
Run No 1: MSCT-GR

to a TD of 3158 m and was sidetracked from 3091 m after a partly unsuccessful fishing operation. The sidetrack (Lopra-1A) well reached TD at 3565 m and the Lopra-1/1A well sections were plugged and abandoned after final wire-line logging. The Lopra-1/1A well has been logged on various occasions. Caliper, gamma ray, resistivity, neutron-neutron porosity and sonic logs were acquired in 1981 (Nielsen *et al.* 1984), but the sonic log and part of the resistivity log turned out to be unsuccessful (Nielsen *et al.* 1984). Successful VSP surveys were carried out in 1988 (Kiørboe & Pedersen 1995) and 1994, and ahead-of-tool predictions were carried out in order to evaluate the remaining thickness of the basalt. The deepened well was logged in 1996 and a large number of logs, including a VSP, were obtained. A total of five suites were run between 196 and 3565 m depth. Suites 1 to 5 were acquired in the intervals 196–2184 m, 2185–3158 m, 3091–3516 m, 3516–3561 m and 2204–3531 m, respectively. Three of the suites have been used in this study, suites 1, 2 and 5 (Table 1).

From the suite of wire-line logs, the calliper, SGR (total gamma ray), CGR gamma ray (computed gamma ray, including measurements of thorium and potassium), P-, S- and Stonely-wave transit time, RHOB (bulk density), NPHI (neutron porosity hydrogen index), resistivity (short and long from 1981), potassium, thorium and uranium logs were selected for this study. After processing (apart from the resistivity logs) by Schlumberger, the data were interpreted on an SGI UNIX workstation using Landmark software (Stratworks® and Petroworks®). There were problems with the logs acquired by the spectral gamma log tool in the deepened part of the Lopra-1 well, probably because calibration had not been carried out properly. The data were corrected by shifting the thorium, potassium and CGR logs to the responses measured in the previously drilled hole. An attempt was made to correlate the wire-line logs from 1981 and 1996, as both suites include a calliper. That task proved not to be simple, probably because of different cable tensions and depth annotations. It is felt that the 1981 resistivity data have been correctly adjusted by manual editing and adjusting the 1981 data to the interpretation of the wire-line suite obtained in 1996.

Characteristics of subaerially extruded basalt

It is known from various workers (e.g. Cashman & Kauahikaua 1997; Self *et al.* 1997; Thordarson & Self 1998; Waagstein 1999) that subaerially extruded lava flows have some characteristics in common and the following discussion focuses on those characteristics which may be expected to be confirmed from the logging suite run in the Lopra-1 well. A lava formed in a single volcanic eruption is called a flow field and consists of one or several lava flows erupted more or less continuously from the same vent area or fissure. The commonest diagnostic criterion likely to be used is the chemical composition of the basalt magma that is assumed to be fairly constant during an eruption.

A lava flow may consist of several flow units, partly or completely surrounded by chilled crust. A flow unit consists of a lava crust, a lava core and a basal zone. The appearance of the crust has been used to define two morphological types, aa and pahoehoe, in both of which the crust is usually much thicker than the basal zone. The core typically consists of massive basalt with few or no vesicles, and sometimes displays flow banding. Thick cores often show a more or less columnar jointing in the lower part which propagated upwards perpendicular to the base of the flow during cooling. Thinner and less regular columns in the upper part may have propagated downwards from the top of the flow. Vesicular zones in the core have been reported by McMillan *et al.* (1987) who showed a two-stage vesiculation of basalt from the Colombia River Basalt Plateau. Walker (1989) studied vesicle distribution in profiles across flow units, on Hawaii primarily of pahoehoe type but also of aa type, and concluded that the distribution of vesicles does not need to be symmetrical about a horizontal median plane.

The rubble near the surface of a flow unit in aa lava may be unconsolidated with fractures and voids filled by tuff, and sometimes the rubble fragments are welded. The fragmentation decreases downwards, and a complete gradation into unbrecciated basalt in the core of the flow unit is commonly seen. Thick flow units in the lower formation on the Faroes are typically from several metres to several tens of metres thick, as seen on Suðuroy (Waagstein 1999). Thick flow units usually have an upper rubbly crust several metres thick whereas the lower crust or basal zone is generally less than one metre. The vesicles and fractures are usually filled with secondary minerals. Aa lavas on Hawaii normally consist of a large number of thin flow units, 0.2–2.0 m thick.

Pahoehoe type lava has a continuous vesicular crust that is distinguished from its core mainly by its vesicularity, and roughly half of the total thickness of a pahoehoe flow consists of crust. The crust is highly vesicular near its top surface with abundant small vesicles that often exceed 50% of the bulk rock volume. The vesicles show an overall decrease in abundance and increase in size downwards reflecting the increase in gas pressure exerted by the thickening lava crust. The vesicles are often arranged in hori-

Table 2. Physical properties of basalt based on wire-line logs

	Kern & Richter (1979) Faroese basalt	Berlitz *et al.* (1988) Chile Japan	Goldberg *et al.* (1994) USA	Planke (1994) ODP Hole 642E	Christensen (1996)	Planke & Flovenz (1996) ODP Hole 917	Singh (1996) Deccan traps
Vp (km/sec)	4.79–6.21		6.2§		5.91§	3–5.5 4§	
Vp massive (km/sec)				5.0–6.0			
Vp sediments (km/sec)				3.0–5.3			
Vs (km/sec)	2.73–3.52				3.03§		
Porosity		10 p.u.	10%#				
Porosity massive				< 5% corrected			
Porosity porous				15–30% corrected			
Porosity sediment				10–20% corrected			
Density (g/cm^3)	2.73–3.52	3.06*; 2.8†	3.05§	2.3–2.8	2.882§	2.5§	
Gamma-ray (GAPI)		15	75 ± 25				
Gamma-ray (mas)				5 GAPI			15–40 cps
Gamma-ray (por)							40–100 cps
Gamma-ray (sed)				20 GAPI			100–300 cps
Unit thickness 6–8 m						6–8 m	

* Chile; † Japan; # uncorrected values; § average
cps: counts per second; p.u.: neutron porosity units; GAPI: Gamma log in API units;
mas: The massive core of a flow unit; por: The porous crust of a flow unit; sed: sediments between flow units.

zontal layers with a vertical spacing of about 10 cm, especially in the upper part of the crust. Horizontal vesicular veins or sheets of basalt up to about 10 cm thick may occur near the top of the core, but otherwise the core of the flow is usually massive with no or only a few relatively large vesicles. The basal vesicular zone is usually a few tens of centimetres thick at most and sometimes sub-vertical pipes are found within it.

Sediments

Thin beds of tuff with a vertical extent of between a few centimetres and few tens of metres are found within the Faroes lava succession. The beds are typically very fine-grained, clayey, fissile with vivid colours. The tuff beds are buried soils (palaeosols) formed by disintegration and chemical break down of volcanic materials. The beds may originate from either airfall volcanic ash or from *in situ* weathering of the lava flows (Hald & Waagstein 1984; Waagstein 1999). Microfossils suggest that the latter formed slowly enough to allow immigration of plants and other living organisms before being covered by the next lava flow, thus representing quiescence in the erupting environment (Lund 1983).

Previous work on the relationship between lithology and logging response

The geophysical response of interbedded sediment/tuff layers and subaerially extruded basalt, characterised both by the rhythmic succession of flow units and the subdivision of the flow unit into three parts, may be examined from wire-line logging data and drilling penetration rate. This has been done by a number of authors from various places around the world: the Faroe Islands (Kern & Richter 1979; Nielsen *et al.* 1984), ODP Hole 642 (Planke & Flovenz 1996), ODP Hole 642E (Planke 1994), Newark Basin (Goldberg *et al.* 1994), North Sea basalt flows from the Middle Jurassic (Rider 1996), Deccan Trap area (Buckley & Oliver 1990; Singh 1996), Japan and Chile (Berlitz *et al.* 1988) and a geothermal well with no cited geographical location (Sanyal *et al.* 1980). Physical parameters obtained from the analyses of wire-line data by these workers are presented in Table 2, and the results from the present study are found in Table 3. In two studies where the layered basalt flows represent the Seaward Dipping Reflector Sequence, from ODP Hole 917 (which also had formation microscanner images) (Planke & Flovenz 1996) and from ODP Hole 642E (Planke 1994), the interpretation of wire-line logs was integrated with continuous coring.

The above studies suggest that the following features are of special interest in relation to the wire-line logs obtained from Lopra-1/1A.

The often vesicular, fractured and altered crust and flow tops are characterised by gradients in the values represented

Table 3. Physical properties of basalt based on wire-line logs from Lopra-1

	Average	Median	(Min–Max)
Vp flow unit	5.53	5.78	(2.94–7.47) km/sec
Vp core	5.83	5.90	(2.94–7.47)
Vp crust	4.69	4.73	(2.94–6.63)
Vp compound flow	4.92	5.02	(2.43–6.57)
Vp dolerite dyke	6.08	6.29	(3.37–7.58)
Vp sediments	4.26	4.30	(2.86–6.31)
Vs flow unit	2.97	3.11	(1.74–4.01) km/sec
Vs core	3.14	3.19	(2.00–4.01)
Vs crust	2.52	2.54	(1.74–3.82)
Vs compound flow	2.59	2.60	(1.82–3.44)
Vs dolerite dyke	3.28	3.39	(1.90–4.03)
Vs sediments	2.34	2.34	(1.90–3.34)
Vst flow unit	1.46	1.47	(1.11–1.52) km/sec
Vst core	1.47	1.48	(1.22–1.52)
Vst crust	1.42	1.43	(1.11–1.50)
Vst compound flow	1.44	1.44	(1.19–1.49)
Vst dolerite dyke	1.45	1.47	(1.28–1.48)
Vst sediments	1.40	1.41	(1.19–1.49)
Porosity flow unit	0.19	0.16	(0.04–0.50) % lspu*
Porosity core	0.15	0.14	(0.04–0.47)
Porosity crust	0.31	0.32	(0.11–0.50)
Porosity compound flow	0.30	0.30	(0.15–0.49)
Porosity dolerite dyke	0.12	0.10	(0.04–0.45)
Porosity sediments	0.31	0.32	(0.15–0.44)
Density flow unit	2.85	2.96	(1.55–3.15) g/cm^3
Density core	2.90	2.93	(1.57–3.15)
Density crust	2.66	2.66	(1.55–3.15)
Density compound flow	2.74	2.76	(2.03–3.01)
Density dolerite dyke	2.90	2.95	(1.51–3.04)
Density sediments	2.58	2.64	(2.53–2.95)
Gamma ray flow unit	10.40	9.50	(0.7–61.1) API
Gamma ray core	10.23	9.39	(0.0–33.77)
Gamma ray crust	9.75	9.43	(0.0–33.76)
Gamma ray compound flow	10.32	9.18	(1.34–36.53)
Gamma ray dolerite dyke	4.74	4.57	(1.36–26.95)
Gamma ray sediments	27.09	25.21	(1.66–78.28)
Calliper flow unit	10.47	10.52	(6.64–15.83) inches
Calliper core	10.15	10.26	(6.64–15.83)
Calliper crust	11.81	11.84	(8.24–15.62)
Calliper compound flow	11.96	11.96	(10.10–14.61)
Calliper dolerite dyke	11.73	11.80	(9.49–18.58)
Calliper sediments	12.12	12.08	(10.09–18.41)
Resistivity (lld) flow unit	558.39	473.36	(24.07–1777.40) om
Resistivity (lld) core	661.47	601.04	(37.35–1777.40)
Resistivity (lld) crust	255.35	164.21	(24.67–1197.98)
Resistivity (lld) compound flow	283.45	187.91	(52.07–1135.72)
Resistivity (lld) dolerite dyke	1038.07	1055.64	(145.01–1773.44)
Resistivity (lld) sediments	178.05	144.09	(26.74–890.36)
Resistivity (lld) flow unit	317.16	288.27	(18.52–766.66) om
Resistivity (lls) core	369.51	356.15	(32.43–766.68)
Resistivity (lls) crust	165.68	122.45	(18.52–731.21)
Resistivity (lls) compound flow	167.66	121.70	(26.32–596.06)
Resistivity (lls) dolerite dyke	515.80	527.20	(22.37–760.66)
Resistivity (lls) sediments	91.91	76.63	(22.37–309.21)

* limestone porosity units; om: ohms m^2/m

by the porosity dependent wire-line logs. The P-wave velocity, density and resistivity values are rather low but increase into the flow, in contrast to the porosity log that shows rather high values that decrease into the flow (Planke & Flovenz 1996). Natural gamma counts are intermediate (Goldberg *et al.* 1994; Planke 1994; Rider 1996; Singh 1996). The crust is often soft and weathered and can be recognised from an increase in the rate of drilling pentration (Buckley & Oliver 1990).

The massive core is characterised by rather high values of P-wave velocity, density and resistivity in contrast to rather low values of porosity and low natural gamma counts (Goldberg *et al.* 1994; Planke 1994; Planke & Flovenz 1996; Rider 1996; Singh 1996). A number of Faroes basalt samples, selected to be free of fractures and secondary alteration, showed in laboratory experiments that the P- and S-wave velocities increase as a function of pressure (Kern & Richter 1979). Two distinct gamma ray count rates of primary potassium and thorium show that high-gamma basalts exist (Buckley & Oliver 1990).

The basal zone is characterised by gradients in values from the wire-line logs representing porosity. P-wave velocity, density and resistivity decrease rapidly downwards whereas porosity increases downwards near the base of the unit (Goldberg *et al.* 1994; Planke 1994; Planke & Flovenz 1996).

The sediments interbedding the flow units show very low resistivity and very high gamma counts (Nielsen *et al.* 1984; Singh 1996) and intermediate porosity and density values (Planke 1994).

Nielsen *et al.* (1984) showed that different series within a large vertical section of basalt flows could be identified primarily from the results of the natural gamma ray log. Sanyal *et al.* (1980) showed that lithology could be discriminated by analysing wire-line logs and making cross-plots of especially the gamma-ray and neutron responses.

Some of the results are of special interest in the context of the present work on the Lopra-1 logs. A positive correlation between flow thickness and mean velocity simply reflects increased proportions of massive basalt in thicker flows (Planke 1994); velocity and density gradients at the top and bottom of a flow unit are largely independent of flow thickness (Planke & Flovenz 1996); Goldberg *et al.* (1994) and Kern & Richter (1979) found that travel time correlates directly with porosity and showed that it also decreases with depth in sediments. Planke (1994) found flows between 0.6 and 18.5 m thick while most sediment was less than 1 m thick. Radioactive gamma ray and potassium logs are asymmetrical, having high values at flow tops, decrease gradually towards a central wide minimum and increase rapidly again near the flow base.

Principles of interpretation of the Lopra-1 well wire-line data

It is assumed that the principles and observations about the wire-line interpretation of subaerial basalt successions discussed in the previous section can be applied to the interpretation of the wire-line logging suite carried out in the Lopra-1 well. The physical properties of a basalt flow are related primarily to active mechanical processes (i.e. growth through inflation, cooling history, the environment into which the flow was extruded, stress, faulting and whether it is a pahoehoe or aa flow type) and to secondary processes such as leaching and mineral growth. Thus it is expected that, within subaerially extruded flows, the responses of the sonic, porosity, density, resistivity and calliper logs, all of which record physical properties, will follow a generalised cyclic pattern. On the other hand the geochemical properties reflect a combination of magma composition, primary mineralogy, weathering, leaching of various elements and growth of secondary minerals so the response from the gamma (SGR and CGR), thorium, potassium and uranium wire-line logs, all of which represent geochemical properties, will not necessarily show similar cyclic patterns.

As a first approach, an idealised cross-section of a flow is envisaged as follows: a porous crust at the top of the flow grades into a massive core. A basal zone below the massive core appears abruptly and is located on top of the preceding tuff/sedimentary layer or, in case such a layer is absent, on top of the crust of the preceding flow.

The porous crust represents a transition zone between the tuff/sediment layer above it and the massive core beneath it. Its physical properties thus change gradually, represented by the readings of the physical logs changing gradually downwards from those observed at the very top of the flow or in the overlying tuff/sediment layer to the values of the underlying massive core. It is thus expected that values for the transit time of both the P- and S- waves, porosity and the diameter of the well will decrease downwards, whereas the density and resistivity will increase downwards. The interpretation of the geochemical logs is ambiguous because the crust could either be leached or enriched in elements compared to the original composition of the flow.

The massive core is often found to be characterised by uniform values of the sonic, porosity, density, resistivity and calliper logs. More specifically, the core is recognised by the low transit time (high velocity) of the P-, S- and Stonely-waves, low values of porosity, the well diameter and drilling rate, but high values of density and resistivity. The chemical logs are expected to show a concentration

for the core and crust that more or less reflect the original chemical composition of the flow.

The thin basal zone is recognised physically as a sharp transition above the underlying lava flow/tuff horizon. An abrupt change downwards of the log patterns is expected. Values of transit time of P-, S- and Stonely-waves are expected to increase downwards (i.e. a downward fall in velocities) as are those of porosity and well diameter, but resistivity and density should decrease downwards.

Sediment deposited on top of a lava flow should appear on the petrophysical logs as follows: high values of transit times of P-, S- and Stonely-wave sonic logs (low velocity), high values of porosity, low values of density, resistivity, distinctly high values of the gamma ray, especially the spectral gamma ray responses (particularly for the compensated gamma ray and potassium curves) and enlarged diameter of the well.

Lopra-1 results

The wire-line-logs are shown on Enclosure 1. Individual curves are arranged such that their visual impression can be correlated easily with the inferred lithology. Inspection shows that while the basal zone of many flow units can be recognised, it is too thin to be treated statistically as has been done for the core, crust, compound flows, dolerite dykes and sediments. Analysis of the basal zone has therefore been included in that of the core.

Calliper

The calliper log shows that the diameter of the borehole varies cyclically in the range of 9–18″ in the upper part of the hole that was drilled in 1981 with an 8.5″ bit (Enclosure 1). The diameter is within the interval 6.5″ to 13″ in the deepened hole drilled with a 6.5″ bit. The diameter tends to decrease with depth in the upper hole but it is close to being gauge only in a few places. The measured calliper was expected to have been close to gauge in size; that the final diameter of the hole is irregular is probably due to the method of drilling (Nielsen *et al.* 1984). In the lower section drilled in 1996 with a different technique, the calliper is much closer to the bit size within cores (e.g. flow units 83, 86). The hole is narrowest in massive basalt and is usually wider in flow crusts and basal zones and is usually widest of all in sediment. In a few places, the largest diameter is found in porous crust rather than in overlying sediment, possibly indicating that the sediment is more compact or less friable than the lava crust. Where the sediment beds are closely spaced, they do not seem to affect the condition of the hole, suggesting that the presence of nearby basalt stabilises the hole and that the sediment beds are rather competent (Enclosure 1). In places, the massive cores of the flows show minor deviations from stable hole condition that might indicate that the core is fractured or not as massive as presumed (e.g. flow units 42, 46 and 58).

P-, S- and Stonely-wave transit time

The log curves in Enclosure 1 have been plotted at the same scale but using different intersects, so that S-transit times are within the range 50–170 μsec/ft and P-transit times within 10–130 μsec/ft. Plotting the curves in this way ensures that they plot on top of one another in massive cores where the hole is at or close to gauge as inferred from the combined interpretation of P-, S- and Stonely transit time, RHOB and NPHI in combination. The steady relationship between the two transit times probably indicates that the physical properties of the cores are fairly stable with a P- to S-wave velocity ratio of 1.31.

Both P- and S-wave transit time logs show a cyclic pattern (Enclosure 1). The sediment beds are characterised by the highest transit time (70–100 μsec/ft sonic-P) followed by porous crusts and massive cores. Maximum separation of the curves is a strong indicator of sediments, and intermediate separation is considered to represent crust. The velocity gradient in the upper part of flow units 24, 26, 28, 40, 41 and 42 seems to be independent of the thickness of the flow. Transit times within the core units seem to be independent of the thickness of the flow (e.g. flow units 21, 29, 52, 59 and 79) (Fig. 1).

The Stonely-wave transit time is a part of the full-wave sonic survey. Attenuation of the Stonely-waves occurs where fractures are open and may also be caused by changes in permeability. Such attenuation will be more marked in hard formations where the acoustic contrast is greatest between the formation and mud-filled voids (Rider 1996). The cyclic pattern outlined by the P- and S-wave transit time logs is also shown on the Stonely-wave curve, and the smallest amount of oscillation of the curve occurs in the dolerite dykes and in the core of the flow units (Enclosure 1).

Density-porosity

The bulk density and NPHI porosity curves (measured in limestone porosity units) also show a cyclic nature. The

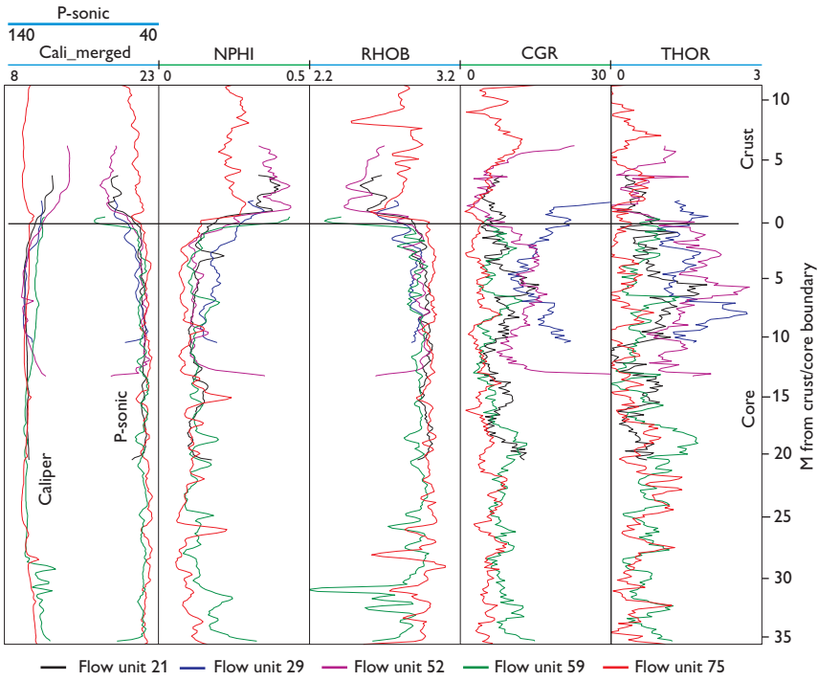

Fig. 1. Variation with depth in five selected flow units. The bimodal behaviour within the flow units is found in the logs representing physical properties but not in the geochemical logs. Variations with depth in the core are most pronounced for the NPHI porosity and RHOB density as compared to the P-sonic transit time and calliper. The P-sonic transit time appears rather constant. The CGR gamma-ray and thorium curves show the large variations present between different flow units.

highest 'porosity' and lowest density values are recorded within the sediments, intermediate values in lava crusts and lowest 'porosity' and highest density values in the lava cores (Enclosure 1). The curves have been plotted at comparable scales, which have been chosen so that they overlap within a typical massive basalt flow, which has been ascribed a density of 2.85–3.00 g/cm^3 and a porosity (NPHI) of 0.1–0.15. Plotted in this way, a positive separation (where the porosity curve is located to the left of the density curve) is diagnostic of sediment or lava crust whereas no separation of the curves is diagnostic of lava core. Negative separations occur within lava cores that have a lower than average porosity.

Resistivity logs

The shallow (lls) and deep (lld) resistivity curves were obtained during the first drilling operations in the Lopra-1 well. The log pattern shows a cyclic behaviour comparable to the other logs representing physical properties, reflecting the separation of flow units into crust, core and basal zones. The resistivity values are highest in the core of the flow units where the lld-log reads higher than the lls-log, showing an increase in resistivity away from the hole and into the formation. That could be due to either the formation water being fresher than the mud water and/or that the basalt becomes more massive away from the well. The values in the flow unit crusts are lower than those in the cores, and the separation between the curves is small. The composite flows have a behaviour similar to that of the crust. Sediments have lowest values but the lld-values are still larger than those of the lls-log. Dolerite dykes have the largest values of resistivity, and a large separation of the logs is found.

Geochemical logs

Five geochemical logs are presented: SGR and CGR gamma ray, potassium, thorium and uranium (Enclosure 1). Basalt that contains both consistently high and consistently low amounts of radioactive material is seen. The shifts from high to low radioactive basalt are remarkably abrupt, and there seems to be no gradual changes, especially for thorium, indicating that thorium represents the original magma (e.g. flow units 7–8, 12–13, 22–23, 23–24, 30–31, 31–32, 46–47, 55–56, Enclosure 1). In general terms, high thorium values are associated with high potassium and thus high CGR gamma ray, as well as high uranium values. There is a close relationship between the CGR gamma ray and potassium spikes and a less pronounced one between CGR gamma ray and uranium spikes. Sediment is characterised by high localised potassium spikes, often recognised in the CGR gamma ray, that correlate to anomalies in the physical properties logs. In some flow unit

crusts, a decrease in potassium values with depth was found.

Lithofacies analysis

The cyclicity of the wire-line log curves has been used to distinguish a number of lithological units including (1) sedimentary layers, (2) flow units of simple type composed of crust, core and basal zone, (3) groups of thin flow units presumably defining composite flows in the sense of Walker (1991), (4) dolerite dykes.

Fifty-two units have been interpreted to be sedimentary beds, identified from a combined interpretation of the potassium, SGR and CGR gamma ray, sonic P-, S- and Stonely-waves, NPHI porosity, RHOB density, calliper and resistivity logs (Enclosure 1). The sediment layers are recognised by gamma ray and potassium spikes relative to the overlying core (and basal zone) and the underlying crust. The gamma ray spike has to be larger than 25 GAPI and be localised within a short thickness interval less than 3.0 m (98% of the sediment layers; Fig. 2) and the pronounced potassium spike must contain more than 1% K. The uranium values are often high too, but are less diagnostic. In addition, the calliper shows a localised maximum deviation from the bit size, the sonic and NPHI logs record high values whereas the density is low. The thicknesses of the sedimentary layers are generally small, and most of the bed thicknesses fall within the intervals 1.0–1.5 m (38%) and 0.5–1.0 m (25%) (Fig. 2). The total thickness of sediments is estimated to be 75.8 m as compared to 40 ± 4 m reported by Nielsen *et al.* (1984). Within the depth intervals displayed in Enclosure 1, the NPHI-porosity and density curves often show a large negative separation. The NPHI-porosity index is large, but the NPHI-porosity often shows a higher value within the crustal part of the underlying flow unit. The density value is low, and generally the lowest value is found in the sediments rather than in the uppermost part of the underlying flow unit (e.g. flow units 12, 20, 29 and 61, Enclosure 1). There are, however, examples where the density values are lower within flow units than within sediments. Thus porosity and density alone are not diagnostic of sediment beds. The P-, S- and Stonely-wave transit times are high within small depth intervals. The shifted transit time curves of the P- and S-waves show large negative separation, but the values are not diagnostic enough to separate sediment layers from the porous crust of the lava flow. The resistivity values are extremely low. Hald & Waagstein (1984) and Waagstein *et al.* (1982) recognised a total of 36 sedimentary beds from analysis of cuttings sampled every 2 m and, among these, 32 are located below the casing of the well and thus within the 1996 log runs. It has been possible to establish a correlation between the sediment layers interpreted from cuttings and the 1996 log curves (Enclosure 1), and 27 out of the 32 sedimentary beds can be confirmed by the criteria put forward here. Thus 22 additional sedimentary layers have been identified within the shallower part of the Lopra-1 well.

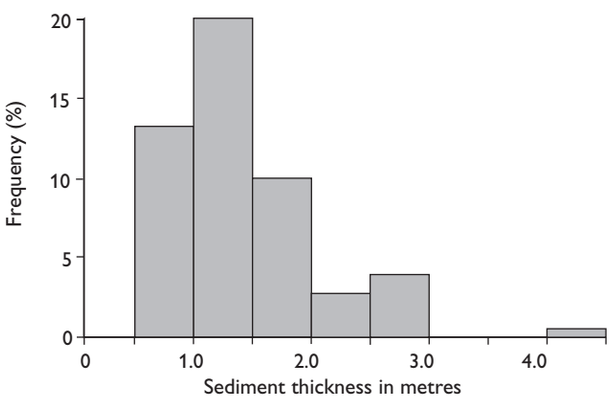

Fig. 2. Frequency diagram illustrating the distribution of sediment thicknesses interpreted in the present study. The sediment layers have been grouped into 0.5 m thickness intervals.

A total of 87 flow units made up of crust, core and basal zone have been identified using a combination of P-, S- and Stonely-wave transit times, porosity and density values, resistivity values and the calliper log. From the top of each unit downwards to the core, the lava crust is indicated by a general gentle decrease in the sonic transit times combined with a decrease in porosity and increase in density and resistivity (Enclosure 1). Below this crustal zone, the log patterns are replaced by fairly constant low values of transit times and porosity combined with a high value of the density and resistivity, defining the lava core. The core is characterised by the calliper being closely in gauge and low values of the shifted sonic transit time curves, low and small oscillations of the Stonely-transit time curve, no separation of the density and porosity curves, and high values of the resistivity values (Enclosure 1). This fairly uniform behaviour of the log curves is abruptly different near the base of the unit where a pronounced increase in sonic transit time, porosity and calliper values combined with a pronounced decrease in density and resistivity values marks the basal zone. The thickness of the basal zone is generally small, and it has not been possible to differentiate it from the overlying core and the underlying sedimentary layer/crust in a consistent manner, so here the

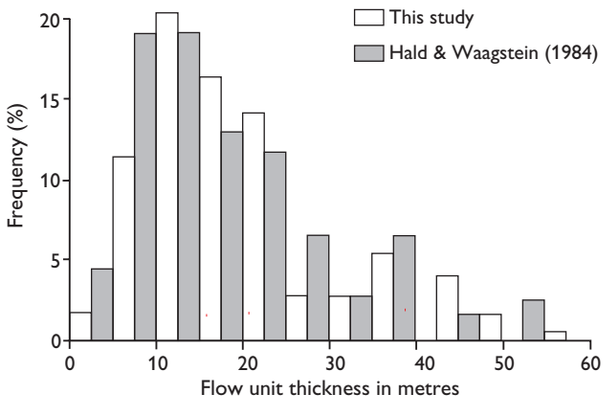

Fig. 3. Frequency diagram illustrating the distribution of flow unit thicknesses interpreted in the present study and in Hald & Waagstein (1984). The flow units have been grouped into 5 m intervals.

basal zones have been included in the cores. The behaviour of the log curves representing the basal zone seems independent of whether or not a sediment layer is present beneath it.

The individual flow units are generally reflected in the geochemical logs, primarily in the thorium curve and secondarily in the potassium curve, whereas the SGR, CGR gamma and uranium curves show unsystematic variations (e.g. flow units 6, 29, 39, 44, 51, 52, Enclosure 1). The unsystematic variations do not allow an overall profile to be established as can be done with the logs representing the physical properties. It is therefore concluded that the geochemical behaviour of the flow units is largely related to the original composition of the magma and that different flow fields may be present. The thicknesses of the flow units have been compared to those interpreted by Hald & Waagstein (1984) and are found typically to be within the range 5–25 m (of which interval flow units of a thickness of 10–15 m represent 23%; Fig. 3).

A closer inspection of the curves through the crust and core parts of individual flow units reveals large fluctuations indicating that the physical properties are not constant in either the crust or the core. The nature of the variations in one crust is illustrated in a few examples; in flow unit 18 the porosity increases with depth and the density is rather constant, in flow unit 46 the porosity increases with depth and density decreases, in flow unit 20 the porosity decreases with depth and density increases. Although the porosity and density figures for the crust differ, the relationship between the crust and core seems to be constant apart from those flow units where the crust and core are of similar thickness.

The idealised core as a massive part of the flow unit characterised by constant low values of transit time, low values of porosity and high density and resistivity values is only true for a few flow units, e.g. 20 and 30, whereas different situations are found in e.g. flow units 13, 19, 26, 30, 36. Most of the flow units penetrated by the Lopra-1/1A well are characterised by the presence of porosity that may be vesicular zones or fractures within the core, though their regularity seems to indicate that they can be ascribed to vesicular zones. These zones are clearly reflected by the density and porosity curves and deflect the S-sonic transit time curves to a larger degree than they do the P-sonic transit time curves. The vesicular zones within the core are not found at a consistent height above the base or below the top, but most of them seem to display some kind of symmetry. The variation from core to core is exemplified by e.g. flow units 26 and 40 which are most massive at the top and porous in the middle; the core of flow unit 41 is most massive in the upper part, and the vesicular zone is displaced towards the base as compared to the core of flow unit 40, the core of flow unit 58 is almost symmetrical with a porous zone in the middle, the cores of flow units 31 and 52 become more massive towards the base, and the core of flow unit 59 shows numerous vesicular zones. A minority of cores are massive in the middle and then are less massive both upwards and downwards (e.g. flow units 45 and 48).

Statistical analysis shows that when vesicular zones are present, the core is at least 70% thicker than the crust, whereas the core and crust are of equal thickness when no vesicular zones are indicated by the logs.

Five flow units (21, 29, 52, 59 and 75), representative of flow units of different thickness between 10 and 50 m, have been chosen to illustrate the relationship between flow thickness and mainly velocity. The thicknesses were correlated with the P-wave transit time, the calliper, the NPHI-porosity, density, gamma ray (CGR) and the thorium content logs (Fig. 1). It can be seen that different values of physical properties are recorded in the flow unit depending on whether crust or core is encountered. The flow units vary considerably in their geochemical expression, and the bimodal behaviour of the flow units is not seen. The crust is represented by high values of the calliper, transit time, NPHI-porosity and low values of density. Transit time in the core seems to be fairly constant and therefore independent of the thickness of the core and the flow unit. The variations in values recorded by the calliper seem independent of the thickness of the flow unit (Fig. 1 and Enclosure 1). The relationship between the flow unit thickness and NPHI-porosity and density values of the core seems to suggest that thin flows exhibit high porosity and low density whereas thick flows show

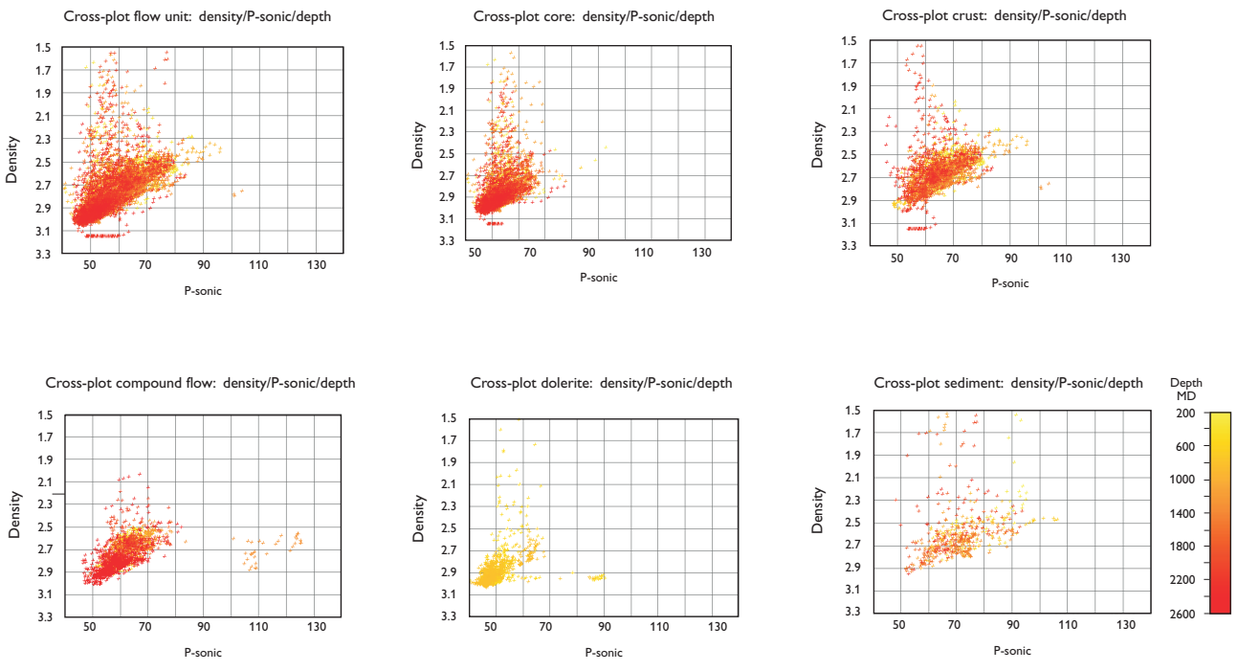

Fig. 4. Cross-plot of inferred lithology: the cross-plots present the statistical behaviour of the flow units, cores, crusts, compound flows, dolerite dykes and sediments plotted for P-sonic transit time versus RHOB density and depth. It is found that the clustering of data is enhanced by plotting the inferred lithology instead of the entire basalt column.

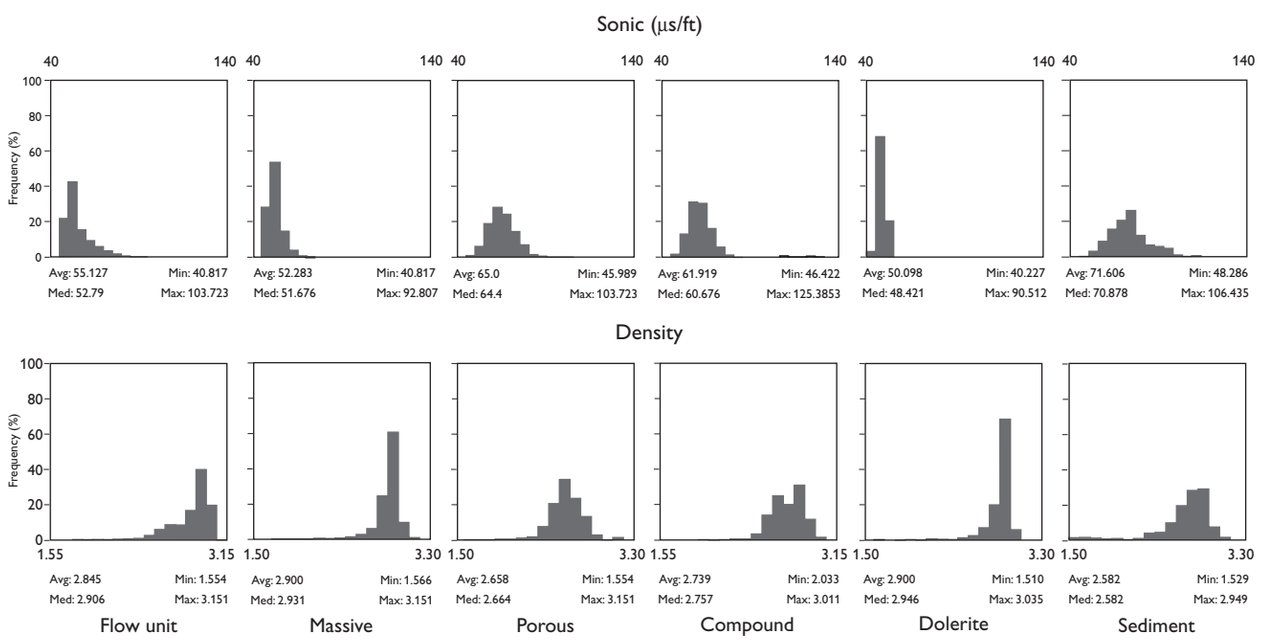

Fig. 5. Histogram and statistical values of the six cross-plots presenting the inferred lithology for P-sonic transit time versus density and depth shown in Fig. 4. The average, median, minimum and maximum values are shown.

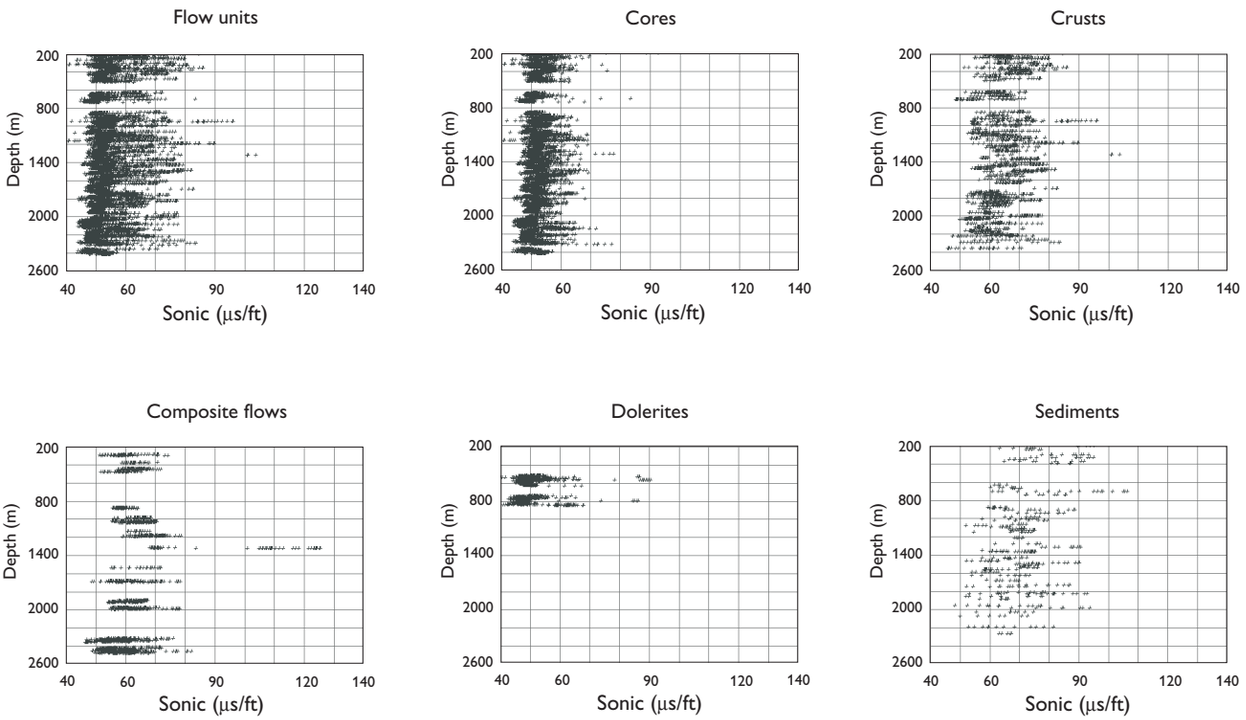

Fig. 6. Cross-plot of P-sonic transit time versus depth for the inferred lithology. The figure shows that the core and sediment lithologies especially show a pronounced trend of decreasing transit time values with depth whereas crust and compound flows are ambiguous. The amount of data representing dolerite dykes is insufficient to describe their relationship with depth. The flow units show a strong increase in transit time with depth but this is due to the core part of the flow unit.

low porosity and high density (Fig. 1) but Enclosure 1 shows that this relation is too simple.

The term 'compound flow' is used for intervals where the cyclicity of the logs representing physical properties suggests strongly that flow units are present, but the individual parts of the flows are poorly defined and log readings do not reach the values normally ascribed to crust or core (Enclosure 1). Eighteen compound flow intervals have been recognised.

Dolerite dykes have previously been encountered at two levels in the Lopra-1 well (Hald & Waagstein 1984). The dykes are represented by constant values of gamma ray, thorium and potassium lower than found in flow units, rather high density and the lowest values of porosity and transit time combined with the highest values of the resistivity measured in the well (Enclosure 1). The calliper shows that pronounced caving occurred in the upper dyke, but no such caving occurred in the lower one. The dyke intervals were expected to show rather constant values of the log curves representing the physical properties but, as is seen on Enclosure 1, a cyclic appearance of those logs is seen. This cyclic appearance is most obviously seen in the lower dolerite dyke where five symmetric intervals are revealed by the RHOB, NPHI, lls and lld logs. This suggests that the lower dolerite dyke consists of five thinner dykes.

Statistics

The lithological division of the volcanic sequence into flow units (consisting of porous crust and massive core), compound flows, dolerite dykes and sediments makes possible a statistical analysis of the properties of the various lithologies found in the Lopra-1 well. The data obtained from especially the physical properties logs as exemplified by the values of P-, S- and Stonely-wave, porosity, density and resistivity logs (Table 3) show a much reduced scatter after being separated into the lithological divisions. A strong correlation, most pronounced for the core and to a lesser extent for the crust and sediment beds, is also found between P- and S-wave transit times, P- and S-wave transit times versus density, P- and S-wave transit times versus porosity, and density versus porosity. Examples are presented in Figs 4 and 5 where six cross-plots with associated histograms and statistical parameters show the benefit

of dividing the geological column into the suggested lithological units.

The relationship between the physical properties of the lithological units and depth has been examined and a correlation is observed. The degree of correlation is strongest for the flow units (due to the core values), core, sediment/tuff layers, dolerite dykes and to a lesser extent for crust and compound flows. P-sonic transit time curves are illustrated versus depth for the different lithologies as an example (Fig. 6). There it is seen that especially the sonic transit time increases with depth for the flow units and a first order regression line has been estimated as P-sonic = 58.1370–0.0022 × depth measured in metres or P-sonic = 58.0934–0.0007 × depth when depth is measured in feet. Likewise a first order regression line estimated for the cores is P-sonic = 54.0165–0.0012 × depth in metres and P-sonic = 54.7769–0.0011 × depth for depths measured in feet. This observation is in accordance with general findings made by Kern & Richter (1979).

The sediment/tuff layers also show a significant correlation with depth and in general terms the crust does too, whereas the compound flows show no systematic variation. A depth relation for dolerite dykes is not justified because of their limited numbers.

The potassium and CGR gamma ray logs show a strong response to the sediment beds, but there is otherwise no correlation between the geochemical logs and the individual flow units. This probably indicates that the geochemical values are related to the original composition of the flow units, which varies strongly, suggesting that one magma type may represent more than one flow unit. This can be illustrated by analysing the thorium content in relation to flow units and compound flows as defined by the petrophysical logs. The intervals covering the dolerite dykes are not included in this part of the study as they are reported to be later intrusions (Hald & Waagstein 1984). The thorium log data have been block averaged into three groups according to their thorium content (group 1 consisting of 72 flow and compound flow units with a thorium content of 0.0–1.0 ppm; group 2 containing 21 flow and compound flow units with 1.0–2.0 ppm Th; group 3 with 11 flow and compound flow units representing a content of 2.0–3.0 ppm Th). This results in 36 groups, tentatively interpreted as flow fields (Enclosure 1). Some flow fields are constructed of a number of flows and compound flow units, but 57% of the flow fields constitute one flow or compound flow unit (Fig. 7). The individual flow fields are separated by sediment/tuff layers in 70% of cases. Since this study is an analysis of the basalt column based primarily on a lithological division from petrophysical logs, further statistical treatment of the geochemical logs is outside its scope and probably should be done by dividing the lava flows into those with high, medium and low radioactivity.

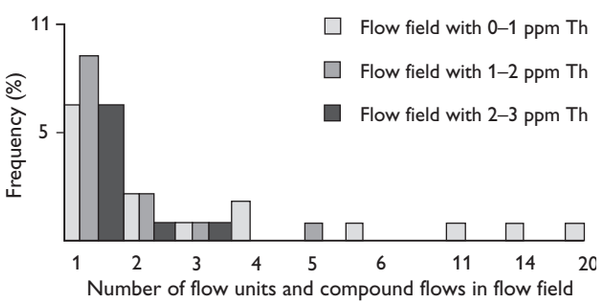

Fig. 7. Frequency diagram illustrating the distribution of the number of flow units or compound flows versus thorium content included in the inferred flow fields. The flow units and compound flows have been grouped into three depending on their thorium content.

Discussion

The flood basalt pile in the interval 200–2486 m depth in the Lopra-1 well has been divided into lithological units based on the wire-line logging (Enclosure 1). Eighty-six flow units consisting of porous crust and massive core (including basal zones), 18 compound flows and two dolerite dykes have been recognised using petrophysical logs (transit time of P-, S- and Stonely-waves, NPHI-porosity, density, resistivity and calliper). Fifty-two sedimentary/tuff layers have been identified mainly by potassium, CGS and SGR gamma logs supplemented by the petrophysical logs. Thirty-seven flow fields have been suggested based on the thorium log in combination with the petrophysical logs.

The flow units have been subdivided into three parts on criteria proposed by various workers based on field evidence or wire-line logs from basalt covered regions (e.g. Planke 1994; Planke & Flovenz 1996; Waagstein 1999). The Lopra-1 results reveal that overall the crust, core and basal zones are similar to other basalt covered areas reported using wire-line log studies, but there are some differences. To describe the crusts as showing a downward increase in density and resistivity, a decrease in porosity and P- and S-wave transit times is too simple. The downward increase in density values is commonly replaced by zones of decreasing values, probably reflecting the presence of vesicular or fractured zones. Likewise the previously reported behaviour of the core as being rather uniform although most massive in its middle part (e.g. Planke 1994) is far from true for the flows of the Lopra-1 well.

Two types of core are commonly present, one type with a 'massive' central part where the logs indicate that only the central part is truly massive. This type, which represents 12% of the flow units, is generally thin, and the crust is of the same thickness as the core. The other type is characterised by varying numbers of zones of high porosity/low density whose relative depth within the core also varies. In these flow units the thickness of the core is at least 70% of the total thickness of the flow unit, and the flow units themselves are of different thicknesses. This zonation is interpreted as vesicular or perhaps occasionally fractured zones. The presence of vesicular zones has been reported by McMillan *et al.* (1987) and Walker (1989). Walker (1989) described the vesicular zonation from spongy pahoehoe lava in Hawaii and mentioned that aa-type lava can also contain vesicular zones. This raises the question whether cores of pahoehoe lavas can be distinguished from those of aa-type lava. Most papers distinguish aa from pahoehoe using surface morphology and perhaps the vertical thickness of the basal zone (Waagstein 1999). Unfortunately surface morphology is not revealed by the present logging suite, and the vertical thicknesses of the basal zone are too small to be treated on their own in the present study. However, Hald & Waagstein (1984) reported that the majority of basalt from the shallower part of the Lopra-1 well was aa-type lava and that pahoehoe lava in the field seems to have a similar crust and core relationship. It is therefore tentatively suggested that flow units with vesicles may represent aa-type flows, and that the flow units where the crust and core are of the same thickness and the core is massive are pahoehoe type. However only a few studies have dealt with the question of how a flow unit is formed in relation to its distribution of vesicles and cooling history based on cross-sections.

The present study has identified 86 flow units and 18 compound flows compared with the 87 reported by Waagstein *et al.* (1982) and Hald & Waagstein (1984). Flow thicknesses of 10–15 m (23%) are most common followed by thicknesses of 15–20 m (18%) (Fig. 3). Thus the flow unit thicknesses reported here are slightly higher than those of Hald & Waagstein (1984).

Five flow units of different thickness – tentatively interpreted as aa-type – were chosen by using the transit time of the P-wave, calliper, NPHI-porosity, density, thorium and gamma ray (CGR) logs to analyse the thickness of the flow units (Fig. 1). The petrophysical logs show clearly that different values are ascribed to the crust and core. The expected overall trend of the flow unit in relation to the petrophysical logs is valid. The P-wave transit time in the core is rather constant and not dependent on the thickness of the core and thus of the flow unit. In contrast to the transit time, the NPHI-porosity and density varies, and in the flow units chosen the density seems to increase and the porosity decrease with thickness of the core and thus of the flow unit. That the transit time is independent of the thickness of the core and thus of the flow unit is somewhat different from the results presented by Planke (1994) from a seaward dipping reflector sequence. The behaviour of the radioactive gamma ray and potassium logs in Lopra-1 also differs as they do not show the cyclicity found in the seaward dipping reflectors studied by Planke (1994). Whether this indicates different depositional settings, lava types, magma type, weathering conditions or the fact that fresh water is encountered in the Lopra-1 well is uncertain.

Eighteen compound flows, characterised by similar values of the logs reflecting the physical properties as the crust, have been interpreted. However a cyclic behaviour similar to that in the flow units can be recognised within the compound flows although the values of the P- and S-wave transit time, density, porosity and resistivity are lower than in the flow units. It is suggested that the compound flows represent a number of thin flows or the toes of flow units.

Two dolerite dykes were encountered and are characterised by the lowest values of SGR and CGR gamma ray, P- and S-wave transit time and porosity combined with the highest level of resistivity, high values of density and a constant level of the Stonely-wave transit time curve. The sonic P- and S-transit time logs and the density, porosity and resistivity curves show a cyclic behaviour resembling the pattern of a flow unit, and it is speculated that the dyke intervals represent a group of thinner dykes.

Fifty-two sedimentary layers have been detected by the combination of potassium, CGR and SGR gamma log, transit time logs of P-, S- and Stonely-waves, NPHI-porosity, density, resistivity and calliper logs. The sediments have been identified on the basis of a locally high spike of the potassium log value in combination with a gamma ray spike larger than 25 GAPI, high values of transit time of P-, S- and Stonely-waves, high values of the NPHI-porosity and low values of the density and resistivity. The number of sedimentary layers is greater than reported by Hald & Waagstein (1984) and Nielsen *et al.* (1984) who reported 27 sediment layers based on the combination of cuttings and geophysical logs acquired in 1981. Of the 27 sediment layers identified by Hald & Waagstein (1984), the recently acquired geophysical logs used in the present study have confirmed 22 of them.

The sedimentary layers are thought to have formed during periods of quiescent volcanism. In that case, at least 51 periods of quiescence occurred in the interval from

184 to 2484 m depth in the Lopra area. Mostly a single flow unit was extruded between each pause, but up to eight flows are found within one interval. The enlarged number of sediment layers indicates that the time intervals between eruptions taking place were shorter than previously thought and thus the extrusion rate of basalt was faster than previously assumed. The amount of basalt produced between the periods of quiescence, measured by the thickness of the flow unit, differs markedly at different depths in the Lopra-1 well. This may indicate that the thickness of basalt produced by a single eruption differed, but to confirm this the location and extension of each eruption needs to be known. The geochemical logs, especially the thorium log, show numerous fluctuations indicating the presence of some highly radioactive basalt flows, similar to those reported in the Deccan Trap area by Buckley & Oliver (1990). To try to systematise these fluctuations three intervals have been defined (0–1 ppm, 1–2 ppm and 2–3 ppm), and the column was subdivided at the same time into smaller units that appear to correlate with the flow units and sedimentary beds, and on this basis it is suggested that a minimum of 36 units exists. This suggests that 36 different compositions of magma have been present during the time represented by the Lopra-1 well, and tentatively it is suggested that a minimum of 36 flow fields exists.

Table 2 lists results of other studies of subaerially extruded basalts whereas Table 3 contains the statistical values of the Lopra-1 well wire-line log data from this study. The Lopra-1 results, which are more detailed due to the subdivision into the suggested lithology units, the large thickness of basalt and the extensive logging suite, are in overall agreement with the range of results obtained from the literature survey. Some scattering in measured values exists; however, the amount of data is not sufficient to conclude whether it is the primary volcanic setting or post-depositional processes that are responsible for these differences.

At a depth of approximately 2417 m, the cyclic nature of the wire-line log curves representing the physical properties of the basalt terminates abruptly, and an increase in transit times and porosity combined with a decrease in density signal a transition into the non-subaerially extruded basalt sequence below this level. The transition generates a negative seismic reflection from this level. It is concluded that the negative reflection interpreted from the VSP by Kiørboe & Pedersen (1995) corresponds to the base of the subaerially extruded basalt. The total known thickness of the flood basalt on the Faroe Islands can therefore be increased by 250 m.

Conclusions

The study shows that it is possible to use wire-line logging combined with results from work carried out in flood basalt regions in other parts of the world to divide the subaerial plateau basalts drilled in the Lopra-1 well into a number of lithological units. Fifty-two sedimentary layers have been identified using geochemical logs supplemented by the logs representing physical properties. Eighty-six basaltic flow units (consisting of a vesicular crust, a massive or partly vesicular core and a thin basal zone), 18 compound flows and two dolerite dykes have been identified using the logs representing physical properties supplemented by the geochemical logs. Tentative aa and pahoehoe lava types are suggested, among which the aa lava is the most common. The geochemical logs appear to respond to the composition of the magma rather than reflecting individual flow units, and it is suggested that the Lopra-1 well penetrated a minimum of 36 flow fields. The present subdivision of the lithology is strongly supported by statistical analysis of the logged physical parameters and shows that a pronounced reduction in data scatter is obtained when the basalts are studied as individual units. Thus the study presents consistent and detailed information about the lower series of the Faroe plateau basalts that has led both to new results and results in greater detail than was previous known, which is of benefit in geophysical and geological studies of basalt and pre-basalt geology.

Acknowledgements

Thanks are due to the Lopra consortium and the Geological Survey of Denmark and Greenland for access to the wire-line log data. Thanks are due to Dr. H. Delius for assistance in correcting the resistivity logs. Thanks are due the reviewers Professor Dr. D. Goldberg and Professor Dr. P.K. Harvey for valuable and constructive suggestions that have improved the content. J.A. Chalmers is thanked for valuable suggestions that improved the language. Landmark is acknowledged for the University Grant issued to the Geological Institute, University of Copenhagen.

References

Berlitz, R. *et al.* 1988: Log interpretation in igneous and metamorphic rocks with five case studies. Technical Review **36**, 30–47.

Berthelsen, O., Noe-Nygaard, A. & Rasmussen, J. (eds) 1984: The deep drilling project 1980–1981 in the Faeroe Islands. Annales

Societatis Scientiarum Faeroensis, Supplementum **IX**, 158 pp. Tórshavn: Føroya Fróðskaparfelag.

Buckley, D.K. & Oliver, D. 1990: Geophysical logging of water exploration boreholes in the Deccan Traps, central India. In: Hurst, A., Lovell, M.A & Morton, A.C. (eds): Geological application of wire-line logs. Geological Society Special Publication (London) **48**, 153–161.

Cashman, K.V. & Kauahikaua, J.P. 1997: Reevaluation of vesicle distribution in basaltic lava flows. Geology **25**, 419–422.

Christensen, N. 1996: Poisson's ratio and crustal seismology. Journal of Geophysical Research **101**(B2), 3139–3156.

Goldberg, D.S., Reynolds, D.J., Williams, C.F., Witte, W.K., Olsen, P.E. & Kent, D.V. 1994: Well logging results from the Newark Rift Basin Coring Project. Scientific Drilling **4**, 267–279.

Hald, N. & Waagstein, R. 1984: Lithology and chemistry of a 2 km-sequence of Lower Tertiary tholeiitic lavas drilled on Suðuroy, Faeroe Islands (Lopra-1). In: Berthelsen, O., Noe-Nygaard, A. & Rasmussen, J. (eds): The deep drilling project 1980–1981 in the Faeroe Islands. Annales Societatis Scientiarum Faeroensis, Supplementum **IX**, 15–38. Tórshavn: Føroya Fróðskaparfelag.

Kern, H. & Richter, A. 1979: Compressional and shear wave velocities at high temperature and confining pressure in basalts from the Faeroe Islands. Tectonophysics **54**, 231–252.

Kiørboe, L.V. & Pedersen, S.A. 1995: VSP seismic experiment in the Faeroes. In: Scrutton, R.A. *et al.* (eds): The tectonics, sedimentation and palaeoceanography of the North Atlantic region. Geological Society Special Publication (London) **90**, 111–123.

Lund, J. 1983: Biostratigraphy of interbasaltic coals from the Faeroe Islands. In: Bott, M.H.P. *et al.* (eds): Structure and development of the Greenland–Scotland Ridge. NATO Conference Series **IV**: Marine Science, 417–423. New York/London: Plenum Press.

McMillan, K., Randal, C.W. & Long P.E. 1987: Two-stage vesiculation in the Cohassett flow of the Grande Ronde Basalt, south-central Washington. Geology **15**, 809–812.

Nielsen, P.H., Stefánsson, V. & Tulinius, H. 1984: Geophysical logs from Lopra-1 and Vestmanna-1. In: Berthelsen, O., Noe-Nygaard, A. & Rasmussen, J. (eds): The deep drilling project 1980–1981 in the Faeroe Islands. Annales Societatis Scientiarum Faeroensis, Supplementum **IX**, 115–135. Tórshavn: Føroya Fróðskaparfelag.

Planke, S. 1994: Geophysical response of flood basalts from analysis of wire-line logs. Ocean Drilling Program Site 642, Vøring volcanic margin. Journal of Geophysical Research **99**(B5), 9279–9296.

Planke, S. & Flovenz, O.G. 1996: Seismic properties of flood basalt (extended abstract), 6 pp. Geophysics for lithology predictions. Kristiansand: Norwegian Petroleum Society.

Rasmussen, J. & Noe-Nygaard, A. 1969: Beskrivelse til geologisk kort over Færøerne i målestok 1:50 000. Danmarks Geologiske Undersøgelse 1. Række **24**, 370 pp. + map vol. (with summaries in Faeroese and English).

Rasmussen, J. & Noe-Nygaard, A. 1970: Geology of the Faeroe Islands (pre-Quaternary). Danmarks Geologiske Undersøgelse 1. Række **25**, 142 pp.

Rasmussen, J. & Noe-Nygaard, A. 1990: The origin of the Faeroe islands in text, pictures and on maps, 64 pp., 6 maps at 1:50 000. Copenhagen: Geological Survey of Denmark (also text in Faeroese and Danish).

Rider, M. 1996: The geological interpretation of well logs, 2nd edition, 256 pp. Houston, Texas: Gulf Publishing.

Sanyal, S.K., Juprasert, S. & Jubasche, M. 1980: An evaluation of a rhyolite-basalt-volcanic ash sequence from well logs. Log Analyst **21**, 3–9.

Self, S., Thordarson, T. & Keszthelyi, L. 1997: Emplacement of continental flood basalt lava flows. In: Mahonney, J.J. & Coffin, M.F (eds): Large igneous provinces: continental, oceanic and planetary flood volcanism. American Geophysical Union Geophysical Monograph **100**, 381–410.

Singh, S.C. 1996: Delineation of basaltic lava flows through geophysical logging. Gondwana Geological Magazine Supplemented **2**, 539 only.

Thordarson, T. & Self, S. 1998: The Roza Member, Columbia River Basalt Group. A gigantic pahoehoe lava flow field formed by endogenous processes? Journal of Geophysical Research **103**, 411–445.

Waagstein, R. 1999: A geological field guide to the Palaeogene flood basalts of Suðuroy, Faroe Islands. Danmarks og Grønlands Geologiske Undersøgelse Rapport **1998/130**, 46 pp.

Waagstein, R., Nielsen, P.H., Fine, S. & Hald, N. 1982: Lopra well no. 1, Suðuroy, Faroe Islands. Geological well completion report, 40 pp. Unpublished report, Geological Survey of Denmark, Copenhagen.

Walker, G.P.L. 1989: Spongey pahoehoe in Hawaii: a study of vesicle-distribution patterns in basalt and their significance. Bulletin of Volcanology **51**, 199–209.

Walker, G.P.L. 1991: Structure, origin by injection of lava under surface crust, of tumuli, 'lava rises', 'lava-rise pits', and 'lava-inflation clefts' in Hawaii. Bulletin of Volcanology **53**, 546–558.

Manuscript received 20 June 2000; revision accepted 11 September 2001.

Borehole seismic studies of a volcanic succession from the Lopra-1/1A borehole in the Faroe Islands, northern North Atlantic

Philip Christie, Ian Gollifer and David Cowper

Extruded basalt flows overlying sedimentary sequences present a challenge to hydrocarbon exploration using reflection seismic techniques. The Lopra-1/1A re-entry well on the Faroese island of Suðuroy allowed us to study the seismic characteristics of a thick sequence of basalt flows from well logs and borehole seismic recordings. Data acquired during the deepening operation in 1996 are presented here.

The re-entry well found that the seismic event at 2340 m, prognosed from the pre-drill Vertical Seismic Profile (VSP) as a decrease in impedance, was not base basalt and the deepened well remained within the lower series basalts. Nonetheless, compressional and shear sonic logs and a density log were recorded over the full open hole interval. These allowed a firm tie to be made with the reflected wavefield from a new VSP. The sonic logs show a compressional to shear wavespeed ratio of 1.84 which is almost constant with depth. Sonic compressional wavespeeds are 3% higher than seismic velocities, suggesting dispersion in the basalt flows. Azimuthal anisotropy was weakly indicated by the shear sonic log but its orientation is consistent with the directions of mapped master joints in the vicinity of the well.

The VSP downgoing compressional wavelet shows good persistence, retaining a dominant period of 28 ms at 3510 m depth. Average vertical velocity is 5248 m/s, higher than previously reported. Attenuation can largely be modelled by geometrical spreading and scattering loss, consistent with other studies. Within the piled flows, the effective Q from scattering is about 35. Elastic layered medium modelling shows some hope that a mode-converted shear wave may be observed at moderate offsets. Like its predecessor, the 1996 VSP indicates a decrease in impedance below the final depth of the well. However, it is unlikely to be basement or sediment and is probably an event within the volcanic sequence.

Keywords: Faroe Islands, Lopra-1/1A borehole, basalt, vertical seismic profile, seismic attenuation

---

P.C., *Schlumberger Cambridge Research, High Cross, Madingley Road, Cambridge CB3 0El, UK.* Formerly: *on secondment to BP, Farburn Industrial Estate, Dyce, Aberdeen AB21 7PB, UK.* E-mail: *pafc1@slb.com*

I.G., *Fugro-Jason UK Ltd., Unit B Kettock Lodge, Campus 2, Aberdeen Science & Technology Park, Balgownie Road, Bridge of Don, Aberdeen AB22 8GU, UK.* (Formerly: *Schlumberger GeoQuest, c/o BP, Farburn Industrial Estate, Dyce, Aberdeen AB21 7PB, UK.*)

D.C., *BP Egypt, 14 Road 252, Digla, Ma'adi, Cairo, Egypt.* (Formerly: *BP, Farburn Industrial Estate, Dyce, Aberdeen AB21 7PB, UK.)*

The North Atlantic igneous province, of which the Faroe Islands are a part, has been estimated to comprise 10 million km^3 of intruded and extruded basaltic igneous rocks (White & McKenzie 1989). They were emplaced by the processes of rifting and sea-floor spreading which resulted in the opening of this northern part of the Atlantic Ocean. The basalts, which were extruded in a relatively short period of time in the early Palaeogene, cover pre-existing sedimentary rocks which may well be prospective hydrocarbon traps. However, the difficulty of using reflection seismic imaging to probe beneath basalts has been recognised for some time and motivates studies into the characteristics of basalt flows which are relevant for seismic wave propagation. Such studies rely on boreholes which have penetrated significant amounts of basaltic material and in which good quality geophysical logs have been recorded. The Lopra-1/1A research well, on the Faroe Islands, is one such borehole which not only has good quality logs but also has a Vertical Seismic Profile (VSP).

The Lopra-1/1A well-site is located near to the coastline on an isthmus on the southern Faroese island of Suðuroy. The exposed basalt sequence on the Faroe Islands has been divided into a lower, a middle and an upper series, each about 1 km in thickness (Rasmussen & Noe-Nygaard 1970, 1990). The 3 km of exposed lava flows in the Faroe Islands are tholeiitic flood basalts whose extrusion was contemporaneous with the opening of the Norwegian–Greenland Sea in the Palaeogene. The exposed and drilled lower series lava sequence is dated to about 56–59 Ma (Larsen *et al.* 1999) and is characterised by flows with an average thickness of 20 m, thought to have originated from fissure eruption sites with a NW–SE trend (Rasmussen & Noe-Nygaard 1970; Kiørboe & Petersen 1995). The basalt flows dip to the north-east and the area around the Lopra-1/1A well-site has mapped sets of near-vertical master joints trending NW–SE and NE–SW. The Lopra-1/1A location was selected for probing the deep basalt layers and their substrata because the ground surface is about 750 m below the top of the lower series.

The Lopra-1 research borehole was originally drilled to a total depth (TD) of 2178 m in 1981. It was logged and suspended with most of the drilled interval left uncased. The well was surveyed by the Geological Survey of Denmark with a zero-offset VSP and a walkaway VSP, acquired by Prakla-Seismos, in 1988. A refraction profile was acquired by the Faroe Islands Natural History Museum and the University of Bergen in 1989. The results and interpretation are summarised by Kiørboe & Petersen (1995). In 1996, the well was re-entered and deepened in a number of stages by the Lopra Deepening Consortium. The original well was extended to 3158 m KB (measured depth relative to the Kelly Bushing) using a larger rig with KB 16.2 m above mean sea level, retaining the original name Lopra-1. For technical reasons, a side-track, Lopra-1A, was drilled from 3091 m KB to TD at 3565 m KB. The well was logged several times during drilling, and logs were run in both the side-track and the original well. In this paper, we deal with data from a composite of the log runs in both the 1 and 1A wells, and therefore we use the name Lopra-1/1A re-entry well or the Lopra-1/1A deepening for the combined extensions drilled in 1996.

One goal of the Lopra project was the seismic characterisation of piled basalt flows. In the event that significant siliciclastic sediments were encountered beneath the basalt sequence, the consortium partners had agreed on a programme of multiple-azimuth, walkaway VSPs to characterise the properties of compressional and shear wave transmission and reflection at a basalt-sediment contact as functions of both the vertical polar angle and the horizontal azimuthal angle. Layered systems of high velocity contrasts, such as basalt flows, are expected to exhibit transverse isotropy with an axis of symmetry perpendicular to the layering, at wavelengths long compared to the layer thickness. Such anisotropy has its fastest velocity in the direction parallel to the layering. Kiørboe & Petersen (1995) had reported velocities higher in the vertical direction than the horizontal and offered an explanation in vertical fractures around basalt columns, possibly in combination with the nearly vertical master joints. Such vertical fractures, if aligned, would be expected to result in an azimuthal variation of seismic velocity which should be fastest in the direction parallel to the fractures.

In fact, neither sediment nor basement was encountered in the well and so the borehole seismic programme was confined to a short-offset VSP and check shot survey designed to measure the short offset reflectivity at the well and to identify depths of intermediate reflectors penetrated by the bit. In particular, Kiørboe & Petersen (1995) had reported a reflection on the VSP at an interpreted depth of 2340 m which was thought to result from a decrease in impedance. Such a reversal in impedance might have corresponded to the base of basalt/top of sediment but turned out not to be the case. Further objectives of the borehole seismic analysis were to calibrate the sonic log, thereby providing a detailed velocity-depth model, and to estimate the seismic attenuation of the basalt sequence.

The VSP was complemented by the acquisition over the full interval of the well of compressional (P) and shear (S) wave sonic logs, acquired in four component mode to estimate azimuthal anisotropy parameters (Esmersoy *et al.* 1994), and a density log. The log data enabled a good well-tie to be made and allowed a modelling study to sup-

port estimates of anisotropy parameters and attenuation.

This paper presents a summary of the data acquisition, compares the results with those reported in previous studies and discusses their interpretation in the context of the seismic characteristics of piled basalt flows. It draws upon previously unpublished data and reports analysed and compiled by the authors for BP, their Atlantic Margin partner Shell, and their associates in the Lopra Deepening Consortium.

Data acquisition

The earlier VSP surveys (Kiørboe & Petersen 1995) had found evidence for a strong seismic reflector at 2340 m, just below the 1981 TD, interpreted as a reversal in impedance. This event, and other deeper events seen on the VSPs, were targets for the deepening of the well in 1996. Further motivation was given by the discovery of methane and nitrogen at a pressure of 20 bar when the well was re-opened in 1983 (Kiørboe & Petersen 1995). As mentioned above, the contingency plan for the 1996 deepening project called for offset VSPs at multiple azimuths in the event of finding 200 m or more of siliciclastic sediments. Exploring a range of offsets was intended to evaluate the angular dependence of P- to S-mode conversions in transmission within the basalt sequence, and their possible conversion back to P at the top of any basalt-sediment contact encountered. This would test the applicability to the Faroese basalts of PS-mode converted imaging, as later reported by Emsley *et al.* (1998).

Kiørboe & Petersen (1995) had reported that the vertical P-velocity was about 10% faster than the horizontal P-velocity in the upper 800 m of the basalt sequence and appealed to fractures to explain this difference. It was hoped that the new VSP would be able to explore the nature of the vertical and azimuthal anisotropy throughout the interval of the deepened well. The location of the Lopra-1/1A well on an isthmus would have facilitated the use of a marine mobile source but because of the establishment of a fish hatchery in the fjord, the 1996 VSP could not make use of a marine airgun and so twin Vibroseis units were shipped to the Faroe Islands for land walkaway VSPs in different azimuths.

In the event, Lopra-1A TD remained in the lower basalt series and so a short-offset VSP was acquired by Schlumberger on 29 October 1996 from 3510 m KB to 1320 m KB with additional checkshots up to 200 m, using the two Vibroseis sources in tandem. The Vibroseis units swept from 10 Hz to 130 Hz over 16 seconds and 2–4 sweeps were recorded at each level using a sample interval of 2 ms. In addition, checkshots were recorded using an airgun source in a water filled pit to calibrate the Vibroseis transit times. The downhole tool used gimballed triaxial geophones mounted in a sensor package decoupled from the body of the tool. The deepened well was surveyed at 20 m intervals for VSP waveform processing. The cased hole section was surveyed at similar intervals to a point above the cement top where it became clear that the casing was unsupported and no longer well coupled to the formation.

Some logs recorded after drilling the original well were uncertain in their calibration. The sonic log was a cement bond tool with a single source-receiver pair and lacked shear sonic information (Nielsen *et al.* 1984). Since a goal for Lopra-1/1A was to characterise seismic propagation characteristics for basalt flows, a set of new logs were acquired over the original open hole section, prior to setting 7-inch casing and drilling on with a 6.5-inch bit. All the drilled intervals were logged with density, P- and S-sonic from a dipole shear tool in four component mode allowing estimates of azimuthal anisotropy, and a formation microscanner. The logs are not subject to petrophysical interpretation in this paper, but were used for geophysical analysis.

Results

VSP

The raw VSP traces were correlated, edited and vertically summed to produce a stacked trace at each level. The stacked vertical geophone data are displayed in Fig. 1a in one-way time, static corrected to mean sea level. From the top of the VSP down to approximately 1840 m KB, the waveforms following the first arriving compressional wave are affected by borehole reverberations caused by unsupported casing in a hard rock environment with a non-attenuative fluid in the hole. The amplitude data in this interval are treated with caution, though the arrival times appear to be representative of basalt velocity.

Below the cement top, the stacks show good waveform consistency from level to level. Clearly visible are:

A. down-going multiples (parallel to, but later than, the first arrivals);
B. up-going primary reflections, both within and below the drilled interval. These are characterised by an almost linear moveout of equal slope but opposite sign to that of the first arrivals;
C. suggestions of down-going shear energy, with a linear moveout greater than that of the first arrivals;
D. a weak tube-wave (visible only above the cement top).

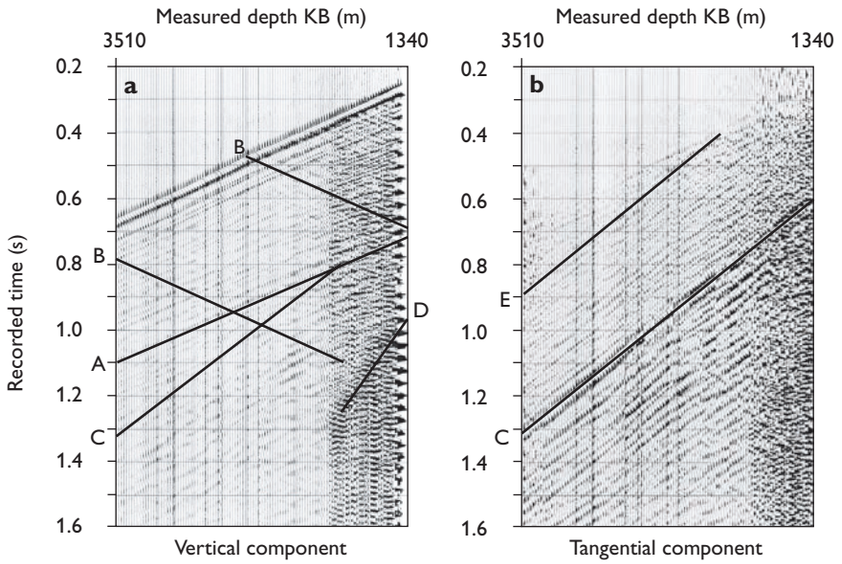

Fig. 1. **a**: Lopra-1/1A VSP: stacked vertical component geophone data. **b**: Lopra-1/1A VSP: stacked tangential component geophone data. Labelled phases are described in the text.

The vertical one-way time from mean sea level to the deepest VSP level at 3510 m KB (equivalent to 3478 m True Vertical Depth Sub-Sea: TVDSS) is 663 ms, corresponding to a compressional velocity of 5248 m/s over the interval. This is higher than values for basalt velocity reported elsewhere in the literature (e.g. Planke & Cambray 1998) and higher than the 4.35 km/s average velocity estimated from the first logs run in Lopra-1 (Nielsen *et al.* 1984). This is partly due to the high velocity dolerites and partly due to the relatively thick flows in Lopra-1/1A, giving a higher thickness ratio of fast, flow-centre material to slower, flow-boundary material. As discussed later, the average compressional wavespeed from the sonic log is slightly higher, supporting the VSP observation.

The trace scaling in Fig. 1a is constant for all levels, revealing the total amplitude loss with depth in the first arrivals. Although the VSP interval, from 3510 m KB to 1320 m KB, comprises 2174.5 m TVD of stacked basalt flows, the amplitude loss from geometrical spreading, scattering and attenuation still leaves a good level of signal above the noise floor in the deepest section.

Fig. 1b shows the Y-component stacks (Y is the horizontal component tangential to the borehole wall) on which the shear energy is most evident. The strongest arrivals are down-going direct shear arrivals, generated by the vertically polarised vibrator acting on the rigid surface. The average shear velocity across the logged interval is about 2900 m/s, resulting in an average V_P/V_S ratio of 1.8, which is in good agreement with the value of 1.84 $\pm$ 0.01 (one standard deviation) estimated below from the sonic log regression of V_S upon V_P.

Also visible on the Y-component stacks are down-going mode-converted shear events, E, generated by impedance contrasts crossed by the drill-bit. These events are parallel to and earlier than the direct shear arrival, C, but originate at the time and depth of the direct compressional wave's encounter with the mode-converting impedance contrast. These arrivals have a frequency content similar to the associated P-wave and higher than the frequency of the direct shear wave due to the lower cumulative attenuation.

Finally, some weak up-going reflected shear events can be seen. No further processing of the shear arrivals has been performed.

The VSP P-wave data were processed through a workflow comprising trace editing, vertical stacking at each depth level, correction to mean sea level, spherical divergence correction, up/down wavefield separation and deconvolution to zero-phase wavelets with bandwidths of 10–70 Hz and 10–40 Hz. The former maximises the resolution at the cost of more high frequency noise, while the latter minimises residual noise at the expense of bandwidth. Correlations of the 10–70 Hz up-going wavefield are presented and discussed in the well-tie section.

Geophysical log data

In this section we examine the 1996 log data and their correlations to infer the seismic properties of the basalt and to compare with the properties of similar basalts penetrated in Hole 917A of the Ocean Drilling Programme, as reported by Planke & Cambray (1998).

The P- and S-sonic and density logs, spliced from the

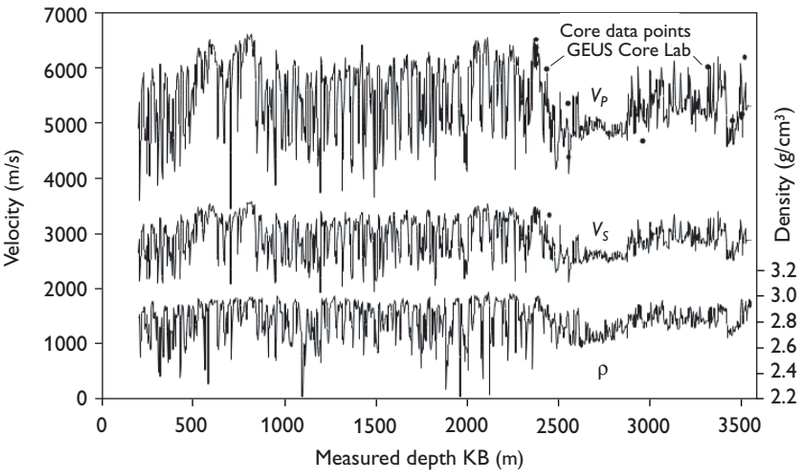

Fig. 2. P-velocity, S-velocity and density logs, upscaled to 3 m sample interval using a Backus average (Backus 1962) and displayed in measured depth relative to KB. Core points are plotted from data supplied by GEUS for comparison.

several logging runs made in the 1 and 1A wells, are shown in Fig. 2 on a measured depth scale relative to KB. The well is close to vertical, so no true vertical depth corrections have been made for this part of the analysis. The logged section comprises 3371 m, with the dipole shear tool logged in four-component mode together with the density tool. The logs are of good quality and allow the identification of many subaerially emplaced flows over much of the section. Figure 2 shows the P- and S-velocity and density logs after re-sampling the data to 3 m using a Backus average (Backus 1962; Folstad & Schoenberg 1992). There are wide variations in P- and S-velocities, in an asymmetric, quasi-periodic manner, though the mean velocities are very consistent over the well. The boundaries of each flow are characterised by a shift to lower velocities and density, caused by the formation of vesicles at the top and base of the flow (Planke & Cambray 1998), and possibly in places by weathering, alteration and rubble. The main exceptions to this character are the high velocity dolerite intrusions, encountered at about 600 m KB and 770 m KB, and the zone of almost constant velocity and density between about 2600 m KB and 2900 m KB, corresponding to a thick, hyaloclastite sequence.

The dots near the compressional velocity log (Vp in Fig. 2) mark depths and values of ultrasonic measurements of P-wave velocity made by GEUS on a number of core samples. The measurements were taken on 25 mm core samples, pressure-saturated with distilled water and using piezo-electric transducers of centre frequency 1 MHz (2380 m core) and 2.5 MHz (all other cores) at room temperature and pressure. Although the scale of the display makes a visual match difficult, it can be seen that there is generally a good correlation between the core measurements of P-wavespeed and the log data. With only two or three exceptions, at 2218 m KB, 2455 m KB and 2972 m KB, the core measurements are either the same as the log values or a little faster, consistent with dispersion of the higher frequency core measurement compared to the sonic log.

Discussion

Layer-induced anisotropy

Backus upscaling applied to a stack of isotropic layers predicts a transversely isotropic model having a symmetry axis perpendicular to the layers. The upscaled elastic parameters can be recast in terms of Thomsen's (1986) weak anisotropic parameters. Figure 3 shows the modelled values of epsilon (ε), and delta (δ), after upscaling the logs to 3 m. The parameters are given by the relations:

$$\varepsilon = \frac{C_{11} - C_{33}}{2C_{33}}$$

and

$$\delta = \frac{(C_{13} + C_{33})(C_{13} - C_{33} + 2C_{55})}{2C_{33}\,(C_{33} - C_{55})}$$

where

$$C_{33} = \rho V_p^2, \quad C_{55} = \rho V_s^2, \quad C_{13} = C_{33} - 2C_{55}$$

and ρ, V_P and V_S are the Backus-upscaled log values of density, compressional wavespeed and shear wavespeed. Epsilon is the measure of axial compressional anisotropy, while delta controls the off-axis behaviour of the phase velocity near to the vertical. Both enter the following relation from Thomsen (1986) governing the compressional phase velocity behaviour as a function of angle θ to the (vertical) axis of symmetry:

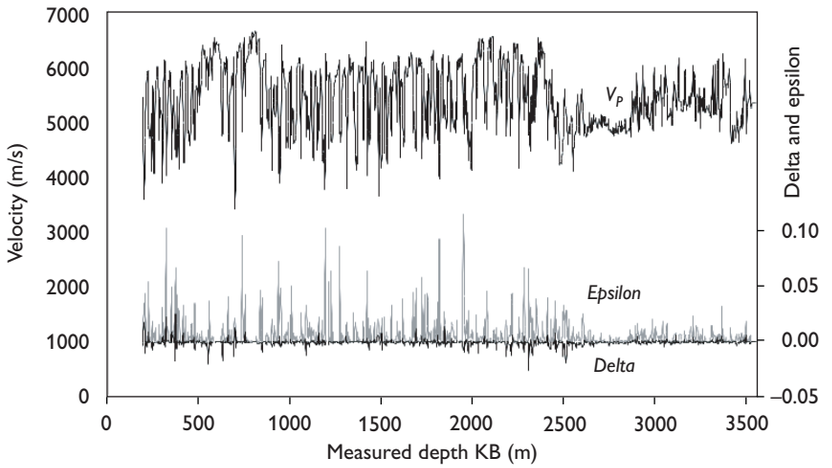

Fig. 3. Log of Thomsen's (1986) weak anisotropic parameters epsilon and delta, modelled from the Backus upscaling of the 15 cm logs to 3 m, assuming isotropic individual layers. The compressional sonic velocity is shown for correlation, also upscaled to 3 m.

$$V_P(\theta) \approx V_P(0)(1 + \delta \sin^2(\theta) \cos^2(\theta) + \varepsilon \sin^4(\theta))$$

In Fig. 3, the anisotropic parameters are greatest where the logs show the most variance over the 3 m averaging interval. They indicate only the layering component of the anisotropy since we have no data on the intrinsic anisotropy of the basalt. However, delta is small with a mean of zero while epsilon is positive with most values less than 0.05 and almost all values less than 0.1. We found a similar range of epsilon and delta when the averaging interval was increased to 10 m. This means that the modelled effect of layering is to produce horizontal compressional wavespeeds around 5% faster than vertical wavespeeds, a prediction which contradicts the observation by Kiørboe & Petersen (1995) of vertical compressional wavespeeds being about 10% higher than horizontal compressional wavespeeds in the upper 800 m of the basalt beds. Kiørboe & Petersen (1995) appeal to vertical fractures associated with columnar basalts and master joints to explain their observation, a point which we discuss below.

Azimuthal anisotropy direction

Aligned vertical fractures would be expected to result in azimuthal anisotropy. To test for this in Lopra-1/1A, the dipole shear sonic tool was logged in four-component mode whereby both of the two orthogonal dipole receiver arrays recorded signals from each of the two orthogonal dipole sources, energised sequentially. The data were processed for the presence of fast and slow shear waves corresponding to shear propagation along the borehole with polarisations parallel and perpendicular to the assumed fractures. One output of the azimuthal processing is a log of the azimuth of the fast shear wave. The direction of the fast shear wave is found by determining the shear waveform rotation which minimises the cross-energy, for example the energy recorded by the Y-polarised receiver from the X-polarised source (Esmersoy *et al.* 1994), then picking the faster of the two shear estimates. The difference in cross-energy between its maximum and minimum excursions as a function of rotation angle is a measure of reliability of the anisotropy estimate. In Figs 4a and 4b we plot the fast shear direction results in different depth intervals, where the vector from the centre of the plot to a given depth point has an azimuth corresponding to that of the fast shear polarisation and a magnitude corresponding to the cross-energy difference normalised by the total energy. In order to display only the most reliable estimates of the fast shear direction, the estimates were windowed according to cut-off values of calliper reading, the estimated error in azimuth, the anisotropy estimate and the normalised cross-energy difference (cut-off values indicated on the figure). The plots are radially symmetric through the origin because of the 180° ambiguity in determining azimuth. In Fig. 4a, from 511–540 m KB, we see that there is a well-defined fast shear direction at N31°E, broadly consistent with the NE–SW strike of one of the two mapped master joint sets (Kiørboe & Petersen 1995, fig. 1). Below 540 m KB, the fast shear direction rotates through 100° to N131°E, although this direction is less well defined. In Fig. 4b, there is a fairly consistent fast shear direction of about N144°E in the interval 2991–3502 m KB, but with a larger scatter in azimuth. The cross-energy cut-off value in Fig. 4b has been reduced, compared to Fig. 4a, to capture more estimates. The estimates of the fast shear direction deeper than 540 m KB are consistent with the NW–SE strike of the second mapped joint set in Kiørboe & Petersen's (1995) fig. 1.

From the earlier VSP and refraction profile data, Kiør-

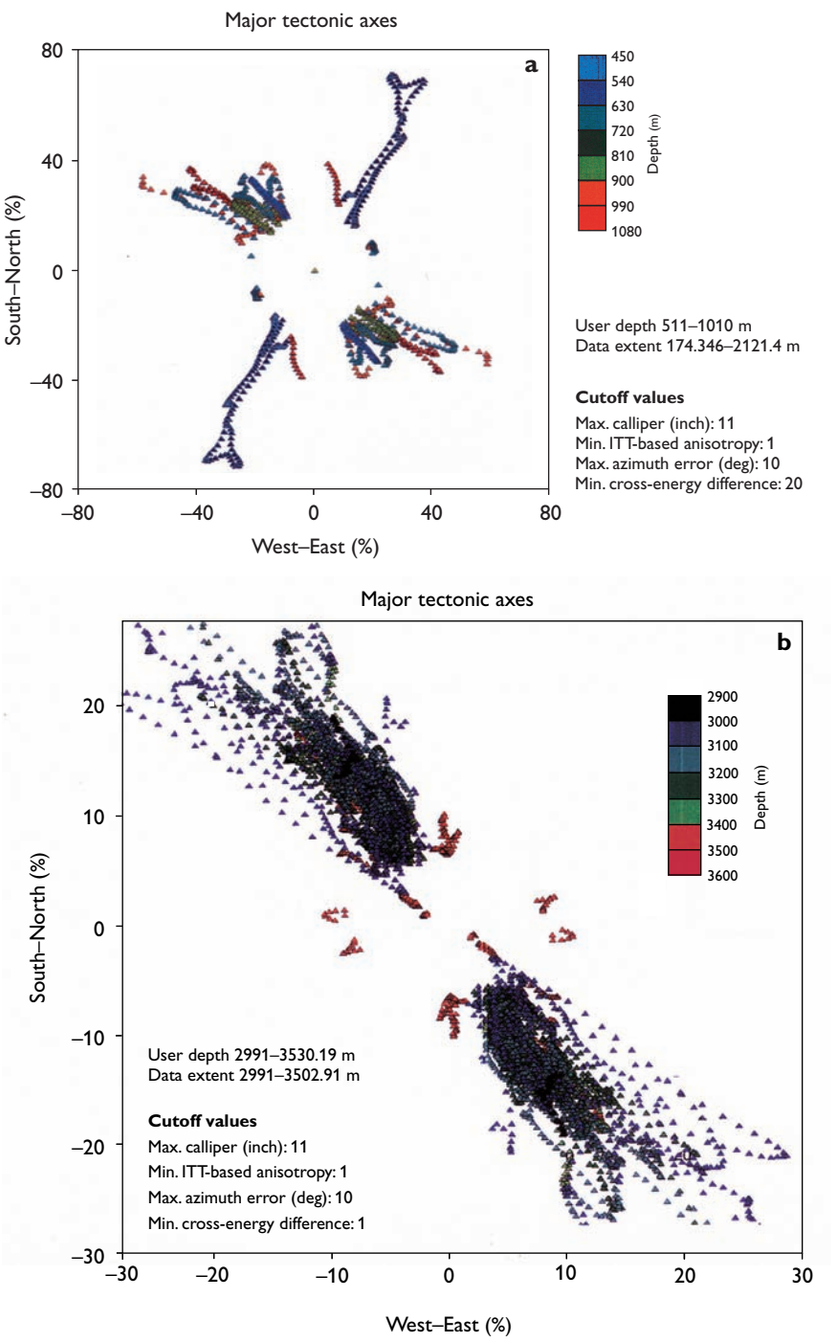

Fig. 4. **a**: Fast shear direction estimated from the dipole shear log over the depth interval 511–1010 m KB. The log was recorded in four component mode and rotated to minimise the cross-energy. Two orthogonal directions are evident. The better-defined direction is over a fairly short interval from 511–540 m KB, consistent with one of the mapped master joints, and parallel to the offset seismic surveys described in Kiørboe & Petersen (1995). **b**: Fast shear direction estimated over the interval 2991–3530 m KB. The fast direction is less well defined than in the shallower interval but is consistent with mapped joints.

boe & Petersen (1995) reported vertical V_P values about 10% higher than horizontal V_P in the upper 800 m of the section around the well and suggested that a combination of vertical, columnar fractures and NW–SE master joints crossing the ray-paths in the refraction profile may be responsible. The present analysis shows little azimuthal anisotropy on the dipole shear log and, while the fast shear direction appears to be N131°E below 540 m KB, there is a well-established, fast shear direction of N31°E from 511–540 m KB. If the shear azimuthal anisotropy results from fractures or stress, then the compressional wavespeed anisotropy should follow the same directions. Formation microscanner data from the Lopra Deepening Project show the presence of sub-horizontal conductive features, suggestive of horizontal fractures, although there is a question as to whether these are natural or drilling induced. The only conventional core (2380 m KB) shows cemented, horizontal fractures (L. Kiørboe, personal communication 1996) but few vertical fractures were observed, consistent with the weak azimuthal anisotropy observed in

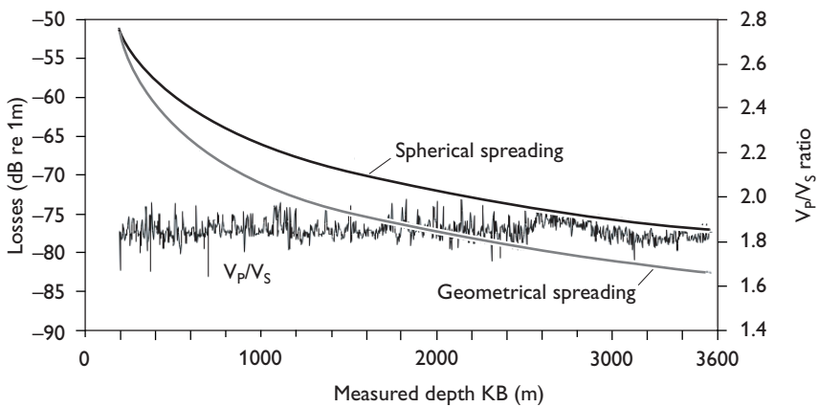

Fig. 5. Plot of logged V_P/V_S ratio and short-offset geometrical spreading computed using Newman's (1973) relation for both the logged velocities and a constant velocity medium. 3 m averaged logs.

the dipole shear log. In addition, the layer-induced anisotropy modelled by upscaling the log data suggests that horizontal compressional wavespeeds should exceed vertical wavespeeds by around 5%. Can we resolve the apparent contradiction? Possible explanations include: (1) the high-wavespeed, dolerite intrusions seen on the logs down to 850 m KB affect the vertical velocity locally; (2) the layering- and fracture-induced anisotropy revealed by the well logs is not representative of the volume sampled by the VSP and earlier refraction profile; (3) the unreversed refraction profile sees low apparent velocities because of the basalt flows that dip 3–7° to the north-east; and (4) there is a mis-correlation of events between the refraction profile and the earlier VSP. Kiørboe & Petersen (1995) reported that a 700 m refraction profile shot towards the WNW from the 1988 VSP source point through the well yielded an apparent V_P of 4.8 km/s, the same as that observed over the offset range 2.3–14 km on the long refraction profile. The azimuth differences of these two profiles weakens the case that structural dip or aligned master joints affect the velocities. That the fractures in the core sample are cemented also discounts the possibility that open, vertical, hexagonal fractures are prevalent, although we cannot disprove this possibility because of the small volumes sampled by core and borehole logs. Our preferred explanation is that the geometry of the dolerite intrusions increases locally the estimate of the vertical velocities at the well. Further support for this hypothesis comes from the well-tie, described below, where there is evidence that the VSP sees a higher velocity than the sonic tool in the shallow section, possibly due to the dolerite intrusions providing a VSP ray-path away from the borehole that is faster than that seen by the sonic tool along the borehole. Kiørboe & Petersen (1995) also found that the velocities derived from the 1988 VSP were too fast to simulate the arrival times on the longer offset data.

Log-derived seismic characteristics and well-tie

In this section we develop further the seismic properties of the stacked basalt flows in Lopra-1/1A as modelled from the log data. Figure 5 displays the V_P/V_S ratio and the normal incidence, two-way geometrical spreading, computed using Newman's (1973) relation:

$$D_{two-way} = 2\frac{\sum d_i V_i}{V_1}$$

for the 3 m Backus-averaged data since there is no expected dependency on sample interval. In this relation, $D_{two-way}$ is the two-way loss, relative to the amplitude at 1 m from the source, of a seismic wave propagating down through a 1D stack of i layers, each of thickness d_i and interval velocity V_i, and back to the surface again. V_1 is the velocity of the first layer and in this case is taken to be 2792 m/s. Because the thickness of the superficial layer between the source and the top of the sonic log is 177.67 m, the two-way loss at the top of the sonic log is:

$$D_{two-way} = -20\log(2 \times 177.67) = -51.01 \text{ dB re 1 m}$$

Figure 5 shows the modelled geometrical spreading in the basalt flows, compared to the spherical loss in a uniform medium for reference. The extra two-way geometrical spreading due to the velocity variations is around 5.5 dB for a reflector at the total depth of the well, resulting in a spreading loss of 82.5 dB re 1 m.

The V_P/V_S ratio from the 3 m averaged logs (Fig. 5) is almost constant over the well at 1.85, with a standard deviation of 0.04. We also cross-plotted the log values of V_P and V_S, upscaled to 1 m to reduce fluctuations, using a Backus average. Figure 6 shows the cross-plot of V_P to V_S with a histogram of each variable indicating the number of data points falling into velocity bins of 100 m/s for V_P

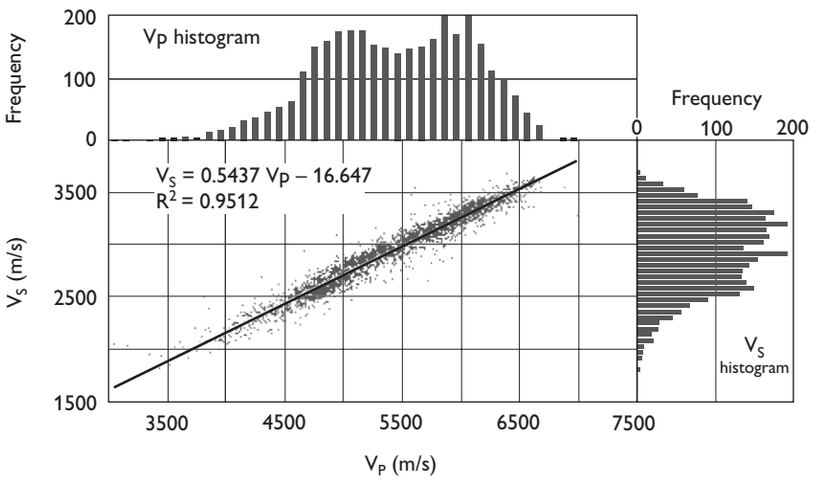

Fig. 6. V_P–V_S cross-plot of 1 m Backus-averaged logs with histograms and linear regression. The histograms show the frequency distributions of V_P and V_S data gathered in bins of 100 m/s and 55 m/s respectively, to maintain the same number of bins for each variable. The regression yields a V_P/V_S ratio of 1.84 with a standard deviation of 0.01. The similarity of the histograms supports the choice of a linear regression.

and 55 m/s for V_S. The bin-widths are scaled approximately by the V_P/V_S ratio, for which a value of 1.84 was obtained by linear regression with a standard deviation of 0.01. The similarity of the histograms supports the linearity of V_P and V_S over such a large range of values. This linearity is consistent with the observation of Planke & Cambray (1998) who studied subaerially emplaced lava piles sampled in Hole 917A of the Ocean Drilling Programme. The absence of a trend, with the possible exception of the hyaloclastite interval from 2600–2850 m KB, suggests that there is no significant compaction effect with depth.

We computed two-way, plane-wave, transmission losses for the 15.24 cm logs as well as for logs Backus-averaged to 30 cm, 50 cm, 1 m, 3 m, 5 m and 10 m (actually, the nearest multiple of 15.24 cm to these values). The transmission losses are the 1D, ray-theoretical loss from a unit amplitude plane-wave source pulse which is partially transmitted and reflected from each interface in its two-way path from the surface to a given reflector and back to the surface again. It is computed from the well-known relation

$$TL = \prod (1 - R_i^2)$$

where R_i is the plane-wave, normal-incidence, reflection coefficient at the i-th boundary

$$R_i = \frac{\rho_{i+1} V_{pi+1} - \rho_i V_{pi}}{\rho_{i+1} V_{pi+1} + \rho_i V_{pi}}$$

and where ρ_i and V_{Pi} are the density and compressional wavespeed of the i-th layer. In this simple model, there is no intrinsic loss. Instead, the loss is due to progressive scattering and consequent removal of energy from the first-arriving, primary pulse. The results are displayed in Fig. 7 along with the V_P log for correlation. Losses over the full interval vary non-linearly from 15 dB (10 m log) to 73 dB (50 cm log), because of the non-linear dependence on the reflection coefficient. The highest loss is seen at the 50 cm sampling. As suggested by O'Doherty & Anstey (1971), an impedance gradient represented by a single large reflection coefficient has more effect on the transmission losses than several smaller coefficients, so very fine sampling (15 cm) can produce a smaller loss than the upscaled logs, as seen here. However, blocking intervals larger than bed thicknesses progressively fail to represent beds at all and so will predict less loss. While there is the expected strong dependency of transmission losses with sample interval, all the curves show broadly similar features, with the lower contrast, hyaloclastite interval below 2600 m KB exhibiting reduced loss compared to the section of high contrast flow units, which resembles the cyclic example in O'Doherty & Anstey (1971) and which is expected to have a high scattering loss.

The combined effects of modelled normal-incidence spreading and plane wave transmission losses range from 97.5 dB to 155.5 dB re 1 m, where the wide margin results from the uncertain effects of the transmission losses. We shall return to this point in the analysis of the VSP amplitudes. However, we emphasise that the loss estimates here are those due to near-normal propagation in a 1D medium. As offset increases, geometrical losses increase rapidly due to refraction effects at high velocity contrast boundaries. Similarly, transmission coefficients vary strongly with incidence angle at high contrast boundaries. The cone of forward propagation of the compressional wave is limited by critical angle effects and offers opportunities for mode conversions to be observed over a wider range of incidence angles and offsets.

The VSP first arrival travel times were picked to derive

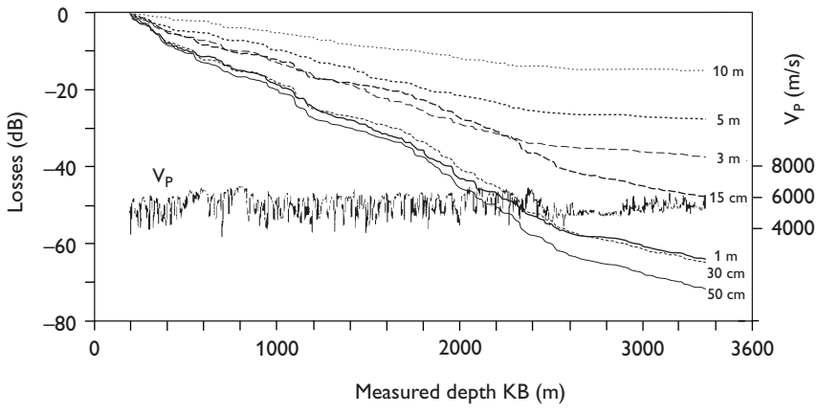

Fig. 7. Modelled plane-wave, normal-incidence, two-way transmission losses as a function of log sampling, together with V_P log for correlation. Losses are non-linear with sampling but show generally similar behaviour with high contrast layering resulting in the greatest scattering loss.

a seismic two-way time to true vertical depth curve. The time–depth curve from the VSP was used to 'calibrate' the TVD-corrected sonic log, provide a fine-scale, seismic time–depth interpolation and to generate a synthetic seismogram. A drift curve was computed by integrating the compressional slowness log between the VSP time-depth pairs and taking the difference between the VSP and sonic interval times. We observed positive drift (VSP interval time greater than sonic) over most of the logged interval. This implies a lack of environmental effects on the sonic (which usually increase the sonic slowness) leaving the normal dispersion effect between seismic and sonic frequencies as the dominant mechanism. Negative drift (sonic interval time greater than VSP) was seen in the shallow part of the well, above 800 m KB. This would be normal in a sedimentary sequence, indicating a washed-out hole or altered, unconsolidated formations. However, in the basalt environment, formation alteration is unlikely; even though the well shallower than 800 m KB is often out of gauge, it is not different from the rest of the borehole drilled in 1981 which displays positive drift. Possible explanations of the negative drift are unreliable VSP picks due to shallow, unsupported casing interference (the compressional wavespeed of the formation is similar to that of the casing extensional mode), or possible refraction along the high velocity (6.5 km/s) dolerite intrusions. If the VSP wave front refracts along the intrusions such that the borehole does not form the VSP raypath, then the VSP interval time will be less than the sonic interval time. In any case, the picks above 800 m have been interpreted in such a way as to avoid undue, and possibly unrealistic, correction to the sonic.

The corrected compressional sonic log was used to convert the shear sonic and the density logs from a common depth scale to a common two-way time scale which is assured to match that of the VSP. Note that this implicitly changes the V_P/V_S ratio, since the VSP was not used to correct the shear sonic slowness values. Deeper than 800 m, the compressional slowness drift is about 15 ms in 2200 m, or 6 µs/m. However, the average interval slowness is about 190 µs/m, so the drift correction is reasonably significant at 3.4% in slowness. Care was taken in choosing the correction points to avoid introducing false reflection events.

The time-based logs drove a 1D model of equal time-thickness layers. The resulting primaries-only, reflection coefficient sequence without transmission losses was convolved with a 40 Hz, zero-phase, Ricker wavelet to create a synthetic seismogram. The synthetic was spliced into the VSP up-going wavefield along the two-way time–depth curve to facilitate event correlation (the right-hand panel of Fig. 8). The VSP has been waveshaped to a zero phase wavelet of bandwidth 10–70 Hz and both the synthetic and VSP traces are displayed in reverse SEG polarity, so that an increase in acoustic impedance with depth is displayed as a black peak. Figure 8 shows the correlation from a Two-Way Time (TWT) of 650 ms, where several events can be seen to tie in time and in character, resulting in an unambiguous correlation. In an igneous province, a tie of this quality is relatively unusual and suggests that the lateral variability of the basalt flows is mild, at least over the extent of a VSP Fresnel zone which is several tens to hundreds of metres, depending on the elevation of the VSP tool above the reflector. Residual ringing from the uncemented casing is visible in the up-going VSP wavefield on the right edge of the section.

Correlations from the well-tie

Using Fig. 8 we discuss the correlation to the lithological summary taken from the Lopra-1/1A End of Well Report (EWR), subsequently modified by R. Waagstein (personal communication 2001). The displayed interval from 650–1430 ms TWT shows V_P, V_S, density and Poisson's

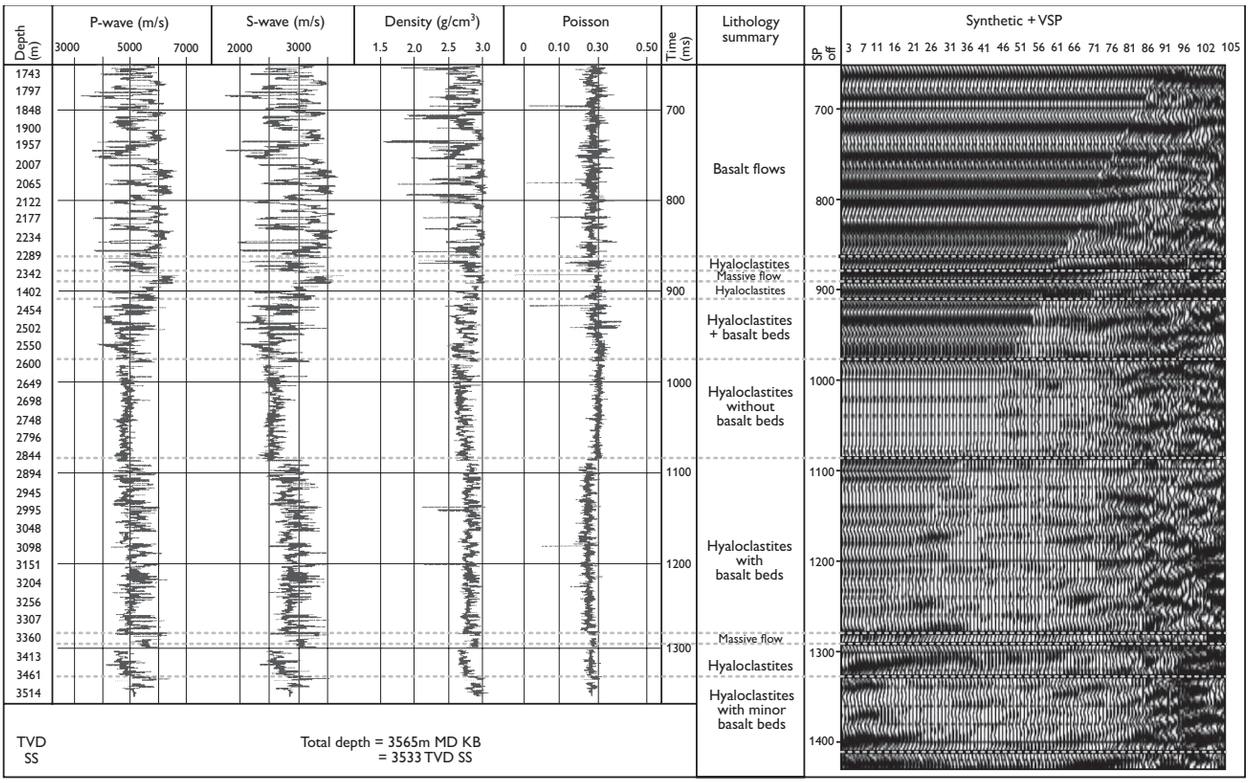

Fig. 8. Correlation of the VSP up-going wavefield with the log-derived, reflection coefficient sequence convolved with a 40 Hz zero-phase Ricker wavelet. The VSP wavefield has been waveshaped to zero phase over the bandwidth 10–70 Hz. The VSP and synthetic are correlated with the time-based logs and lithostratigraphy (R. Waagstein, personal communication 2001) as listed in Table 1.

Ratio logs. At the left edge of the display is a non-linear scale in True Vertical Depth extending from 1714 m to TD at 3533 m TVDSS, which corresponds to 3565 m KB. Horizontal lines mark particular correlations between the well logs, the lithology summary, the synthetic seismogram and the VSP. These correlations are summarised in Table 1 and further comments relating to the pre-drill targets are made below.

From 882–912 ms, the VSP shows a package of strong reflections, with a white trough at 894 ms, seen on the pre-drill VSP at 920 ms and identified as one of the target horizons for the well. This event was prognosed by Kiørboe & Petersen (1995) at 2.34 km, 162 m below the original TD of Lopra-1 and interpreted as a decrease in impedance. In fact, the reflection package comprises at least two near-tuning events. A sharp increase in impedance at 882 ms (2361 m KB, 2345 m TVDSS) corresponds to the top of a massive basalt flow that gives rise to a black peak on the VSP. The trough associated with the sidelobe to this wavelet reinforces a broad, weak trough caused by the decrease in impedance at the base of the flow around 894 ms (2401 m KB, 2385 m TVDSS), which reflects the highly amygdaloidal top of an underlying flow. The reflection package is seen more strongly on the VSP than on the synthetic seismogram, possibly due to lateral heterogeneity near the well.

Another package of strong events was drilled above TD from 1274–1340 ms. During drilling, it was hoped that these reflections, seen at 1350 ms on the pre-deepening VSP (Kiørboe & Petersen 1995), might mark either siliciclastic sediment or basement. However, the sharp drop in impedance at 3427 m KB (3397 m TVDSS) at the base of a thick, massive basalt bed results in the trough at 1294 ms seen on both the VSP and the synthetic, which correlates with another hyaloclastite sequence with a thin tuff at the top (R. Waagstein, personal communication 2001). Another drop in impedance was drilled at 3512 m KB (3480 m TVDSS), which also corresponds to a strong white trough at 1328 ms on both the synthetic and the VSP. It probably corresponds to the event at 1350 ms seen on the pre-drill VSP. It displays moveout to earlier times with decreasing geophone depth, indicating dip of the beds.

Just below TD, at 1412 ms on the VSP, is a persistent, large-amplitude, symmetric, white trough, which may be

Table 1. VSP events

		Lopra-1/1A VSP			VSP before deepening†		Dansk Olie- og Gasproduktion & Dansk Operatørselskab (1997)	
VSP event	Lithological unit*	TWT millisec.	Depth below KB metres	TVDSS metres	TWT millisec.	Depth below KB metres	Depth below KB metres	Lithostratigraphic units
Top of VSP	Basalt flows	496	1320	1304				lower basalt series
	Hyaloclastites	865	2319	2303				
Top of package of strong reflections; sharp increase in impedance	Top massive basalt flow (2361–2401 m)	882	2361	2345				
Decrease in impedance	Amygdaloidal basalt flow (2401–2417 m)	894	2491	2385	920	2340	2398	pillow lava series
Base of package of strong reflections		912						
Moderate reflections	Hyaloclastites with basalt beds	912	2450	2434			2443	pillow debris series + basaltic tuff 1 + tuffaceous sand 1
Top of low reflection interval	Hyaloclastites with no basalt beds	980	2616	2600			2612	basaltic tuff 2 + basaltic sand 1 + tuffs 1–2
Base of low reflection interval	Hyaloclastites with basalt beds	1088	2882	2864			2880	tuffs 3–9
Top of package of strong reflections		1274			1350			
Increase in impedance	Massive basalt bed (3396–3427 m)	1282	3396	3366				basal part of tuff 9
Sharp decrease in impendence	Base massive basalt bed; top hyaloclastites (0.9 m tuff at top)	1294	3427	3397			3426	tuff 10
Bottom of VSP		1326	3510	3478				
Decrease in impedence, dipping bed	Base massive basalt bed (3504–3512 m); hyaloclastites with minor basalt beds (3512–? m)	1328	3512	3480			3512	pre-basaltic tuff series B (tuffs 11–12)
Bottom of package of strong reflections		1340						
TD (total depth of Lopra-1/1A)		1347	3565	3533				
Significant decrease in impedance		1412	3732	3700				

* FMS log interpretation (R. Waagstein, personal communication 2001)
† Kiørboe & Petersen (1995)

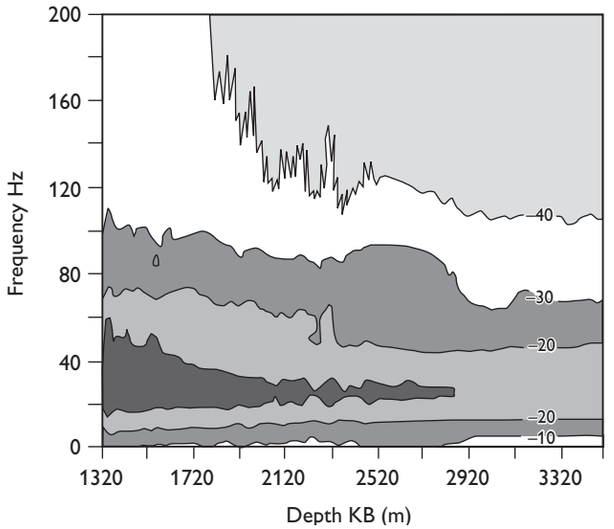

Fig. 9. Contoured power spectrum of the energy in a 150 ms window around the down-going first arrivals in the VSP. The upgoing wavefield was removed first. The contour levels are dB down from the peak value.

interpreted as a significant drop in impedance. This is about 86 ms, or 222 m, below the deepest VSP level at 3510 m KB (3478 m TVDSS) and therefore 167 m below the final TD of 3565 m KB (3533 m TVDSS), assuming an extrapolation velocity of 5150 m/s. The event is as tantalising as that seen at 920 ms on the pre-deepening VSP, which was drilled some 162 m below the original TD of Lopra-1. However, similar, though weaker, 'soft kicks' seen on the seismic data have turned out to be due to contrasts within the volcanic pile and the reflection at 1412 ms TWT is unlikely to be basement, so it is probable that more volcanic sequence lies below the present TD. In contrast with the event at 1328 ms, this strong arrival below TD shows little moveout and suggests low dip.

VSP loss estimates and amplitude modelling

As noted above, ray-theoretical estimates of transmission losses are strongly dependent on the log sampling, so we derived loss estimates from the VSP downwave before turning to full waveform modelling to simulate the observed propagation effects. The contoured power spectrum by depth is shown in Fig. 9, after windowing the first 150 ms of data from the 2 ms sampled downgoing wavefield. Two points are apparent: (1) there is a low-frequency roll-off to the data caused by the start frequency of the vibrator sweep at 10 Hz, (2) there is a smooth decline in frequency content with depth.

We estimated the root mean square (RMS) amplitudes within a window of 150 ms about the VSP first breaks, corrected the amplitudes for geometrical spreading using the spreading loss curve displayed in Fig. 5 and plotted the results in Fig. 10 together with the ray-theoretical transmission losses at 3 m, 5 m and 10 m sampling. Since the amplitude of the VSP top level is arbitrary, we matched the slopes of the transmission loss curves by eye. The VSP amplitude decay curve, after spreading correction, shows a character similar to the modelled transmission losses, although, given our earlier comments on the unreliability of transmission losses, the match to the transmission loss curve at 5 m sampling is probably coincidental. However, the change in slope around 2500 m KB on the modelled curves, which is due to the transition from high contrast basalt beds to low contrast hyaloclastites, is also evident on the VSP. By reciprocity, the transmission seismogram going back up through the basalt sequence is the same as that going down through the sequence. Hence, the reflection seismogram should be the time-delayed, one-sided correlation of the down-going wave. Strictly speaking, the two-way loss estimates should be made after convolving

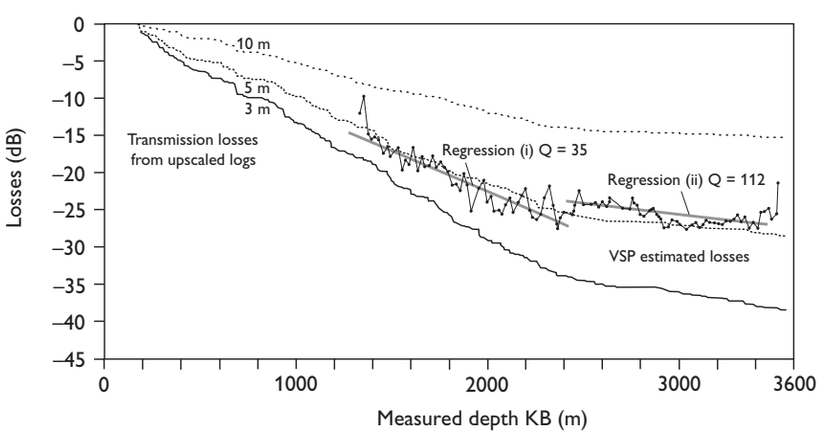

Fig. 10. Losses from RMS amplitudes estimated in 150 ms window around the first arrivals in the VSP, after correcting for geometrical spreading using the log-derived spreading loss estimates from Fig. 5. The first VSP level amplitude is arbitrary and has been selected visually to overlie the upscaled log curve of modelled transmission losses with the most similar slope. Regression lines have been fitted over the VSP intervals indicated to estimate effective Q for a wavelet dominant frequency of 36 Hz.

the down-going wave with itself. Since the amplitude effect of cascaded filters is to take the product of their gain functions, we have approximated the amplitude effect of the two-way propagation by doubling the dB loss estimated from the one-way measurement of RMS time-domain amplitudes.

Because of the change in slope of the transmission loss curves around 2500 m KB, we estimated two effective Q factors to represent the scattering loss. Over the interval of periodic layering, from 1350 m KB to 2450 m KB, we fitted a linear trend and estimated losses corresponding to an effective Q of 35 for a dominant period wavelet of 27.5 ms. The 95% confidence limits on the regression map to a range in effective Q of 32 to 40.

From 2450 m KB to 3510 m KB, the loss curve is reduced and a linear regression resulted in a loss corresponding to an effective Q in excess of 100. The inverse correlation of effective Q values with the change in impedance contrasts further supports the inference that the volcanic sequence has low intrinsic loss and that its attenuation is principally due to scattering. This is consistent with the results of other, similar studies (e.g. Pujol & Smithson 1991) which found that spreading and scattering losses could account for observed VSP amplitude behaviour in basalt sequences. Evidently, we can find a log sample rate such that the ray-theoretical losses match the VSP loss estimates. However, given the large variability in the transmission losses with sampling, we undertook further analysis to test the hypothesis that scattering loss is the dominant mechanism.

We estimated spectral ratios of windowed VSP downwave traces at 2420 m, 2980 m, 3044 m and 3500 m KB, using the downwave at 1880 m KB as a reference. The spectral ratios are plotted in Fig. 11 with the amplitude spectrum of the reference level. Over the rather limited frequency interval of the strongest signal (17–40 Hz), the slopes of the spectral ratios are effectively the same and rather flat. In a lossy medium, the slopes are modelled by

$$-\frac{20\,\pi\Delta z}{Qc}\log_{10}e$$

where c is the average velocity over the interval Δz. The four slopes in Fig. 11 correspond to depth intervals of 548 m, 1100 m, 1164 m and 1620 m, but there appears to be little variation of slope with the depth interval. The real VSP amplitude loss is not well modelled by frequency-dependent attenuation.

Nevertheless, the variation in spectral power with depth in Fig. 9 does show a loss of high frequencies with depth, mainly in the shallower part of the section, with little apparent bandwidth change over much of the deeper part of the volcanic sequence. We therefore modelled the propagation of a VSP pulse generated at ground level (GL) through a 185 m uniform layer on top of the pile of basalt flows logged from 185 m below GL and emerging into a uniform half-space at 2160 m below GL (Fig. 12). The 1975 m interval was modelled using a full-elastic, 1D modelling code based upon the Kennett algorithm (Kennett 1974, 1983) and developed at Schlumberger Cambridge Research. The 15 cm log data were upscaled to 3 m by Backus averaging to reduce the computational cost. Equivalent medium averaging, using windows of approximately 1/20th of the dominant seismic wavelength, provides a convenient method of upscaling logged data to allow efficient elastic waveform modelling, while retaining fidelity of both the travel time and amplitude information of the log scale model (Folstad & Schoenberg 1992, 1993).

Propagation was modelled both with and without multiple scattering, with 3D geometrical spreading from a point source. The injected wavelet at the top of the stack is a zero-phase, 60 Hz Ricker wavelet. (The wavelet appears not to be zero phase because of near field effects.) At the base of the stack, the escaping wavelet modelled without multiples is zero phase, but its amplitude has been diminished, undergoing a one-way loss of 46.9 dB due to

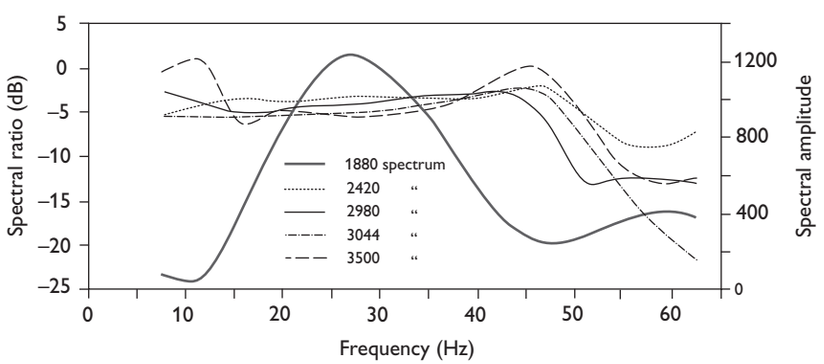

Fig. 11. Spectral ratios computed from four VSP levels relative to a reference level at 1880 m KB. The amplitude spectrum of the reference trace is also shown to indicate the signal frequency band.

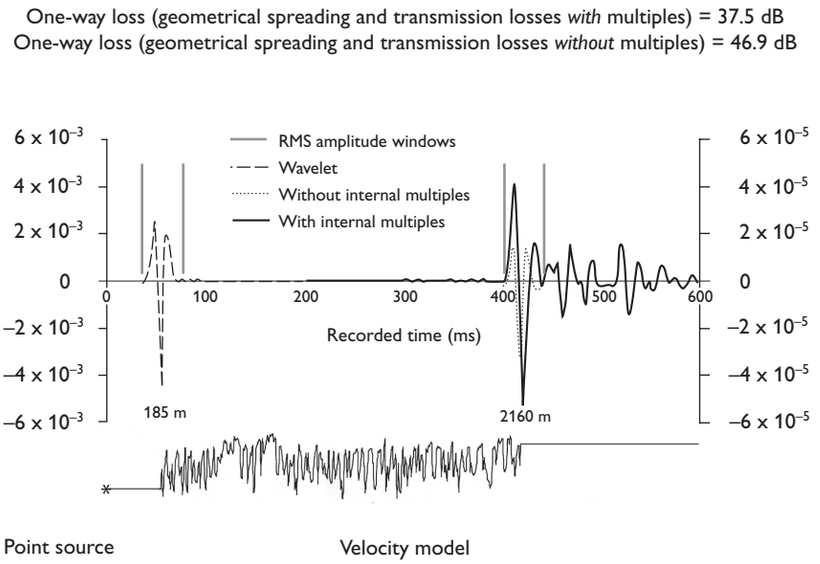

Fig. 12. Full elastic model of VSP downwave propagation through a stack of 3 m layers derived from the Backus average of the V_P, V_S and density logs between 185 m below ground level (GL) and 2160 m below GL. Propagation was modelled with and without peg-leg multiples and amplitudes were estimated in a 40 ms window about the wavelets.

the combination of one-way geometrical spreading and transmission losses. The escaping wave modelled with all internal multiples has been phase rotated within the 40 ms analysis window and has a higher RMS amplitude than the wavelet propagated without multiples, because short-period multiples have served to boost amplitudes within the analysis window. The RMS amplitude of the escaping wave with multiples is –37.5 dB relative to the input wavelet at the top of the stack. However, energy has been removed from the front of the wavelet, its trough-to-trough duration has increased and a coda has developed. These effects are due to scattering by the high-contrast layering.

We ran a further model, with multiples, to study the frequency-dependent effects of multiple scattering by the periodic layering by using a wide-band source signature defined in the frequency domain from DC to the Nyquist frequency at 125 Hz, corresponding to 4 ms sampling (in contrast to the real VSP which was acquired at 2 ms sampling). We also altered the model by adding a lower half-space simulating a massive sand unit and placing the deeper receiver at 300 m into the sand below the base basalt which was again modelled at 2160 m.

The Fourier domain amplitudes of the deep- and shallow-receiver down-going compressional waves are displayed in Fig. 13a, where the low-pass filtering effect of the basalt sequence can be seen, with quite deep notches appearing from 39 Hz, although higher frequency peaks also appear, such as that at 85 Hz.

The spectral ratios of the wide-band synthetics are shown in Fig. 13b with a linear regression to 80 Hz, avoiding the higher frequency side-lobes. The regression provides an effective Q estimate of 32, with 95% confidence limits of 26 and 42, which is consistent with the time domain estimate of 35 from the real VSP over the interval of basalt flows shown in Fig. 10. However, we note that while the real VSP displayed little or no frequency-dependent loss over the interval from 1880–3500 m KB, the full elastic modelling does support the assertion that the amplitude loss can be modelled by scattering and geometrical spreading alone.

Loss estimates from the literature

Rutledge & Winkler (1989) made estimates of attenuation from VSP data in the Upper Basalt Series in the Vøring Plateau area of the eastern Norwegian Sea. From 451 to 1111 m below the sea-floor in 1289 m of water, they found 105 basalt flows with about 10% of the section comprising volcaniclastic sediments. Their estimates of overall scattering attenuation of 2.7×10^{-4} dB/m (effective Q = 25) could be accounted for by scattering loss modelled from the sonic and density logs recorded in the well, leaving an intrinsic attenuation of less than 0.6×10^{-4} dB/m (Q > 115). Their Q of 25 is somewhat less than the estimated effective Q of 35 from the Lopra-1/1A VSP.

Pujol & Smithson (1991) reported values of effective Q around 48, estimated from VSP data in thick, Columbia Plateau basalt sequences containing some interbedded clay zones. They also reported that scattering was the dominant loss mechanism, since elastic modelling was able to account for all the observed loss. The intrinsic losses in

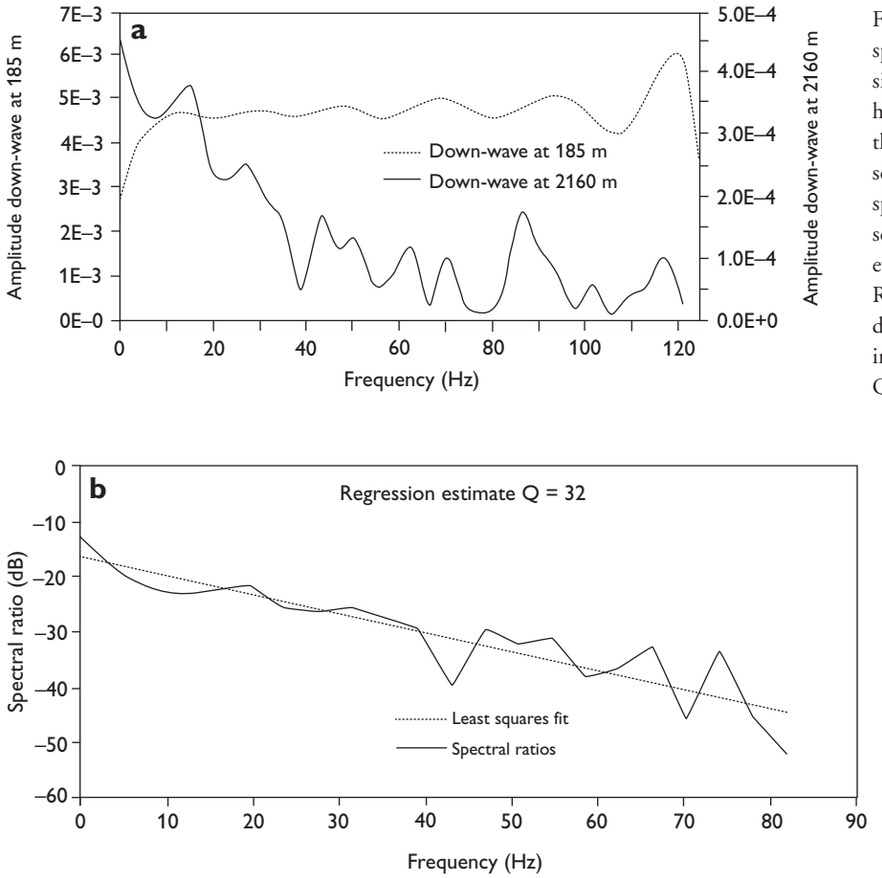

Fig. 13: **a**: Input and escaping wave spectra for a VSP downwave in a model similar to that in Fig. 12, but with a half space representing a sand unit at the base of the basalt sequence. The source wavelet is white over the full spectrum to Nyquist. The effects of scattering on the escaping wavelet are evident in the loss and the sidelobes. **b**: Regression of spectral ratios of the downgoing wave referenced to the input wavelet. The estimated effective Q is 32.

basalt were low and could not be determined from the field data.

The values of effective Q estimated from Lopra-1/1A is bracketed by those reported in the literature, and the general trends and inferred loss mechanisms are consistent. It is almost certain that more data points from west of the Shetlands will result in a greater scatter of effective Q estimates, corresponding to the variety of basalt environments.

Modelled offset VSP

Figure 14 shows the wide-band P- and S-downwaves simulated at a horizontal array of receivers spaced 100 m apart and located 300 m below the base basalt in a half-space of sand. The volume injection source is located in a uniform, elastic layer, which is the overburden above the modelled basalt interval. The horizontal array of receivers in a 1D earth simulates a walkaway VSP shot into a single level geophone. Multiples are included in the simulation. The direct P arrival is evident and its amplitude decays rapidly with offset due probably to a combination of strong geometrical spreading and critical angle effects at larger offsets in a medium with strong velocity contrasts.

Also evident is a strong, low-frequency event which dominates the shear record and is probably a mode conversion, propagating through the basalt sequence and emerging into the half space below. At the base basalt–sand contact, it converts to a P-wave and is also recorded as a strong event on the P-section, with an earlier arrival time. Both events are visible over the offset interval 2000–4500 m but neither event can be traced to zero offset. The asymptotic velocity of about 3.4 km/s is high and although it could correspond to the shear velocity of the shallow dolerites, which display the highest interval velocities in the sequence (Fig. 2), the event arrives before the direct shear arrival curve and it must therefore have a compressional leg for part of its ray path. The limited offset interval makes interpretation difficult and such conversions may be sensitive to the particular velocity-depth function, but the observation offers some encouragement

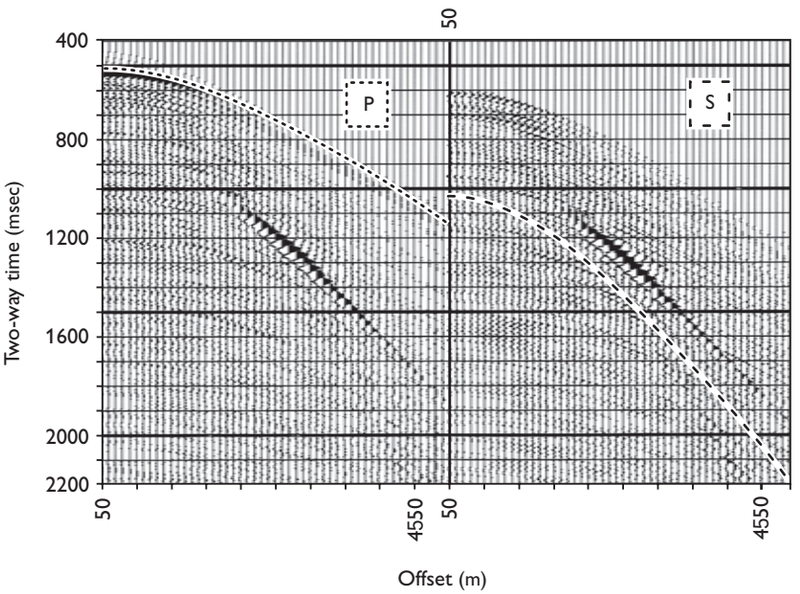

Fig. 14. Full elastic model of single level walkaway VSP with the geophone located 300 m below the basalt-sand contact. The left panel are P-waves while the right panel are S-waves. The ray-traced first P and pure S arrivals are superimposed. A mixed mode conversion can be seen with significant but low frequency amplitude over a limited offset interval.

for the use of mode-converted shear waves to probe below piled basalt flows, as described by Emsley *et al.* (1998).

Conclusions

The borehole seismic data recorded in the Lopra-1/1A well show that the average P-wave velocity is high at 5248 m/s from mean sea level to the deepest geophone level at 3510 m KB. Amplitude loss over the stacked basalt flows is moderate, corresponding to an effective Q of 35. However, this amplitude loss can be modelled by geometrical spreading and elastic scattering, implying that intrinsic attenuation is low. Persistent up-going events are evident within the interval logged by the VSP, even before wavefield separation, suggesting that lateral continuity of the basalt flow contacts is consistent over the several hundreds of metres that correspond to the VSP Fresnel zone radius. We observed an unambiguous tie between the VSP and a primaries synthetic seismogram which allows a detailed correlation between the stratigraphy revealed by the drill-bit with the events on the VSP reflected wavefield. Both the pre-deepening targets at 920 ms and 1350 ms appear on the VSP at earlier times of 894 ms and 1330 ms. Both events result from impedance contrasts within the volcanic sequence and it is likely that a strong reflection event, visible at 1412 ms TWT is also within the volcanic sequence. Its polarity indicates a decrease in acoustic impedance with depth so it is therefore unlikely to be basement. The prognosed depth of this event is 3732 m KB, or 167 m below the final TD of the well at 3565 m KB.

The unprocessed horizontal components suggest the presence of a persistent down-going shear wave, directly generated by the twin vibrators used as a VSP source, which in turn gives rise to up-going shear reflections. The V_P/V_S ratio from the VSP is 1.8 ± 0.1 (estimated error), which is in good agreement with the estimate of 1.84 ± 0.01 (one standard deviation) obtained from the P- and S-sonic log data, and is rather constant over the logged interval. We estimate layer-induced anisotropy of about 5% due to the high elastic parameter contrasts in the basalt flows. Azimuthal anisotropy estimated from the dipole shear log is low, but the direction of the anisotropy is consistent with mapped master joint sets: the well-defined NE–SW direction gives way to the less well-defined NW–SE direction at about 540 m KB. Our preferred explanation for the vertical P-wavespeed being 10% higher than the horizontal, as reported by Kiørboe & Petersen (1995), is that vertical velocities are locally raised by the presence of fast, dolerite intrusions.

Reflection seismic data are difficult to process and interpret in basalt covered areas. The Lopra-1/1A borehole dataset offers insight into the seismic properties of basalts which we anticipate will be of benefit in designing and processing reflection surveys, a topic which has attracted considerable interest but brings with it acknowledged challenges. An immediate result is that 'basalt', in seismic terms, cannot be represented by a uniform slab of hard rock a couple of kilometres thick. We observe challenges in the geometrical spreading, scattering losses, multiple development and spectral colouring which point towards low frequencies as the best hope for imaging beneath ba-

salts. This observation has been reported elsewhere in the literature but this paper may allow some more specific numbers to be applied to the basalt flows in the Faroese area.

On the positive side, intrinsic attenuation is low and propagation has been demonstrated through 3533 m of basalts, tuffs and volcaniclastic sequences. Coherent reflections have been tied from the VSP to the synthetic seismogram with confidence and another event below TD has been prognosed. Modelled offset VSP propagation also gave some hope for mode conversions, though with a limited offset range and low frequencies.

Acknowledgements

This work was carried out while the first author was engaged on a secondment with BP in Aberdeen. During this time he enjoyed considerable support from colleagues in BP, Shell and Schlumberger. In particular he would like to acknowledge many discussions and guidance from Matt Luheshi, Cameron Crook and Brian Mitchener. Chris Chapman answered many modelling questions and Fraser Louden recorded the VSP.

References

Backus, G.E. 1962: Long-wave elastic anisotropy produced by horizontal layering. Journal of Geophysical Research **67**, 4427–4440.

Dansk Olie- og Gasproduktion & Dansk Operatørselskab 1997: End of Well Report, Well Lopra-1, 80 pp. + 11 appendices. Thorshavn, Faroe Islands: Jardfeingi/Faroese Earth and Energy Directorate.

Emsley, D., Boswell, P. & Davis, P. 1998: Sub-basalt imaging using long-offset reflection seismic data. 60th Meeting, European Association of Geoscientists and Engineers Expanded Abstract, 1–48.

Esmersoy, C., Koster, K., Williams, M., Boyd, A. & Kane, M. 1994: Dipole shear anisotropy logging. 64th Annual International Meeting, Society of Exploration Geophysicists, Expanded Abstracts 1139–1142.

Folstad, P.G. & Schoenberg, M. 1992: Low frequency propagation through fine-layering. 62nd Annual International Meeting, Society of Exploration Geophysicists, Expanded Abstracts 1278–1281.

Folstad, P.G. & Schoenberg, M. 1993: Scattering from a set of anisotropic layers to second order in frequency. 55th Meeting, European Association of Exploration Geophysicists, Extended Abstracts Paper, 105 only.

Kennett, B.L.N. 1974: Reflections, rays and reverberations. Bulletin of the Seismological Society of America **64**, 1685–1696.

Kennett, B.L.N. 1983: Seismic wave propagation in stratified media, 342 pp. Cambridge: Cambridge University Press.

Kiørboe, L. & Petersen, S.A. 1995: Seismic investigation of the Faroe basalts and their substratum. In: Scrutton, R.A. *et al.* (eds): The tectonics, sedimentation and palaeoceanography of the North Atlantic region. Geological Society Special Publication (London) **90**, 111–123.

Larsen, L.M., Waagstein, R., Pedersen, A.K. & Storey, M. 1999: Trans-Atlantic correlation of the Palaeogene volcanic successions in the Faeroe Islands and East Greenland. Journal of the Geological Society (London) **156**, 1081–1095.

Newman, P. 1973: Divergence effects in a layered earth. Geophysics **38**, 481–488.

Nielsen, P.H., Stefánsson, V. & Tulinius, H. 1984: Geophysical logs from Lopra-1 and Vestmanna-1. In: Berthelsen, O., Noe-Nygaard, A. & Rasmussen, J. (eds): The Deep Drilling Project 1980–1981 in the Faroe Islands, 115–135.Tórshavn: Føroya Fróðskaparfelag.

O'Doherty, R.F. & Anstey, N.A. 1971: Reflections on amplitudes. Geophysical Prospecting **19**, 430–458.

Planke, S. & Cambray, H. 1998: Seismic properties of flood basalts from Hole 917A downhole data, southeast Greenland volcanic margin. In: Sanders, A.D., Larsen, H.C. & Wise, S.W. Jr. (eds): Proceedings of the Ocean Drilling Program, Scientific Results **152**, 453–462.

Pujol, J. & Smithson, S.B. 1991: Seismic wave attenuation in volcanic rocks from VSP experiments. Geophysics **56**, 1441–1455.

Rasmussen, J. & Noe-Nygaard, A. 1970: Geology of the Faeroe Islands. Danmarks Geologiske Undersøgelse 1. Række **25**, 142 pp.

Rasmussen, J. & Noe-Nygaard, A. 1990: The origin of the Faeroe Islands in text, pictures and on maps, 64 pp., 6 maps at 1:50 000. Copenhagen: Geological Survey of Denmark (also text in Faeroese and Danish).

Rutledge, J.T. & Winkler, H. 1989: Attenuation measurements from vertical seismic profile data: leg 104, site 642. In: Eldholm, O. *et al.* (eds): Proceedings of the Ocean Drilling Program, Scientific Results **104**, 965–972.

Thomsen, L. 1986: Weak elastic anisotropy. Geophysics **51**, 1954–1966.

White, R. & McKenzie, D. 1989: Magmatism at rift zones: the generation of volcanic continental margins and flood basalts. Journal of Geophysical Research **94**, 7685–7729.

Manuscript received 16 October 2001; revision accepted 14 March 2003.

Magnetic logs from the Lopra-1/1A and Vestmanna-1 wells, Faroe Islands

Niels Abrahamsen and Regin Waagstein

Susceptibility measurements from cores (representing basalt, lapilli-tuffs and tuffs) and magnetic logs from the Lopra-1/1A well are presented. The basalts fall into high- and low-susceptibility groups with no overlap. The high-susceptibility basalts (seven cores) have susceptibilities between 4 and 88 $\times 10^{-3}$ SI and consist of basalt with < 1% vesicles from thick massive units. The low-susceptibility basalts are intergranular, intersertal or hypocrystalline and contain no or very little (< 1%) visible magnetite, are generally more altered than the high-susceptibility basalts and have susceptibilities in the range from 0.6 to 1.4 × 10^{-3} SI (seven cores). The susceptibility of ten volcaniclastites of lapilli-tuff or tuff varies from 0.4 to 3.8 × 10^{-3} SI. The cores from the Lopra-1/1A well reveal a bimodal distribution of magnetic susceptibility. Low susceptibilities ranging from 0.4 to 4 are characteristic of altered basalts poor in magnetite, lapilli-tuffs and tuffs. Thus single measurements of susceptibility are of little use in discriminating between these three types of rock.

Susceptibility logs from the Lopra-1/1A well show that the variation below 3315 m distinguishes clearly between volcaniclastics (hyaloclastites) with low and fairly constant susceptibility and basalt beds of between 5 and 10 m thickness (with high susceptibility). The volcaniclastics comprise some 60–70% of the sequence between 3315 and 3515 m with the maximum continuous sediment layer being 80 m thick. A 1½ m core of solid basalt at 2381 m and sidewall cores of basalt from the Lopra-1/1A well have a mean susceptibility of 22.1 ± 3.5 × 10^{-3} SI (standard deviation (σ) = 23.6, number of samples (N) = 46), while samples of hyaloclastite (lapilli-tuff and tuff) have a mean susceptibility of 0.85 × 10^{-3} SI (σ = 0.39, N = 17).

The mean values of the rock magnetic parameters for 303 basalt plugs from the Vestmanna-1 well are: Q_{ave} = 13.3 ± 0.6 (σ = 11), S_{ave} = 11.8 ± 0.6 × 10^{-3} SI (σ = 11) and J_{ave} = 4.64 ± 0.25 A/m (σ = 4.4). The reversely polarised, lowermost (hidden) part of the *c.* 4½ km thick lower basalt formation correlates with Chron C26r. The upper (exposed) part of the lower basalt formation correlates with Chrons C26n, C25r and C25n and the more than 2.3 km thick middle and upper basalt formations correlate with Chron C24n.3r.

Keywords: Magnetic logging, rock magnetism, susceptibility, NRM, magnetic reversals, Faroe Islands, Lopra, Vestmanna, North Atlantic

---

N.A., *Department of Earth Sciences, University of Aarhus, Finlandsgade 8, DK-8200 Aarhus N, Denmark.*
E-mail*: Abraham@geo.au.dk*
R.W., *Geological Survey of Denmark and Greenland, Øster Voldgade 10, DK-1350 Copenhagen K, Denmark.*

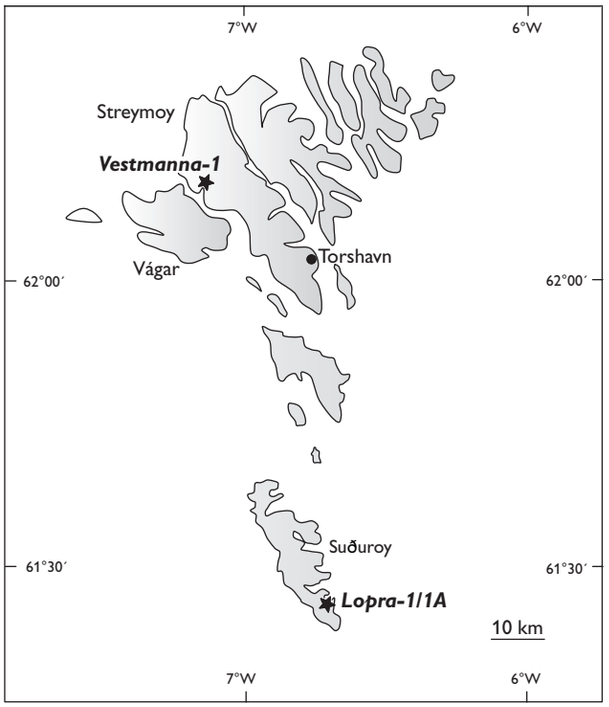

Fig. 1. Index map of the Faroe Islands with the positions of the Lopra-1/1A and Vestmanna-1 wells indicated with **stars**.

Information on rock magnetic properties, susceptibility and natural remanent magnetisation (NRM) may be useful for detecting changes in rock type, structure and magnetic mineral content of rocks penetrated by boreholes. Magnetic polarity is also a tool potentially of use in dating. Although magnetic surveying has a long history in prospecting and mining geophysics (e.g. Parasnis 1979), magnetic logging (using susceptibility) in boreholes was first developed in the 1950s with new electronic types of equipment (e.g. Broding *et al.*1952; Levanto 1958; Barthés *et al.* 1999).

Logging with the purpose of magnetic polarity determinations began even later (e.g. Pozzi *et al.*1988, 1993; Bouisset & Augustin 1993; Ito & Nogi 1995). Magnetic logging instruments were developed for down-hole mapping of the magnetic field as a correlation- and dating-tool using magnetostratigraphy. Reversals recorded in a borehole may be used for dating if they can be correlated with the geomagnetic polarity time scale (GPTS). The GPTS was firmly established in the early 1960s by radiometric dating of reversals recorded in young volcanic sequences on land (e.g. Cox *et al.*1963) and by relating the polarity reversals from land to marine magnetic anomalies observed over the oceans (Vine & Matthews 1963). This revived the idea of continental drift and supported the new paradigm of plate tectonics. In the following years the polarity scale was extended linearly backwards through Mesozoic time by correlation of long sequences of marine anomalies with the shorter land-based records (Heirtzler *et al.*1968).

The present paper deals with the results of magnetic logging of the Lopra-1/1A well, situated on Suðuroy, the southernmost of the Faroe Islands (Fig. 1). The magnetic logs were acquired by Schlumberger Ltd. in 1997 as part of an extensive logging programme run in connection with deepening of the well. The logs cover a major part of the Faroes lower basalt formation (Waagstein 1988, Waagstein *et al.* 2001). The log-like results of rock magnetic properties obtained from the continuously cored Vestmanna-1 well through a younger part of the Faroes basalt succession (Abrahamsen *et al.* 1984) are summarised for comparison.

Magnetic logging in Lopra-1/1A

A geological high-resolution magnetometer tool (GHMT) was run by Slumberger Ltd. from 3101 to 2168 m in the deepened part of the Lopra-1 well and subsequently from 3519 to 2998 m in the sidetracked Lopra-1A.The kick-off depth of the sidetrack is 3091 m, which means that the two log sections overlap from 3091 to 2998 m. The two logs have been combined into a single log using an arbitrary splicing point at 3000 m.

The GHMT tool records two types of magnetic measurements; the magnetic susceptibility (RMAGS) and the total magnetic induction (MAGB). Examples of the records obtained are shown for the whole sequence in Figs 2–5. A shorter section is shown in more detail in Fig. 6.

The main objective of the deepening of the Lopra-1 well was to drill through the basalt formations to the expected underlying sediments. The dipole–dipole sensor susceptibility measurement tool (SUMT) was therefore set to the low-resolution mode. The nuclear magnetic resonance magnetometer (NRMT) was designed to measure the total magnetic induction in the borehole within a working range of only 5000 nT around a preset expected value (Schlumberger Ltd., personal communication 1997) which was unfortunately much less than the actual ranges of 30 000 and 70 000 nT present within the hole. Another purpose of the short working ranges applied was to protect the tool electronics, which were designed for weakly magnetic sediments rather than strongly magnetic volcanic rocks.

The settings for the magnetic tools were not optimal for the basalt-dominated section actually drilled, as the

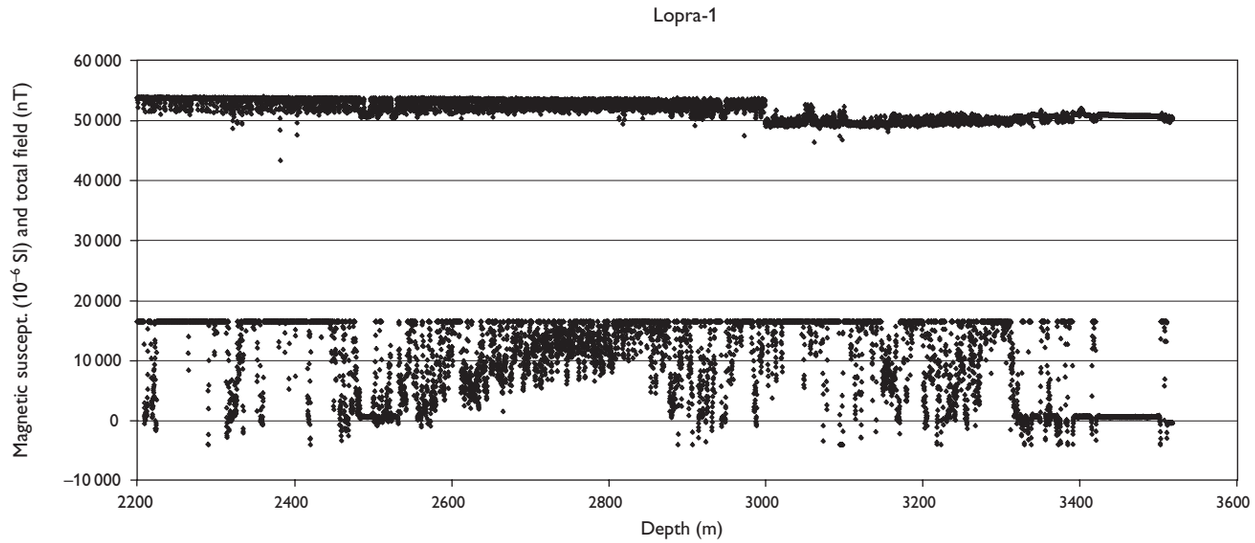

Fig. 2. Magnetic susceptibility (× 10^{-6} SI) and the magnetic induction total field (nT) logged in the Lopra-1/1A well between depths of 2200 and 3520 m.

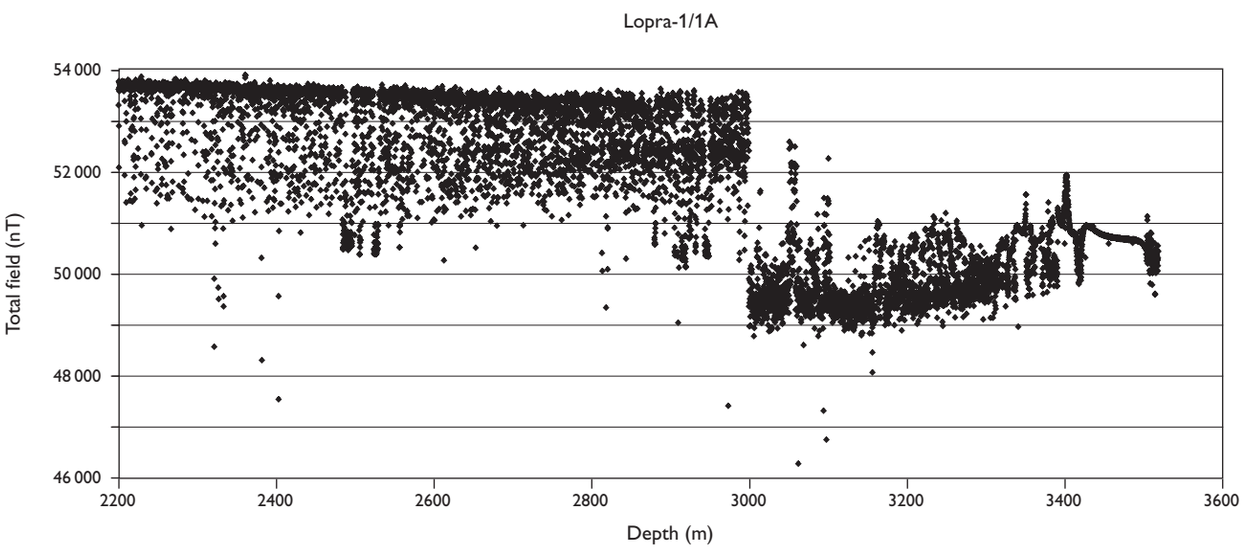

Fig. 3. Total magnetic field (magnetic induction, nT) in the Lopra-1/1A well. A jump in the general level of about 4000 nT is seen at 3000 m.

susceptibility was mostly outside the working range of the susceptometer. Because of this, the polarity of the remanent magnetisation and hence the interplay between the susceptibility and the induced magnetisation could not be deduced from these results and a reversal chronology could not be obtained from the *in situ* logged data.

Information about the remanent polarity of the rocks drilled by the Lopra-1/1A and Vestmanna-1 wells (Fig. 1) has, however, been obtained from drilled cores. These cores were investigated by traditional palaeomagnetic laboratory techniques and the results have been reported and presented elsewhere (Schönharting & Abrahamsen 1984; Abrahamsen *et al* 1984; Waagstein 1988; Abrahamsen 2006, this volume). Abrahamsen (2006, this volume) correlated the lowermost (unexposed) part of the *c.* 4½ km thick lower basalt formation with Chron 26r (Selandian) and the upper (exposed) part of the lower basalt formation with Chrons C26n, C25r and C25n (Selandian and Thanetian). The more than 2.3 km thick middle and upper basalt formations are correlated with Chron C24n.3r (Ypresian).

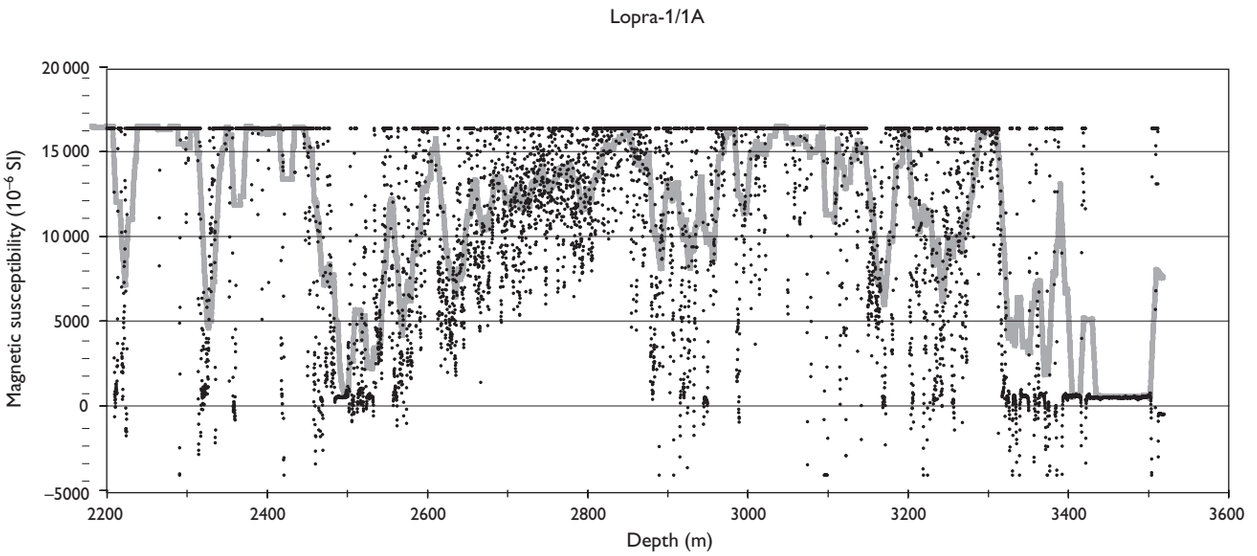

Fig. 4. Magnetic susceptibility log from the Lopra-1/1A well. The **solid pale curve** is a 100 point moving average (likely to be biased due to saturation of the instrument).

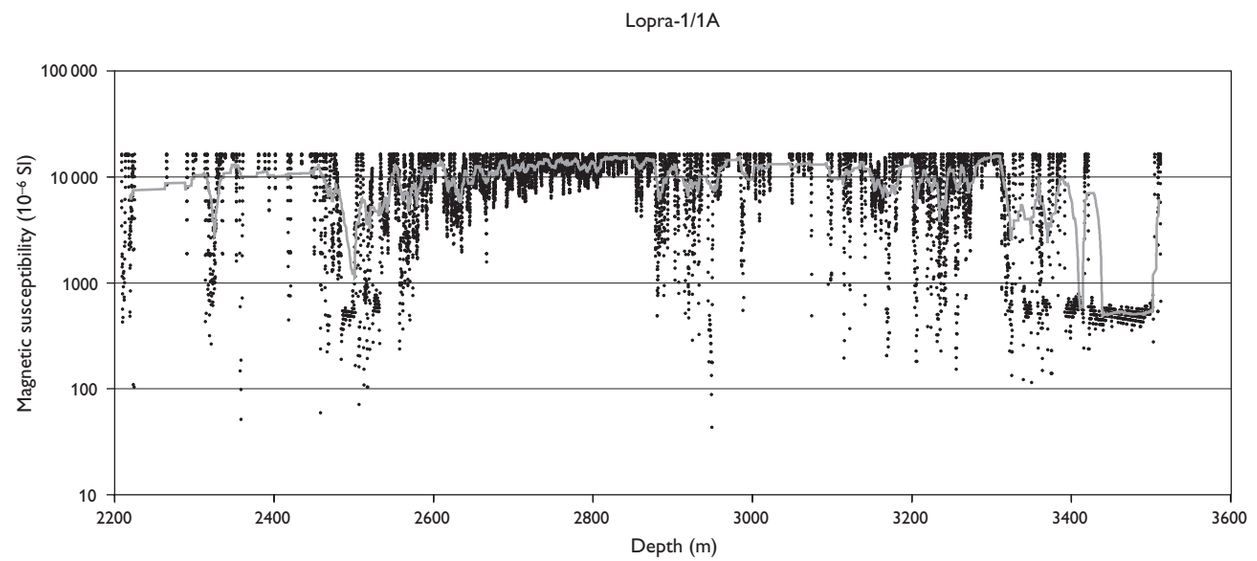

Fig. 5. Magnetic susceptibility from the Lopra-1/1A well (logarithmic scale). The **solid pale curve** is a 100 point moving average (likely to be strongly biased due to saturation of the instrument).

Susceptibility of cores from the Lopra-1/1A borehole

The magnetic susceptibility of 1 conventional and 24 rotary sidewall cores drilled at regular intervals within the deepened part of the Lopra-1/1A well between 2275 and 3514.5 m has been measured in the laboratory. The cores include 14 basalts, 8 lapilli-tuffs and 2 tuffs (Table 1). A single plug from each sidewall core and 22 plugs from the 1.5 m long conventional core were measured.

The basalts fall into high- and low-susceptibility groups with no overlap. The high-susceptibility basalts are represented by seven cores with susceptibilities between 4 and 88 × 10^{-3} SI. They consist of basalt with < 1% vesicles from thick massive units. The texture of the groundmass varies from intergranular with a few per cent matrix (mesostasis) to hyaline with almost 50% matrix. The matrix consists of cryptocrystalline quench crystals and secondary minerals replacing glass or filling interstitial voids. The groundmass of the intergranular basalts has an estimated

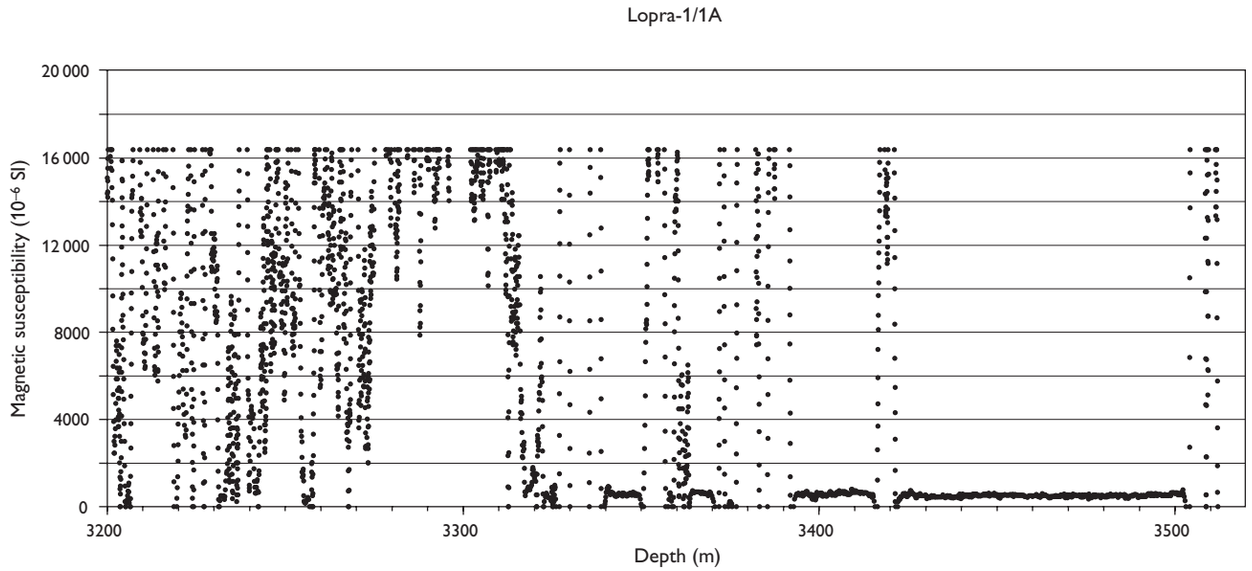

Fig. 6. Magnetic susceptibility details between 3200 and 3510 m of the Lopra-1/1A well.

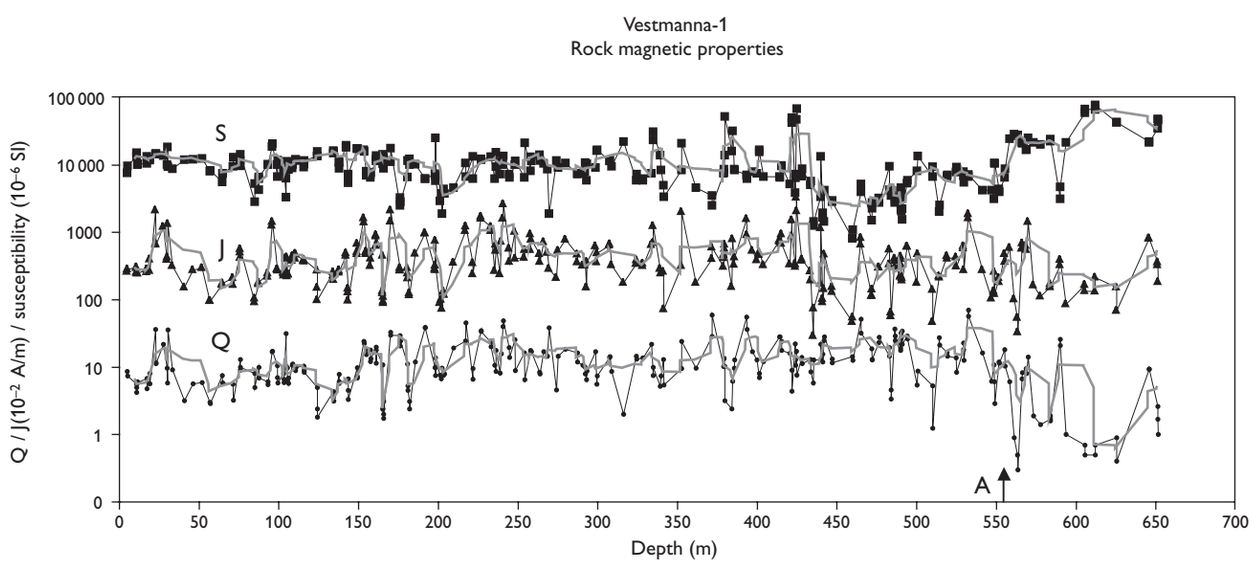

Fig. 7. Rock magnetic properties (susceptibility, NRM and Q-ratio) of the Vestmanna-1 well (modified from Abrahamsen *et al.* 1984). **Pale curves** are 5 point moving averages (logarithmic scale). The A horizon, between the lower and upper basalt formations, is marked by an **arrow** and the letter **A** at 557 m.

content of 3–10 vol.% titanomagnetite with a maximum size between < 0.03 and 0.2 mm. The titanomagnetite in the less crystalline basalts is too fine-grained to be estimated or cannot be seen, although the presence of an opaque or dark turbid matrix suggests that it is likely to be present.

Susceptibilities from seven cores from the low-susceptibility basalts vary from 0.6 to 1.4 × 10^{-3} SI. The low-susceptibility basalts are intergranular, intersertal or hypocrystalline and contain no or very little (< 1%) visible magnetite. They are generally more altered than the high-susceptibility basalts and lose on average about 3.7 wt% volatiles on ignition compared to 1.8 wt% for the latter group (Table 1). The volatiles are dominantly crystal-bound water in secondary minerals including clay, zeolites, pumpellyite and phrenite. Three of the basalts are highly vesicular with 20–25% vesicles filled with secondary minerals.

The susceptibility of the ten volcaniclastites of lapillituff or tuff varies from 0.4 to 3.8 × 10^{-3} SI with an average of 1.1 × 10^{-3} SI. The susceptibilities of the four deepest

Table 1. Petrography and magnetic susceptibility of core samples from Lopra-1/1A

Sample ID	Rock type	Depth	Max. clast size (mm)	Volatiles wt%	Groundmass texture	Magnetite vol.%	Magnetite max. size (mm)	Vesicles vol.%	Core suscept. x 10^{-3} SI	Mean log suscept. x 10^{-3} SI	Min. log suscept. x 10^{-3} SI	Max. log suscept. x 10^{-3} SI
L1-swc57	High-suscept. basalt	2275		1.26	intergranular	7%	≤ 0.1	< 1	88	> 16.4	> 16.4	> 16.4
L1-core 1	High-suscept. basalt	2380–2381.5		1.72	intergranular	3%	≤ 0.2		4–46	> 15.7	12.1	> 16.4
L1-swc46	High-suscept. basalt	2441		2.31	intergranular	sparse	≤ 0.06	0.5	47	> 16.4	> 16.4	> 16.4
L1-swc34	High-suscept. basalt	2610		1.89	cryptocrystalline	abundant		0	69	> 15.7	13.9	> 16.4
L1-swc30	High-suscept. basalt	2780		1.3	hyaline			0	77	> 13.5	10.5	> 16.4
L1-swc25	High-suscept. basalt	3030		2.33	intergr.-intersertal	no		0	27	> 16.4	> 16.4	> 16.4
L1A-swc15	High-suscept. basalt	3382		1.51	intergranular	10%	≤ 0.03	0	63	> 14.3	7.2	> 16.4
L1-swc59	Low-suscept. basalt	2219		6.84	intergranular			0	1.4	1.4	0.4	2.9
L1-swc43	Low-suscept. basalt	2475		4.94	intergr.-intersertal	no		20	0.6	5.5	1.7	13.5
L1-swc40	Low-suscept. basalt	2558		3.16	hypocrystalline			25	0.7	1.1	0.4	2.1
L1-swc39	Low-suscept. basalt	2559.8		2.89	intersertal	< 1%	≤ 0.1	20	0.6	1.1	0.9	1.2
L1A-swc16	Low-suscept. basalt	3328		2.22	intergranular	no		0	1.1	> 16.4		> 16.4
L1A-swc9	Low-suscept. basalt	3500.5		2.62	intergranular	no		0	0.8	0.6	0.5	0.6
L1A-swc4	Low-suscept. basalt	3531		3.13	intergranular			0	0.9			
L1-swc38	Lapilli-tuff	2560.2	10	5.37	hyaline	no		5	0.6	1.0	0.8	1.2
L1-swc36	Lapilli-tuff	2570	10	4.05	hypocrystalline	no		0	0.7	2.4	0.2	10.0
L1-swc33	Lapilli-tuff	2630	> 15	4.35	hyaline			2	1.6	3.9	3.1	4.2
L1-swc31	Lapilli-tuff	2690	14	5.28	hyaline			< 1	1.8	> 16.3	16.1	> 16.4
L1-swc26	Lapilli-tuff	2970	> 23	5.63	hyaline			2	3.8	> 14.8	12.4	> 16.4
L1A-swc13	Lapilli-tuff	3438	12	4.02	hypocrystalline	sparse	≤ 0.08	< 1	0.6	0.4	0.4	0.5
L1A-swc12	Lapilli-tuff	3464.5	25	3.84	hypocrystalline	no		2	0.6	0.5	0.4	0.5
L1A-swc5	Lapilli-tuff	3514.5	30	8.43	hypocrystalline	no		1	0.6			
L1A-swc19	Tuff	3233.5	0.5	6.62	hyaline			+	0.7	1.5	0.4	5.5
L1A-swc6	Tuff	3512.5	2	4.16	hyaline			2	0.4			

suscept.: susceptibility; intergr.: intergranular.
Petrographic parameters are based on visual estimates of cores and thin-sections.
Volatiles are determined from loss on ignition corrected for oxidation of iron.
Core susceptibility is measured on 8–32 mm long sections of sidewall core with a diameter of 23.2 mm and on several plugs from conventional core 1.
Mean, minimum and maximum log susceptibilities are based on 1 m intervals of the GHMT log centred at the core.
The mean is computed assuming a log-normal distribution of magnetic susceptibilities.
The sign '>' indicates that some susceptibility measurements exceed the saturation level of the tool (16.4 x 10^{-3} SI).
The differences between core and log values probably partly reflect the uncertainty in depths of sidewall-cores (0.5 m) and magnetic logs (0–2 m).

volcaniclastites from between 3438 and 3514.50 m average only 0.6×10^{-3} SI.

The study of cores from the Lopra-1/1A well thus reveals a bimodal distribution of magnetic susceptibility. High-susceptibility rocks range between 4 and 88×10^{-3} SI with the great majority falling above 15×10^{-3} SI. These rocks are all relatively fresh basalts from thick massive units cooled slowly enough to crystallise titanomagnetite (visible or not). The five cores from the original Lopra-1 well all consist of intergranular basalts from the massive centre of thick flows (Hald & Waagstein 1984) with susceptibilities between 16 and 39×10^{-3} SI (Schönharting & Abrahamsen 1984) and thus belong to the group of high-susceptibility basalts.

Low susceptibilities from the Lopra-1/1A borehole, ranging from 0.4 to 4×10^{-3} SI, are characteristic of both altered basalts poor in magnetite ($0.6–1.4 \times 10^{-3}$ SI), lapilli-tuffs ($0.6–3.8 \times 10^{-3}$ SI) and tuffs ($0.4–0.7 \times 10^{-3}$ SI). This means that single measurements of susceptibility are of little use in discriminating between these three types of rock.

The Lopra-1/1A magnetic log

Because the recorder was run in its low-resolution mode, the susceptibilities of most of the rocks through which it passed were mostly outside its recording range. Nevertheless, some general lithological features may be deduced (Schlumberger Ltd., personal communication 1997). The upper recording limit of 16.4×10^{-3} SI is close to the typical lower limit of relatively fresh, massive basalt. This means that major intervals of saturation are a good indicator of massive basalt units.

This makes it possible to divide the logged interval into two parts, below and above 3315 m (cf. Figs 4–6).

Below 3315 m

The lower part displays a highly bimodal pattern with two distinct susceptibility levels. About 85% of the logged section below 3315 m shows average susceptibilities around 0.7×10^{-3} SI that we interpret as hyaloclastites. Basalt layers with a thickness from 2 to 6 m are clearly identifiable within the hyaloclastites showing sharp contacts and much higher susceptibility values (to above the recorded saturation limit of 16.4×10^{-3} SI). Low-susceptibility basalt has been cored nearby (Table 1) so the high-susceptibility intervals give only a minimum estimate of the thickness of basalt present.

For comparison, a 1½ m solid basalt core from 2381 m and 24 sidewall basalt cores (Abrahamsen 2006, this volume) had a mean susceptibility of 22.1×10^{-3} SI ± 3.5 (one standard deviation (σ) = 23.6, number of samples (N) = 46), whereas samples of hyaloclastite (tuffs and lapilli-tuff) had a mean value of 0.85×10^{-3} SI (σ = 0.39, N = 17). These results thus compare quite well with the average of the susceptibility log data.

The total magnetic field (magnetic induction) shows a jump of about 4000 nT between the two partly overlapping log runs (log sections spliced at 3000 m; Figs 2–3), which must be an artifact. The magnetometer record of the total field below 3315 m (Fig. 3) shows the typical effect of a highly magnetised layer within a weakly magnetised formation. The induction recorded through the volcaniclastics below and above the basalt is strongly affected by the distance to the basalt. Several occurrences of such basaltic layers give rise to mixed effects through the volcaniclastics.

Above 3315 m

The total-field magnetometer was saturated above 53 500 nT during most of the first logged section between 3101 and 2168 m (Figs 2–3). This value is stronger than the local Earth's magnetic field of around 50 000 nT and could indicate a large local magnetic source of unknown origin, but is more likely a tool or calibration error. In contrast, despite the very variable character of the lower section, this is not the case for the uppermost part of the lower section (below 3315 m, Fig. 3). In both cases the magnetometer was preset for maximum sensitivity of values centred at the expected value of the local Earth's magnetic field strength of 50 000 nT.

Above 3315 m, *c.* 70% of the susceptibility data (Figs 2, 4–6) are greater than 16.4×10^{-3} SI (the saturation level of the instrument). Thick intervals above saturation level are dominant above 2550 m and reflect subaerial basalt flows. Between about 2550 and 3315 m, the susceptibility log is characterised by large short-scale variations. Strong variability is especially observed in the interval from 2613 to 2816 m (Fig. 4). The high-frequency pattern originates from a succession of hyaloclastites and minor basalt beds. The hyaloclastites consist of lapilli-tuffs, tuff-breccias, breccias and subordinate tuffs. The variability may be explained by the presence of large clasts of basalts showing high susceptibilities set in a low-susceptibility tuffaceous matrix. Only a few longer intervals of low susceptibility ($< 1 \times 10^{-3}$ SI) can be recognised above 3315 m, the thickest ones being between 2945 and 2950 m, between 2523 and 2533 and between 2484 and 2500 m.

The other rock magnetic properties of the Lopra-1/1A well, including the magnetic polarity and correlation with the GPTS, have been summarised and discussed in details elsewhere (Abrahamsen 2006, this volume).

Rock magnetic properties in the Vestmanna-1 well

The 660 m deep Vestmanna-1 well on Streymoy (Fig. 1) was drilled in 1980 through the lower part of the Faroes middle basalt formation and into the top of the lower basalt formation using wireline coring technique.

No magnetic in-hole logging was made during or after the drilling. However, detailed magnetic laboratory investigations of sub-sampled plugs of the fully recovered core have been published (Abrahamsen *et al.* 1984). An illustration of most of the rock magnetic information obtained (susceptibility S, NRM intensity J, and Q-ratio) is shown in Fig. 7 on logarithmic scales (modified from the original data presented by Abrahamsen *et al.* 1984). The thick pale curves are five point moving averages.

The well reached 101 m into the upper part of the *c.* 4½ km thick lower basalt formation (Waagstein 1988) whose top is indicated in Fig. 7, where a 0.7 m thick basaltic conglomerate of local origin separates the lower and the middle basalt formations (Waagstein & Hald 1984). Rocks penetrated by the overlying part of the well (0–557 m in Fig. 7) all belong to the middle basalt formation. The conglomerate is stratigraphically equivalent to a *c.* 10 m thick sediment sequence in the south and southwestern parts of the Faroe Islands that includes thin beds of coal indicating a long quiescence in the magmatic activity between eruption of the lower and middle basalt formations.

All three rock magnetic parameters vary more than one order of magnitude, which is not uncommon for the magnetic properties of volcanic rocks. The mean values for each of them (N = 303 samples) are Q_{ave} = 13.3 ± 0.6 (σ = 11), S_{ave} = 11.8 ± 0.6 × 10^{-3} SI (σ = 11) and J_{ave} = 4.64 ± 0.25 A/m (σ = 4.4). The only readily apparent systematic trend appears to be a decrease in the susceptibility from high values at 610 m to low values at 440 m. At shallower depths, the susceptibility fluctuates around 10^{-2} SI. The trend is mirrored in the Q-ratio below 470 m, but with a slight decrease in Q above this level, whereas no systematic trends appear visible in the NRM intensity.

The magnetic polarity of the Vestmanna-1 well was determined in detail by palaeomagnetic investigations of 303 up-oriented plugs from the fully cored borehole, that indicate a short normal polarity interval between 660 and 640 m only, all the younger samples (N = 275) being reversed (Abrahamsen *et al.* 1984).

Conclusions

Due to instrument problems, the valuable information from the magnetic logs of the Lopra-1/1A well is limited. Based upon the logged susceptibility, the variation below 3315 m is clearly diagnostic between volcaniclastics (with low and fairly constant susceptibility) and basalt flows of between 5 and 10 m in thickness (with high susceptibility). Between 3315 and 3515 m the volcaniclastics comprise some 60–70% of the sequence, the maximum continuous layer being 80 m thick.

A 1½ m long core of solid basalt from 2381 m and sidewall cores of basalt from the Lopra-1/1A well have a mean susceptibility of 22.1 × 10^{-3} SI ± 3.5 (σ = 23.6, N = 46), while samples of volcaniclastics (lapilli-tuff and tuff) have a mean value of 0.85 × 10^{-3} SI (σ = 0.39, N = 17).

The mean values of rock magnetic parameters for 303 basalt plugs from the Vestmanna-1 well are: Q_{ave} = 13.3 ± 0.6 (σ = 11), S_{ave} = 11.8 ± 0.6 × 10^{-3} SI (σ = 11) and J_{ave} = 4.64 ± 0.25 A/m (σ = 4.4). The reversely polarised, lowermost (hidden) part of the *c.* 4½ km thick lower basalt formation correlates with Chron C26r. The upper (exposed) part of the lower basalt formation correlates with Chrons C26n, C25r and C25n and the more than 2.3 km thick middle and upper basalt formations correlate with Chron C24n.3r.

References

Abrahamsen, N. 2006: Palaeomagnetic results from the Lopra-1/1A re-entry well, Faroe Islands. Geological Survey of Denmark and Greenland Bulletin **9**, 51–65 (this volume).

Abrahamsen, N., Schönharting, G. & Heinesen, M. 1984: Palaeomagnetism of the Vestmanna core and magnetic age and evolution of the Faeroe Islands. In: Berthelsen, O., Noe-Nygaard, A. & Rasmussen, J. (eds): The Deep Drilling Project 1980–81 in the Faeroe Islands. Annales Societatis Scientiarum Faeroensis, Supplementum **IX**, 93–108. Tórshavn: Føroya Fróðskaparfelag.

Barthés,V., Pozzi, J.P., Vibert-Charbonnel, P., Thibal, J. & Mélières, M.A. 1999: High-resolution chronostratigraphy from downhole susceptibility logging tuned palaeoclimatical orbital frequencies. Earth and Planetary Science Letters **165**, 97–116.

Bouisset, P.M. & Augustin, A.M. 1993: Borehole magnetostratigraphy, absolute age dating and correlation of sedimentary rocks, with examples from the Paris Basin, France. American Association of Petroleum Geologists Bulletin 77, 569–587.

Broding, R.A., Zimmermann, C.W., Sommers, E.V., Wilhelm, E.S. & Stripling, A.A. 1952: Magnetic well logging. Geophysics **17**, 1–26.

Cox, A., Doell, R. & Dalrymple, G.B. 1963: Geomagnetic polarity epochs and Pleistocene geochronometry. Nature **198**, 1049–1051.

Hald, N. & Waagstein, R. 1984: Lithology and chemistry of a 2-km sequence of lower Tertiary tholeiitic lavas drilled on Suðuroy, Faeroe Islands (Lopra-1). In: Berthelsen, O., Noe-Nygaard, A. & Rasmussen, J. (eds): The Deep Drilling Project 1980–81 in the Faeroe Islands. Annales Societatis Scientiarum Faeroensis, Supplementum **IX**, 15–38. Tórshavn: Føroya Fróðskaparfelag.

Heirtzler, J.R., Dickson, G.O., Herron, E.M., Pitman III, W.C. & Le Pichon, X. 1968: Marine magnetic anomalies, geomagnetic field reversals and motions of the ocean floor and continents. Journal of Geophysical Research **73**, 2119–2136.

Ito, H. & Nogi, Y. 1995: Magnetic structures of seamounts in the western Pacific Ocean deduced from Leg 144 downhole magnetometer logs. Proceedings of the Ocean Drilling Program, Scientific Results **144**, 631–638.

Levanto, A.E. 1958: A three-component magnetometer for small drill-holes and its use in ore prospecting. Geophysical Prospecting **7**, 183–195.

Parasnis, D.S. 1979: Principles of applied geophysics, 275 pp. London: Chapman & Hall.

Pozzi, J.P., Martin, J.P., Pocachard, J., Feinberg, H. & Galdeano, A. 1988: *In situ* magnetostratigraphy: interpretation of magnetic logging in sediments. Earth and Planetary Science Letters **88**, 357–373.

Pozzi, J.P., Barthés, V., Thibal, J., Pocachard, J., Lim, M., Thomas, T. & Pagès, G. 1993: Downhole magnetostratigraphy in sediments: comparison with the paleomagnetism of a core. Journal of Geophysical Research **98**, 7939–7958.

Schönharting, G. & Abrahamsen, N. 1984: Magnetic investigations on cores from the Lopra-1 drillhole, Faeroe Islands. In: Berthelsen, O., Noe-Nygaard, A. & Rasmussen, J. (eds): The Deep Drilling Project 1980–81 in the Faeroe Islands. Annales Societatis Scientiarum Faeroensis, Supplementum **IX**, 109–114. Tórshavn: Føroya Fróðskaparfelag.

Vine, F.J. & Matthews, D.H. 1963: Magnetic anomalies over ocean ridges. Nature **199**, 947 only.

Waagstein, R. 1988: Structure, composition and age of the Faeroe basalt plateau. In: Morton, A.C. & Parson, L.M. (eds): Early Tertiary volcanism and the opening of the NE Atlantic. Geological Society Special Publication (London) **39**, 225–238.

Waagstein, R. & Hald, N. 1984: Structure and petrography of a 660 m lava sequence from the Vestmanna-1 drill hole, lower and middle basalt series, Faeroe Islands. In: Berthelsen, O., Noe-Nygaard, A. & Rasmussen, J. (eds): The Deep Drilling Project 1980–81 in the Faeroe Islands. Annales Societatis Scientiarum Faeroensis, Supplementum **IX**, 39–70. Tórshavn: Føroya Fróðskaparfelag.

Waagstein, R., Guise, P. & Rex, D. 2001: K/Ar and $^{39}Ar/^{40}Ar$ whole-rock dating of zeolite-facies metamorphosed flood basalts: the upper Paleocene basalts of the Faroe Islands, NE Atlantic. In: Jolley, D.W. & Bell, B.R. (eds): The North Atlantic igneous province: stratigraphy, tectonic, volcanic and magmatic processes. Geological Society Special Publication (London) **197**, 219–252.

Manuscript received 22 December 2000; revision accepted 13 September 2005.

Palaeomagnetic results from the Lopra-1/1A re-entry well, Faroe Islands

Niels Abrahamsen

The palaeomagnetic dating and evolution of the Faroe Islands are discussed in the context of new density and rock magnetic results from the deepened Lopra-1/1A well. The reversal chronology of the *c.* 6½ km thick basalt succession is also described. The polarity record of the Faroe Islands may now be correlated in detail with the Geomagnetic Polarity Time Scale. The lowermost (hidden) part of the lower basalt formation correlates with Chron C26r (Selandian age), the top (exposed) part of the lower basalt formation correlates with Chrons C26n, C25r and C25n (Selandian and Thanetian age) and the middle and upper basalt formations correlate with Chron C24n.3r (Ypresian). Inclinations indicate a far-sided position of the palaeomagnetic poles, which is characteristic of results from most Palaeogene volcanics from the northern North Atlantic region.

The density, magnetic susceptibility and magnetic remanence of 20 specimens from one solid core (1½ m in length) and 26 sidewall cores from the well between –2219 and –3531 m below sea level (b.s.l.) suggest that the volcanic materials can be divided into two characteristic groups: solid unaltered basalts and altered basalts and tuffs. The magnetic properties are typically log-normally distributed and the carriers of remanence are Ti-poor Ti-magnetites with Curie temperatures close to 580°C. The inclination of the 1½ m core at 2380 m b.s.l. is dominantly negative (two plugs at the very top of the core do show normal polarity, but they are likely to be misoriented as all specimens appear to be from one flow). Magnetic logging (magnetic susceptibility and field intensity) down to 3515 m b.s.l. was made in Lopra-1/1A together with other geophysical logs but did not yield conclusive inclination data.

Keywords: Palaeomagnetism, rock magnetism, magnetic reversals, plate tectonics, Faroe Islands, Lopra-1/1A well, North Atlantic, large igneous province

Department of Earth Sciences, University of Aarhus, Finlandsgade 8, DK-8200 Aarhus N, Denmark.
E-mail*: Abraham@geo.au.dk*

Review of the geology

The Faroe Islands are situated on the eastern side of the northern North Atlantic between the Shetland Islands and Iceland on the northern part of the NE–SW-trending elongated Faroe Rise (Fig. 1). The volcanic islands are a result of the hotspot-related plume activity recorded by the Brito-Arctic Large Igneous Province (LIP) (Lawver & Muller 1994; Larsen & Saunders 1998; T.B. Larsen *et al.* 1999; Burke & Torsvik 2004) that stretches from present-day central West Greenland to the north-western parts of the UK.

Seismic (e.g. Richardson *et al.* 1998) and gravity investigations (e.g. Saxov & Abrahamsen 1964) suggest that the invisible basement of the islands is composed of continental lithospheric crust, somewhat thinned by lithospheric stretching processes during the continental breakup that formed the North Atlantic.

The exposed part of the Faroe Islands is composed of a *c.* 3 km thick pile of Palaeogene flood basalts (Rasmussen & Noe-Nygaard 1969, 1970; Noe-Nygaard & Rasmussen 1984) situated above a *c.* 3½ km unexposed volcanic sequence below sea level (Fig. 2). Only minor sedimenta-

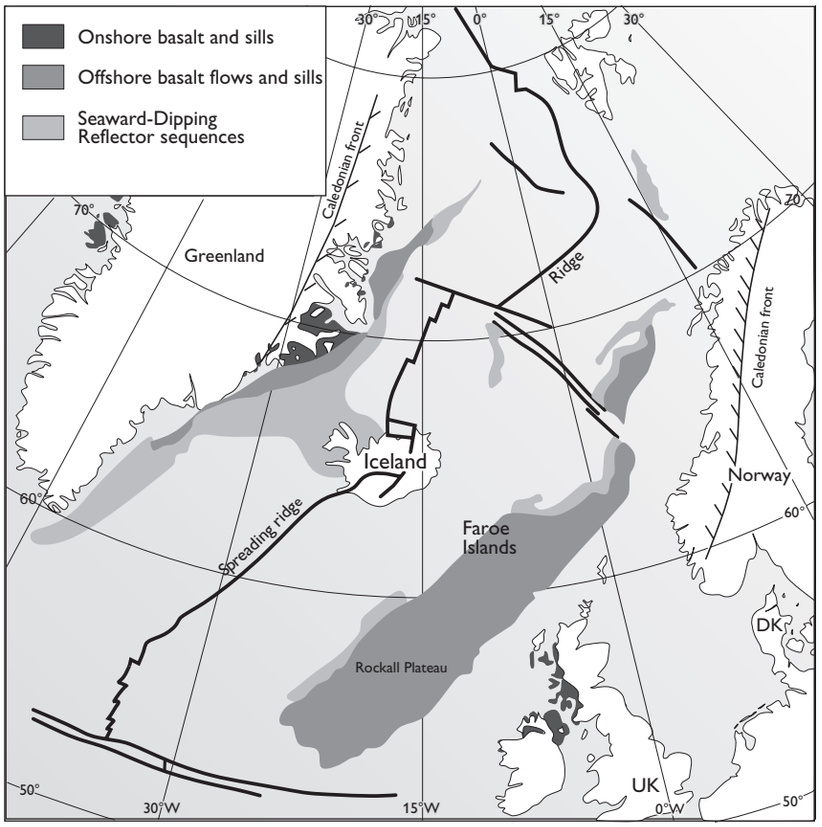

Fig. 1. Index map of the eastern North Atlantic showing the Faroe Islands (modified from Larsen *et al.* 1995).

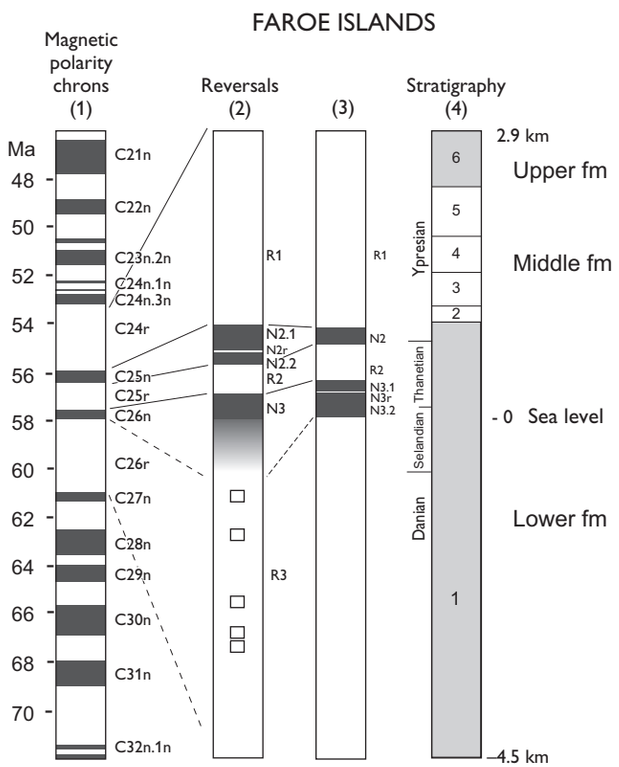

ry layers are intercalated in the whole volcanic sequence.

The volcanic sequence, more than 6½ km in total thickness (Waagstein 1988; L.M. Larsen *et al.* 1999), is divided into three parts, the lower (> 4½ km thick), the middle (1.4 km thick) and the upper basalt (> 0.9 km thick) formations. The basalts are cut by numerous dykes and a few sills. An up to 10 m thick coal-bearing formation of lacustrine claystones and shales was deposited on top of the slightly eroded surface of the lower basalt formation (the A-level). Two other stratigraphical levels, B (in the middle formation) and C (separating the middle and upper formations), are also useful for stratigraphical purposes (Fig. 2).

The purpose of the present contribution is to present

Fig. 2. Compilation of magnetic reversals within the *c.* 6½ km thick basalt pile of the Faroe Islands, showing stratigraphy and the correlation with the Geomagnetic Polarity Time Scale. The four columns are based upon information compiled from: (1) Ogg (1995); (2) Abrahamsen (1965, 1967), Abrahamsen *et al.* (1984), Waagstein (1988) and Riisager *et al.* 2002a; (3) Tarling & Gale (1968); (4) Rasmussen & Noe-Nygaard (1970), Waagstein (1988) and L.M. Larsen *et al.* (1999).

Table 1. Palaeomagnetic results from the Faroe Islands

Formation/site/core depth	N(Dg)	Decl °	Incl °	α_{95} °	k	Plat °N	Plon °E	δ_{95} °	A_{95} °	Palaeo-lat (°N)	No.	Polarity	Reference
All formations	33	176.0	± 69.0	6	14	80.0	159.0	10.3		52.5	1	R&N	(1)
All formations	1809	185.0	± 66.4	1.9		76.7	161.0	3.1		48.9	2	R&N	(2)
ubf, Torshavn	34	171.9	–72.2	3.5	53	84.0	218.0	6.3		57.3	3	R	(3)
ubf, Argir	8	175.1	–53.9*	2.2	258	62.3	182.4	3.1		34.4*	*	R	(3)
mbf, Argisfossar	18	156.0	–36.0*			48				20.0*	*	R	(4)
mbf, Vestmanna core	275		–61.8	1.2	53.4	70.8		1.9		43.0	4	R	(5)
lbf, Vestmanna core	28		± 63.4	6.3	19.4	72.8		10.0		45.0	5	R&N	(5)
mbf + lbf, Vestm. core	303		± 61.9*	1.2	46.1	70.9		1.9		43.1*	*	R&N	(5)
mbf + lbf	548(43)	7.7	± 60.9	4.5	24.5	71.4	154.7		6.0	41.9	6	R&N	(6)
lbf, Lopra-1; 862 mbf	6		–75.0	1						61.8	7	R	(7)
lbf, Lopra-1; 1219 mbf	8		–62.0							43.2	8	?R	(7)
lbf, Lopra-1; 1923 mbf	5		–73.0	3						58.6	9	R	(7)
lbf, Lopra-1; 2178 mbf	7		–55.0*							35.5*	*	?R	(7)
lbf, Lopra-1A; 2380 mbf	20		–71.7	2.0	709					56.5	10	R	(8)
Average, Nos 1–10, except *	(10)		± 67.2	1.4						50.0	11	R&N	(8)
Average, Nos 1, 2, 3 & 6	(4)	181.2	± 67.3	6.3	213	78.7	164.4		8.0	50.1	12	R&N	(8)

lbf, mbf, ubf: lower, middle and upper basalt formations; No.: number in palaeolatitude figure; * Not used in average; N: number of samples; Dg: directional groups; Decl: mean of cleaned declination; Incl: mean of cleaned inclination; α_{95}: cone of 95% confidence. For core data the inclination statistics of Kono (1980) were used for k and α_{95} (Tarling 1983); k: Fisher precision parameter; Plat: latitude of apparent palaeomagnetic pole; Plon: longitude of apparent palaeomagnetic pole; δ_{95} and A_{95}: error angles of app. latitude and app. palaeopole at 95% confidence level; (1) Abrahamsen 1967; (2) Tarling 1970; (3) Løvlie & Kvingedahl 1975; (4) Løvlie 1975; (5) Abrahamsen *et al.* 1984; (6) Riisager *et al.* 2002a; (7) Schönharting & Abrahamsen 1984; (8) This work.

the magnetic results from a core of basaltic rock obtained from the Lopra-1/1A reentry well and to discuss these data in relation to other palaeomagnetic results from the Faroe Islands.

Previous work

Magnetic investigations in relation to the Faroe Islands have been made since the early 1960s (Abrahamsen 1965, 1967; Saxov & Abrahamsen 1966; Tarling & Gale 1968; Tarling 1970; Schrøder 1971; Løvlie 1975; Løvlie & Kvingedal 1975; Abrahamsen *et al.*1984; Schönharting & Abrahamsen 1984; Tarling *et al.* 1988). Density determinations (Saxov & Abrahamsen 1964) as well as gravity measurements (Saxov 1969) and seismic investigations (Pálmason 1965; Bott *et al.* 1974, 1976; Casten 1974; Nielsen *et al.* 1981; Richardson *et al.* 1998) have been made on and around the islands. Geophysical logs from the Lopra-1/1A and Vestmanna-1 boreholes have been published by Nielsen *et al.* (1984), Boldreel (2006, this volume) and Abrahamsen & Waagstein (2006, this volume). Geothermal measurements were described by Balling *et al.* (1984) and Balling *et al.* (2006, this volume).

Palaeomagnetic results from the Faroe Islands have been published by Abrahamsen (1965, 1967), Tarling & Gale (1968), Tarling (1970), Løvlie (1975), Løvlie & Kvingedal (1975), Abrahamsen *et al.* (1984), Schönharting & Abrahamsen (1984) and Riisager *et al.* (2002a, b). A comparison of palaeomagnetic results from East Greenland and other results from the Palaeogene of the North Atlantic Igneous Province (NAIP) was published by Tarling *et al.* (1988) and a critical review of palaeomagnetic poles from the Eurasian part of the NAIP together with a new pole for the Faroe Islands was presented by Riisager *et al.* (2002a). A summary of all published palaeomagnetic directional data from the Faroe Islands is shown in Table 1.

The magnetic results for the exposed part of the basalt succession were extended by the wells at Vestmanna-1 and Lopra-1 in 1980–1981 (Abrahamsen *et al.* 1984; Schönharting & Abrahamsen 1984) and by the re-entry of the Lopra-1/1A hole in 1996, the results of which are presented in this paper. Despite intentions, the re-entry hole at Lopra-1/1A reached a depth of 3565 m without penetrating to the base of the lower basalt formation volcanics.

The polarity sequence and the compiled total stratigraphic column of the Faroe Islands as now known are shown in Fig. 2, together with the Geomagnetic Polarity Time Scale (GPTS). Essentially we find three intervals of reverse magnetic polarity (R1, R2, R3) with two normal

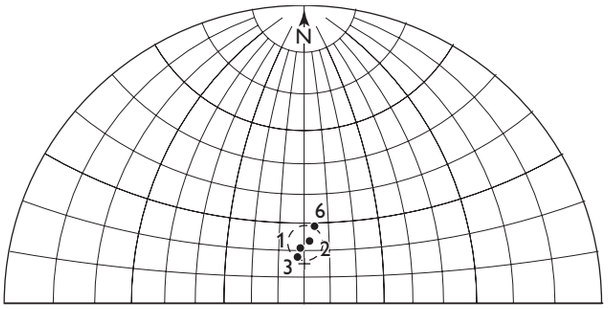

Fig. 3. Palaeomagnetic directions from the Faroe Islands (from Table 1, results Nos 1, 2, 3 and 6) with α_{95} circle. The axial dipole field direction is indicated by a **cross**.

Fig. 4. Apparent palaeomagnetic pole positions (solid circles) with 95% significance circle (Table 1, poles Nos 1, 2, 3 and 6). All poles appear 'farsided' as seen from the Faroe Islands (**diamond**). Further discussion in the text.

polarity intervals in between (N2 and N3). Minor differences between columns (2) and (3) in Fig. 2 are likely to be due to somewhat different positions of the profiles investigated on Suðuroy, the southernmost of the Faroe Islands.

According to recent high-precision ^{40}Ar-^{39}Ar datings (Storey *et al.* 1996; L.M. Larsen *et al.* 1999), the basalt formations in the Faroe Islands as well as the contemporaneous East Greenland basalts can be divided into an older part with ages of about 59–56 Ma, followed (after a pause or a period with much reduced volcanic activity) by a younger part, with ages of 56–55.5 Ma for the Faroes and 56–54.5 for East Greenland.

Based upon these radiometric datings, the polarity record of the Faroe Islands may now be correlated to the GPTS as shown in Fig. 2. The lowermost (hidden) part of the lower basalt formation correlates with Chron C26r (Selandian age), the upper (exposed) part of the lower basalt formation correlates with Chrons C26n, C25r and C25n (Selandian and Thanetian) and the middle and upper basalt formations correlate with Chron C24r (Ypresian). This correlation follows the suggestion by Waagstein (1988), who revised the original interpretation of Abrahamsen *et al.* (1984) by suggesting that R3 belongs to Chron C26r rather than to C24r. More details in relation to magnetic inclinations from the Lopra-1/1A data are discussed below.

Assuming the geomagnetic field to have been a central, axial dipole field, the palaeolatitude may be determined from the characteristic (primary) inclination of the volcanics, combining both polarities. A compilation of all inclination values obtained from the Faroe Islands is listed in Table 1. Using inclination statistics (Kono 1980; Tarling 1983) the fisherian mean of published inclinations (group numbers 1–10, Table 1) is 67.2° ± 1.4° (equivalent to a palaeolatitude of 50.0° ± 2.1°), whereas the average of the palaeolatitudes listed is 50.9° ± 2.3° (± 1 sigma). Further discussion of the shallow inclinations and the palaeolatitude question will be given below.

Palaeogeography

Many palaeogeographic reconstructions of the North Atlantic have been published since the early work of Bullard *et al.* (1965) (e.g. Ziegler 1990; Knott *et al.* 1993; L.M. Larsen *et al.* 1999; Torsvik *et al.* 2001; Mosar *et al.* 2002). Before about 60 Ma, the supposed mantle hotspot (just south-east of Iceland at the present day) lay under the volcanic areas of Disko and Nuussuaq in West Greenland (O'Connor *et al.* 2000; Nielsen *et al.* 2002; Chambers *et al.* 2005), far from the Faroe Islands that are situated just north-west of the continental margin of Europe. The whole volcanic pile of the Faroe Islands, more than 6½ km thick, was formed in the time interval between Chron 26 (61.65 Ma) and Chron 24n.3n (*c.* 53.286 Ma) (Chron ages are the orbitally tuned age calibration of Gradstein *et al.* 2004, table 5.2). During this time interval, the hotspot moved eastwards under Greenland as Greenland moved west-north-west relative to Europe and the North Atlantic gradually opened between the Faroe Islands and Greenland.

Absolute declinations are known from only four of the palaeomagnetic investigations from the Faroe Islands (Ta-

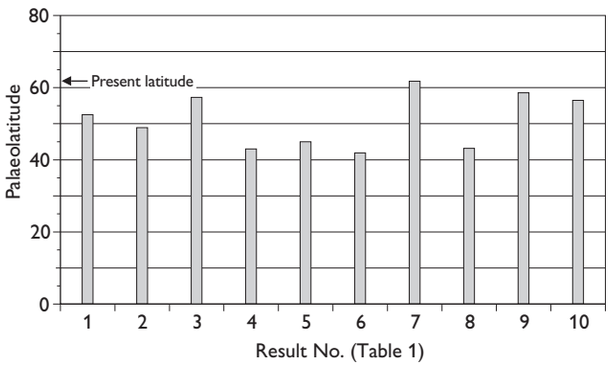

Fig. 5. Histogram of apparent palaeolatitudes according to Table 1 (poles Nos 1–10). Most results appear systematically low compared to the present-day latitude. For further discussion see the text.

ble 1, Nos 1, 2, 3 and 6). If both normal and reverse polarities are combined and assumed to be normal directions towards the north with steep down-dip (positive) inclinations, the four directions appear as shown in Fig. 3. The equivalent apparent palaeomagnetic pole positions are shown in Fig. 4. All four poles are seen to be 'farsided' (Wilson 1971; Merrill *et al.* 1998), the apparent palaeomagnetic poles falling beyond the geographic pole as seen from the Faroe Islands. An equivalent histogram of all published apparent palaeolatitudes (Table 1) is also illustrated in Fig. 5, most of which show low values as compared to the present-day latitude.

Lopra-1/1A investigations

Sampling, instruments and techniques used

The material investigated from the extended Lopra-1/1A well consists of two types: core plugs from the solid core (2380.0 to 2381.3 m) and sidewall cores (between 2219 and 3531 m). The solid core is 1.4 m long and in several pieces, but some fit together, as shown in Fig. 6. After marking the core with an upward directed arrow in the core lab at GEUS, 20 plugs with a diameter of 2.5 cm were drilled orthogonal to the main core and cut to a standard length of 2.2 cm. The major part of the present magnetic investigation is concentrated upon these 20 plugs. In addition some rotary sidewall cores were investigated. The pieces from the sidewall cores had a diameter of 2.33 cm and varied in length, which limited the possibility of fitting these samples into the magnetic instrument holders.

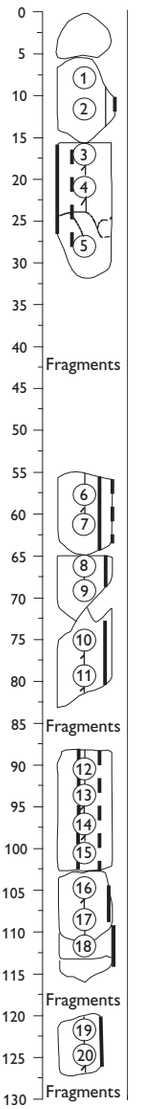

Fig. 6. Sketch from a photograph of the Lopra-1/1A core between 2380 and 2381.4 m. The fragments containing the numbered 1-inch core plugs are indicated. The absolute azimuths of the individual segments and fragments are not known. The top segment containing plugs Nos 1 and 2 appears to have been turned upside-down before the core was archived.

Bulk density

To avoid problems with air bubbles adhering to the relatively small specimens if they were weighted in water, the bulk density was determined by weighing in air only (to an accuracy of ± 0.001 g), then determining the volume by measuring the shape of the specimens (to an accuracy of ± 0.02 cm). The likely accuracy in the finally determined density is about ± 2–3%, depending on the rough-

Table 2a. Lopra-1/1A: magnetic susceptibility, NRM, Q-ratio, density
Solid core (d = 25 mm)

Sample No.	Depth m	Rock type	Weight g	Density g/cm³	NRM corr mA/m	Suscept-bridge 10^{-3} SI	Q-ratio NRM/(F × Sus)
1V	2380.08	basalt	69.040	2.992			
1H	2380.08	basalt	36.000	2.981		46.26	
1	2380.08	basalt	31.79		17997	41.62	10.868
2	2380.12	basalt	28.66		3258	17.32	4.728
3	2380.17	basalt	30.38		327	3.903	2.105
4	2380.21	basalt	28.78		1247	6.945	4.513
5	2380.28	basalt	29.76		673	4.340	3.897
6	2380.58	basalt	28.22		2319	11.773	4.951
6V	2380.58	basalt	38.240	2.885			
6H	2380.58	basalt	44.907	2.868			
7	2380.62	basalt	31.37		2553	18.850	3.404
8	2380.66	basalt	26.24		1227	11.459	2.691
9	2380.69	basalt	28.84		1391	16.865	2.073
10	2380.75	basalt	29.92		971	33.756	0.723
11	2380.79	basalt	27.31		1539	34.636	1.117
12	2380.91	basalt	29.37		333	32.987	0.254
13	2380.94	basalt	30.07		1782	37.825	1.184
14	2380.97	basalt	27.08		1628	36.450	1.123
15	2381.00	basalt	26.96		984	38.704	0.639
16	2381.05	basalt	30.99		359	43.323	0.208
17	2381.09	basalt	29.11		887	31.722	0.703
18	2381.12	basalt	30.24		322	35.241	0.230
19	2381.22	basalt	29.87		2616	41.288	1.592
20	2381.25	basalt	25.87		2705	36.890	1.843
20V	2381.25	basalt	71.848	2.922			
20H	2381.25	basalt	27.740	2.869		43.15	
	a:	Mean		2.92	2256	28.40	2.44
		Standard deviation		0.05	3808	14.00	2.51
		Mean error		0.02	851	2.98	0.56
		N		6	20	22	20

ness of the shape. A total of 34 specimens were determined (Table 2).

Susceptibility

Two types of susceptibility instruments were used. Initial whole core measurements were made by a handheld Czech kappameter KT5 (sensitivity ± 0.00001 SI) before drilling plugs from the core. A Molspin bulk susceptibility bridge (sensitivity ± 0.000001 SI) was then used to measure the susceptibility of the core plugs and to monitor possible chemical changes during thermal demagnetisation experiments. A total of 46 specimens were measured (Table 2).

Remanence

The direction (declination and inclination) and intensity of the natural remanent magnetisation (NRM) was determined using a Molspin spinner magnetometer. The plugs with preferred dimensions of 2.2 cm in length and a diameter of 2.5 cm (plugs from the solid core) were all measured and demagnetised in detail, see below. The NRM of the sidewall cores was also measured but, due to the variable length of the core pieces, only one (SWC57) was investigated in detail (Table 2). The sensitivity of the Molspin spinner is ± 0.02 mA/m and the direction of the remanence within the plug was determined to within ± 1°. The declination and inclination is given with respect to the local specimen coordinates, assuming the axis of the plug (= specimen) to be approximately horizontal (i.e. orthogonal to the Lopra-1/1A drill hole). As the azimuth of the vertical core is not known, the true magnetic decli-

Table 2b. Lopra-1/1A: magnetic susceptibility, NRM, Q-ratio, density
Sidewall cores (d = 23.3 mm)

Sample No.	Depth m	Rock type	Weight g	Density g/cm³	NRM mA/m	Suscept-bridge 10^{-3} SI	High > 2×10^{-3} 10^{-3} SI	Low < 2×10^{-3} 10^{-3} SI	Q-ratio NRM/(F × Sus)
59	2219.00	basalt	18.966	2.361	4406	1.43		1.43	77.4
57	2275.00	basalt	22.222	2.857	2180	87.96	87.96		0.623
46	2441.00	basalt	23.857	2.865	9027	46.65	46.65		4.864
44	2456.00	basalt, ves.	33.653	2.488					
43	2475.00	basalt, ves.	18.421	1.981	0.7	0.55		0.55	0.032
40	2558.00	basalt, ves.	17.973	2.708	1.3	0.71		0.71	0.046
39	2559.80	basalt, ves.	22.920	2.711	1.5	0.64		0.64	0.060
38	2560.20	tuff, lapilli	21.428	2.336	0.4	0.61		0.61	0.015
37	2562.00	tuff	29.838	2.345					
36	2570.00	basalt	9.353	2.379	38.5	0.69		0.69	1.406
34	2610.00	basalt, alt.	18.741	3.167	3412	69.17	69.17		1.240
33	2630.00	tuff, lapilli	13.720	2.404	587	1.60		1.60	9.224
31	2690.00	tuf, lapilli	8.082	2.276	365	1.83		1.83	5.022
30	2780.00	basalt	21.170	2.929	7171	76.89	76.89		2.344
26	2970.00	tuf, lapilli	18.744	2.553	304	3.77	3.77		2.030
25	3030.00	basalt	18.515	2.808	1146	26.67	26.67		1.080
19	3233.50	tuff	9.915	2.572		0.72		0.72	
16	3328.00	basalt	18.471	2.875	106	1.13		1.13	2.346
15	3382.00	basalt	14.066	2.919		63.36	63.36		
13	3438.00	tuf, lapilli	19.505	2.549	1.8	0.62		0.62	0.074
12	3464.50	tuf, lapilli	17.287	2.605	12.0	0.64		0.64	0.470
9	3500.50	basalt	16.494	3.001	0.8	0.83		0.83	0.024
6	3512.50	tuff	23.953	2.648	38.2	0.39		0.39	2.433
5	3514.50	tuf, lapilli	13.372	2.511		0.58		0.58	
5	3514.50	tuf, lapilli	15.648	2.607		0.58		0.58	
4	3531.00	basalt	27.341	2.940		0.88		0.88	
	b:	Mean		2.63	1516	16.20	34.47	0.85	1.85
		Standard deviation		0.27	2585	28.80	21.00	0.39	2.34
		Mean error		0.05	593	5.88	3.90	0.10	0.55
		N		26	19	24	29	17	18*)
	a & b:	Mean		2.68	1895	22.1	34.5		2.16
		Standard deviation		0.27	3276	23.6	21.4		2.45
		Mean error		0.05	525	3.5	4.0		0.40
		N		32	39	46	29		38*)

*) Excluding sample No. 59

nation is not known. A further description of the palaeomagnetic experimental standard laboratory procedures may be found in e.g. Butler (1992).

AF-demagnetisation

After measuring the initial NRM intensity, 16 of the 20 plugs were AF-demagnetised in stepwise increasing alternating magnetic fields (Table 3) using a Molspin AF-demagnetiser. Minimum and maximum AF-fields were 2.5 mT (25 Oe) and 100 mT (1000 Oe), respectively.

Thermal demagnetisation

Stepwise thermal demagnetisation was made in a Schonstedt furnace on four plugs from the solid core. An initially moderate AF-demagnetisation of up to between 7.5 and 15 mT removed recently induced viscous magnetisation components, most likely acquired during the drilling operations (details in Table 2), after which the thermal demagnetisation was applied.

Table 3. Lopra-1/1A: palaeomagnetic results

Sample No.	Depth m	Polarity	Weight g	Treatment AF mT/°C	NRM intensity A/m	Characteristic direction		MAD	Demag interval AF thermal	
						Decl (rel.)	Incl	Degrees	mT	Tmax °C
1	2380.08	(?N)	31.79	0–40	18.00	335	81	6	15–50	
2	2380.12	(?N)	28.66	0–40	3.26	350	71	2	5–40	
3	2380.17	R	30.38	0–70	0.33	358	–70	2	15–70	
4	2380.21	R	28.78	0–7.5	1.25	175	–70	4		
5	2380.28	R	29.76	0–95	0.67	345	–69	1	10–95	
6	2380.58	R	28.22	0–40	2.32	51	–67	1	5–40	
7	2380.62	R	31.37	0–70	2.55	62	–71	1	5–70	
8	2380.66	R	26.24	0–40	1.23	75	–69	1	5–40	
9	2380.69	R	28.84	0–50	1.39	80	–71	1	5–50	T630
10	2380.75	R	29.92	0–630	0.97	289	–75	3		
11	2380.79	R	27.21	0–50	1.54	106	–72	2	5–50	T600
12	2380.91	R	29.37	0–600	0.33	7	–72	2		
13	2380.94	R	30.07	0–50	1.78	169	–70	2	5–50	
14	2380.97	R	27.08	0–40	1.63	204	–71	1	5–40	
15	2381.00	R	26.96	0–50	0.98	195	–70	2	5–50	T630
16	2381.05	R	30.99	0–630	0.36	334	–74	2		
17	2381.09	R	29.11	0–70	0.89	163	–73	3	10–70	T630
18	2381.12	R	30.24	0–630	0.32	334	–74	2		
19	2381.22	R	29.87	0–50	2.62	32	–73	3	5–50	
20	2381.25	R	25.87	0–50	2.71	24	–71	4	0–50	

Rev.:	Mean inclination	–71.22	
	Standard deviation	1.99	
	N	18	
Norm:	Mean inclination	76.00	
	Standard deviation	5	
	N	2	
All Rev:	Mean inclination	–71.70	
	Standard deviation	2.85	α_{95} = 1.95
	N	20	k = 709

Results

Bulk density

The bulk density of sidewall cores and plugs are listed in Table 2. The mean bulk density of the solid basaltic core was well-determined as 2.92 ± 0.02 (standard deviation (σ) = 0.05) g/cm^3, although the determination was based on only six specimens. The bulk density of the SWC-cores was lower and much more scattered, 2.63 ± 0.05 (σ = 0.27) g/cm^3. The low bulk density and high scatter is likely to be due to differences in porosity and the abundance of secondary minerals.

Susceptibility

The magnetic susceptibility is also listed in Table 2 and shown in Fig. 7. In contrast to for instance the bulk density, the magnetic susceptibility and remanence intensity may vary considerably, and they are known typically to be logarithmically normal distributed (e.g. Tarling 1983; Abrahamsen & Nordgerd 1994). This is also the case here, as two log-normal distributions are found. The core susceptibility varies between 4 and 46 × 10^{-3} SI, and the susceptibility of the SWC-cores varies even more, between 0.4 and 88 × 10^{-3} SI. The data thus fall into two populations, the limit between the two groups being about 2 × 10^{-3} SI. The higher group yields an average susceptibility of 34 ± 4 (σ = 21) × 10^{-3} SI and the lower group an average susceptibility of 0.85 ± 0.1 (σ = 0.39) × 10^{-3} SI.

The more strongly magnetised group is represented mostly by unaltered basalts, whereas the less strongly magnetised group is more typical of most sediments including tuffaceous sediments, as well as vitrinites and deuterically altered or weathered basalts. In the present case the difference between high and low values in the basalts is likely to be caused by alterations of the primary Ti-magnetites, since Ti-magnetite is the main carrier of the remanence (see below).

NRM intensity

The intensity of the NRM (natural remanent magnetisation) is listed in Table 2 and shown in Fig. 7. Values of the

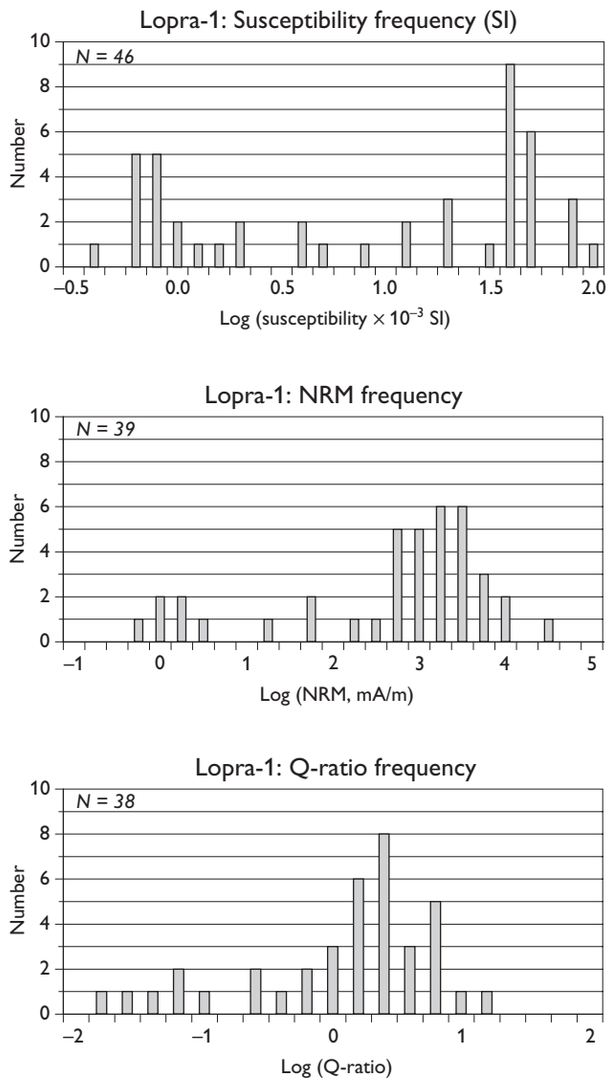

Fig. 7. Histograms of susceptibility, NRM intensity and Q-ratio. All appear bimodal on a logarithmic scale.

order of 1 A/m are typical for the unaltered basalts, whereas tuffs and altered basalts may have lower values. The mean NRM intensity value of the core plugs is 2.26 ± 0.85 (σ = 3.8) A/m, and the mean NRM intensity value of the SWC-cores is 1.52 ± 0.59 (σ = 2.6) A/m. Due to the high scatter, the mean NRM intensities of the two groups are not significantly different. The combined populations plotted logarithmically (Fig. 9) again show two overlapping log-normal distributions, as do the susceptibilities (Fig. 8).

Q-ratio

The Q-ratio (Koenigsberger ratio) illustrated in Fig. 10 is the ratio between the remanent (J_{NRM}) and the induced (J_i = k·F) magnetisation, $Q = J_{NRM}/J_i = J_{NRM}/(k \cdot F)$, F being the intensity of the local geomagnetic field, F ≈ 0.05 mT. For basaltic rocks, values between 0.2 and 10 are characteristic. Generally, the higher value the more fresh and unaltered the samples are. Mean values for Q is found to be 2.4 ± 0.6 (σ = 2.5) for the core plugs, and 1.8 ± 0.6 (σ = 2.3) for the SWC-cores, respectively (omitting a single extraordinary high value of Q = 77 for SWC59). The Q-ratios of the two groups are not significantly different, but again the combined population has a tendency to two log-normal distributions.

Magnetic carriers

Two examples of isothermal remanent magnetisation (IRM) acquisition of plugs Nos 3 and 7 are shown in Fig. 11. Both specimens show magnetic saturation around 0.1 T, which indicate that the dominant carrier of the remanence is magnetite or Ti-magnetite, although maghemite may also be present. The thermal demagnetisations (see below) show blocking temperatures between 560 and

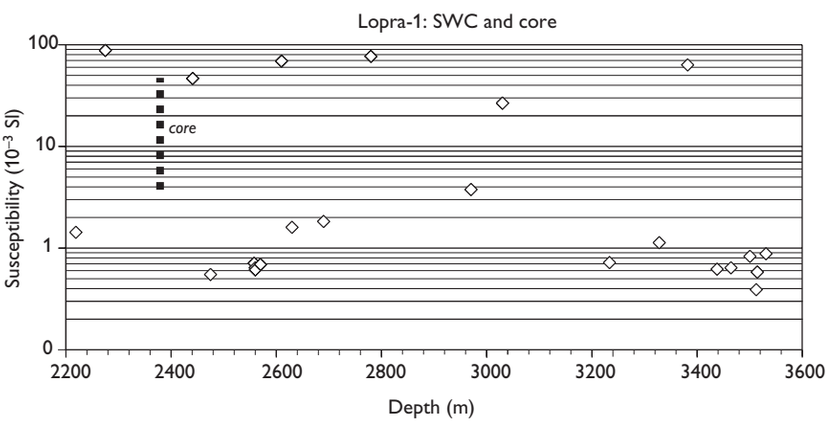

Fig. 8. Magnetic susceptibility of side-wall cores (**diamonds**) and core plugs (**dotted line** shows extent), logarithmic scale.

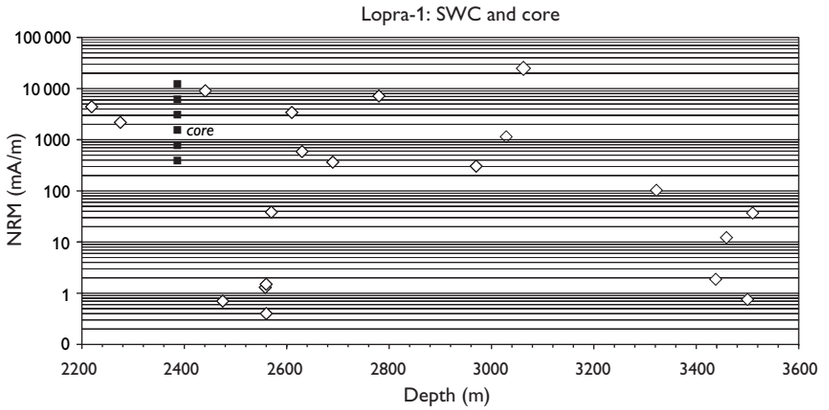

Fig. 9. NRM intensity of side-wall cores (**diamonds**) and core plugs (**dotted line** shows extent), logarithmic scale.

580°C, indicating that the Ti-content is low, pure magnetite having a Curie temperature of 580°C (e.g. Dunlop & Özdemir 1997).

AF and thermal demagnetisations

The NRM values of the 20 cores and the SWC-cores are listed in Tables 2a & b, and examples of characteristic results of the AF and thermal demagnetisation experiments performed are illustrated in Fig. 12. Thermal demagnetisations were made on cores Nos 10, 12, 16 and 18 and AF-demagnetisations were made on the remaining 16 cores. Values chosen for the AF-field were in most cases 0, 5, 7.5, 10, 15, 20, 25, 30, 40, 50 and 60 mT. Some plugs were further demagnetised to 70, 80, 90 and 100 mT. Four thermally demagnetised plugs were first AF-demagnetised in 2.5, 5, 7.5, and 10 mT fields, to remove the recent drillstem-induced viscous remanence (see below), and then stepwise demagnetised at temperatures of 150, 250, 350, 450, 550, 570, 600 and 630°C.

The examples in Fig. 12 show stereographic plots (left) of the direction of the unit vector of the remanent magnetisation (solid signature: positive inclination, open signature: negative inclination). All except the first example show characteristic stable negative inclinations. To the right, the corresponding intensity decay of the sample is shown (normalised to the initial value $J_0 = J_{NRM}$), the horizontal scale indicating the peak value of the applied alternating field in Oe (× 0.1 mT), or the temperature in C.

Inclination

Prior to the demagnetisation experiments, about half of the plugs showed a low coercivity NRM with positive inclination (down-dip), which is most likely due to a drillstem induced viscous remanent magnetisation (VRM). The VRM was easily removed by AF-demagnetisation in low fields, typically between 2.5 and 5 mT.

Based upon the AF- and Thermal demagnetisation data, the characteristic (stable) remanent magnetisations for each plug were determined by the principal component analysis (PCA) method of Kirschvink (1980), as implemented in the IAPD-programme by Torsvik (1986). In all cases a stable characteristic, supposed primary, mag-

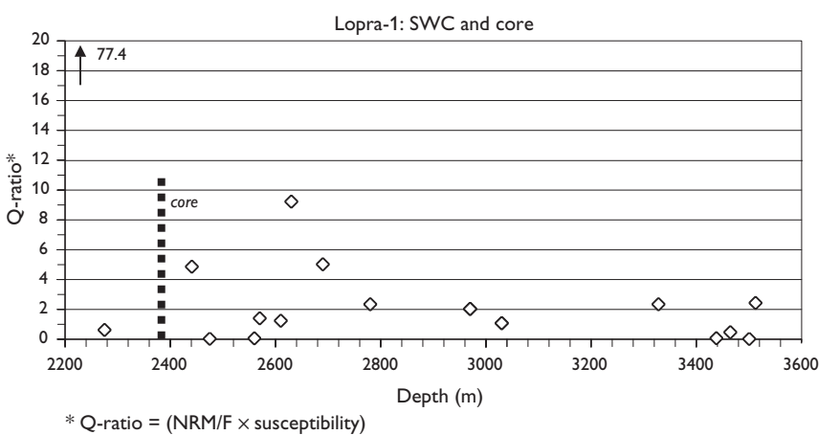

Fig. 10. Q-ratio of side-wall cores (**diamonds**) and core plugs (**dotted line** shows extent).

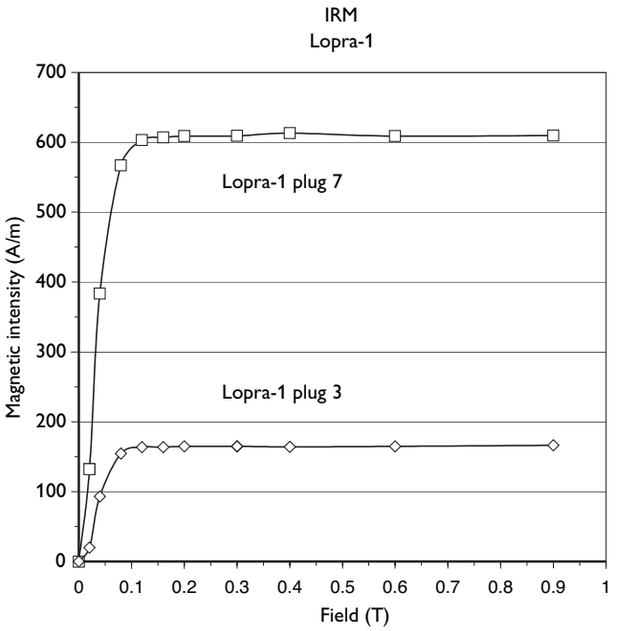

Fig. 11. Isothermal remanent magnetisation (IRM) of plugs Nos 3 and 7. Both specimens show magnetic saturation around 0.1 T, indicating that the dominating carrier of the remanent magnetisation is magnetite.

netisation was isolated, as listed in Table 3, and illustrated in the stereogram of Fig. 13. (Bearing in mind that the azimuth of the core is not known, only the inclinations are diagnostic, declinations being relative.)

After cleaning, plugs Nos 3 to 20 show typical steep negative inclinations. Only plugs 1 and 2 show normal inclinations and they are both from the topmost 10 cm long core-piece. The broken core is from the massive centre of a very thick flow and it is most unlikely that the inclination should shift the sign within the core. It is therefore suggested that the top part of the core has been turned upside-down, most likely during the initial handling at the core site.

As the azimuth of the core is not known, ordinary Fisher statistics are not applicable, but the modified inclination statistics of Kono (1980) may be used. Supposing all 20 plugs to have negative inclinations, the mean value is found to be:

$$I_m = -71.7°, \text{ with } \alpha_{95} = 1.95° \text{ (k = 709, N = 20)}$$

provided that the drilling was truly vertical. This would give an unusually accurate determination of the palaeofield inclination. However, as the geomagnetic secular variation cannot be recorded from one flow only, this low value

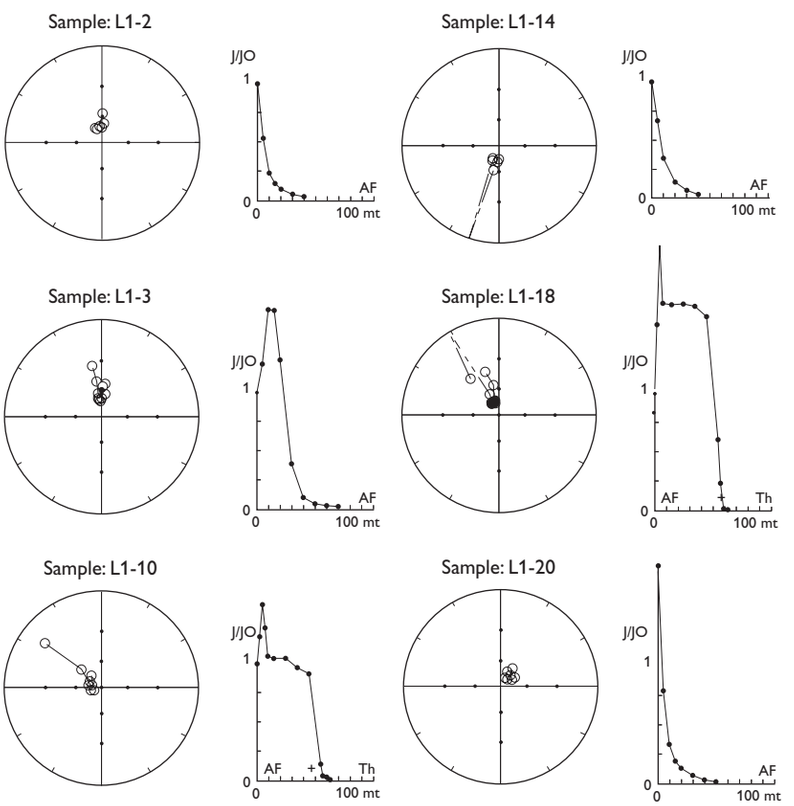

Fig. 12. Examples of typical behaviour of samples during AF and thermal demagnetisation. Plugs Nos 2 (AF 0–40 mT), 3 (AF 0–70 mT) and 10 (AF 0–10 mT, combined with heating up to 630°C). Plugs Nos 14 (AF 0–40 mT), 18 (AF 0–10 mT, combined with heating up to 630°C) and 20 (AF 0–50 mT).

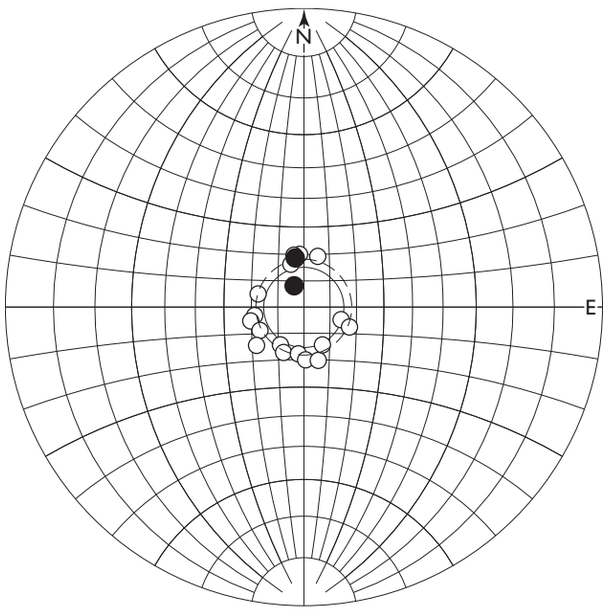

Fig. 13. Characteristic AF-cleaned inclinations of the 20 plugs from the Lopra-1/1A core at depths between 2380 and 2381.4 m. Plugs other than Nos 1 and 2 (with positive inclinations, **solid symbols**) have negative inclinations (**open symbols**). The declinations are arbitrary since the azimuth of the core is not known. **Full circle** shows the expected axially centred dipole inclination of 74.7° at the Lopra-1/1A drill site, i.e. 3° steeper than the numerical average of –71.7° (**dashed circle**) of the 20 core plugs (See Table 1).

of α_{95} does not give a realistic estimate for the accuracy of the average palaeomagnetic field inclination. Furthermore an angle of *c.* 2.5° from the vertical towards the southeast has been obtained from the GHMT-log of the hole at 2380 m (R. Waagstein, personal communication 2005).

The inclination I_0 of the geocentral axial dipole (GAD) field at the site of Lopra/Suðuroy with a latitude of 61.4°N is equivalent to a value of I_0 = 74.8°, which is about 3° steeper than that found for the core. Based on McElhinny & McFadden's (1997) analysis of a large number of volcanic data from the last 5 Ma in the global palaeomagntic database, the expected geomagnetic dispersion of a VGP (virtual geomagnetic pole) at the latitude of the Faroe Islands may further be estimated to be *c.* 20°. Earlier palaeomagnetic investigations have typically given systematically lower mean values (see Figs 3, 5) for the palaeomagnetic inclination (Table 1) except the one of –72° for a site near Torshavn (Løvlie & Kvingedal 1975). If we suppose the value from the Lopra-1/1A core of I_m = –71.7° to be the optimum one, this would correspond to an axial dipole palaeolatitude for the Lopra-1/1A site of 56.2°N at the time of extrusion. Most Cenozoic palaeopoles tend to be 'farsided' (Wilson 1971; Merrill *et al.* 1998), i.e. the palaeofield recorded in the rocks shows a more shallow inclination than does the present-day geomagnetic field at the site and biased shallow inclinations are also the case for most of the Palaeogene volcanic palaeomagnetic data from the North Atlantic region. This phenomenon may be due either to northward plate tectonic movements after the formation of the sample, non-symmetric behaviour of the geomagnetic field at the time of formation or unusual magnetic properties of the rocks investigated – or a combination of all three effects. A systematic error due to the latter cause (magnetic refraction) is not likely, as this requires rather strong values of the magnetic properties of the lavas (e.g. Knudsen *et al.* 2003). If the palaeogeomagnetic field was exactly a geocentral axial dipole field (the GAD-hypothesis), this would imply that the lithospheric plate carrying the Faroe Islands had moved about 5.2° northward during the last *c.* 60 Ma with an average northward component of velocity of *c*. 1 cm/year. An octopole contribution of the order of 10% (i.e. $g_3°/g_1° = 0.1$) to the central axial dipole field would alone suffice to explain the observed farsidedness of the Faroe Islands. An octopole contribution of this order of magnitude has been considered for Precambrian and Palaeozoic as well as Mesozoic times (e.g. Kent & Smethurst 1998; Torsvik *et al.* 2001; Van der Voo & Torsvik 2001). However, Merrill & McFadden's (2003) analysis of data in the palaeomagnetic global database for the last 5 Ma concluded that a non-dipole bias appears less likely for the younger periods.

Therefore, rather than claming that the shallower value of inclination indicates fully either a northward plate movement of 5.2° (the 'traditional' palaeomagnetic interpretation), or is due entirely to a deficiency in the GAD-hypothesis, a more cautious interpretation may be a combination of both, implying that the GAD-hypothesis may not be exactly valid for the early Palaeogene, i.e. that the palaeomagnetic field was not a perfect central and axial dipole field at that time. To solve this palaeomagnetic important question fully, more global data from the period is needed.

Reversal stratigraphy and age at Lopra-1/1A

As mentioned above, the reversal stratigraphy of the 6½ km thick Faroe basalt formations was re-interpreted by Waagstein (1988), based upon published data then available (Abrahamsen 1967; Tarling & Gale 1968; Schönharting & Abrahamsen 1984; Abrahamsen *et al.* 1984), including the former palaeomagnetic results from Lopra-

1, the cored information of which at that time reached a depth of 2178 m. All five cores from Lopra-1, at depths of 338, 862, 1219, 1923 and 2178 m, showed negative inclinations, i.e. reversed polarity, although no stable values were obtained after demagnetising the cores from 338 and 1219 m (Schönharting & Abrahamsen 1984). The bottom of Lopra-1 was interpreted by Waagstein (1988) to match marine anomaly 26r, thus superseding two earlier alternative correlations discussed by Abrahamsen *et al.* (1984), in which this level was suggested to match either marine anomaly 25r or 24r.

The present data from Lopra-1/1A, with negative inclinations in the single core from 2380 m depth, indicates a reversed polarity at this level. Provided that there are no reversals in the unsampled interval above, the present data extend the reversed sequence of the lower basalt formation from the core at TD of the original well (2178 m) to the present level of the solid core at 2380 m. The SWC-cores reach the deeper level of 3531 m. However, as the up–down orientation of the individual SWC-cores is not known, no inclination information has yet been obtained from below 2381 m.

Combining all polarity evidence available from the Faroe Islands and comparing with the Paleocene time scale by Berggren *et al.* (2000), we conclude that the lower part (below sea level) of the lower basalt formation may be correlated with Chron C26r (Selandian age), while the upper (exposed) part of the lower basalt formation correlates with Chrons C26n, C25r and C25n (Selandian and Thanetian age). The middle and upper basalt formations correlate with Chron C24r (Ypresian age).

Magnetic logging (magnetic susceptibility and field intensity) was also attempted in the Lopra-1/1A well together with other geophysical logs (Boldreel 2006, this volume) but, due to technical problems with the magnetic logging tool, no reliable inclination data were obtained (Abrahamsen & Waagstein 2006, this volume).

Summary and conclusions

A compilation of the palaeomagnetic age, the reversal chronology and evolution of the *c.* 6½ km thick basalt formations of the Faroe Islands is presented, together with new petrophysical results from the Lopra-1/1A well.

1. The polarity record of the Faroe Islands has been correlated in detail with the Global Polarity Time Scale. The lower part (below sea level) of the lower basalt formation correlates with Chron C26r (Selandian age).The upper (exposed) part of the lower basalt formation correlates with Chrons C26n, C25r and C25n (Selandian and Thanetian age). The middle and upper basalt formations correlate with Chron C24r (Ypresian age).
2. The inclinations yield farsided positions for the palaeomagnetic poles, which is characteristic of most Palaeogene volcanics and sediments from the North Atlantic region.
3. The density and the rock magnetic properties of a solid core (1½ m in length) and 26 sidewall cores from the Lopra-1/1A well between –2219 and –3531 m are bimodal and suggest two characteristic groups of volcanic materials, solid unaltered basalts and altered basalts and tuffs.
4. The magnetic properties are typically log-normally distributed and the carriers of remanence appear to be Ti-poor Ti-magnetites with Curie temperatures close to 580°C.
5. The inclination of the 1½ m core at –2380 m is predominantly negative.
6. Magnetic logging of magnetic susceptibility and field intensity was made in Lopra-1/1A down to –3515 m together with other geophysical logging, but yielded inconclusive inclinations.

Acknowledgements

The rock and palaeomagnetic measurements were made in the Geophysical Laboratory of the Department of Earth Sciences, University of Aarhus. Informative discussions with Regin Waagstein and the access to material from the Lopra-1/1A well at GEUS are acknowledged. Suggestions for improvements of the manuscript from Regin Waagstein, John Piper, the editor and an anonymous referee are also acknowledged.

References

Abrahamsen, N. 1965: Geofysiske undersøgelser på Færøerne, 144 pp. Unpublished cand. scient. thesis, Aarhus Universitet, Danmark.

Abrahamsen, N. 1967: Some palaeomagnetic investigations in the Faeroe Islands. Bulletin of the Geological Society of Denmark **17**, 371–384.

Abrahamsen, N. & Nordgerd, P. 1994: Rock magnetism of Tertiary volcanics from North-East Greenland. Rapport Grønlands Geologiske Undersøgelse **162**, 195–200.

Abrahamsen, N. & Waagstein, R. 2006: Magnetic logs from the Lopra-1/1A and Vestmanna-1 wells, Faroe Islands. Geological

Survey of Denmark and Greenland Bulletin **9**, 41–49 (this volume).

Abrahamsen, N., Schönharting, G. & Heinesen, M. 1984: Palaeomagnetism of the Vestmanna-1 core and magnetic age and evolution of the Faeroe Islands. In: Berthelsen, O., Noe-Nygaard, A. & Rasmussen, J. (eds): The Deep Drilling Project 1980–81 in the Faeroe Islands. Annales Societatis Scientiarum Faeroensis, Supplementum **IX**, 93–108. Tórshavn: Føroya Fróðskaparfelag.

Balling, N., Kristiansen, J.I. & Saxov, S. 1984: Geothermal measurements from the Vestmanna-1 and Lopra-1 boreholes. In: Berthelsen, O., Noe-Nygaard, A. & Rasmussen, J. (eds): The Deep Drilling Project 1980–81 in the Faeroe Islands. Annales Societatis Scientiarum Faeroensis, Supplementum **IX**, 137–147. Tórshavn: Føroya Fróðskaparfelag.

Balling, N., Breiner, N. & Waagstein, R. 2006: Thermal structure of the deep Lopra-1/1A borehole in the Faroe Islands. Geological Survey of Denmark and Greenland Bulletin **9**, 91–107 (this volume).

Berggren, W.A., Aubry, M.-P., van Fossen, M., Kent, D.V., Norris, R.D. & Quillévéré, F. 2000: Integrated Paleocene calcareous plankton magnetobiochronology and stable isotope stratigraphy: DSDP Site 384 (NW Atlantic Ocean). Palaeogeography, Palaeoclimatology, Palaeoecology **159**, 1–51.

Boldreel, L.O. 2006: Wire-line log-based stratigraphy of flood basalts from the Lopra-1/1A well, Faroe Islands. Geological Survey of Denmark and Greenland Bulletin **9**, 7–22 (this volume).

Bott, M.H.P., Sunderland, J., Smith, P.J., Casten, U. & Saxov, S. 1974: Evidence for continental crust beneath the Faeroe Islands. Nature **248**, 202–204.

Bott, M.H.P., Nielsen, P.H. & Sunderland, J. 1976: Continental P-waves originating at the continental margin between the Iceland–Faeroe Ridge and the Faeroe Block. Geophysical Journal of the Royal Astronomical Society **44**, 229–238.

Bullard, E.C., Everett, J.E. & Smith, A.G. 1965: The fit of the continents around the Atlantic. Philosophical Transactions of the Royal Society of London **A243**, 67–92.

Burke, K. & Torsvik, T.H. 2004: Derivation of Large Igneous Provinces of the past 200 million years from long-term heterogeneities in the deep mantle. Earth and Planetary Science Letters **227**, 531–538.

Butler, R.F. 1992: Paleomagnetism: magnetic domains to geologic terranes, 319 pp. Boston: Blackwell Scientific Publications.

Casten, U. 1974: Eine Analyse seismischer Registrierungen von den Färöer Inseln. Hamburger Geophysikalische Einzelschriften, Geophysikalische Institut der Universität Hamburg **21**, 109 pp.

Chambers, L.M., Pringle, M.S. & Parrish, R.R. 2005: Rapid formation of the Small Isles Tertiary centre constrained by precise $^{40}Ar/^{39}Ar$ and U-Pb ages. Lithos **79**, 367–384.

Dunlop, D.J. & Özdemir, Ö. 1997: Rock magnetism: fundamentals and frontiers, 595 pp. Cambridge: University Press.

Kent, D.V. & Smethurst, M.A. 1998: Shallow bias of palaeomagnetic inclinations in the Palaeozoic and Precambrian. Earth and Planetary Science Letters **160**, 391–402.

Kirschvink, J. 1980: The least squares line and plane and the analysis of palaeomagnetic data. Geophysical Journal of the Royal Astronomical Society **62**, 699–718.

Knott, S.D., Burchell, M.T., Jolley, E.J. & Fraser, A.J. 1993: Mesozoic to Cenozoic plate reconstructions of the North Atlantic and hydrocarbon plays of the Atlantic margins. In: Parker, J.R. (ed.): Petroleum geology of Northwest Europe: Proceedings of the 4th Conference, 953–974. London: Geological Society.

Knudsen, M.F., Jacobsen, B.H. & Abrahamsen, N. 2003: Palaeomagnetic distortion modelling and possible recovery by inversion. Physics of the Earth and Planetary Interiors **135**, 55–73.

Kono, M. 1980: Statistics of paleomagnetic inclination data. Journal of Geophysical Research **85**, 3878–3882.

Larsen, H.C. & Saunders, A.D. 1998: Tectonism and volcanism at the southeast Greenland rifted margin: a record of plume impact and later continental rupture. In: Saunders, A.D., Larsen, H.C. & Wise, S.W.J. (eds): Proceedings of the Ocean Drilling Program, Scientific Results **152**, 503–533. College Station, Texas (Ocean Drilling Program).

Larsen, H.C., Brooks, C.K., Hopper, J.R., Dahl-Jensen, T., Pedersen, A.K., Nielsen, T.F.D. & field parties 1995: The Tertiary opening of the North Atlantic: DLC investigations along the east coast of Greenland. Rapport Grønlands Geologiske Undersøgelse **165**, 106–115.

Larsen, L.M., Waagstein, R., Pedersen, A.K. & Storey, M. 1999: Trans-Atlantic correlation of the Palaeogene volcanic successions in the Faeroe Islands and East Greenland. Journal of the Geological Society (London) **156**, 1081–1095.

Larsen, T.B., Yuen, D.A. & Storey, M. 1999: Ultrafast mantle plumes and implications for flood basalt volcanism in the Northern Atlantic Region. Tectonophysics **311**, 31–43.

Lawver, L.A. & Muller, R.D. 1994: Iceland hotspot track. Geology **22**, 311–314.

Løvlie, R. 1975: The oxidation state of some Tertiary rocks from the Faeroe Islands and its implications for palaeomagnetism. Geophysical Journal of the Royal Astronomical Society **40**, 55–65.

Løvlie, R. & Kvingedal, M. 1975: A palaeomagnetic discordance between a lava sequence and an associated interbasaltic horizon from the Faeroe Islands. Geophysical Journal of the Royal Astronomical Society **40**, 45–54.

McElhinny, M.W. & McFadden, P.L. 1997: Palaeosecular variation over the past 5 Myr based on a new generalized database. Geophysical Journal International **131**, 240–252.

Merrill, R.T. & McFadden, P.L. 2003: The geomagnetic axial dipole field assumption. Physics of the Earth and Planetary Interiors **139**, 171–185.

Merrill, R.T., McElhinny, M.W. & McFadden, P.L. 1998: The magnetic field of the Earth, 527 pp. London: Academic Press.

Mosar, J., Eide, E.A., Osmundsen, P.T., Sommaruga, A. & Torsvik, T.H. 2002: Greenland–Norway separation: a geodynamic model for the North Atlantic. Norwegian Journal of Geology **82**, 281–298.

Nielsen, P.H. 1976: Seismic refraction measurements around the Faeroe Islands. Frodskaparrit **24**, 9–45.

Nielsen, P.H., Waagstein, R., Rasmussen, J. & Larsen, B. 1981: Marine seismic investigation of the shelf around the Faroe Islands. Danmarks Geologiske Undersøgelse Årbog **1981**, 101–109.

Nielsen, P.H., Stefànsson, V. & Tulinius, H. 1984: Geophysical logs from Lopra-1 and Vestmanna-1. In: Berthelsen, O., Noe-Nygaard, A. & Rasmussen, J. (eds): The Deep Drilling Project 1980–81 in the Faeroe Islands. Annales Societatis Scientiarum Faeroensis, Supplementum **IX**, 115–135. Tórshavn: Føroya Fróðskaparfelag.

Nielsen, T.K., Larsen, H.C. & Hopper, J.R. 2002: Contrasting rifted margin styles south of Greenland: implications for mantle plume dynamics. Earth and Planetary Science Letters 200, 271–286.

Noe-Nygaard, A. & Rasmussen, J. 1984: Introduction: Geological review and choice of drilling sites. In: Berthelsen, O., Noe-Nygaard, A. & Rasmussen, J. (eds): The Deep Drilling Project 1980–81 in the Faeroe Islands. Annales Societatis Scientiarum Faeroensis, Supplementum **IX**, 9–13. Tórshavn: Føroya Fróðskaparfelag.

O'Connor, J.M., Stoffers, P., Wijbrans, J.R., Shannon, P.M. & Morrissey, T. 2000: Evidence from episodic seamount volcanism for pulsing of the Iceland plume in the past 70 Myr. Nature 408, 954–958.

Ogg, J.C. 1995: Magnetic polarity time scale of the Phanerozoic. Ahrens, T.J. (ed.): Global earth physics: a handbook of physical constants, 240–270. Washington D.C: American Geophysical Union.

Pálmason, G. 1965: Seismic refraction measurements of the basalt lavas of the Faeroe Islands. Tectonophysics **2**, 475–482.

Rasmussen, J. & Noe-Nygaard, A. 1969: Beskrivelse til geologisk kort over Færøerne i målestok 1:50 000. Danmarks Geologiske Undersøgelse I. Række **24**, 370 pp. + map vol. (with summaries in Faroese and English).

Rasmussen, J. & Noe-Nygaard, A. 1970: Geology of the Faeroe Islands. Danmarks Geologiske Undersøgelse I. Række **25**, 142 pp.

Richardson, K.R., Smallwood, J.R., White, R.S., Snyder, D.B. & Maguire, P.K.H. 1998: Crustal structure beneath the Faeroe Islands and the Faeroe–Iceland Ridge. Tectonophysics **300**, 159–180.

Riisager, P., Riisager, J., Abrahamsen, N. & Waagstein, R. 2002a: New paleomagnetic pole and magnetostratigraphy of Faroe Islands flood volcanics, North Atlantic igneous province. Earth and Planetary Science Letters **201**, 261–276.

Riisager, P., Riisager, J., Abrahamsen, N. & Waagstein, R. 2002b: Thellier palaeointensity experiments on Faroes flood basalts: technical aspects and geomagnetic implications. Physics of the Earth and Planetary Interiors **131**, 91–100.

Saxov, S. 1969: Gravimetry in the Faeroe Islands. Geodætisk Institut Meddelelse **43**, 24 pp.

Saxov, S. & Abrahamsen, N. 1964: A note on some gravity and density measurings in the Faeroe Islands. Bollettino di Geofisica, Teorica ed Applicata **VI**, 49–62.

Saxov, S. & Abrahamsen, N. 1966: Some geophysical investigations in the Faeroe Islands. Zeitschrift für Geophysik **32**, 455–471.

Schönharting, G. & Abrahamsen, N. 1984: Magnetic investigations on cores from the Lopra-1 drillhole, Faeroe Islands. In: Berthelsen, O., Noe-Nygaard, A. & Rasmussen, J. (eds): The Deep Drilling Project 1980–81 in the Faeroe Islands. Annales Societatis Scientiarum Faeroensis, Supplementum **IX**, 109–114. Tórshavn: Føroya Fróðskaparfelag.

Schrøder, N.F. 1971: Magnetic anomalies around the Faeroe Islands. Fródskaparrit **19**, 20–29. Tórshavn: Føroya Fróðskaparfelag.

Storey, M., Duncan, R.A., Larsen, H.C., Waagstein, R., Larsen, L.M., Tegner, C. & Lesher, C.E. 1996: Impact and rapid flow of the Iceland plume beneath Greenland at 61 Ma. Eos, Transactions, American Geophysical Union 77, 839 only.

Tarling, D.H. 1970: Palaeomagnetic results from the Faeroe Islands. In: Runcorn, S.K. (ed.): Palaeogeophysics, 193–208. London: Academic Press.

Tarling, D.H. 1983: Palaeomagnetism, 379 pp. London: Chapman & Hall.

Tarling, D.H. & Gale, N.H. 1968: Isotopic dating and palaeomagnetic polarity in the Faeroe Islands. Nature **218**, 1043–1044.

Tarling, D.H., Hailwood, E.A. & Løvlie, R. 1988: A palaeomagnetic study of lower Tertiary lavas in E Greenland and comparison with other lower Tertiary observations in the northern Atlantic. In: Morton, A.C. & Parson, L.M. (eds): Early Tertiary volcanism and the opening of the NE Atlantic. Geological Society Special Publication (London) **39**, 215–224.

Torsvik, T. 1986: Interactive analysis of palaeomagnetic data. IAPD user-guide, 74 pp. Bergen: Universitetet i Bergen.

Torsvik, T., Van der Voo, R., Meert, J.G., Mosar, J. & Walderhaug, H. 2001: Reconstructions of the continents around the North Atlantic at about the 60th parallel. Earth and Planetary Science Letters **187**, 55–69.

Van der Voo, R. & Torsvik, T. 2001: Evidence for late Paleozoic and Mesozoic non-dipole fields provides an explanation for the Pangea reconstruction problems. Earth and Planetary Science Letters **187**, 71–81.

Waagstein, R. 1988: Structure, composition and age of the Faeroe basalt plateau. In: Morton, A.C. & Parson, L.M. (eds): Early Tertiary volcanism and the opening of the NE Atlantic. Geological Society Special Publication (London) **39**, 225–238.

Wilson, R.L. 1971: Dipole offset – the time average palaeomagnetic field over the past 25 million years. Geophysical Journal of the Royal Astronomical Society **22**, 491–504.

Ziegler, P.A. 1990: Geological atlas of western and central Europe. Amsterdam: Elsevier.

Manuscipt received December 1999; revision accepted 16 June 2005.

Petroleum geochemistry of the deepened Lopra-1/1A re-entry well, Faroe Islands

Jørgen A. Bojesen-Koefoed and H. Peter Nytoft

The Lopra-1/1A re-entry well was drilled as a stratigraphic test with no immediate exploration objectives. Hence, petroleum geochemical studies were of limited extent, and restricted to non-destructive analyses. The presence of natural petroleum hydrocarbons could not be confirmed with certainty, but hydrocarbons extracted from the hydrochloric acid solute of a calcite vug present in RSWC #1 (3543 m), may represent indigenous petroleum since hydrocarbon-bearing fluid inclusions have been reported from the same sample. These hydrocarbons show some similarities to petroleum generated from the Upper Jurassic – Lower Cretaceous Kimmeridge Clay type source rocks present in surrounding areas. Except for this sample, the results generally show the presence of a variety of contaminants of different origins such as 'naturally greasy fingers' (squalene and cholesterol), cosmetics such as chap stick or hand lotion (e.g. esters such as butyl-stearate, stearyl-palmitate, vitamin A), plasticisers (phthalates), diesel oil and 'pipe dope'.

Keywords: oil traces, organic geochemistry, contamination, Faroes, North Atlantic, Lopra

Geological Survey of Denmark and Greenland, Øster Voldgade 10, DK-1350 Copenhagen K, Denmark. E-mail: *jbk@geus.dk*

As part of the preparatory activities prior to an expected future licensing round on Faroese territory, a consortium of oil companies (see Heinesen *et al.* 2006, this volume) undertook to drill the Lopra-1/1A re-entry well as a stratigraphic test. The primary objectives of the well were to obtain lithological and stratigraphic information on the deepest parts of the Faroese flood basalt sequence as well as its substratum, and to acquire information related to the assessment of the petroleum exploration prospectivity of the area.

The original Lopra-1 well was drilled in 1981 and reached a total depth (TD) of 2178 m. The well penetrated a succession of flood basalts with minor tuffs and two dolerites (probably dykes). The drilled sequence was interpreted as part of the Faroese lower basalt formation or series (Waagstein *et al.* 1984; Waagstein 1988). The Lopra-1 well was re-entered in 1996 and deepened to a TD of 3565 m. The new drilling showed that the subaerial flood basalt sequence was underlain by a subaqueous hyaloclastite-basalt succession, comprising the interval 2550–3565 m and consisting predominantly of lapilli-tuffs, tuff-breccias and beds of blocks of basalt. No clastic sedimentary rocks were recorded (Boldreel 2006, this volume).

The deepened Lopra-1/1A re-entry well had no direct hydrocarbon exploration objectives and, as a technical consequence, other types of investigations took priority over petroleum geochemistry. This was particularly the case since no sedimentary rocks were penetrated and neither were any evident shows detected during drilling. Accordingly, the analytical programme carried out with respect to petroleum geochemistry was somewhat limited in scope and character.

Previously, various indications had been recorded of the presence of hydrocarbons in the original Lopra-1 well prior to deepening (Jørgensen 1984; Laier *et al.* 1997):

1. During drilling in 1981, a gas show was noted at 2008 m bRKB and 'wax'/bitumen was observed on zeolites.
2. In 1983, gas at a pressure of 19 bar was sampled at the wellhead. The gas flowed at approximately 1 m^3 per day and consisted of methane (72%), N2 (27%), and traces of higher hydrocarbons (Jacobsen & Laier 1984).

Table 1. Sample identification, solvent extraction and gas chromatographic key data

Sample	Depth (m b. KB)	Lithology	Comment	Extract recovery (mg)	Asphaltenes[a]	Saturates[b]	Aromatics[b]	NSO[b]	pr/ph[c]	CPI[d]
RSWC #51	2361	Vesicular basalt	Entire RSWC immersed in DCM	1.0	n.a.	n.a.	n.a.	n.a.	1.61	1.11
RSWC #45	2450	Basalt	Entire RSWC immersed in DCM	0.8	n.a.	n.a	n.a.	n.a.	1.50	1.17
RSWC #36	2570	Welded tuff	Entire RSWC immersed in DCM	0.6	n.a.	n.a.	n.a.	n.a.	1.52	n.a.
RSWC #33	2630	Welded tuff	Entire RSWC immersed in DCM	0.8	n.a.	n.a.	n.a.	n.a.	1.41	n.a.
RSWC #24	3076	Basalt	Entire RSWC immersed in DCM	0.7	n.a.	n.a.	n.a.	n.a.	1.36	n.a.
RSWC #13	3438	Lapillic tuff	Entire RSWC immersed in DCM	1.1	n.a.	n.a.	n.a.	n.a.	1.34	n.a.
RSWC #1	3543	Tuff w. calcite vug	Entire RSWC immersed in DCM	n.d.	n.a.	n.a.	n.a.	n.a.	1.38	n.a.
RSWC #1	3543	Tuff w. calcite vug	Calcite vug dissolved in HCl, organic extract recovered by shaking with DCM	1.1	27.3	n.a.	n.a.	n.a.	1.02	1.24
RSWC #1	3543	Tuff w. calcite vug	Tuff chip, counterpart of calcite vug, crushed and extracted	6.3	76.2	22.2	11.1	66.7	1.20	1.33
Drilling mud	2900		Approximately 10 g of drilling mud before addition of diesel, rinsed by DCM	5.7	7.0	67.3	19.2	13.5	1.15	1.17
Drilling mud	3200		Approximately 10 g of drilling mud after addition of diesel, rinsed by DCM	23.9	2.5	68.0	22.2	9.9	1.66	1.05
Pipe dope			Anti-seize compound for drilling rods sample supplied by DANOP	n.a.	2.1	57.8	24.5	17.7	n.a.	n.a.

[a] in wt% of total extract.
[b] in wt% of maltene fraction.
[c] pristane/phytane ratio, from gas chromatography.
[d] carbon preference index, calculated over the interval $nC_{22–32}$.

RSWC: rotary sidewall core.
DCM: dichloromethane.
n.a.: not analysed.
n.d.: not detected.
KB: Kelly Bushing.

In addition, water with an oil-film was produced by the well, but the oil film was not analysed in detail. Based on its isotopic composition, it was concluded that the gas was principally of thermogenic origin, although the gas was unusually 'dry' (Laier *et al.* 1997).

3. In 1992, oil-film on water from the well was sampled, and minor amounts of gas escaped from the wellhead. Based on geochemical analysis, it was suggested that the oil originated from a mature siliciclastic source rock, which was presumed to be present below the basaltic cover (Laier *et al.* 1997).
4. During a VSP-survey in 1994, a logging tool was lowered into the well and a thick, oil-smelling mud-slurry was observed sticking to the tool and wire when returned to the surface. Minor amounts of gas were noted. Analysis of the slurry revealed the presence of petroleum components similar to those detected in water samples from the well.

Moreover, wax-coatings on zeolite minerals have been recorded in several outcrops on the Faroe Islands (Jørgensen 1984; Laier *et al.* 1997).

In order to check if these indications of the presence of petroleum in the Lopra-1 well prior to deepening could be further substantiated, a minor petroleum geochemical analytical programme was carried out on samples from the deepened well, the results of which are reported below.

Samples and methods

Since the Lopra-1/1A re-entry well was drilled as a stratigraphic test, samples were principally reserved for investigations directly related to the main objectives of the programme, and petroleum geochemical studies were generally restricted to non-destructive analyses. Hence, samples could not be crushed and analyses had to rely on organic matter extracted from the surface and the directly accessible pore-spaces of the recovered rock samples. This procedure is necessarily sub-optimal, since, as will be demonstrated, the risk of contamination is overwhelming. However, for pre-determined reasons other types of investigations had been assigned greater priority.

All analyses were carried out on rotary sidewall cores (RSWC), 58 of which were collected over the section penetrated in the deepened well below the TD of the original Lopra-1 well, i.e. deeper than 2178 m bRKB. All samples consisted of basaltic volcanics, i.e. lavas, tuffs and hyaloclastic breccias.

Upon receipt, all RSWC samples, which came in screw-cap glass containers, were taken to a darkroom and checked by organolfactoric means for petroleum odour, and for visible fluorescence by means of a hand-held UV-lamp. Based on the presence of a distinct petroleum odour and weak to clear fluorescence, seven samples were selected for further study (Table 1).

In order to preserve the samples intact for other investigations, extracts were recovered from the surface and the immediately accessible pore spaces of the samples by immersing entire RSWCs into dichloromethane (DCM) for approximately 15 minutes in a glass beaker placed in an ultrasonification device. Rock fragments were separated by centrifugation, DCM was removed by evaporation, and the recovery was determined by weighing.

Due to very low recoveries, no further preparative procedures were applied. Total extracts were re-dissolved in isooctane and analysed by gas chromatography (GC) and by coupled gas chromatography – mass spectrometry (GC-MS).

RSWC #1 (3543 m) was treated as described above, but a small chip containing a calcite-filled vug was removed from the sample. The vug was dissolved in dilute hydrochloric acid (HCl, 2N), and an organic extract was recovered by several stages of shaking the solute with dichloromethane (DCM) in a separatory funnel (Table 1). The basaltic counterpart of the vug was coarsely crushed and extracted for four hours in a Soxtec apparatus (1h reflux in DCM, followed by 3h rinsing). Asphaltenes were precipitated from both extracts by addition of 40-fold excess of *n*-pentane, and the maltenes were separated into saturated, aromatic and polar compounds by Medium Pressure Liquid Chromatography (MPLC), using a method modified from Radke *et al.* (1980). Saturate fractions were analysed by GC and GC-MS.

In order to remedy problems with a stuck pipe, diesel was added to the well at a depth of approximately 3100 m. Neither samples of the diesel, nor of the drilling mud, were preserved for analysis. Instead, drilling mud from bagged drill cutting samples collected before and after addition of diesel were analysed in order to check for possible contamination. Approximately 10 g of sample (drilling mud plus cuttings) were ultrasonically extracted with DCM (app. 100 ml). Extracts were recovered by decantation and centrifugation, and the DCM removed by evaporation. Asphaltenes were precipitated by addition of 40-fold excess of *n*-pentane, with the maltenes being separated into saturated, aromatic and polar components as described above. The saturate fractions were analysed by GC and GC-MS.

An additional possible source of contamination was pipe dope, an anti-seize compound used when joining drilling rods. A sample of the pipe-dope used during drilling of the Lopra-1/1A re-entry well was supplied by DANOP and analysed using standard procedures for oil analysis. Asphaltenes were precipitated by addition of 40-fold excess of *n*-pentane, and the maltenes were separated into saturated, aromatic and polar components as described above. Again the saturate fractions were analysed by GC and GC-MS.

Gas chromatographic analyses were carried out by means of a Hewlett-Packard 5890 Series II plus gas chromatograph, using splitless injection, a 25 HP-1 WCOT column and a flame ionisation detector (FID).

Biological marker analyses were carried out by means of a Hewlett-Packard 5980A Series II gas chromatograph interfaced to a Hewlett-Packard 5971 mass selective detector (MSD) using splitless injection and a 25 m HP-5 WCOT column.

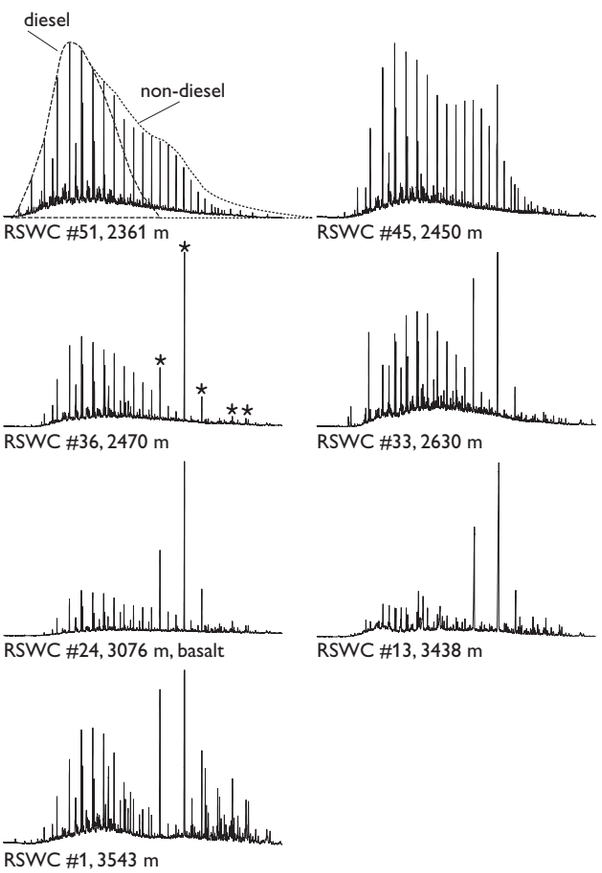

Fig. 1. Gas chromatograms obtained from analysis of RSWCs rinsed in DCM. Approximate shapes and positions of 'diesel' and 'non-diesel' envelopes are shown in sample RSWC #51. Examples of 'prominent unknowns' are indicated by asterisks in sample RSWC #36, see Fig. 3. Note that all samples show some degree of diesel contamination, although this adulterant was not added until a depth of approximately 3100 m. This observation suggests that diesel contamination is pervasive throughout the entire uncased section of the well.

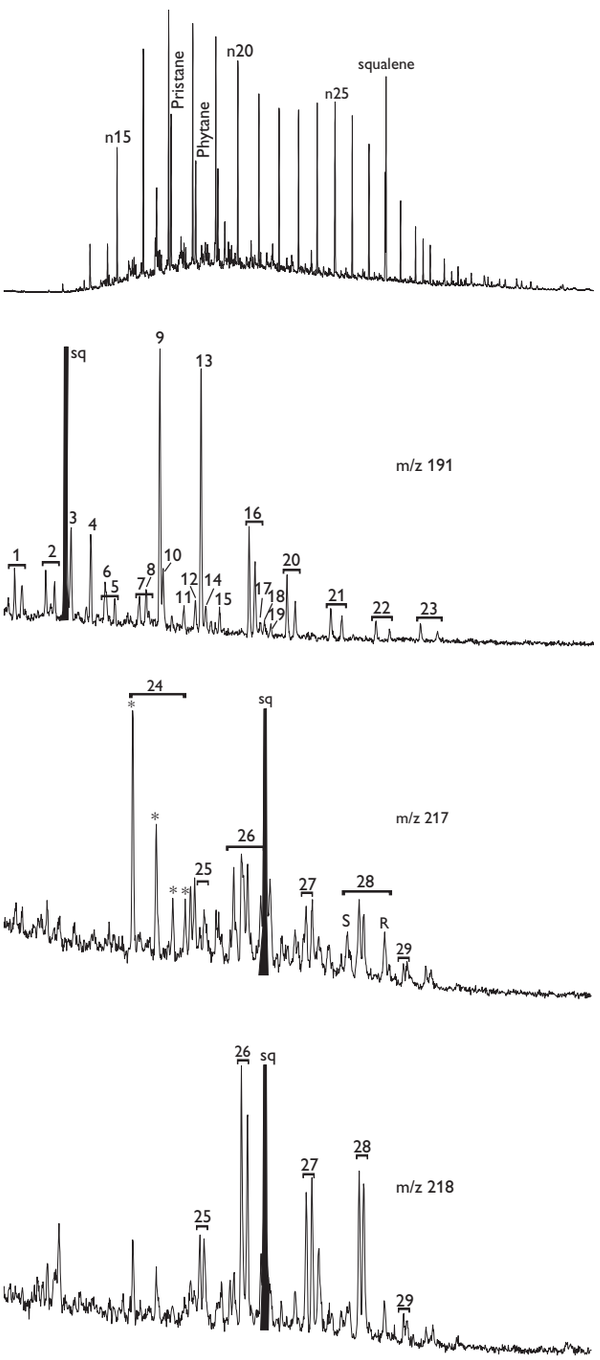

Fig. 2. Gas chromatogram and representative ion fragmentograms m/z 191, m/z 217 and m/z 218 (sample RSWC #45, 2450 m). Filled black peak labelled '**sq**' is the contaminant squalene – a compound found on the skin of humans. Compound identification is shown in Table 5.

Results

RSWCs rinsed in DCM

Total extract recoveries were generally close to 1 mg, and no attempt was made to fractionate the residues. Gas chromatograms of the bulk extracts (Fig. 1) show that most samples contain a more or less well-developed series of *n*-alkanes. The distributions are generally light-end skewed and unimodal, but two samples show evidence of bimodal distributions with higher proportions of waxy (22+) *n*-alkanes. Pristane/phytane ratios range from 1.34 to 1.61, and no odd- or even-number predominance is noted among the *n*-alkanes. In addition to *n*-alkanes, a number of prominent peaks of unknown identity are noted in all but one of the chromatograms, see below. Key parameters are listed in Table 1.

Biological marker maturity indications are consistent, with homohopane and bishomohopane 22S/(22S + 22R) epimerisation ratios at equilibrium (i.e. close to 0.60), and C_{29} sterane 20S/(20S + 20R) epimerisation ratios slightly below equilibrium (i.e. slightly less than 0.52), indicating early to mid oil-window maturity (Table 2). Sterane and triterpane biological marker distributions display only minor variations among the samples. Representative ion fragmentograms m/z 191, m/z 217, and m/z 218 are shown in Fig. 2, with key biological marker parameter ratios tabulated in Tables 3, 4. Triterpane distributions generally comprise fairly high proportions of tricyclic triterpanes. Among the pentacyclics the presence of 30-norhopanes plus 25-norhopanes is noted together with a peak eluting fractionally earlier than hopane. This peak is routinely assigned to 18α(H)-oleanane, a well-known marker of angiosperm higher plant inputs, and hence of source ages younger than the mid Cretaceous. However, scan-mode mass spectrometric analysis could not confirm the identity of this compound. Rather the peak represents several co-eluting compounds, probably comprising oleanane, lupane, and one or more unknowns. Limited amounts of sample precluded further investigation of this problem of identification. Norhopane to hopane ratios are close to unity and extended hopanes are relatively abundant. Moreover, gammacerane and notable proportions of hexahydrobenzohopane are present.

Sterane distributions are very similar for all samples, comprising a clear predominance of C_{27} steranes over the C_{28} plus C_{29} steranes, but with the co-occurrence of C_{30} as well as of C_{26} steranes. Prominence of ββ-sterane epimers is noted in both the m/z 217 and m/z 218 ion fragmentograms.

A number of prominent unknowns are noted in the

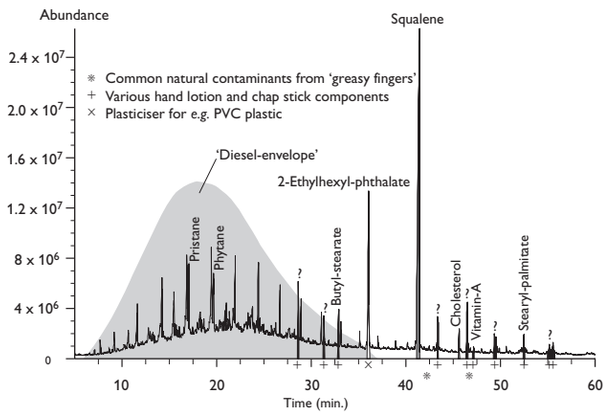

Fig. 3. Full scan total ion fragmentogram, RSWC #1. The approximate shape and position of a 'diesel envelope' are shown by **shading**. Interpretation of the origins of various contaminants is shown.

gas chromatograms as described above. Scan-mode mass spectrometric analyses of the extract obtained from RSWC #1, in which these compounds are particularly abundant, identifies: squalene and cholesterol; 2-ethylhexyl-phthalate; vitamin A and various esters such as butyl-stearate, stearyl-palmitate and a series of similar compounds (Fig. 3).

Calcite vug dissolved in HCl and basalt coarsely crushed

Total extract recovery of the acid-digested calcite vug was only 1.1 mg, whereas solvent extraction of the tuff host-rock yielded 6.3 mg. The comparatively high extraction yield of the latter sample is probably due to the more efficient extraction procedure, i.e. crushing and Soxtec extraction as opposed to ultrasonical extraction of entire samples.

Gas chromatograms of saturate fractions of the two sub-samples (Fig. 4) are different. The extract recovered from the acid-digested calcite vug shows a strongly unimodal *n*-alkane distribution, centred around C_{20}, with notable light-end depletion and a rather poor signal-to-noise ratio. The basalt extract shows a well-developed unimodal distribution of *n*-alkanes, centred around C_{17}, and a clear odd-predominance in the $C_{25–32}$ range. Pristane/phytane ratios are 1.02 and 1.20, respectively.

Biological marker distributions are similar in the two samples, although the signal-to-noise ratio observed in the acid-digested sample is rather poor (Fig. 4). These distributions are significantly different from the picture provided by other samples, including both sidewall cores (see above), drilling mud and pipe dope (see below). Triterpane distributions comprise low proportions of tricyclic triterpanes. Amongst the pentacyclics the presence of 28,30-bisnorhopane is noted, while 30-norhopanes, 25-norhopanes, and 'oleanane' are absent, or cannot be identified with any degree of certainty. H29/H30 ratios are close to 0.3 and extended hopanes are relatively scarce. Regular sterane distributions comprise a clear predominance of C_{27} steranes over the C_{28} plus C_{29} homologues with the presence of C_{30} as well as C_{26} steranes.

Drilling mud

Total extract recovery from the drilling mud samples differs widely before and after the addition of diesel to the drilling mud at a depth of approximately 3100 m bRKB (Table 1). This difference recurs in the gas chromatograms of saturate fractions of the two samples (Fig. 5). The sample collected before addition of diesel yields a rather irregular light-end skewed *n*-alkane distribution with high proportions of 'Unresolved Complex Mixture' (UCM). The sample collected after addition of diesel yields a well-defined, nearly symmetrical, unimodal *n*-alkane distribution, centred around C_{16}. Pristane/phytane ratios are 1.15 and 1.66, respectively.

Except for a minor enhancement of C_{27} diasteranes, and a slightly more pronounced enhancement of low molecular weight tricyclic triterpanes in the diesel-containing sample, biological marker distributions, however, are similar in the two samples and indistinguishable from

Table 2. Biological marker maturity data

Sample	S29 S/(S+R)[a]	S29 βα/(ββ+αα)[b]	H31 S/(S+R)[c]	H32 S/(S+R)[d]
RSWC #51	0.49	0.62	0.61	0.63
RSWC #45	0.48	0.60	0.59	0.61
RSWC #36	0.46	0.60	0.60	0.60
RSWC #33	0.43	0.63	0.59	0.63
RSWC #24	0.48	0.61	0.56	0.59
RSWC #13	0.49	0.60	0.57	0.60
RSWC #1	0.47	0.60	0.59	0.59
RSWC #1	0.44	0.58	0.58	0.59
RSWC #1	0.51	0.54	0.58	0.61
Drilling mud[e]	0.45	0.61	0.59	0.62
Drilling mud[f]	0.50	0.64	0.59	0.59
Pipe dope	0.42	0.42	0.65	0.57

[a] C_{29} regular sterane αα20S/(αα20S+αα20R) epimer ratio.
[b] C_{29} regular sterane ββ/(ββ+αα) epimer ratio.
[c] homohopane 22S/(22S+22R) epimer ratio.
[d] bishomohopane 22S/(22S+22R) epimer ratio.
[e] before addition of diesel.
[f] after addition of diesel.
RSWC: rotary sidewall core.

Table 3. Key triterpane biological marker parameter ratio

Sample	T23/H30[a]	Ts/(Ts+Tm)[b]	H28/H29[c]	H29/H30[d]	OL/H30[e]
RSWC #51	0.93	0.49	0.00	0.96	0.00
RSWC #45	1.00	0.52	0.00	1.06	0.14
RSWC #36	1.00	0.52	0.00	0.96	0.18
RSWC #33	1.14	0.54	0.00	0.93	0.14
RSWC #24	1.00	0.57	0.00	1.01	0.52
RSWC #13	1.06	n.a.	0.00	0.96	0.80
RSWC #1	0.64	n.a.	0.00	0.94	0.36
RSWC #1	0.13	0.43	0.35	0.33	0.00
RSWC #1	0.12	0.44	0.37	0.28	0.00
Drilling mud[f]	0.50	0.51	0.00	0.99	0.03
Drilling mud[g]	1.28	0.51	0.00	1.02	0.04
Pipe dope	0.44	0.41	0.00	0.12	0.16

[a] C_{23} tricyclic terpane to hopane ratio.
[b] Ts: 18α(H)-trisnorneohopane, Tm: trisnorhopane.
[c] H28: 28,30-bisnorhopane, H29: norhopane.
[d] H29: norhopane, H30: hopane.
[e] OL: 18α(H)-oleanane, H30: hopane.
[f] before addition of diesel.
[g] after addition of diesel.
n.a.: not analysed.
RSWC: rotary sidewall core.

Table 4. Key sterane biological marker parameter ratios

Sample	D27/S27[a]	S28 (%)[b]	S27 (%)[b]	S29 (%)[b]	S27/S29[c]	S30[d]
RSWC #51	1.33	19.0	50.8	30.2	1.7	present
RSWC #45	1.27	21.3	46.7	32.0	1.5	present
RSWC #36	1.39	23.0	46.0	31.0	1.5	present
RSWC #33	1.53	20.0	50.0	30.0	1.7	present
RSWC #24	1.20	19.56	51.0	29.4	1.7	present
RSWC #13	1.22	21.7	47.8	30.4	1.6	present
RSWC #1	0.95	22.4	47.4	30.3	1.6	present
RSWC #1	1.04	21.3	46.8	31.9	1.5	present
RSWC #1	1.06	21.4	48.2	30.4	1.6	present
Drilling mud[e]	0.81	19.5	47.0	33.5	1.4	present
Drilling mud[f]	1.19	24.6	45.9	29.5	1.6	present
Pipe dope	0.47	23.8	43.3	32.8	1.3	present

[a] (sum C_{27} diateranes)/(sum C_{27} regular steranes), m/z 217.
[b] relative distribution of C_{27-29} regular steranes, based on αα20R epimers in m/z 217.
[c] C_{27}/C_{29} regular sterane ratio, based on αα20R epimers in m/z 217.
[d] C_{30} regular steranes.
[e] before addition of diesel.
[f] after addition of diesel.
RSWC: rotary sidewall core.

the biological marker distributions yielded by RSWCs rinsed in DCM (Fig. 5).

Pipe dope

The gas chromatogram of the saturate fraction does not allow identification of any components, but simply shows a large hump of 'Unresolved Complex Mixture' (Fig. 6).

Biological marker maturity parameters indicate early to mid-oil window maturity (Table 2). Triterpane distributions generally comprise high proportions of tricyclic triterpanes, and among the pentacyclics the presence of 30-norhopanes plus abundant 25-norhopanes is noted together with a peak eluting fractionally earlier than hopane, probably representing several co-eluting compounds. These possibly comprise oleanane, lupane and one or more unknowns (Fig. 6). The H29/H30 ratio is 1.12 with extended hopanes being abundant. Gammacerane and notable proportions of hexahydrobenzohopane are present.

The distribution of regular steranes shows a clear predominance of C_{27} steranes over the C_{28} and C_{29} homologues plus the presence of C_{30} as well as C_{26} steranes. Prominence of ββ-sterane epimers is noted in both the m/z 217 and m/z 218 ion fragmentograms.

Discussion

The amounts of extract recovered from the RSWC samples are generally very low, which naturally limits the possibilities for detailed studies and implementation of extensive sample preparation techniques in order to optimise the quality of analytical data obtained. Furthermore, since total recoveries are low, even minor random contamination, which normally would be insignificant and ignored, may cause notable problems. Hence, considerable uncertainty is attached to the conclusions made on the basis of the analyses reported here.

Analyses of mud samples collected before and after addition of diesel show a profound influence of diesel on the content and distribution of *n*-alkanes, whereas the biological marker characteristics, except for minor enhancement of C_{27} diasteranes and low molecular weight tricyclic triterpanes, are largely unaffected. Hence for most practical purposes, this particular diesel distillate fraction will not severely influence any of the biomarker ratios. The biomarker distributions observed in the two mud samples are largely identical to the distributions yielded by DCM-rinsed RSWC samples.

Based on gas chromatography data, most DCM-rinsed RSWC samples are seen to contain diesel, but some extracts also contain longer chain-length *n*-alkanes and biological markers which are unlikely to originate from diesel contamination. In addition to diesel, contamination from various other sources is present in most samples:

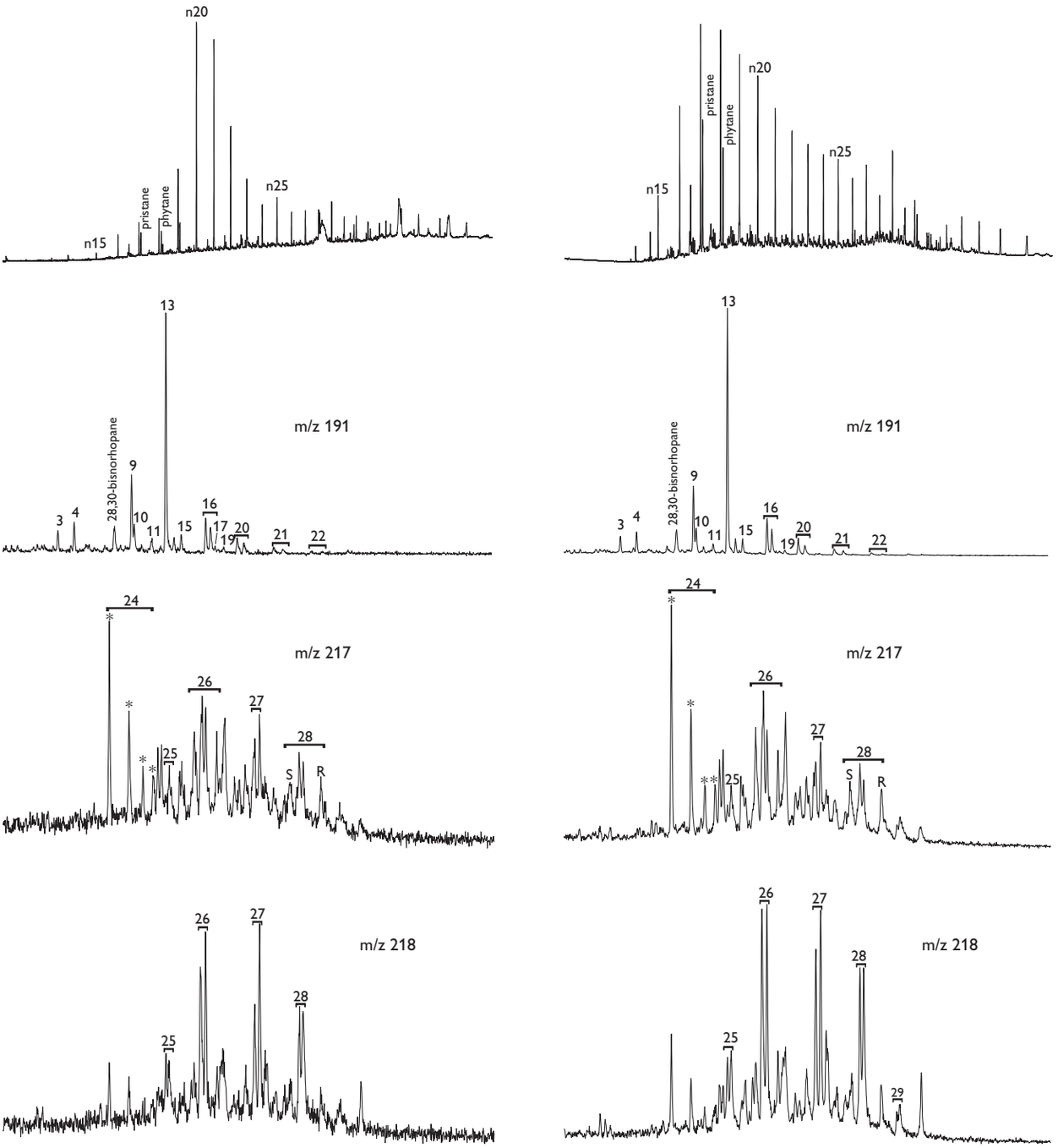

Fig. 4. Gas chromatograms and ion fragmentograms m/z 191, m/z 217 and m/z 218, RSWC #1, calcite vug dissolved in HCl (left), and its coarsely crushed tuff host rock (right). Note mutual similarity of biological marker distributions and differences when compared to distributions shown in Figs 2, 5, 6. Compound identification is shown in Table 5.

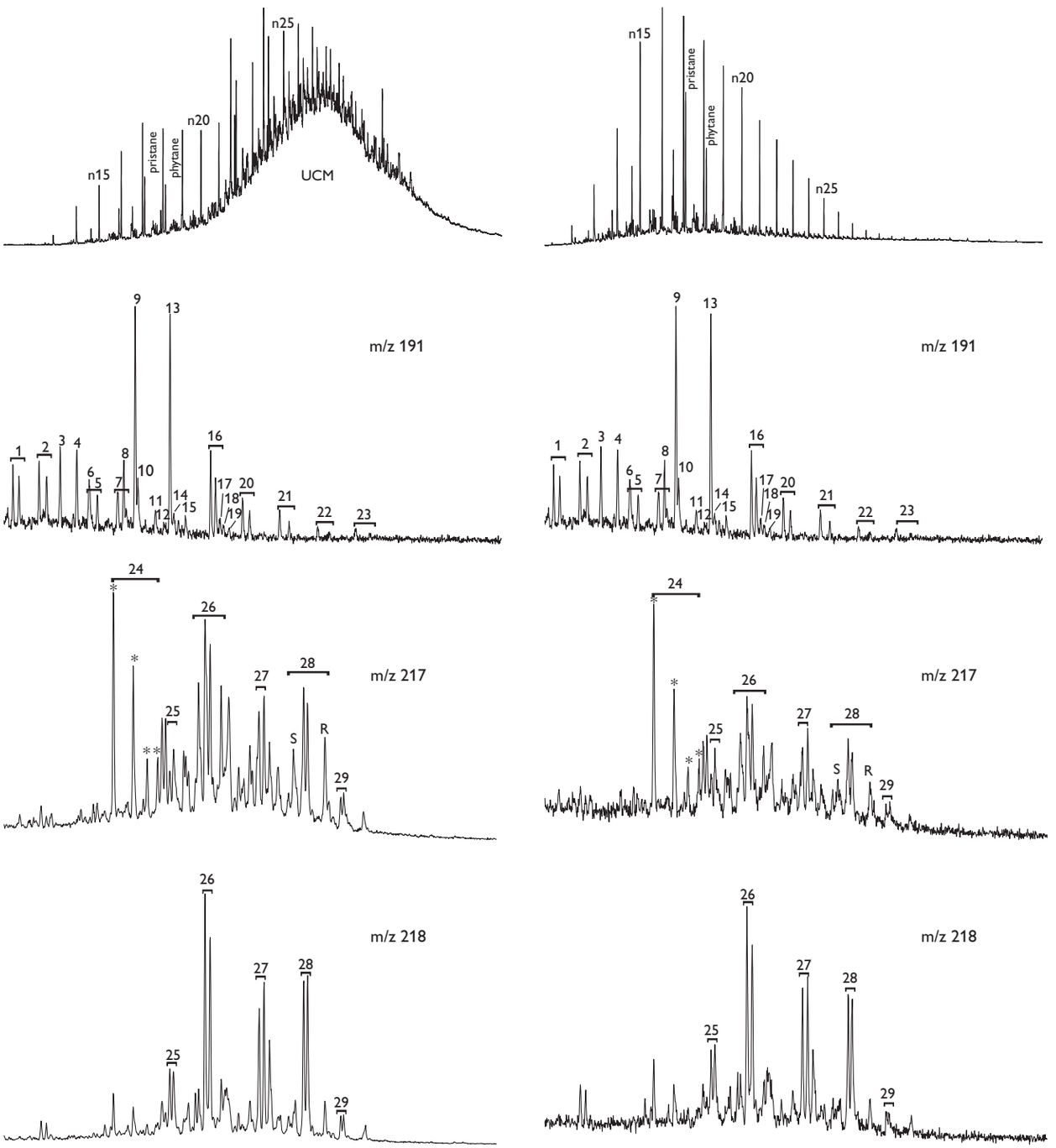

Fig. 5. Gas chromatograms and ion fragmentograms m/z 191, m/z 217 and m/z 218, extract of drilling mud before addition of diesel (left), and extract of drilling mud after addition of diesel (right). **UCM**, Unresolved Complex Mixture. Note profound influence of diesel on the *n*-alkane distribution, and the lack of, or limited effect on, biological marker distributions. Compound identification is shown in Table 5.

squalene and cholesterol are commonly occurring natural compounds present on the skin of humans, for instance on the hands ('naturally greasy fingers'); 2-ethylhexyl-phthalate is a widely used plasticiser for various polymers; vitamin A, esters such as butyl-stearate, stearyl-palmitate and similar compounds detected in the sample are commonly used in cosmetics, including hand lotion and chap-stick.

The absence of both acyclic isoprenoids and *n*-alkanes from pipe dope plus the presence of abundant 25-norhopanes suggest that this product is based on a heavily biodegraded oil (corresponding to level 6 of Peters & Moldowan (1993)). Based on the presence of 30-norhopanes, which is also manifest in norhopane to hopane ratio close to unity plus the prominence of ββ-sterane epimers and comparatively high proportions of homohopanes (in particular tetrakishomohopane to pentakishomohopane ratio close to unity), this oil was presumably generated from a marine marly source rock, deposited in a highly anoxic environment. In addition, the presence of angiosperm higher land plant markers such as 18α(H)-oleanane suggest a source age younger than the mid-Cretaceous. Normal and acyclic isoprenoid alkanes are absent, but the biological marker distribution shows clear similarities to the distributions yielded by DCM-rinsed RSWCs discussed above, such that the presence of contamination from pipe dope, in addition to adulteration from other sources, seems obvious. However, differences are observed: pipe dope contains very high proportions of 25-norhopanes, whereas the proportion in the RSWCs are but minor; the relative abundance of Ts and Tm is reversed in pipe dope compared to DCM-rinsed RSWC samples. Similarly, the proportion of C_{27} diasteranes relative to C_{27} regular steranes is much lower in pipe dope extracts than in the DCM-rinsed RSWC samples. The latter feature may, however, be wholly or partly caused by the addition of diesel, which was shown above to result in minor enhancement of low boiling-range tricyclics and diasteranes relative to non-contaminated samples.

In summary, DCM-rinsed samples are contaminated by a variety of compounds originating from several sources, including diesel, pipe dope, plasticisers, naturally greasy fingers and cosmetics, possibly hand lotion and/or chap stick. However, the samples also contain petroleum components that do not seem to originate from these sources of contamination. An origin from other sources of contamination or from indigenous crude oil is conceivable. Laier *et al.* (1997) show the presence of traces of heavy petroleum hydrocarbons and wax in samples from the original Lopra-1 well, prior to deepening. The 'unexplainable' petroleum components found in DCM-rinsed samples from the deepened well may represent similar occurrences.

Table 5. Compound identification key

Level	Compound
n15	C_{15} normal alkane
a	pristane
b	phytane
n20	C_{20} normal alkane
n25	C_{25} normal alkane
sq	squalene
n30	C_{30} normal alkane
1	C_{28} tricyclic terpanes (2 isomers)
2	C_{29} tricyclic terpanes (2 isomers)
3	Ts = trisnorneohopane
4	Tm = trisnorhopane
5	C_{30} tricyclic terpanes (2 isomers)
6	C_{28} 25,30 bisnorhopane, coeluting with "5"
7	C_{31} tricyclic terpanes (2 isomers)
8	C_{29} 25-norhopane, partially coeluting with "7"
9	norhopane = 30-norhopane
10	29Ts = norneohopane
11	normoretane
12	mixture of oleanane, lupane and unknown
13	hopane
14	C_{30} 30-norhopane
15	moretane
16	homohopane, 22S and 22R isomers
17	gammacerane
18	C_{31} hexahydrobenzohopane
19	homomoretane
20	bishomohopane, 22S and 22R isomers
21	trishomohopane, 22S and 22R isomers
22	tetrakishomohopane, 22S and 22R isomers
23	pentakishomohopane, 22S and 22R isomers
24	C_{27} diasteranes, 4 isomers labelled with asterisks
25	C_{26} regular steranes, ββ isomers only
26	C_{27} regular steranes, αα and ββ isomers
27	C_{28} regular steranes, ββ isomers only
28	C_{29} regular steranes, ααS, ααR and ββ isomers
29	C_{30} regular steranes, ββ isomers only

Biological marker, in particular triterpane, distributions in extracts recovered from DCM-rinsing of RSWC samples from the deepened Lopra-1 well show a number of striking similarities to distributions yielded by certain samples collected in the original Lopra-1 well prior to re-entry. These samples include petroleum extracted from water samples in 1992 (Laier *et al.* 1997), and a sample collected from slurry sticking to a VSP-tool, which was lowered into the hole in 1994. The biological marker characteristics include features such as the presence of 30-norhopanes, 25-norhopanes, gammacerane, hexahydrobenzohopane, H29/H30 ratios close to or greater than 1 and a high relative abundance of extended hopanes plus prominence of the ββ-sterane epimers. Minor differences between pipe dope and the 'slurry' and the oil film are also observed, principally with respect to the presence of *n*-alkanes and the proportions of C_{28} regular steranes relative to the pro-

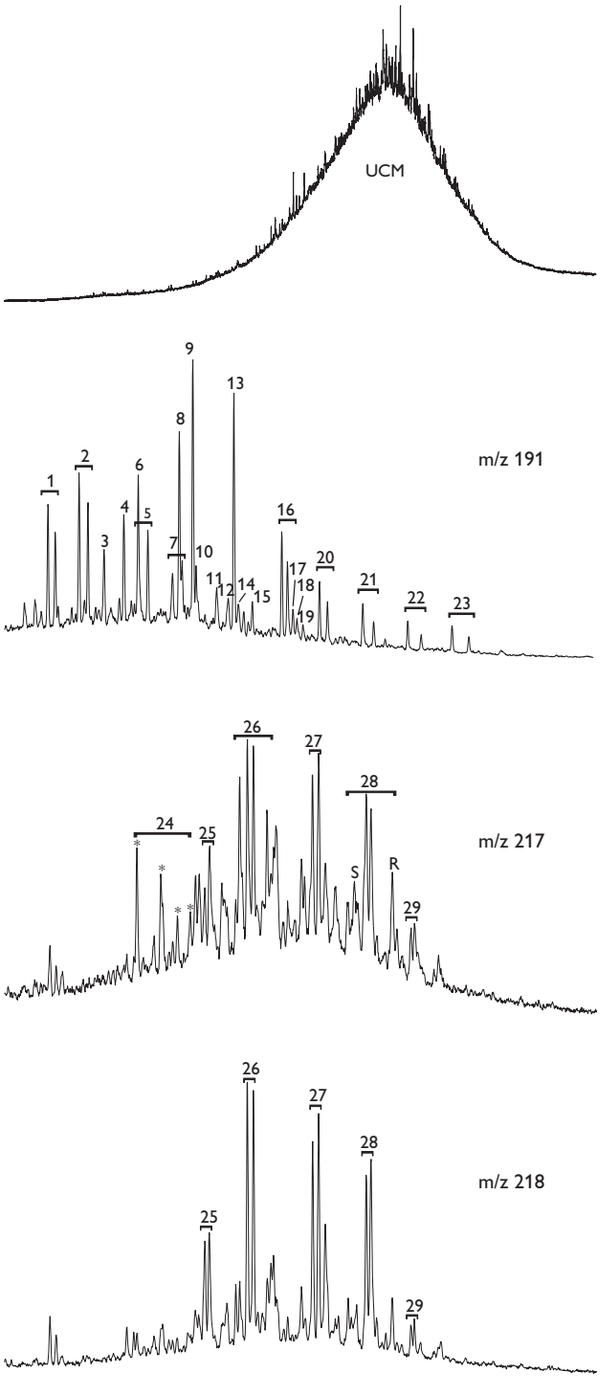

Fig. 6. Gas chromatogram and ion fragmentograms m/z 191, m/z 217 and m/z 218, pipe dope. **UCM**, Unresolved Complex Mixture. Compound identification is shown in Table 5.

portions of C_{27} and C_{29} regular steranes. However, the striking similarities and the presence of somewhat unusual components in pipe dope, as well as in the samples collected from the Lopra-1 well, prior to deepening, may suggest the presence of pipe dope contamination in the original borehole as well, the differences being accounted for by presumed differences between the pipe dopes used in the original and the deepened Lopra wells. Furthermore, the presence of a mid-Cretaceous or younger marly, anoxic marine source rock in the area, as implied by the geochemical data, seems geologically problematical. Carbonate or marly source rocks typically occur in lower latitude regions, i.e. areas within and close to the arid tropical belts (Tissot & Welte 1984). It is estimated that during the Cretaceous, the Faroe Islands area was situated at 40–45°N, and northward movement has prevailed since then (Habicht 1979; Scotese *et al.* 1988).

The biological marker characteristics of the extracts recovered from acid-digestion of a calcite-filled vug, and from its crushed tuff host-rock are totally dissimilar to the characteristics shown by all other samples from the well, including pipe dope. Principally, the distribution of triterpanes serves to distinguish these two samples from the remainder of the samples analysed. Hence, the following characteristic are noteworthy: lower proportions of tricyclic triterpanes, low norhopane to hopane ratio and the presence of 28,30-bisnorhopane. The signal-to-noise ratio is comparatively poor, but the overall biological marker characteristics show some similarities to oils generated from Upper Jurassic Kimmeridge Clay Formation sediments and their equivalents. This source system is known to be present in West of Shetlands basins (e.g. Scotchman *et al.* 1998) as well as in the North Sea basins, and can be prognosed for Faroese waters.

Glassley (2006, this volume) estimates that the maximum temperature reached at TD of the Lopra-1/1A reentry well was 200°C. Provided that this estimate is correct, the temperature may be too high to allow preservation of higher molecular weight liquid hydrocarbons if maintained over prolonged periods of time. The maximum temperature actually recorded in the well was 98°C, and assuming that the hydrocarbons found in RSWC #1 represent a thermogenic natural petroleum, this may have entered the tuff at a temperature lower than the maximum estimated by Glassley (2006, this volume), probably in connection with the formation of the calcite vug. Petroleum-bearing fluid inclusions have been observed in the same sample (Konnerup-Madsen 2006, this volume). Based on fluorescence colours (orange-yellow to green), an API gravity of 20–35 is estimated. No homogenisation temperature data have been recorded for the petroleum-bearing inclusions, but data from non-hydrocarbon bearing inclusions fall in the range 101–186°C, with the higher temperatures probably being caused by partial decrepitation. Hence, entrapment temperatures were probably con-

siderably lower than the maximum temperature as estimated by Glassley (2006, this volume), and it is conceivable that the signal obtained represents indigenous crude oil. If so, this observation is very encouraging for future exploration in Faroese territorial areas.

Conclusions

All samples are to variable degrees contaminated by a number of adulterants of different origins. The adulterants include:

1. *n*-alkanes and other petroleum components originating from commercial diesel fuel;
2. pipe dope, an anti-seize compound used, for instance, when joining drilling rods;
3. squalene and cholesterol originating from naturally greasy fingers;
4. vitamin A and various esters used in cosmetics, including chap stick and hand lotion;
5. 2-ethylhexyl-phthalate, a widely used plasticiser for polymers/plastics.

A number of striking similarities in biological marker distributions between pipe dope and samples collected in the well prior to re-entry and deepening may suggest the presence of pipe dope contamination in the original well too, in addition to the presence of traces of petroleum hydrocarbons as shown by Laier *et al.* (1997).

Organic extracts recovered from dissolution of a calcite vug in RSWC #1 (3543 m) and from its tuff host rock yield biological marker distributions different from all other samples collected in the Lopra-1 well. The distribution hints at generation from a marine anoxic shale source rock similar to the Kimmeridge Clay Formation and equivalents known from surrounding areas. It is conceivable that this organic extract represents an indigenous thermogenic petroleum, in particular since oil-bearing fluid inclusions have been observed in the same sample.

Acknowledgements

DANOP kindly supplied a sample of the pipe dope used during drilling of the well. Ditte Kiel-Dühring assisted in the preparation and analysis of the samples. Troels Laier and the reviewers Dr. R. Burwood and Dr. G. van Graas provided helpful comments and suggestions, which significantly improved the manuscript.

References

Boldreel, L.O. 2006: Wire-line log-based stratigraphy of flood basalts from the Lopra-1/1A well, Faroe Islands. Geological Survey of Denmark and Greenland Bulletin **9**, 7–22 (this volume).

Glassley, W.E. 2006: Mineralogical and thermodynamic constraints on Palaeogene palaeotemperature conditions during low-grade metamorphism of basaltic lavas recovered from the Lopra-1/1A deep hole, Faroe Islands. Geological Survey of Denmark and Greenland Bulletin **9**, 109–118 (this volume).

Habicht, J.K.A. 1979: Paleoclimate, paleomagnetism, and continental drift. AAPG Studies in Geology **9**, 31 pp. + maps.

Heinesen, M.V., Larsen, A.R. & Sørensen, K. 2006: Introduction. Geological Survey of Denmark and Greenland Bulletin **9**, 5–6 (this volume).

Jacobsen, O.S. & Laier, T. 1984: Analysis of gas and water samples from the Vestmanna-1 and Lopra-1 wells, Faeroe Islands. In: Berthelsen, O., Noe-Nygaard, A. & Rasmussen, J. (eds): The deep drilling project 1980–91 in the Faeroe Islands. Annales Societatis Scientiarum Færoensis Supplementum **IX**, 149–155. Tórshavn: Føroya Frodskaparfelag.

Jørgensen, O. 1984: Zeolite zones in the basaltic lavas of the Faeroe Islands. In: Berthelsen, O., Noe-Nygaard, A. & Rasmussen, J. (eds): The deep drilling project 1980–91 in the Faeroe Islands. Annales Societatis Scientiarum Færoensis Supplementum **IX**, 71–91. Tórshavn: Føroya Frodskaparfelag.

Konnerup-Madsen, J. 2006: A reconnaissance study of fluid inclusions in fracture filling quartz and calcite from the Lopra-1/1A well, Faroe Islands. Geological Survey of Denmark and Greenland Bulletin **9**, 119–122 (this volume).

Laier, T., Nytoft, H.P., Jørgensen, O. & Isaksen, G.H. 1997: Hydrocarbon traces in the Tertiary basalts of the Faeroe Islands. Marine and Petroleum Geology **14**, 257–266.

Peters, K.E. & Moldowan, J.M. 1993: The biomarker guide, 363 pp. New Jersey: Prentice Hall.

Radke, M., Willsch, H. & Welte, D.H. 1980: Preparative hydrocarbon group type determination by automated Medium Pressure Liquid Chromatography. Analytical Chemistry **52**, 406–411.

Scotchman, I., Griffith, C.E., Holmes, A.J. & Jones, D.M. 1998: The Jurassic petroleum system north and west of Britain: a geochemical oil–source correlation study. Organic Geochemistry **29**, 671–700.

Scotese, C.R., Gahagan, L.M. & Larson, R.L. 1988: Plate tectonic reconstruction of the Cretaceous and Cenozoic ocean basins. Tectonophysics **155**, 27–48.

Tissot, B. & Welte, D.H. 1984: Petroleum formation and occurrence, 2nd edition, 699 pp. Berlin: Springer Verlag.

Waagstein, R. 1988: Structure, composition and age of the Faeroe basalt plateau. In: Morton, A.C. & Parson, L.M. (eds): Early Tertiary volcanism and the opening of the NE Atlantic. Geological Society Special Publication (London) **39**, 225–238.

Waagstein, R., Hald, N., Jørgensen, O., Nielsen, P.H., Noe-Nygaard, A., Rasmussen, J. & Schönharting, G. 1984: Deep drilling on the Faeroe Islands. Bulletin of the Geological Society of Denmark **32**, 133–138.

Manuscipt received 16 June 2000; revision accepted 9 November 2000.

Hydrocarbon gases in Palaeogene volcanic rocks from the Lopra-1/1A well, Faroe Islands

Troels Laier

Hydrocarbon gases were monitored in the drilling fluid during deepening of the Lopra-1 well from 2178–3565 m, in which thermogenic, methane-rich gases had been found previously. The mud gas concentration, up to 10^5 ppm of methane, was generally higher in the hyaloclastite sequence, 2470 m – terminal depth (TD), than in the overlying lavas of the lower basalt formation. The highest concentrations of mud gas in the lower basalt formation were associated with the more porous tuffaceous zones, whereas no simple relationship could be established between measured mud gas concentrations and porosity of the hyaloclastic rocks, which showed less marked porosity variations than the lavas.

Chemical (C_{2+} < 1%) and isotopic ($\delta^{13}C_1$: –34 to –39‰) compositions of seven samples of mud gas collected at peak gas concentrations between 2657 m and 3442 m compare well with those of the hydrocarbon gases which had been seeping more or less continuously into the existing well since 1983, suggesting a common origin of the gases.

Headspace methane concentrations measured in 135 canned samples of cuttings were scattered between 10 ppm and 6 × 10^3 ppm, with the exception of six samples from a short interval, 2685–2745 m, which showed consistently high values > 10^4 ppm. No particularly gas-rich zones were indicated, however, by the mud gas, nor was any significant change in lithology noted for this interval. It is possible that the technique of turbo-drilling, that had been attempted over a short interval, 2657–2675 m prior to collection of the high-level methane samples, may have caused enhanced degassing due to the very fine cuttings produced. Chemical and isotopic composition of headspace gas and mud gas indicated the same type of gas throughout the well, although headspace methane tended to be more enriched with respect to the ^{13}C isotope.

The origin of the Lopra-1 gas is discussed in the light of recent information obtained from source rock studies of central East Greenland and the Faroe–Shetland Basin.

Keywords: Faroes, Lopra-1/1A, volcanics hydrocarbon gas, isotopes, headspace methane, cuttings

Geological Survey of Denmark and Greenland, Øster Voldgade 10, DK-1350 Copenhagen K, Denmark. E-mail: *tl@geus.dk*

As hydrocarbons were not expected to occur in the basalts of the Faroe Islands, no monitoring of hydrocarbon gases in the drilling fluid was performed while drilling the 2178 m deep scientific Lopra-1 well in 1981. A few observations made while drilling, however, indicated negligible amounts of gases in the basalts (Waagstein *et al.* 1984). None of these observations suggested larger accumulations of gas so, after having reached TD in November 1981, the drilling fluid in the well was replaced by fresh water. Soon afterwards, the well began to flow approximately 9.5 litres/min. (K. Højgård, personal communication 1982) and it was decided after a few days to shut-in the well. The Lopra-1 well was not re-opened until March 1983, when temperature logging was to be performed. By that time the wellhead pressure had increased to 19.5 bars (Balling *et al.* 1984) and an inflammable gas had accumulated within the 190 m long casing at the top of the well (P.H. Nielsen, personal communication 1983). The volume of the gas was estimated to be roughly 9 m^3 at 1 bar pressure (P.H. Nielsen, personal communication 1983)

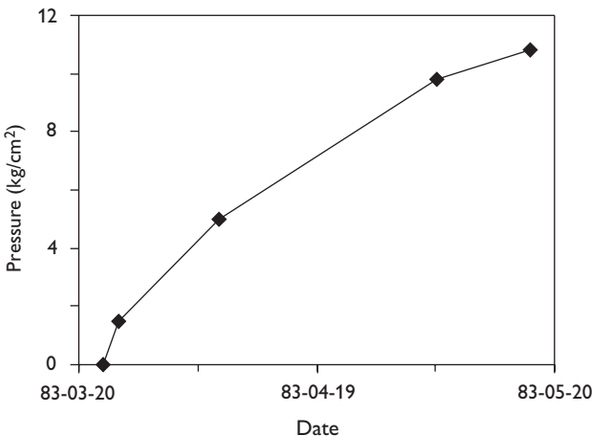

Fig. 1. Wellhead pressure of the Lopra-1 well during the shut-in period after temperature logging (P.H. Nielsen, personal communication 1983).

and gas chromatographic analysis of a sample collected at the wellhead showed the gas to consist of methane (72%) and nitrogen (27%) plus traces of higher hydrocarbons (Jacobsen & Laier 1984). After temperature logging, the well was shut-in again and an increase in wellhead pressure was noted shortly after. Two months later, the wellhead pressure had increased to 10.8 bars (Fig. 1). Collection of a new gas sample showed that the composition of the gas was almost identical to that of the sample collected two months earlier. Furthermore, isotopic analyses indicated that the gas was thermogenic in origin, the $\delta^{13}C$ of methane being –39.6‰ (Jacobsen & Laier 1984).

Encouraged by the hydrocarbon discoveries of Foinaven in 1992 and Schiehallion in 1993 in the British sector 160 km south-east of the Faroe Islands, new investigations of the hydrocarbon traces in the Lopra-1 well were carried out in 1992–1993, including stable isotopic analysis of gases and biomarker analyses of the small quantities of higher hydrocarbons extracted from the water flowing out of the well (Laier *et al.* 1997). An additional gas sample was taken for isotopic analysis in July 1994, before the deepening of the Lopra-1 well commenced in July 1996 (Table 1).

This paper presents the results of new chemical and isotopic analyses of both mud gas samples and headspace gas of canned cuttings collected during a deepening of the Lopra-1/1A well in 1996. The results of the continuous mud gas readings are compared with well logs in order to identify any particular gas-rich zones, and the possible origin of the hydrocarbon gases in the basalts is discussed.

Sampling and methods

Mud gas

Gas samples were taken at the mud-logging unit on different occasions (Table 2). The gas samples were stored in 100 cm^3 steel bottles which had been flushed with mud gas for two minutes before closing the valves. The samples were sent to the Geological Survey of Denmark and Greenland (GEUS) within a week for chemical and isotopic analyses.

The concentrations of hydrocarbon gases in the gas samples were analysed using a Shimadzu GC9 gas chromatograph equipped with a flame ionisation detector (FID). Separation of the gas constituents was performed on a 4 m $^1/_8$" diameter SS column packed with silica gel 70/80 mesh using helium as carrier gas (20 ml/min.) using a temperature programme beginning at 100°C, increasing 20°C/min. to 250°C final temperature.

Headspace gas of canned cuttings

Unwashed cuttings were sampled at approximately 10 m intervals and stored in 0.5 litre cans to which bactericide had been added. The cans were sent to GEUS for headspace gas and isotopic analyses after the completion of the well. The cans were generally in a good condition when received by GEUS, except for a few cans where the lid was not sealed tightly. The cans were placed upside down, punctured through a septum and 0.2 ml of headspace gas

Table 1. Chemical and isotopic composition of gases from the original Lopra-1 well collected at the wellhead

Year	CH_4	C_2H_6	C_3H_8	iC_4H_{10}	nC_4H_{10}	N_2	O_2+Ar	CO_2	H_2	$\delta^{13}C_1$	$\delta^{13}C_2$	$\delta^{13}C_3$	δD_1
1994	60.2	0.31	0.048	0.014	0.012	39.1	0.06	0.01	<0.01	–39.9	–32.1	–26.5	–150
1992	40.6	0.14	0.025	0.008	0.007	59.1	n.d.	0.01	<0.01	–41.5	–32.4	–26.5	–148
1983	1.9	0.41	0.064	0.015	0.018	27.5	0.04	0.01	<0.01	–39.6	–32.5	n.a.	–133

n.a.: not analysed; n.d.: not determined. Concentrations are given in vol%. Stable isotopic ratios are given (in parts per thousand) relative to the Pee Dee Belemnite (PDB) and Standard Mean Ocean Water (SMOW) standards.

Table 2. Drilling events which may influence hydrocarbon gas measurements

Interval (m)	Event	Comments
2360–2450	Sour smell and low pH of drilling fluid	Indication of bacterial activity. Bacteria may generate/consume methane. Low pH may cause corrosion and generation of artificial gas.
2657–2675	Turbo drilling	Finer cuttings. Possible enhanced degassing. Potential risk of gas generation due to high temperature.
2680–2822	One shale shaker out of order	Specific gravity increase, 1.11–1.18 g/cm^3, of drilling fluid due to solids build-up.
2992	20% dilution of mud	Reduction of specific gravity, 1.18–1.13 g/cm^3.
3023	Mud centrifuge installed	Reduction of specific gravity to 1.06–1.08 g/cm^3.
3158	String got stuck	5 m^3 diesel pill added.
3091–3565	Side track, Lopra-1A	1% oil in drilling fluid according to daily analysis.

was withdrawn using a gas-tight syringe to be analysed by gas chromatography as described above. If a high concentration of methane was found, 60 ml of headspace gas was transferred to an evacuated serum bottle for later isotopic analysis. The volume of headspace gas in the cans, generally between 100–150 ml, was checked by addition of water. No corrections on headspace gas concentrations were attempted to account for the difference in headspace volumes.

Isotopic analyses

Headspace gas and mud gas samples were transferred to a ¼" column packed with Porepak Q immersed in liquid nitrogen. Separation of the gas constituents was then performed allowing the column to heat to ambient temperature. Methane and ethane were combusted over CuO at 900°C and the resulting carbon dioxide was isolated in flame-sealed glass ampoules using cryogenic traps. Isotopic measurements were performed on a Finnigan Mat 251 mass spectrometer at the University of Copenhagen.

The isotopic ratio is expressed in the usual delta notation relative to the PDB standard.

$$\delta^{13}C(‰) = (R_{sample}/(R_{standard} - 1)) \times 1000$$

where

$$R = {}^{13}C/{}^{12}C$$

The analytical precision of the isotopic measurements is ± 0.2‰ for larger quantities of gas (> 20 µl CO_2 STP), typical of the amounts of methane in all of the analysed samples, and ± 0.5‰ for smaller quantities of gas (< 10 µl CO_2 STP), typical of the ethane.

Results and discussion

Gases from the original Lopra-1 well

No casing had been set in the old Lopra-1 well except for the upper 190 m of the borehole. Therefore, the substantial amount of gas which had accumulated at the wellhead during the 16 months shut-in period after drilling, could in theory have entered from any part of the open hole. However, Jacobsen & Laier (1984) observed an increase in the gas to water ratio with depth suggesting that the gas entered mainly in the deeper parts of the well. The flow of gas (0.8 litre/min., ambient pressure and temperature) from the well measured by Jacobsen & Laier (1984) during their field work in June 1983 also suggested that the gas continued to seep into the open borehole of the Lopra-1 well. Taking into account the methane dissolved in the water flowing out of the well (at a water flow rate of 12.8 litres/min.), the total flow of methane is estimated to have been approximately 0.9 litre/min.; 0.56 litre/min. in the gas phase (72% CH_4) plus 0.3 litre/min. dissolved in water. So the total flow of methane in June 1983 was over 1 m^3 per day. If the influx of methane had been the same during the initial 16 months shut-in period, a much larger quantity of gas would be expected than the 9 m^3 (ambient pressure) noted when the well was re-opened in March 1983. However, the flux may have been slower during the shut-in period due to higher pressure (19.5 bars) at the wellhead.

Gas was still seeping into the borehole 13 years after drilling of the Lopra-1 well. The composition of the hydrocarbon gas had not changed significantly during that period (Table 1) and this suggests a major single source of the gas. The source provided mainly methane, as the nitrogen content in the gas-to-water ratio measured at well-

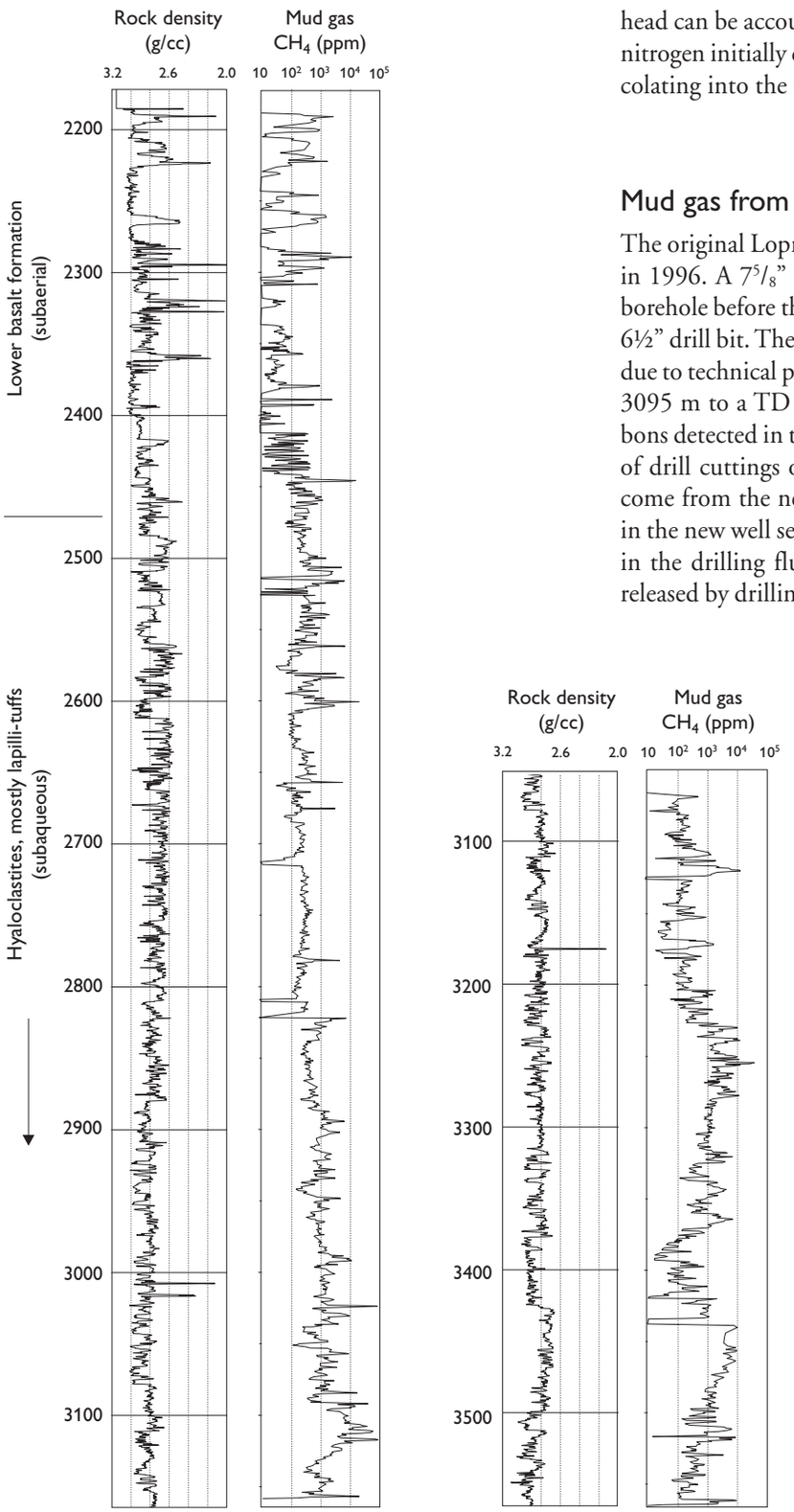

Fig. 2. Rock density and mud gas recorded in the extended Lopra-1/1A well.

head can be accounted for by the amount of atmospheric nitrogen initially dissolved in meteoric water (at 6°C) percolating into the basalts.

Mud gas from the Lopra-1/1A deepening

The original Lopra-1 well, drilled in 1981, was deepened in 1996. A $7^5/_8$" casing was first set in the existing 8½" borehole before the well was extended downwards using a 6½" drill bit. The Lopra-1 well was terminated at 3158 m due to technical problems and a sidetrack was drilled from 3095 m to a TD of 3565 m (Lopra-1A). Any hydrocarbons detected in the drilling fluid or in the sealed samples of drill cuttings of the extended well section must have come from the new drilling activities. No casing was set in the new well sections, which means that gases detected in the drilling fluid (Fig. 2) represent the sum of gases released by drilling in addition to the gases that may have

seeped through the sidewall of the entire open hole. A KCl-polymer mud was used as drilling fluid and the well logs indicate that no substantial mud cake had been built up in the hole. Therefore, gas seepage from the sidewall of the open hole was probably more significant for the Lopra-1/1A well compared to conventional exploration wells in sedimentary rocks.

The mud gas and headspace gas data from the Lopra-1/1A well are the only information available on hydrocarbon gases in the basalts penetrated, as no further tests were performed in the well after drilling. Drilling was optimised to detect hydrocarbon gases in the rocks penetrated, i.e. the specific gravity of the drilling fluid was kept low and the trap for continuous hydrocarbon measurement was placed in an almost closed mudline system. However, the mud gas and headspace gas must be interpreted with caution. It is important to consider any possible effects of the drilling process itself. The drilling events which may have influenced the hydrocarbon measurements and which could give a false impression of the hydrocarbon variation in the rocks, have been listed in Table 2, together with their possible implications.

The specific gravity of the mud could not be kept constant until a centrifuge had been installed (when drilling had reached 3023 m), after which the specific gravity remained at 1.06–1.08 g/cm^3. During drilling of the lower basalt formation from 2184 to 2470 m the specific gravity remained almost constant at 1.03–1.05 g/cm^3. At greater depths, the cuttings became finer and the specific gravity of the mud was increased gradually to 1.18 g/cm^3 at 2992 m by increasing the content of solids. An increase in mud weight suppresses degassing from the rocks, which lowers the gas concentration in the mud. On the other hand, an elevated solids content may increase gas concentration, depending on how fast the cuttings degas. With these uncertainties in mind, a more detailed interpretation of the mud gas will be presented below.

Mud gas concentration varied from less than 10 ppm to 90 000 ppm of methane down to 3120 m depth, showing a general increase from 2400 m to 3120 m (Fig. 2). Higher hydrocarbons, mostly ethane, constituted less than one percent of the total gas throughout the drilling of the well and will not be dealt with in detail in the following. The intervals with very low mud gas concentrations, < 10 ppm, were observed only in the lower basalt formation above 2470 m. Comparing mud gas concentration versus depth with various well logs as well as changes in various drilling parameters (rate of penetration, mud density etc.) it appears that rock porosity and rock density are the most important rock properties affecting the mud gas concentration in the upper 300 m of the extended well (Fig. 2).

Table 3. Samples of mud gas collected from the Lopra-1/1A well on various occasions

Sample No.	Date	Depth (m)	Event
1	96/08/28	2657	Resumed mud circulation after changing of drill bit
2	96/09/07	2822	Resumed mud circulation after changing of drill bit
3	96/09/09	2946	Gas collected after short drilling break
4	96/09/10	2989	Gas collected at peak concentration while drilling
5	96/09/19	3107.5	Gas collected at peak concentration while drilling
6	96/10/23	3343	Gas collected at peak concentration while drilling
7	96/10/26	3442	Gas collected after having drilled 6 m after trip

Variations in rock density and porosity correlate closely, so only the most complete log, the density log, is shown on Fig. 2. Assuming that the gas is indigenous to the rock and not an artefact of drilling, the highest gas concentrations should be found in the more porous, less dense rocks, as is also indicated by the data for the upper 300 m of the extended Lopra-1/1A well. However, this simple relationship is not observed for the deeper parts of the well. From 2610 m to 3080 m the density of the rock generally increases and porosity decreases, yet a general increase in mud gas concentration is observed in this same interval, an increase that may be explained by the increased sidewall surface area. This suggests that degassing through the sidewall of the hole contributes more to the mud gas compared to the gas released by the drilling process itself.

The presumed gas seepage through the sidewall of the open hole makes it difficult to decide which part of the well actually contributes to the gases recorded in the mud. However, for the deepest part of the well, below 3430 m, changes in the mud gas concentration appear to be correlated positively with porosity (and inversely with rock density), which may indicate that gas is present even in the deepest rocks penetrated by the Lopra-1/1A well. Thus, it may be concluded that hydrocarbons are most likely present in all of the rocks penetrated, particularly in the more porous rocks. However, no particular hydrocarbon-rich zones and no cap rock were identified.

Samples of mud gas were collected at maximum gas concentrations as far as possible (Table 3). Three of the samples were taken when mud circulation was resumed after changing the drill bit, and the rest of the samples were taken at maximum concentration while drilling. The

Table 4. Chemical and isotopic composition of mud gas samples

Depth (m)	CH_4 ppm	C_2H_6 ppm	C_3H_8 ppm	iC_4H_{10} ppm	nC_4H_{10} ppm	$\delta^{13}C_1$ (‰)	$\delta^{13}C_2$ (‰)	C_1/C_2
2657	4420	31.6	4.06	0.44	0.63	–38.6	–31.8	140
2822	4820	31.7	3.02	n.d.	n.d.	–38.2	–35.0	152
2946	2400	19.0	1.56	n.d.	n.d.	–36.7	n.a.	126
2989	10440	81.6	6.78	0.36	0.40	–37.3	–32.3	128
3107.5	10200	74.4	9.34	0.92	1.36	–38.1	–33.4	137
3343	2740	17.3	3.44	0.66	1.10	–34.2	n.a.	158
3442	4290	28.4	5.86	0.98	1.45	–36.0	–33.6	151

n.d.: not detected. n.a.: not analysed.

concentrations of hydrocarbon gases in the mud gas samples were usually lower compared to mud gas concentrations recorded in the mud by the time of sampling (Table 4) although the chemical composition of the gas was the same. The reason for this is not clear, but insufficient flushing of the 100 cc steel bottle during sampling could be one reason. The chemical and isotopic composition of the mud gas (Table 4) is not very different from that of the wellhead gas collected from the old Lopra-1 well (Table 1) suggesting a common origin for the gases.

Headspace gas of sealed cuttings

Methane concentration in the headspace gas of the 135 canned samples of cuttings from the Lopra-1/1A well varied from 7 ppm to over 33 000 ppm, the highest concentrations being measured at 2273 m and in the interval from 2685 to 2745 m (Fig. 3). The sample at 2273 m was collected just after drilling through a 2–3 m thick layer of lapilli tuff with a distinctly higher porosity compared to the massive lavas above and below. A higher mud gas concentration was also noted for this porous layer (Fig. 2). The methane concentration in the samples from the 2685–2745 m interval is more than one order of magnitude higher than that of most other samples from the well. This interval corresponds to the upper part of a section of dominantly lapilli tuff (2610–2880 m) and could indicate that these rocks contain more gas than those at other levels. However, the mud gas concentration did not shift to higher values as one might have expected if the gas content was generally much higher in the rocks of this particular interval (Fig. 3). Furthermore, the well logs show no correlation between the increase in headspace methane and any change in rock properties, such as porosity or density. A shift from rotary drilling to turbo-drilling using a diamond bit took place at 2657 m, and turbo-drilling continued to 2675 m where rotary drilling was resumed. Cuttings produced by turbo-drilling are generally much smaller than cuttings produced by normal rotary drilling. It is possible that the decrease in cutting size may have led to enhanced degassing and thereby higher headspace methane concentrations. Furthermore, one of the two shale shakers was out of order due to motor failure during drilling from 2680 to 2822 m. This may be one of the reasons for the observed build up of solids in the drilling fluid, which, combined with the finer cuttings produced by turbo-drilling, may have been the cause of the significantly higher methane concentrations in the headspace gas.

Alternatively, the much higher concentration of methane measured in the headspace gas shortly after turbo-drilling could be explained by generation of artificial gas due to the very high temperatures which often occur using this drilling technique. If, however, the gases were generated by some artificial process, an increase in mud gas methane concentration should be expected, which is not the case (Fig. 3). Furthermore, the stable isotopic ratio of the methane is not markedly different in the zone with high methane concentrations compared to headspace methane from other levels (Fig. 3).

Ethene, with concentrations up to 39 ppm, was observed in a number of headspace samples, particularly from the upper 300 m of the extended well where the pH of the drilling fluid was relatively low (7–8 compared with a typical value of 10) according to the daily drill reports. Unsaturates like ethene are very uncommon among light hydrocarbons in natural gas, so this constituent was most likely formed artificially, either during drilling (Faber *et*

Facing page:
Fig. 3. Summary of mud gas and headspace results of the extended Lopra-1 well (**A**) and Lopra-1A sidetrack (**B**). Larger circles represent C_1/C_2 ratio corrected for artificial gas indicated by ethene (C_2=). Numbers are stable isotopic values of methane.

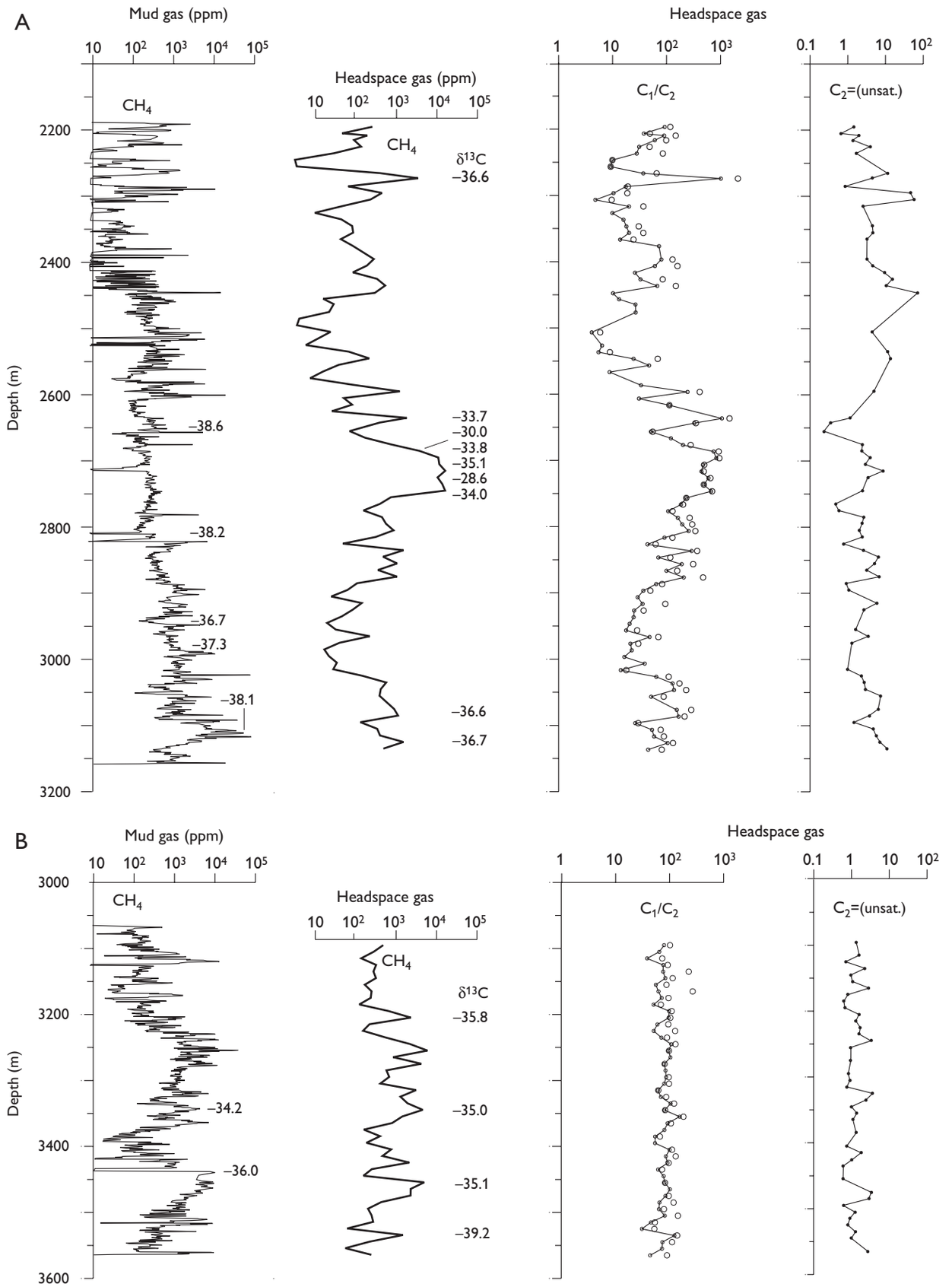

al. 1988) or as a result of corrosion (Laier 1999). Samples of cuttings generally contain iron filings from the drilling. Unsaturates can be generated by a catalytic reaction of the Fischer-Tropsch type, and may occur in canned cuttings with relatively low pH, as was demonstrated for the Swedish deep gas well at Lake Siljan (Laier 1999). The concentration of ethene decreased when pH had been raised to over 10, by adding caustic soda and bactericide to the drilling fluid below 2500 m (Fig. 3).

The methane-to-ethane ratio of the gas may be useful in determining the origin of the gas in the volcanics, but a correction should be made for the artificial gas which may influence this ratio. The methane-to-ethane ratio of artificial gas varied between 3–5 in the Siljan well (Laier 1999), which is much lower than that of the gases in the Lopra-1/1A well (Fig. 3). Equal amounts of ethene and ethane were noted in the artificial gas of the Siljan well (Laier 1999); assuming a similar ratio of 1:1 for the artificial gas component in the Lopra headspace samples, a correction has been made (Fig. 3). Headspace samples with methane concentrations below 100 ppm have generally lower methane-to-ethane ratios, but this cannot be taken as evidence of a different origin of the gas. This is more likely due to uncertainties of the headspace method as well as the analytical uncertainty for the very low ethane concentrations. The methane-to-ethane ratio varied between 10^2 and 10^3 for headspace gas samples with higher methane concentrations (> 100 ppm) that have less analytical uncertainty (Fig. 3). The methane-to-ethane ratio remained fairly constant, around 10^2, in samples from the side track Lopra-1A. Thus, given the uncertainties of the headspace method, it may be concluded that the hydrocarbon gas of the sealed cuttings mainly has the same origin as that of the mud gas and the previous wellhead gas.

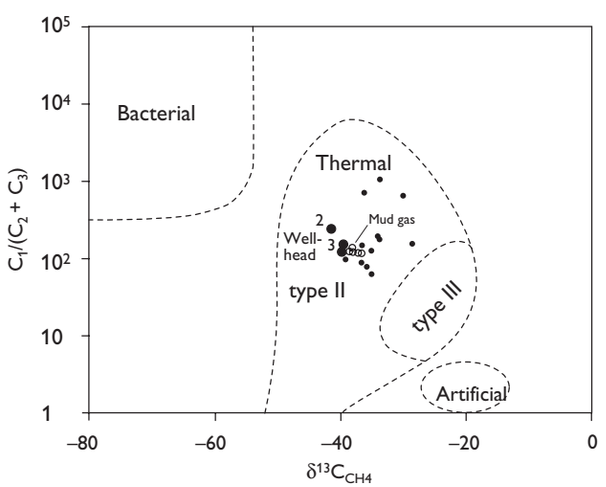

Fig. 4. Plot of $C_1/C_2 + C_3$ vs. $\delta^{13}C_{CH4}$ for Lopra-1/1A gases. Small solid circles represent headspace gas. (Diagram modified from Faber *et al.* 1999.)

Origin of the gasses

The chemical and isotopic data for the gasses from the original Lopra-1 well and the extended well sections have been plotted in the well-known classification diagram for hydrocarbon gases (Fig. 4). The mud gas of the extended well plots fairly close to the wellhead gases of the old Lopra-1 well, suggesting that they have a common origin. Headspace gases, however, exhibit a much larger variation and are generally slightly more enriched with respect to carbon-13. Such enrichment could result from either bacterial oxidation of methane (Coleman *et al.* 1981) during storage or fractionation due to diffusion. The most carbon-13 enriched gases are found among the headspace samples with the highest methane concentration (Fig. 3), therefore bacterial oxidation is unlikely to have been responsible for the carbon-13 enrichment. If degassing from the cuttings occurred mainly via diffusion, the gas may have fractionated due to degassing prior to storage in the tight cans.

The hydrocarbon gases are thermogenic in origin, and the relatively low C_{2+} content indicates either a gas-prone source rock or a high maturity of the source rock. Comparing the stable isotope values ($\delta^{13}C$) of methane through propane (Tables 1, 4) with the $\delta^{13}C$ versus source maturity lines published by Rooney *et al.* (1995), a highly mature marine source rock (type II kerogen) is most likely for the Lopra gases. This is more obvious for the wellhead gases than for the mud gases as can be seen from Fig. 5. The larger variation in $\delta^{13}C$ among the mud gas samples compared to the wellhead gases, particularly for ethane, may be due to the much smaller quantities of hydrocarbons making the mud gases more susceptible to sampling and analytical errors.

Rooney *et al.* (1995) estimated that the reservoir gases used to construct the $\delta^{13}C$ versus maturity line for the type (II) kerogen had been generated in the temperature range 170–190°C, the upper part of which is not very different from the maximum palaeotemperature estimated for the base of the Lopra-1/1A well (Glassley 2006, this volume). Furthermore, the reservoir gases used by Rooney *et al.* (1995), which had isotopic values in the same range as those of the Lopra-1 gases, were also very dry (M.A. Rooney, personal communication 2000). On the other hand, using $\delta^{13}C$ versus source maturity lines constructed by other researchers such as Faber (1987) and Berner & Faber (1996), a somewhat lower maturity is

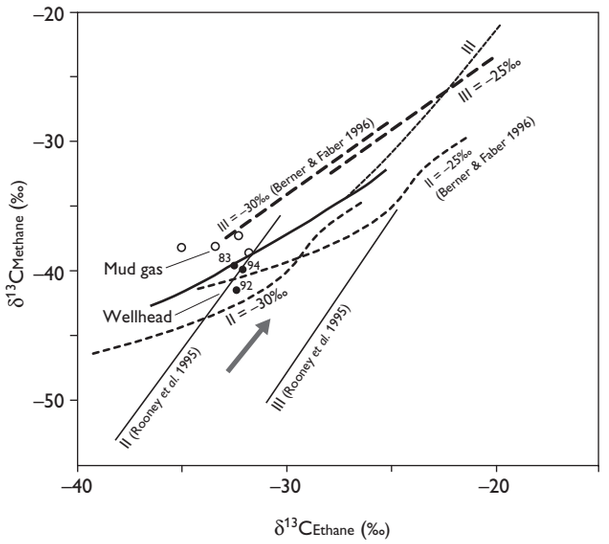

Fig. 5. Cross-plot of isotope values ($\delta^{13}C$) of methane vs. ethane of wellhead and mud gas samples from the Lopra-1/1A well. Maturity lines, from Faber (1987) and Rooney *et al.* (1995), were based on reservoir data, whereas those of Berner & Faber (1996) were obtained from laboratory experiments. Numbers attached to wellhead samples refer to sampling year.

predicted for the source of the Lopra-1 gases (Fig. 5). Therefore, the maturity of the source rock that generated the gases is still not certain.

The presence of a source rock is, however, very likely as was indicated by the continued and fairly significant flux of gas into the original Lopra-1 well over a 13-year period. The gases entering the open Lopra-1 well most likely came from the more porous layers of tuffs beneath the massive lavas of the lower basalt formation. No layers of coal were penetrated by the extended Lopra-1/1A well, so the source is most likely located below the hyaloclastites that were extruded subaqueously (Waagstein 2006, this volume).

Traces of higher hydrocarbons

The traces of higher hydrocarbons measured in mud samples derived mainly from various additives (Bojesen-Koefoed & Nytoft 2006, this volume) and cannot give any clues as to the possible origin of the Lopra gases. Fluid inclusion studies by Konnerup-Madsen (2006, this volume) do, however, indicate that hydrocarbon fluids were present in the volcanics at one time. But analysis of a fluid extracted from one calcite sample containing fluid inclu-

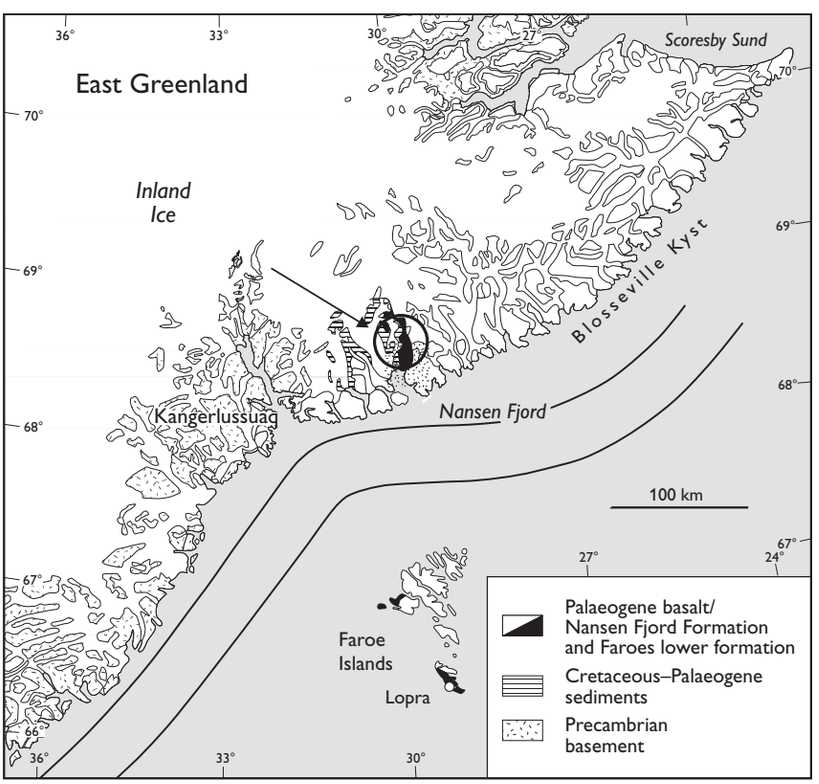

Fig. 6. Pre-drift reconstruction of central East Greenland and the Faroes block, modified from L.M. Larsen *et al.* (1999). The **arrow** indicates the location of organic-rich sediments having Ro = 1.2% (M. Larsen, personal communication 2000).

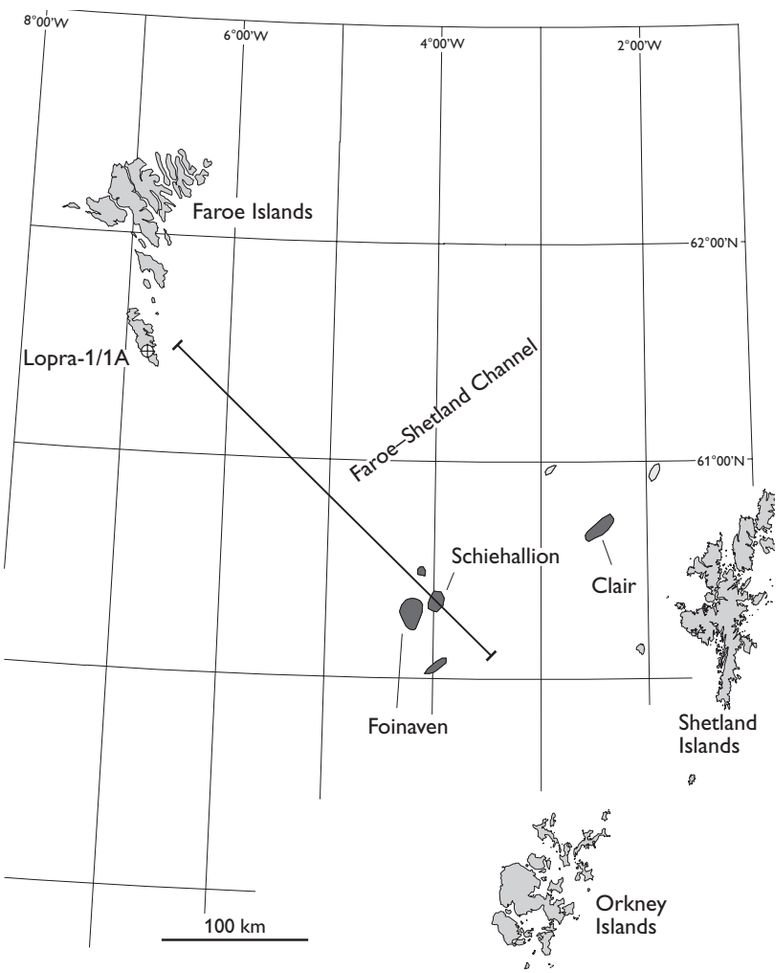

Fig. 7. Oil and gas fields west of Shetland.

sion could not be related unambiguously to a particular source (Bojesen-Koefoed & Nytoft 2006, this volume).

Waxes associated with zeolites reported from other parts of the Faroe Islands (Laier *et al.* 1997) appeared to have been generated by a less mature source than that of the Lopra-1/1A gases. Thus, the presence of traces of higher hydrocarbons supports the assumption that hydrocarbons migrate or migrated in the volcanics of the area, but no direct connection between these higher hydrocarbons and the Lopra gases have been documented.

Source rocks of the Faroe Islands area

The scientific Lopra-1 drilling was termined in November 1981 at 2178 m for technical reasons without having fulfilled its primary objective of penetrating the substratum of the lower basalt formation. The deepening of the Lopra-1/1A well in 1996 to 3565 m penetrated hyaloclastites, mostly lapilli tuffs, under the base of the lower basalt formation at about 2470 m, but gave no definite clue as to the type of rocks occurring beneath the volcanics. The fact that the volcanics below the lower basalt formation were deposited subaqueously suggests that sediments were present in the area prior to the volcanic eruptions. Such sediments would probably be similar in age to the sediments exposed beneath the basalts in the Kangerlussuaq area in East Greenland reported by M. Larsen *et al.* (1999), sediments that probably give us the best clue as to what type of source rocks might exist beneath the volcanics at Lopra, since the palaeodistance between the Faroes block and central East Greenland was only 100–120 km before the break-up of the northern North Atlantic (Fig. 6). The close connection between the two areas is emphasised by the similarity in chemical composition of the oldest basalts on either side of the northern North Atlantic (L.M. Larsen *et al.* 1999).

The organic-rich rocks of the Kangerlussuaq area range in age from late Aptian to late Paleocene. They proved to be post-mature with respect to hydrocarbon generation

at most localities examined by M. Larsen *et al.* (1999). However, a vitrinite reflectance value of Ro = 1.2 measured on a late Paleocene lacustrine mudstone (TOC = 7%) 22 km north of Nansen Fjord (Fig. 6) shows that source rocks with hydrocarbon generation potential do exist beneath the basalts in this area.

An estimate of organic matter maturation related to burial depth alone may be obtained from the Nansen Fjord area which was covered by approximately 6 km of volcanic rocks prior to uplift (L.M. Larsen *et al.* 1999). The total thickness of the Faroe Islands volcanics may exceed the 6.5 km presently known from exposures and drillings (Waagstein 2006, this volume); however, a more precise estimate of the thickness is difficult to give. It seems realistic to assume that possible source rocks below the Faroe Islands volcanic succession still have some potential for hydrocarbon generation, given the close connection between the two areas prior to continental split-up. Thus, the more or less continuous seepage of methane-rich gas into the open Lopra-1 well during 1983–1994 may originate from a highly mature source rock located beneath the volcanics in the area.

Hydrocarbon migration from the Faroe–Shetland Basin

Hydrocarbons may also have migrated into the Faroe Islands area from the Faroe–Shetland Basin, though little is known of the possible migration pathways. The Foinaven and Schiehallion oil fields, 160 km south-east of the Lopra-1 well, are the nearest known hydrocarbon occurrences around the Faroe Islands (Fig. 7), but hydrocarbons are likely to have been generated closer to the Faroe Islands in basalt-covered rift basins beneath the Faroe Shelf (Fig. 8). Subsequently, these hydrocarbons may have migrated towards the Faroe Islands area via sandy turbidites located under the volcanics or via intrabasaltic sandstones. Redeposition of coarse-grained sediments onto the Faroe Shelf during mid-Paleocene uplift of East Greenland has been inferred by M. Larsen *et al.* (1999) but such sediments are not indicated on the geological profile of Fig. 7, which shows only strata recognised on seismic sections.

Since much of the Faroe–Shetland Basin is highly mature thermally, its lack of large gas accumulations has been explained by the presence of very oil-prone source rocks that have only little potential for later gas generation (Scotchman *et al.* 1998). This assumption was based on kinetic studies of Middle and Upper Jurassic kerogens from a number of exploration wells west of Shetland. If that is the case, the assumption that the gases observed in the Lopra-1 well came from the Faroe–Shetland Basin is not supported by observations from this basin obtained within a reasonable distance from the Faroe Islands.

Conclusions

Thermogenic gas, mostly methane, exists in the Lopra-1/1A well in the hyaloclastites and in the more porous tuffaceous zones of the overlying lower basalt formation.

Chemical and isotopic data suggest that gases in the hyaloclastites were responsible for the more or less continuous seepage of gas into the original Lopra-1 well since 1983.

The location and the type of source rock that generated the gases observed in the Lopra-1 well are still uncertain. However, recent information on the pre-volcanic, organic-rich sediments of central East Greenland shows that these still have a potential for generating hydrocar-

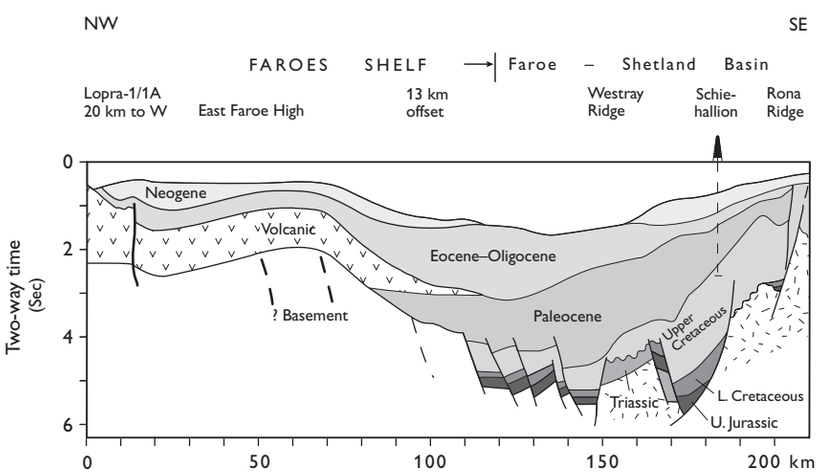

Fig. 8. Geological profile modified from Spencer *et al.* (1999). Location shown on Fig. 7.

bons (Ro = 1.2%) after having been buried below 6 km of volcanic rocks. Given the close connection demonstrated between central East Greenland and the Faroes block prior to continental break-up, it is probable that the source rock for the gases in Lopra-1/1A exists below the volcanics of the Faroe Islands area.

The possibility of migration of gas from the Faroe–Shetland Basin towards the Faroes cannot be excluded, although no evidence in support of this hypothesis has yet been found.

Acknowledgements

The two reviewers, Melody A. Rooney and Ger van Graas, are thankfully acknowledged for their careful review of the manuscript and valuable comments which helped improve the clarity of the paper.

References

Balling, N., Kristiansen, J.I. & Saxov, S. 1984: Geothermal measurements from the Vestmanna-1 and Lopra-1 boreholes. In: Berthelsen, O., Noe-Nygaard, A. & Rasmussen, J. (eds): The Deep Drilling Project 1980–1981 in the Faeroe Islands. Annales Societatis Scientiarum Faeroensis, Supplementum **IX**, 137–147. Tórshavn: Føroya Fródskaparfelag.

Berner, U. & Faber, E. 1996: Empirical carbon isotope/maturity relationships for gases from algal kerogens and terrigenous organic matter, based on dry, open-system pyrolysis. Organic Geochemistry **24**, 947–955.

Bojesen-Koefoed, J. & Nytoft, H.P. 2006: Petroleum geochemistry of the deepened Lopra-1/1A re-entry well, Faroe Islands. Geological Survey of Denmark and Greenland Bulletin **9**, 67–77 (this volume).

Coleman, D.D., Risatti, J.B. & Schoell, M. 1981: Fractionation of carbon and hydrogen isotopes by methane-oxidizing bacteria. Geochimica et Cosmochimica Acta **45**, 1033–1037.

Faber, E. 1987: Zur Isotopengeochemie gasförmiger Kohlenwasserstoffe. Erdöl, Erdgas, Kohle **103**, 210–218.

Faber, E., Gerling, P. & Dumke, I. 1988: Gaseous hydrocarbons of unknown origin found while drilling. Organic Geochemistry **13**, 875–879.

Faber, E., Whiticar, J. & Gerling, P. 1999: Comparison of hydrocarbons from unconventional sources: KTB, EPR and bit metamorphism. Geologisches Jahrbuch **D107**, 175–194.

Glassley, W.E. 2006: Mineralogical and thermodynamic constraints on Palaeogene palaeotemperature conditions during low-grade metamorphism of basaltic lavas recovered from the Lopra-1/1A deep hole, Faroe Islands. Geological Survey of Denmark and Greenland Bulletin **9**, 109–118 (this volume).

Jacobsen, O.S. & Laier, T. 1984: Analysis of gas and water samples from the Vestmanna-1 and Lopra-1 wells, Faeroe Islands. In: Berthelsen, O., Noe-Nygaard, A. & Rasmussen, J. (eds): The Deep Drilling Project 1980–1981 in the Faeroe Islands. Annales Societatis Scientiarum Faeroensis, Supplementum **IX**, 149–155. Tórshavn: Føroya Fródskaparfelag.

Konnerup-Madsen, J. 2006: A reconnaissance study of fluid inclusions in fracture-filling quartz and calcite from the Lopra-1/1A well, Faroe Islands. Geological Survey of Denmark and Greenland Bulletin **9**, 119–122 (this volume).

Laier, T. 1999: The Siljan Deep Well – hydrocarbon gas results. Geologisches Jahrbuch **D107**, 153–163.

Laier, T., Nytoft H.P., Jørgensen, O. & Isaksen, G.H. 1997: Hydrocarbon traces in the Tertiary of the Faeroe Islands. Marine and Petroleum Geology **14**, 257–266.

Larsen, L.M., Waagstein, R., Pedersen, A.K. & Storey, M. 1999: Trans-Atlantic correlation of the Palaeogene volcanic successions in the Faeroe Islands and East Greenland. Journal of the Geological Society (London) **156**, 1081–1095.

Larsen, M., Hamberg, L., Olaussen, S., Nørgård-Pedersen, N. & Stemmerik, L. 1999: Basin evolution in southern East Greenland: an outcrop analog for Cretaceous–Paleogene basins on the North Atlantic volcanic margin. American Association of Petroleum Geologists Bulletin **88**, 1236–1261.

Rooney, M.A., Claypool, G.E. & Chung, H.M. 1995: Modelling gas generation using carbon isotope ratios of natural gas hydrocarbons. Chemical Geology **126**, 219–232.

Scotchman, I.C., Griffith, C.E., Holmes, A.J. & Jones, D.M. 1998: The Jurassic petroleum system north and west of Britain: a geochemical oil source correlation study. Organic Geochemistry **29**, 671–700.

Spencer, A.M., Birkeland, Ø., Knag, G.Ø. & Fredsted, R. 1999: Petroleum systems of the Atlantic margin of northwest Europe. In: Fleet, A.J. & Boldy, S.A.R. (eds): Petroleum geology of Northwest Europe: Proceedings of the 5th Conference, 231–246. London: Geological Society.

Waagstein, R. 2006: Composite log from the Lopra-1/1A well, Faroe Islands. Geological Survey of Denmark and Greenland Bulletin **9**, in pocket inside back cover (this volume).

Waagstein, R., Hald, N., Jørgensen, O., Nielsen, P.H., Noe-Nygaard, A., Rasmussen, J. & Schönharting, G. 1984: Deep drilling on the Faeroe Islands. Bulletin of the Geological Society of Denmark **32**, 133–138.

Manuscipt received 17 June 2000; revision accepted 30 January 2001.

Thermal structure of the deep Lopra-1/1A borehole in the Faroe Islands

Niels Balling, Niels Breiner and Regin Waagstein

Information on temperature, temperature gradients, thermal conductivity and heat flow from the *c.* 3.5 km deep Lopra-1/1A borehole in the Faroe Islands is presented and analysed. The upper 2450 m of the drilled sequence consists of thick tholeiitic basalt flows and the deeper parts of hyaloclastites and thin beds of basalt. Temperature data originate from high precision temperature logging a long time after drilling to a depth of 2175 m (the original Lopra-1 borehole) and from commercial temperature logs measured a short time after drilling to a depth of 3430 m (Lopra-1/1A). The high-precision temperature log determines accurately levels of inflow of groundwater to the borehole and significant thermal disturbances to a depth of *c.* 1250 m. Below 1300 m, no significant disturbances are seen and interval temperature gradients for large depth intervals show only small variations between 28 and 33°C/km. The mean least-squares gradient for the depth interval of 1400–3430 m is 31.4°C/km. In clear contrast to these overall very homogeneous, large-interval, mean temperature gradients, great local variability, between gradients of 20–25°C/km and 45°C/km, was observed between about 1300 and 2175 m (maximum depth of the high-resolution temperature log). These gradient variations are interpreted to be due to thermal conductivity variations and to reflect varying secondary mineralisation and mineral alterations.

A preliminary analysis of the Lopra-1/1A temperature–depth function in terms of long-term palaeoclimatic signals indicates subsurface temperatures below about 1300 m to be in equilibrium with mean surface temperatures significantly below zero during the last glacial period. A subsequent temperature increase of 12–16°C occurred at around the termination of the last glaciation. The measured temperatures (some after correction) and the thermal regime below 1300 m seem to represent conductive equilibrium conditions without significant disturbances from the effect of drilling, groundwater flow or long-term palaeoclimatic surface temperature variations.

Thermal conductivity measured on samples of basalt taken from drill cores and surface outcrops in the area of the borehole shows values within a rather narrow range and a well-defined mean value for low porosity basalts of about 1.8 W/m°C , while a few samples of lapilli-tuff/tuff from the borehole gave values around 1.9 W/m°C . Lapilli-tuff and tuff seem to have higher matrix (grain) conductivity than basalt. Heat flow is estimated at 60 ± 5 mW/m^2. A heat flow of this magnitude is consistent with the Faroe Islands being underlain by continental crust.

Keywords: Lopra-1/1A borehole, Faroe Islands, temperature gradients, thermal conductivity, heat flow

---

N.B. & N.B., *Department of Earth Sciences, University of Aarhus, Finlandsgade 8, DK-8200 Aarhus N, Denmark.*
E-mail: *niels.balling@geo.au.dk*
R.W., *Geological Survey of Denmark and Greenland, Øster Voldgade 10, DK-1350 Copenhagen K, Denmark.*

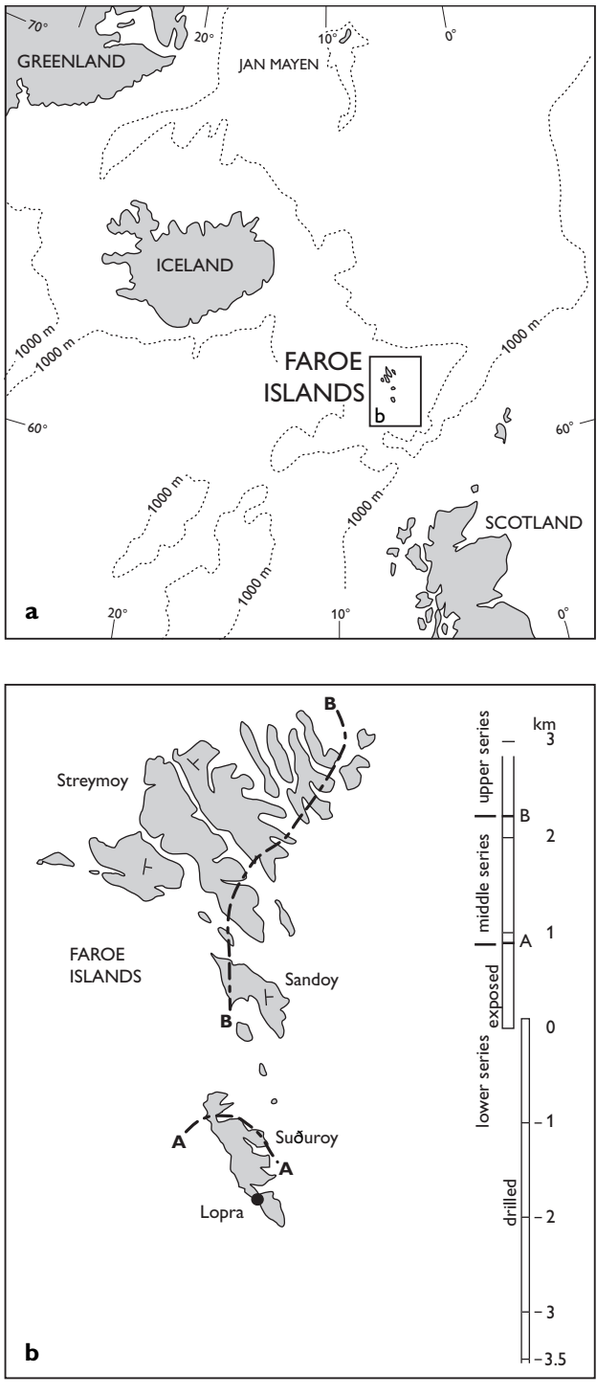

Fig. 1. **a**: Location map of the Faroe Islands in the northern North Atlantic. **b**: The Lopra-1/1A borehole was drilled in the southern Faroese island of Suðuroy. The total thickness of volcanic sequences in the Faroe Islands is at least 6.5 km. About 3 km is exposed, and 3.54 km was drilled at Lopra-1/1A. **Dashed lines A** and **B** mark boundaries between lower and middle and middle and upper basalt series respectively.

Deep boreholes generally provide the most reliable and undisturbed direct information on temperature, temperature gradients, thermal conductivity and heat flow. Temperatures and temperature gradients measured in shallow boreholes may be perturbed for a variety of reasons including local effects of groundwater movements, topography and short- and long-term palaeoclimatic surface temperature variations. The deep Lopra-1/1A borehole provides a unique opportunity for obtaining deep thermal information from an area of the North Atlantic that is of considerable interest to both the general geoscience community and to the hydrocarbon industry.

The Lopra-1/1A borehole is situated in the southern island (Suðuroy) of the Faroe Islands (Fig. 1) (at 61°26′ 36″N, 6°46′30″E). It was drilled in 1981 as a research borehole to a depth of 2175 m below ground level (Berthelsen *et al.* 1984). In 1996 the borehole was re-entered by a consortium of exploration companies and deepened to 3565 m measured depth corresponding to a vertical depth below ground level of 3540 m. All depth values given in this paper (if not stated otherwise) are vertical depths measured from ground level 8.8 m above mean sea level.

Thermal measuring results from the original Lopra-1 borehole were presented by Balling *et al.* (1984). The purpose of the present paper is to integrate, analyse and discuss all available thermal information from the whole depth range of the Lopra-1/1A borehole. It includes new high-precision continuous temperature logging results from the original hole measured a long time after drilling, temperature measurements from the deepened part acquired as part of the commercial logging runs during and shortly after drilling. New thermal conductivity measurements from core material from the deepened section and from surface exposures in the Lopra-1/1A area have also been made.

Temperatures and temperature gradient variations are analysed in relation to disturbances from groundwater flow, variations in rock thermal conductivity and information on long-term palaeoclimatic surface temperature variations. A new terrestrial heat-flow value for the Lopra-1/1A site is presented.

Geological environment and lithology

The volcanic succession of the Faroe Islands

The Faroe Islands form part of the Palaeogene North Atlantic Province of tholeiitic flood basalts. The Faroe volcanic succession has been divided informally into the upper,

middle and lower basalt series or formations with a total thickness of more than 6.5 km (Rasmussen & Noe-Nygaard 1970; Waagstein 1988). The lowermost 3.5 km, which is entirely in the lower basalt formation, is known only from the Lopra-1/1A borehole (Fig. 1).

Both seismic and other geophysical evidence (Bott *et al.* 1974; Richardson *et al.* 1998) and geochemical data (Garièpy *et al.* 1983; Hald & Waagstein 1983; Holm *et al.* 2001) indicate that the Faroe Islands are underlain by continental crust. Pre-volcanic rocks have not been reached by drilling. Linear magnetic anomalies associated with oceanic crust occur 60–70 km north of the islands (Skogseid *et al.* 2000).

The flood basalts were formed by extensive volcanism associated with the continental splitting between NW Europe and East Greenland in upper Paleocene to lowermost Eocene time (e.g. Skogseid *et al.* 2000). Larsen *et al.* (1999) used geochemical analyses and stratigraphic correlations between the volcanic successions in the Faroe Islands and East Greenland to interpret the Faroese lower basalt formation as a pre-breakup sequence and the middle and upper basalt formations as syn-breakup sequences. Since deposition of the upper basalt formation, little or no deposition has occurred in the Faroes. Volcanic activity continued, however, on the Greenland side of the rift with the eruption of an additional 3–3.5 km of basalts in an area then located close to the centre of the Icelandic mantle plume.

Lithology

The upper 2450 m of the Lopra-1/1A borehole consists of subaerial lava flows of tholeiitic basalt with an average thickness of about 20 m. Most of the flows have a massive core and a vesicular rubbly top. The lavas are commonly separated by palaeosols made up of volcanic ash or material eroded from the flow tops. The sediments range from a few centimetres to more than 4 m in thickness. The deeper part of the well, from about 2450 m to total depth, consists of hyaloclastites (lapilli-tuff and tuff) and thin beds of basalt.

Since deposition, secondary mineralisation and mineral alterations have occurred. The bulk thermal properties of the basaltic sequences seem to be controlled mainly by the two major minerals feldspar and pyroxene, which occur in roughly equal amounts in common basalts. However, it appears from our thermal gradient analysis that within-flow variations of the degree of alteration of the basalt is an important controlling factor for local variations in rock thermal properties and hence temperature gradient variability. Some information on secondary mineral alterations and mineralisation is thus required for a proper thermal analysis.

Olivine is a minor constituent that has been generally replaced by clay. Haematite has formed from iron-rich minerals under oxidising conditions, especially within flow tops and interbasaltic sediments. The original plagioclase feldspar is partly or completely replaced by albite in the deepest part of the borehole due to very low-grade burial metamorphism. Originally variable amounts of interstitial glass representing frozen melt are completely altered to clay and other secondary minerals. Most gas vesicles and pores and fractures once filled with free water are now, particularly at great depth, partly or completely filled with low-temperature minerals deposited by flowing groundwater. These mineralisations consist dominantly of clay and zeolite minerals, silica minerals (chalcedony, agate, quartz) or calcite. The vertical distribution of secondary minerals and zeolite zones of the Lopra-1/1A borehole are described by Jørgensen (1984, 2006, this volume). The lithology and chemistry of the upper 2.2 km sequence is described in detail by Hald & Waagstein (1984).

Temperature and temperature gradients

Temperature logs and conditions of measurements

Temperature information is available from several temperature logs. Measurements have been carried out by several techniques, either as dedicated temperature logging or in combination with other log operations. Temperatures were measured both during interruptions in the drilling and after the drilling was completed. This applies both to the original Lopra-1 borehole and to the deepened part of Lopra-1/1A.

Temperature logs were run in the original Lopra-1 borehole by The Icelandic Energy Authority, Orkustofnun, the operator of the original hole. The last one was run in 1983, 17 months after drilling. These results are described in detail in Balling *et al.* (1984). A more detailed continuous temperature log has since been run in the original Lopra-1 hole. It was carried out by the present research group in 1994 to a depth of 2175 km, almost 13 years after drilling, using the high-precision quartz-oscillator system of the University of Aarhus. Measurements were taken while running down-hole at a nominal speed of 10 cm/s with a sample rate of two seconds resulting in a sample interval of about 20 cm. Relative temperature resolu-

Table 1. Basic information about temperature logs from the Lopra-1/1A borehole

Temp. log*	Date of measurement	Depth of borehole (m)	Depth interval of temperature data (m)	Time after drilling/circulation†	Measuring agency
1	23.03.1983	2175	0–1974	17 months	Orkustofnun, Reykjavik
2	04.08.1994	2175	0–2175	12 years 9 months	University of Aarhus
3	01.10.1996	3144	3020–3095	27 hours	Schlumberger, Esbjerg
4	02.10.1996	3144	2170–3075	50 hours	Schlumberger, Esbjerg
5	30.10.1996	3496	2990–3430	53 hours	Schlumberger, Esbjerg

* Five logs have been selected to give the most valuable temperature information.
† The time elapsed between the last significant disturbance from drilling or last circulation of drilling fluid and temperature logging.

tion is better than 0.005°C and absolute accuracy is calibrated to about 0.05°C.

All temperature logs from the Lopra-1/1A deepened section below 2175 m were acquired by the company Schlumberger in combination with other logging operations relatively soon after drilling activities and circulation of drilling fluid. The temperature data are available as standard six-inch point measurements taken by thermistor probes and are estimated to have an accuracy better than 0.1°C.

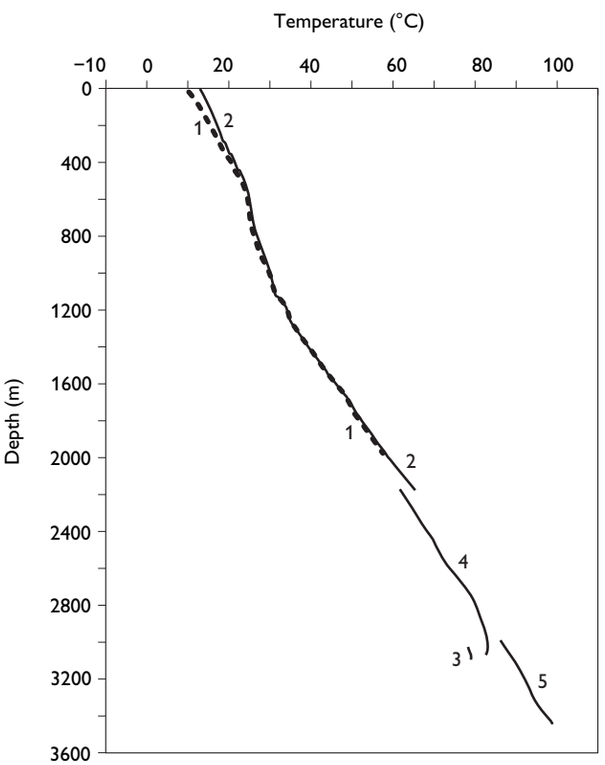

Fig. 2. Selected measured temperature–depth profiles. Logs 1 and 2 are from the original borehole Lopra-1 and logs 3, 4 and 5 were measured in the deepened part. Information on time of measurements, details of depth intervals and time after drilling or last drilling fluid circulation are given in Table 1. Log temperatures presented here are uncorrected. Corrected temperatures are given in Fig. 3.

Several temperature logs are thus available both for the original Lopra-1 hole and the deepened Lopra-1/1A section. Five of these have been selected as those giving the most valuable information for interpretation (Table 1 and Fig. 2). They cover depths from the surface to 3430 m.

Drilling and circulation of drilling fluid disturb significantly the temperature structure of the borehole and the unperturbed so-called equilibrium temperature–depth distribution can be measured only a relatively long time after drilling. If sufficient time has not passed, corrections to measurements must be applied (cf. Beck & Balling 1988).

In general, during circulation of drilling fluid, the upper part of the hole is heated and the lower part is cooled. The time needed for a borehole to reach temperature equilibrium depends on several factors including drilling history, temperature of the drilling mud and the required accuracy of temperature and temperature gradients, but may be relatively long compared to the duration of the drilling. For deep boreholes like the Lopra-1/1A borehole, at least one to two years may be needed to obtain both accurate equilibrium temperatures over the whole section and accurate local temperature gradients. Only for the bottom part of the hole and the neutral zone of least disturbances may near-equilibrium temperatures be measured much sooner after drilling and last drilling fluid circulation.

As mentioned above, temperature measurements were carried out in the original Lopra-1 borehole to a depth of 2175 m a long time (up to almost 13 years) after drilling. The temperature logging results from the new section

drilled in 1996 were, however, carried out no more than 27–53 hours after last drilling fluid circulation, cf. Table 1, and corrections must be considered.

Temperature disturbances are created not only by the process of drilling. The upper part of the borehole is also affected by upward water flow inside the borehole. After drilling, the Lopra-1 hole (total depth 2175 m) started to flow at a rate of about 10 l/min when the drilling mud was replaced by fresh water of lower density. The well head was closed between the end of drilling and the time of log number 1 (17 months after drilling, cf. Table 1) preventing water from flowing freely to the surface. The hole was opened on the day of temperature logging and after one hour it began to flow at a rate of about 10 l/min. Temperature measurements were carried out from 3 to 6 hours after opening. At the time of log number 2, measured in 1994, the hole was flowing freely at about the same rate and had not been closed for several years.

The highest recorded temperature of 98.6°C was measured at a depth of 3430 m, 53 hours after circulation when the hole was 3496 m deep (log 5 from 30 October 1996). The deepest point of temperature information is 3527 m where 92°C was measured on 2 November 1996, 17 hours after the latest drilling fluid circulation. Two days later, when the drilling had reached its final vertical depth of 3540 m (3565 m measured depth below rotary table), a temperature of 91°C was measured at 3507 m, 22 hours after circulation of drilling fluid. These lower temperatures measured later at slightly deeper levels demonstrate the effect of cooling by drilling fluid circulation.

Correction of temperatures

A comparison of the raw temperature data of logs 1 (measured in 1983) and 2 (measured in 1994) shows a difference of 2–3°C at depths below 400 m and an almost constant offset of 2°C between 1000 and 1600 m. Such an almost constant difference is very unlikely to be caused by water flow or any other effect associated with the borehole and, from further data analysis, this difference is ascribed to an instrumental calibration offset in log 1 by about 2.0°C. (Equipment used for log 2 measurements was carefully calibrated before and after logging.) After adding 2.0°C to the original log 1 values, log 1 and log 2 measurements agree to within ± 0.2°C between 1000 and 1600 m, increasing to a maximum difference of 0.7°C at 1974 m, the maximum depth of log 1. In the topmost part of the borehole, log 2 shows slightly higher temperature differences (by up to 2–3°C) due to a longer time of temperature disturbance from up-hole water flow (cf. Fig. 2).

Measured log 1 and log 2 temperatures are both clearly elevated in the upper part of the hole because of water flow. At near-surface level, measured temperatures (Fig. 2) are well above the mean ground temperature of about 7°C. By temperature gradient analysis (se below), levels of water inflow have been localised accurately. Below a depth of about 1250 m, measured temperatures of logs 1 and 2 are unlikely to be disturbed significantly by flow of water in the borehole, and log 2 temperatures are assumed to represent undisturbed equilibrium values.

The temperatures on logs 3, 4 and 5, from depths between 2170 and 3430 m (Table 1 and Fig. 2), were measured between 27 hours (log 3) and 53 hours (log 5) after drilling fluid circulation following drilling activities and are thus disturbed. Measured temperatures on logs 3, 4 and 5 are, due to their deep position in the hole, lowered

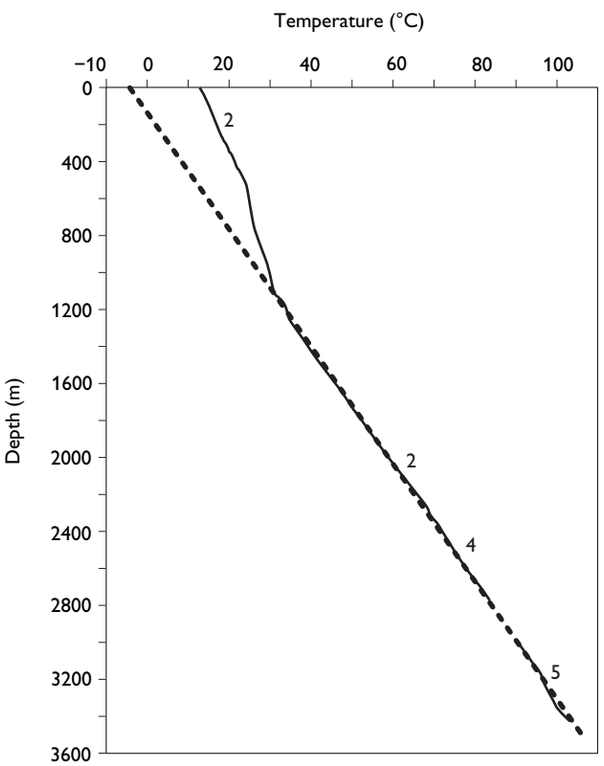

Fig. 3. Measured temperatures on log 2 and corrected temperatures of logs 4 and 5. Corrections were applied for the estimated effect of drilling and drilling fluid circulation. The **dashed line** has a constant gradient of 31.4°C/km calculated by least-squares for the depth interval of 1400–3450 m and extrapolated to the surface. The upper part of the borehole (above *c.* 1200 m) is disturbed by upward flow of water inside the borehole. The negative temperature at the surface intercept indicates that temperatures below about 1200–1300 m are in equilibrium with a palaeosurface-temperature significantly below that of the present-day mean surface temperature of about 7°C.

Table 2. Listing of selected temperatures from logs 2, 4 and 5

	Temperatures (°C)*		
Depth (m)	Log 2†	Log 4‡	Log 5‡
1200	34.1		
1300	36.2		
1400	39.4		
1500	42.6		
1600	46.1		
1700	49.4		
1800	52.3		
1900	55.6		
2000	58.8		
2100	62.5		
2200		66.2	
2300		69.1	
2400		72.0	
2500		74.7	
2600		77.8	
2700		81.5	
2800		n.d.	
2900			n.d.
3000			90.5
3100			93.7
3200			96.4
3300			98.9
3400			102.4
3430			103.5

* Measured temperatures above 1200 m are disturbed by water flow inside the borehole (cf. Fig. 3) and are not listed.

† Temperatures of log 2 are assumed to represent accurately the undisturbed equilibrium temperatures.

‡ Temperatures of logs 4 and 5 are corrected for the estimated influence of drilling disturbances and may represent equilibrium temperatures to within ± 1–3°C.

n.d.: no data.

Table 3. Least-squares mean temperature gradients for various depth intervals

Log	Depth interval (m)	Temp. gradient (°C/km)	Intercept* (°C)
2	1400–2175	32.9	–6.7
4	2170–2770	30.1	0.0
5	2995–3430	28.2	6.2
2, 4, 5	1400–3430	31.4	–3.9

* Intercept temperature value (linearly extrapolated temperature at zero depth) associated with each depth section.

by the circulation of drilling fluid to temperatures below formation temperature. They are thus all lower than the undisturbed formation equilibrium values.

The depth intervals over which measurements were made at different times overlap partly. This makes it possible to estimate the size of temperature disturbances and correct for them. The upper part of log 4 overlaps with the lowest part of log 2 in the depth interval 2170–2175 m. Log 4 temperatures were here 3.7°C below the temperatures of log 2, which are assumed to be undisturbed. The increase in temperature between logs 3, 4 and 5 (Fig. 2), combined with additional log data not shown, has been used to estimate the amount of disturbance by Horner-type analysis. In the deepest part of log 5 a temperature of 98.6°C was measured at a depth of 3430 m, 53 hours after drilling fluid circulation. Temperatures are estimated to have been reduced by 3–7%, so, applying a correction of 5%, the undisturbed value is about 103.5°C. In the final selection of temperature data, only the almost linear part of log 4 (2170–2775 m, Fig. 2) with corrections between 3.7°C (top) and 4.0°C (bottom) was used.

After corrections of logs 4 and 5 for the estimated disturbance due to drilling, the corrected temperatures follow the same depth trend as that of the deeper part of log 2. Below 1100 m, measured temperatures on log 2 and the corrected values on logs 4 and 5 fall within 1.2°C of a constant gradient least-squares temperature line (Fig. 3). As discussed above, the corrected temperatures on logs 4 and 5 are thought to represent equilibrium temperatures to a good approximation (within 1–3°C) and to be sufficiently accurate to calculate accurate mean temperature gradients for the larger depth intervals. Measured temperatures on log 2 (below 1200 m) and corrected values on logs 4 and 5 are listed at 100 m depth intervals in Table 2.

Equilibrium temperatures and temperature gradients

Mean least-squares temperature gradients from selected logs and depth intervals have been calculated and are listed in Table 3. In order to ensure a homogeneous base for the calculation of temperature gradients, all logs were resampled to depth increments of 5 m. Mean gradients show only small variations between 28 and 33°C/km. Log 2 yields a mean gradient of 32.9°C/km between 1400 and 2175 m and the combined data from logs 2, 4 and 5 for the depth interval 1400 to 3430 m yield a temperature gradient of 31.4°C/km. This demonstrates an overall very homogeneous thermal gradient structure.

In clear contrast to the above overall small gradient variations, significant local temperature gradient variability is observed. Figure 4 shows running mean least-squares interval temperature gradients (covering 5, 25 and 100 m depth intervals) derived from the high-resolution log 2 run from surface to 2175 m.

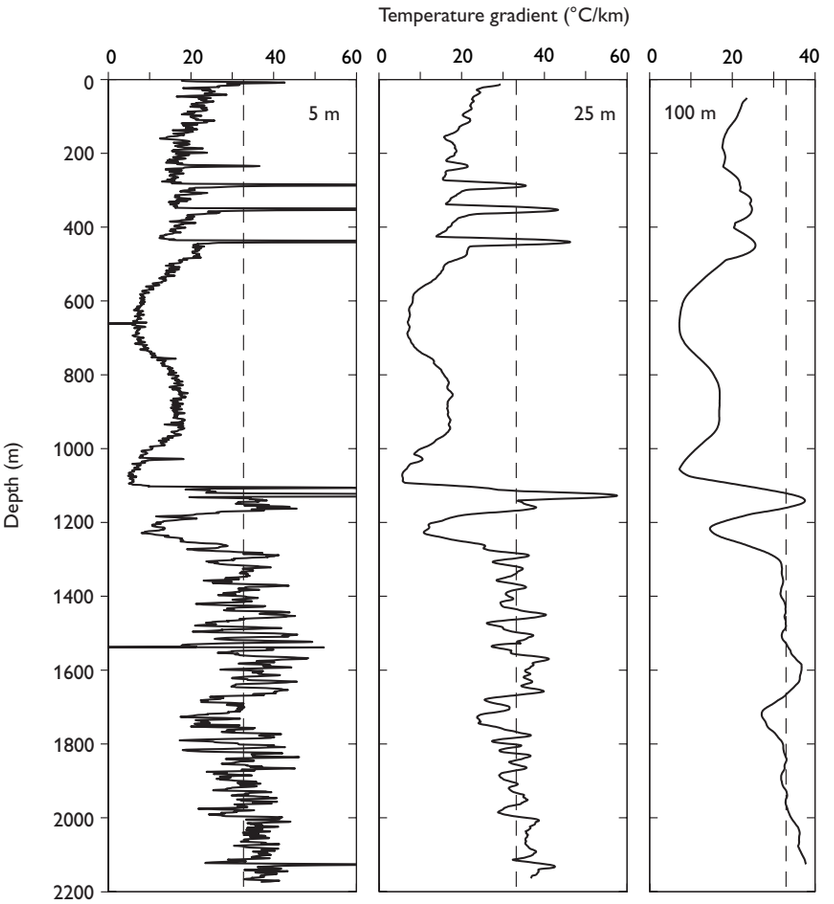

Fig. 4. Running mean least-squares temperature gradients for 5, 25 and 100 m depth intervals as indicated. Temperature gradients were taken from the high resolution log 2. The **dashed line** shows the assumed unperturbed mean background gradient of 32.9°C/km calculated for the depth interval of 1400–2175 m (cf. Table 3). Levels of significant inflow of groundwater into the upper part of the borehole are clearly seen as local gradient maxima. Below about 1250 m, temperatures and temperature gradients are thought to represent generally conductive equilibrium conditions and gradient variability is mostly due to variations in rock thermal conductivity (see also Fig. 5).

The upper part of the log is disturbed by water flow. The original hole was uncased below 180 m and water at above hydrostatic pressure was able to enter the hole through local fractures or permeable beds. The temperature and temperature gradient logs combined show clearly levels of significant disturbance due to inflow of water to the borehole. They are characterised by a locally high temperature gradient. Above the level of inflow, both temperature gradients and temperatures are reduced. At the approximate depths of 292, 360, 444, 1111, 1132 and 2130 m, temperature drops of between 0.2 and 0.6°C are observed, resulting in locally high temperature gradients. The highest local temperature anomalies of 0.5–0.6°C occur at 444 and 1132 m, where also maximal temperature gradient perturbations are observed (Fig. 4). A local minor disturbance is seen around 1538 m (see also Fig. 5). Most of these thermal perturbations, in particular those above 1100–1200 m, are easily interpreted in terms of inflow of ground water at approximately local formation temperature into a section of the borehole where temperatures are artificially elevated due to upwards-flowing water coming from deeper levels of higher formation temperature. Local lowering of borehole temperature may also occur if water flows downwards through inclined fractures from levels of lower formation temperature to levels of higher formation temperature. However, this does not seem to have happened here.

Longer wavelength temperature-gradient minima are observed at about 550–800 m and 1160–1250 m that are not clearly associated with localised zones of inflow of water (Fig. 4). These zones of low gradient may be due to broader zones of water flow into the borehole, perhaps associated with an almost steady migration of ground water within porous or fractured parts of the formation that was initiated long before drilling.

Below 1200–1300 m, the temperature–depth function of log 2 follows the overall almost linear trend of temperature increase with depth (Fig. 3). This trend is overprinted by significant local temperature gradient variations down to the maximum depth of log 2 of 2175m (Fig. 4). The local gradient variations are of a different character from those discussed above, but might at first

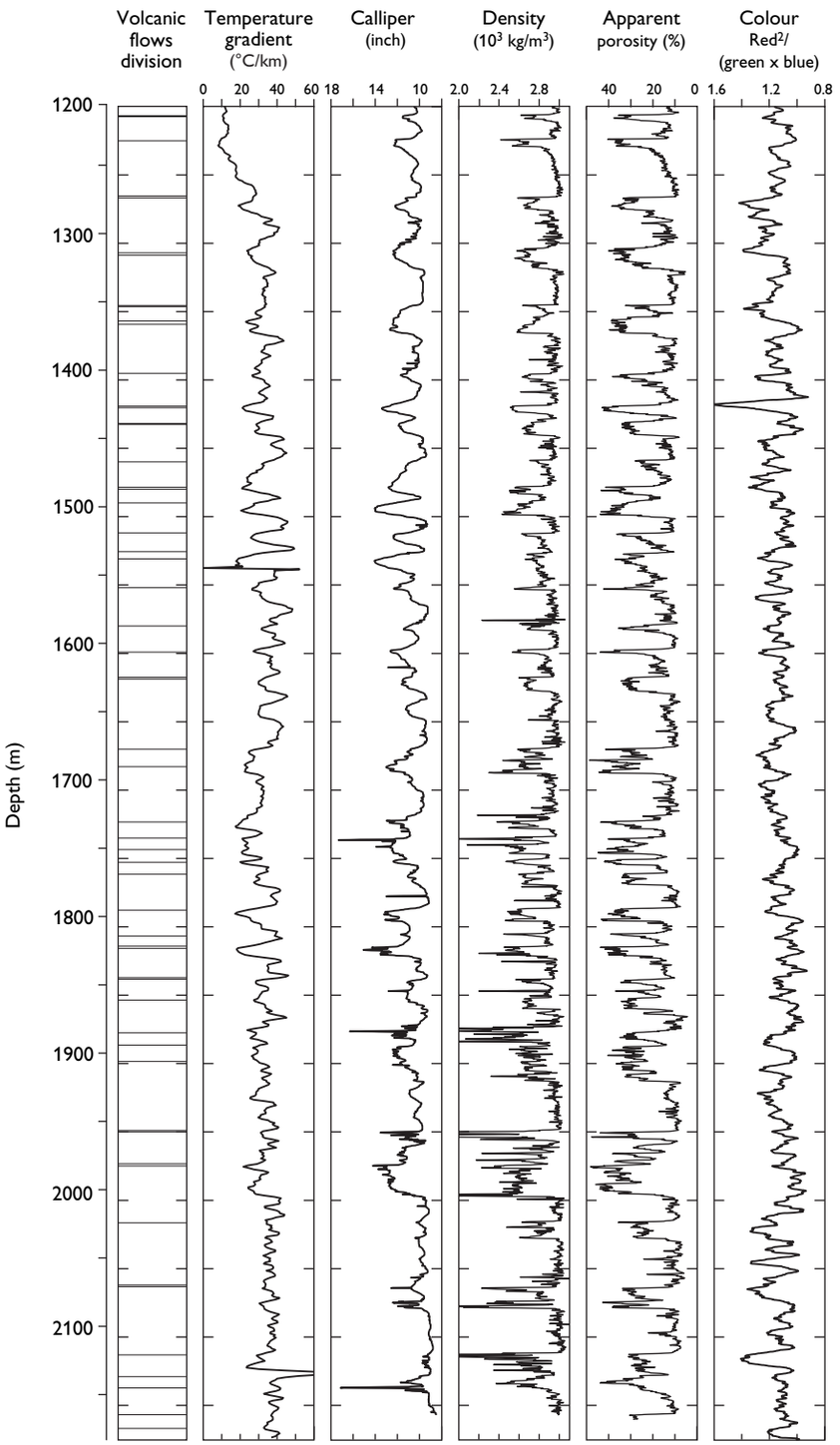

Fig. 5. Running 5 m mean temperature gradients from log 2 shown together with the calliper, density and neutron porosity logs over the depth interval 1200–2170 m. The left-hand column shows the interpreted volcanic flow boundaries (Hald & Waagstein 1984) with closely spaced lines generally indicating thin beds of sediment and the right-hand column shows the relative intensity of red measured from cuttings. See text for further details. Note the reversed scale for calliper, apparent porosity and colour.

sight indicate similar disturbances from flow of water. However, a detailed comparison between temperature gradient variability and other petrophysical log characteristics, including density and neutron porosity logs as well as calliper log data, shows remarkable correlations beginning at a depth of 1250–1300 m (Fig. 5). Mean least-squares temperature gradients based on 5 m averaging intervals reveal local maximum gradients of up to 40–45°C/km and local minimum values down to 20–25°C/km. Local intervals of high temperature gradient correlate with intervals of high density, low neutron porosity and decreased calliper. Intervals of low temperature gradient correlate with intervals of low density, high neutron porosity and increased calliper. The correlation between temperature gradient variability and short-range variations in borehole calliper is particularly remarkable. Maximum temperature gradient variability and close correlations are most pronounced around 1450–1550 m and 1750–1850 m, but a good general correlation with the physical properties of the various basaltic flow units is observed for most of the depth range shown in Fig. 5.

A correlation of low calliper with increased temperature gradients cannot be explained by potential water flow inside the borehole at these greater depths. Any flow of water would have the opposite effect of lowering gradients in narrow parts of the borehole due to locally increased flow rates. Above a depth of about 1200 m no correlation is observed. Here temperature gradients seem to be controlled by the flow of water. The temperature gradient variations below about 1250 m consequently need to be explained in terms of a linkage between resistance to the drill bit, the mineralogical composition and structure and bulk rock thermal properties of the formation. These observed correlations and the inferred variations in rock thermal conductivity are discussed in detail below.

Influence of palaeoclimate

Surface temperature variations penetrate into the subsurface, and temperature and temperature gradient measurements from boreholes may be used to extract information on short-term as well as long-term surface palaeoclimatic temperature variations (e.g. Dahl-Jensen *et al.* 1998; Huang *et al.* 2000; Kukkonen & Joeleht 2003). The Lopra-1/1A borehole is not particularly well-suited for such purpose due to disturbances of the upper part of the hole by water flow. We shall not, therefore, go into detail, but deal only with some main effects of long-term climatic variations.

Simple linear extrapolation of the temperature–depth function from the deeper parts of the borehole to the surface yields a negative intercept temperature of –3.9°C for the depth interval of 1400–3430 m and of –6.7°C for the interval 1400–2175 m (Fig. 3 and Table 3). The low intercept temperatures indicate that temperatures in the deeper parts of the borehole are in equilibrium with a surface temperature significantly below the present-day mean ground temperature of about 7°C. This simple linear extrapolation of deep mean temperature gradients seems justified in our preliminary study because of the apparent homogeneity of mean thermal conductivity and temperature gradients over large depth intervals (see also next section). The shorter intervals of 2175–2770 m and 2995–3430 m give higher intercept values, but these are considered uncertain because of the short length of the intervals that make the extrapolation more sensitive to local variations in thermal conductivity.

Forward thermal modelling using a thermal diffusivity of basalt of 0.7×10^{-6} m^2/s shows that long-term surface temperature variations of the magnitude associated with glaciation and deglaciation are reduced in amplitude to less than 1–2°C (depending on surface temperature amplitudes) at depths below 1300–1500 m. The most accurate temperature gradient and temperature intercept value is probably that from the depth interval 1400–2175 m. Since porosity is likely to decrease with depth, porosities in the rocks sampled by the upper part of the borehole may on average be slightly greater than in those sampled by the deeper parts. This could point towards a slightly lower thermal conductivity and hence a slighthly higher temperature gradient at shallow depths. This effect may, however, be more or less cancelled by secondary mineralisation, which tends to increase the conductivity of porous sections. This means that the mean characteristic conductivity of the upper 1400 m may not differ much from that of the interval 1400–2175 m, justifying the extrapolation with a constant gradient.

We may thus interpret the surface intercept temperature of –6.7°C as an estimate of the long-term characteristic mean for the cold period of the last glaciation. We estimate the increase in surface temperature associated with the termination of the last glaciation to be of the order of 12–16°C. This is a preliminary estimate considering the approximate nature of our procedure, uncertainties related to the lack of good temperature data from the upper part of the borehole (which prevents extraction of a detailed past temperature-time function) and uncertainties related to possible vertical variations in thermal conductivity.

A more detailed analysis of this problem, including inverse modelling, must be based on thermal information from other boreholes, in particular from near-surface in-

tervals where the Lopra-1/1A borehole is disturbed thermally. This is beyond the scope of this paper. From inverse analyses of the temperature–depth function from the GRIP-borehole on the Greenland ice sheet, Dahl-Jensen *et al.* (1998) calculated a surface-temperature increase of 23°C following the last glacial maximum. Using a similar procedure on many boreholes, Kukkonen & Joeleht (2003) obtained an average warming of 8°C for NW Europe at the termination of the last glaciation.

The deviation in the upper part of the Lopra-1/1A borehole from the general linear trend of temperatures deeper down (Fig. 3) thus has two main causes. The increase at surface level from about 7°C to the measured borehole temperature at surface of about 12°C (log 2) is due to the upward flow of warm water inside the borehole. The remaining part, the increase from negative intercept values to about 7°C, is interpreted to reflect the increase of temperature at around the termination of the last glacial period. The penetration of this heating effect to a depth of about 1200 m (Fig. 3) is in agreement with model calculations. Unfortunately, this depth level is also the approximate level above which temperatures and temperature gradients are significantly disturbed from the flow of water inside the borehole.

Thermal conductivity

A limited amount of suitable sample material was available for thermal conductivity measurements. Only one conventional core was drilled within the deepened section below 2175 m. However, a few rotary sidewall cores were also long enough to be measured. Including published measurements on four cored sections from the original borehole, a total of 11 samples have been measured covering the depth range of 337 to 3531 m (driller's depths). Rock materials measured represent massive basalt (7 samples), lapilli-tuff (3 samples) and tuff (1 sample). In addition to thermal conductivity, rock density and porosity were also measured. Measuring results on samples from the Lopra-1/1A borehole are summarised in Table 4. Supplementary preliminary conductivity measurements were additionally carried out on 14 samples taken from surface exposures of basalts near the borehole.

Measuring techniques

Both the needle-probe transient line source technique and the steady-state divided bar technique were applied to measure thermal conductivity. These are standard techniques

Table 4. Measured thermal conductivity, porosity and density and calculated matrix (grain) thermal conductivity and density

Sample	Rock type	Depth* (m)	Thermal conductivity (W/m°C)	Matrix thermal conductivity (W/m°C)	Porosity (%)	Bulk density (10^3kg/m^3)	Matrix density (10^3kg/m^3)
C1†	basalt	337.5	1.75	1.81	3.0	2.96	3.02
C2	basalt	860.1	1.85	1.95	4.5	2.98	3.07
C3	basalt	1218.1	1.74	1.80	3.0	2.94	3.00
C4	basalt	2177.3	1.79	1.82	1.7	3.00	3.03
C5	basalt	2380.0	1.79	1.85	2.7	3.00	3.06
Swc 46‡	basalt	2441.0	1.87	1.96	3.9	2.93	3.01
Swc 37	lapilli-tuff	2562.0	1.35	1.60	17.3	2.47	2.78
Swc 13	lapilli-tuff	3438.0	1.88	2.29	14.8	2.76	3.07
Swc 6	tuff	3512.5	1.91	2.17	9.9	2.78	2.98
Swc 5	lapilli-tuff	3514.5	1.93	2.27	12.1	2.68	2.91
Swc 4	basalt	3531.0	1.84	1.90	2.7	3.10	3.16
Mean values, all samples (11)			1.79	1.95	6.9	2.87	3.01
Standard deviation			0.16	0.21	5.6	0.18	0.10
Mean values, basalt (7)			1.80	1.87	3.1	2.99	3.05
Standard deviation			0.05	0.07	0.9	0.06	0.05
Mean values, lapilli-tuff/tuff (except outlier Swc 37) (3)			1.91	2.24	12.3	2.74	2.99
Standard deviation			0.03	0.06	2.5	0.06	0.08

* Driller's depth below rotary table (to top of core).
† Samples C1 to C5 are from conventional cores taken during drilling.
‡ The Swc samples are small rotary sidewall cores taken after drilling.

for laboratory rock thermal conductivity measurements (e.g. Beck 1988). All measurements were carried out in the geophysical laboratories of the University of Aarhus. Equipment and measuring procedures were similar to those described in Balling *et al.* (1981).

Most rock materials from the deepened section of the borehole and from surface exposures were measured by the needle probe technique. The needle probes used have a nominal length of 50 mm and an outer diameter of 1.5 mm. The measured sidewall cores are cylindrical with a diameter of about 24 mm and lengths ranging from 18 to 30 mm. The probe length cannot be reduced significantly since interpretation is based on line source approximations. The probe length thus exceeds that of the samples to be measured. This difficulty was largely overcome by placing the rock sample of unknown conductivity along the critical central position of the needle probe where the temperature rise function is measured and extending the sample by 'end materials' of known conductivity close to that of the material to be measured. By iterative trial and error procedure, the difference between conductivity of end materials and conductivity of rock sample was reduced to less than 0.3 W/m °C. Experience suggests that this is sufficiently small for an accurate sample conductivity measurement. Any further boundary effects due to the small size of samples were minimised by immersing the samples in water-saturated sand with conductivity close to that of the rock samples being measured.

All samples were water-saturated under vacuum before measurement, which was carried out at normal laboratory temperature (about 20°C) and pressure (1 atm.) conditions. All needle probes were calibrated and tested by measurement of standard materials of known thermal conductivity. The heating period for the probes was 40–60 seconds and the temperature rise at probe centre typically 2–4°C. Sample conductivity was determined as a mean value of at least three individual measurements and individual measurements on the same sample generally did not differ by more than 3–5%. The unknown thermal conductivity was calculated from the temperature rise data using the iterative least-squares inversion technique of Kristiansen (1991).

Samples c1 to c5 (Table 4) were originally measured by the divided bar technique and the results were reported in Balling *et al.* (1984). These older measurements seem to be somewhat too low. A comparison of new needle probe measurements with old divided bar measuring results on material from the same basalt cores shows that the old measurements are systematically about 15% too low. The older low results seem due to the small dimensions of the samples. Previous measurements are thus corrected by + 15%. Considering all sources of experimental uncertainty, reported conductivity values are estimated to be accurate to ± 0.1 W/m °C.

Rock bulk density of water saturated samples and porosity were measured on all samples. Density was measured by using the Archimedes principle of buoyancy. Weight of samples in air and immersed in water, respectively, yields sample weight and volume. Porosity was determined by measuring loss of weight of the water-saturated samples when drying them at about 110°C for 1–2 days. Repeated determinations of porosity on selected samples suggest a precision of ± 1% for low porosity samples (2–5%) and ± 1–2% for samples of higher porosity (10–20%).

With known porosity, bulk density and bulk thermal conductivity, the solid matrix (grain) density and thermal conductivity may be estimated. The computation of matrix density is straightforward assuming proportional contribution of solid matrix and water. Matrix thermal conductivity was computed from the geometric mean formula relating bulk conductivity, k_b, matrix conductivity, k_m, conductivity of water, k_w, and porosity (pore fraction), φ, by $k_b = k_m^{(1-\varphi)} k_w^{\varphi}$. Bulk conductivity and porosity are measured. The conductivity of water at room temperature is 0.6 W/m °C.

Measuring results

Thermal conductivity measuring results are listed together with the density and porosity determinations in Table 4. Mean values and standard deviations were calculated for all 11 samples, for the basalts alone (seven samples) and for lapilli-tuff/tuff alone (three samples, excluding the sample swc 37). Variations between samples are small. All basalts are of low porosity (< 5%) and the conductivity is within the range of 1.75–1.87 W/m °C with a well defined mean value of 1.80 W/m °C. The lapilli-tuff and tuff samples have higher porosity (10–17%) and show a wider range of conductivity, between 1.35 and 1.93 W/m °C. Except for sample swc 37, the lapilli-tuff/tuff samples have a higher solid matrix conductivity than the basalts. Omitting swc 37, mean matrix conductivity of lapilli-tuff and tuff is 2.24 W/m °C as compared to 1.87 W/m °C for basalt. This difference in matrix conductivity explains why lapilli-tuff and tuff have slightly higher conductivity than basalt despite a higher porosity and higher content of free water of low conductivity. The anomalous sample swc 37 has the highest porosity (17.3%) and lowest bulk and matrix conductivity measured. This is possibly due to the presence of a significant amount of secondary analcite, a mineral of very low conductivity (1.3 W/m °C) (Horai 1971).

The thermal conductivity measurements on core materials from the Lopra-1/1A borehole have been supplemented by preliminary measurements of samples of basalts taken from surface exposures in the local area of the borehole. A total of 14 samples were measured. Measurements were again carried out on water-saturated samples using the needle probe technique. Eight samples of low porosity (≤ 4%) have a mean conductivity of 1.77 W/m °C (range 1.67–1.86 W/m °C) and six samples of higher porosity (porosity range 5–26% and mean porosity 13%) have a mean of 1.51 W/m °C (range 1.38–1.59 W/m °C). The conductivity of low-porosity basalts is thus well defined, having a value of about 1.8 ± 0.1 W/m °C. Conductivity decreases with increasing porosity due to the presence of water of low conductivity. Details of these measurements are not shown, but the results conform well to and supplement those from the borehole samples.

Other studies

Our conductivity results on basalts agree well with results obtained by others. Oxburgh & Agrell (1982) measured more than one hundred samples of basaltic flows, intrusions and breccias covering the full depth range of the 2 km deep Reydarfjordur borehole in eastern Iceland. Their measurements on water-saturated samples show increasing thermal conductivity with decreasing porosity and increasing sample depth. Single measurements from basaltic flows and intrusions range between 1.4 and 2.2 W/m °C. Mean values over 500 m intervals increased with depth from about 1.6 in the upper part of the borehole to 1.7–1.9 W/m °C in the central and deeper part of the hole. Measurements on 17 rock samples classified as breccias showed the highest values of conductivity and the widest spread, 1.6–2.8 W/m °C.

As part of heat-flow measurements in shallow boreholes in the south-eastern part of the Deccan Volcanic Province, central India, Roy & Rao (1999) measured thermal conductivity on about 25 core samples of basalt and several samples of fresh massive basalt from outcrops. They obtained sample values within the narrow range of 1.6–1.8 W/m °C with a well-defined mean value of about 1.7 W/m °C.

The same range of measured thermal conductivity is found in the large dataset of Robertson & Peck (1974) on basalts from Hawaii for water-saturated samples of low porosity (2% to about 10%) and low olivine content (0–5%). With increasing porosity and pore-water content, conductivity decreased significantly and variations in mineral content played an important role (see also Horai 1991).

Conductivity variations at Lopra-1/1A and their causes

In a conductive steady-state geothermal regime, variations of the temperature gradient are related to variations in rock thermal conductivity. Intervals of high thermal conductivity result in low temperature gradients and intervals of low thermal conductivity result in high temperature gradients. This simple inverse relation follows from Fourier's law of heat conduction, which relates heat flow to the product of thermal conductivity and temperature gradient. For depth sections of low heat production, conductive heat flow is almost constant and temperature gradient variations will reflect variations in rock thermal conductivity.

Water has a thermal conductivity of 0.6 W/m °C, which is much less than a rock matrix of overall basaltic composition with a mean conductivity around 2 W/m °C. Significant variations in porosity of the basalt will therefore result in major conductivity variations and associated variations in conductive temperature gradient. Thermal conductivity will decrease with increased content of pore water and the temperature gradient will increase. We observe that sections of high neutron porosity are intervals of local low temperature gradient (Fig. 5). This means that a significant part of the water in rocks of apparent high porosity must be bound in water-bearing secondary minerals. Furthermore, some of the secondary minerals (water-free or not) must have a thermal conductivity significantly above that of the mean value of the minerals of unaltered basalt.

Maximum temperature gradients are generally observed within the massive (non-porous) cores of basalt flows, which are characterised by high density and low neutron porosity (Fig. 5). This mainly reflects the presence of feldspar, a primary igneous minerals of low conductivity. However, secondary minerals of even lower conductivity must be present as well.

The large local conductive temperature gradient variations observed between about 1250 and 2175 m (Figs 4, 5) are thus interpreted to originate from significant vertical variations in mean thermal conductivity. In order to maintain a constant heat flow of around 60 mW/m^2 (see next section), local intervals of minimum temperature gradient of 20–25°C/km must indicate conductivities within the approximate range of 2.5–3.0 W/m °C, and local intervals of maximum temperature gradients of about 45°C/km must indicate conductivities around 1.3–1.4 W/m °C. The thickness of lithological units of maximum temperature gradient variations and inferred maximum conductivity variations is typically in the range of 5–20 m (Fig. 5).

Such variations of rock thermal conductivity by a factor of about two are not directly represented in our set of conductivity measurements (Table 4). A potential for variation is, however, indicated by the observation that the mean solid matrix conductivity of lapilli-tuff and tuff is 20% higher than that of basalt. Zones of inferred increase of conductivity are observed to be closely related to zones of reduced density in the originally porous part of the basalt flows. This may be explained by the presence of secondary minerals of high conductivity. The secondary filling of pores, voids and cracks must include minerals of thermal conductivity significantly above that of normal basalt matrix with a conductivity around 2 W/m °C.

This interpretation is consistent with observations of Oxburgh & Agrell (1982) who found that thermal conductivity in the Reydarfjordur borehole generally increased with the degree of alteration, with the highest conductivity of up to 2.8 W/m °C occurring in rock samples broadly classified as breccias.

In general, the thin sediment intervals occur within the broader intervals of low temperature gradient (Fig. 5), indicating a mean thermal conductivity of the sediments very close to that of the adjacent basalt flows. Values of thermal conductivity quoted below are mostly from the comprehensive study and listing of conductivity of rock forming minerals by Horai (1971). High-conductivity secondary minerals present locally in variable amounts in the Reydarfjordur borehole include calcite (3.4 W/m °C), chlorite (4–6 W/m °C), quartz (7.7 W/m °C), epidote (2.6–3.0 W/m °C) and haematite (about 11 W/m °C). In the Lopra-1/1A borehole, zones of maximum temperature gradient and inferred minimum mean conductivity are generally found within the massive cores of the basalt flows characterised by high density and low porosity (Fig. 5). This clearly points to a local increase in low-conductivity secondary minerals such as clay minerals (about 1.5–2 W/m °C), analcite (1.3 W/m °C) and hydrous zeolite minerals like stilbite (1.2 W/m °C).

In order to take a step further into the analysis of the temperature-gradient variability related to mineralogical variations, Fig. 5 also presents a curve showing the relative intensity of red colour reflected from the formation. The colour information is extracted from a digital colour photograph with 24-bit resolution of a montage of cutting samples from the borehole (using the public domain program ImageJ). The relative intensity of red is computed from the values of the red, green and blue channels as the function $red^2/(green \times blue)$. The main idea is to test without extensive mineralogical analysis whether the mineral haematite might play an important role. Haematite (Fe_2O_3) has a bright reddish colour and very high thermal conductivity. It is formed mainly by oxidation of primary magnetite and secondary iron hydroxides. The colour curve shows that many intervals of maximum reddish colour more or less coincide with intervals of low temperature gradient. A close correlation is seen particularly within the depth interval 1550–1700 m. An average cuttings lag time correction of 3 m is applied for the whole section. However, the lag varies with drilling rate, which varies with the hardness of the formation, and a locally better correlation may be obtained by applying a slightly different depth shift of the colour curve.

From the continuously cored Vestmanna-1 borehole, also in the Faroe Islands, the content of haematite in highly oxidised tuffaceous claystone may be as high as 25% estimated from bulk rock chemistry (unpublished data, R. Waagstein). A unit of highly altered basalt or tuff consisting of silicate minerals like pyroxene, plagioclase, clay and zeolites with an assumed average matrix thermal conductivity of about 2 W/m °C plus 25% of haematite (conductivity about 11 W/m °C) will have a bulk conductivity of about 3 W/m °C , as calculated using the geometric mean formula, (see above). This is sufficiently high to produce the lowest temperature gradients of about 20°C/km. Nonetheless, units of increased thermal conductivity generally also have a high (apparent) neutron porosity, which requires minerals of high hydrogen content. This means that, although haematite may play an important part, other components are contributing and further studies are needed for a better understanding of the relation between rock thermal properties and secondary mineralogical components.

Estimates of heat flow

Basalts have low concentrations of the heat producing isotopes U, Th and K, resulting in low heat production, generally within the range of $0.2–0.6 \times 10^{-6}$ W/m^3 (e.g. Verdoya *et al.* 1998; Chiozzi *et al.* 2003). The contribution to surface heat flow from a 3.5 km deep section is thus very small, of the order of 1–2 mW/m^2. If not significantly perturbed by effects of topography, groundwater flow or potential long-term palaeoclimatic surface-temperature variations, heat flow should be almost constant along the drilled section. For sections of the Lopra-1/1A borehole where temperature measurements are assumed to represent conductive equilibrium values, heat flow may therefore be estimated from the product of mean temperature gradient and mean characteristic thermal conductivity.

There seems to be no significant perturbing effects at depths below 1300 m. The Lopra-1/1A borehole is in an

area of small topographic height variations and the effect of topography upon temperature and temperature gradient was modelled to be insignificant. Temperature perturbations are below 1°C. The artesian flow of water in the borehole is localised to levels above 1150–1200 m. As discussed above, both observations and model calculations show that the influence of palaeoclimatic surface temperature variations is insignificant at depths greater than 1200–1300 m.

Mean temperature gradients from long depth intervals vary within the narrow range of 28–33°C/km (Table 3) and are thus well defined. The main source of error in estimating heat flow is thus the choice of mean characteristic thermal conductivity. The uncertainty arises from the presence of local variations of the temperature gradient interpreted in the previous section in terms of conductivity variations associated with mineralogical changes. These changes are difficult to quantify in detail and thus not fully understood.

By transferring thermal conductivity from laboratory measurements to representative *in situ* values, temperature and pressure dependency needs consideration. However, for basalt this dependency is small compared to most other crystalline rocks. The decrease of thermal conductivity of basalt with increasing temperature is of the order of only 5–10% for a temperature increase from 20°C in the laboratory to a temperature of 50–100°C in a borehole (cf. compilations in Kappelmeyer & Haenel 1974). A conductivity decrease of this magnitude is likely to be almost compensated by an equivalent increase of conductivity with pressure. The slightly lower temperature gradient in the deeper parts of the borehole (Table 3) may indicate a slight general increase in average thermal conductivity with depth. This increase may be explained by decreasing porosity resulting from secondary mineralisation.

The most accurate large interval temperature gradient is the assumed conductive mean equilibrium gradient of 32.9°C/km between 1400 and 2175 m. Using our rock thermal conductivity measurements in the range of 1.7–1.9 W/m °C with a mean of about 1.8 W/m °C, we obtain a heat flow within the range of 56–63 mW/m^2. For the deeper parts of the borehole between 2200 and 3430 m, the temperature gradient is between 30 and 31°C/km. The lithology is here represented by roughly equal amounts of basalt and lapilli-tuff. Low-porosity lapilli-tuff may have a mean conductivity of about 2.0–2.2 W/m °C and basalt of about 1.8 to 1.9 W/m °C. This yields a mean conductivity of about 2.0 W/m °C and a heat-flow estimate close to 60 mW/m^2.

Some local intervals of massive basalt at depths between 2000 and 2115 m have well-defined temperature gradients between 35 and 38°C/km with a mean value of 36°C/km. Although massive basalt units are inferred to have a slightly reduced conductivity judged by their temperature gradients, average conductivity (inferred from our measurements) seems unlikely to be lower than 1.6 and not above 1.8 W/m °C, resulting in heat flow in the range 57–65 mW/m^2.

Despite some uncertainty about details of the conductivity variations and their causes, we therefore estimate terrestrial heat flow for the Lopra-1/1A borehole to be of the order 60 ± 5 mW/m^2. This value is about 15 mW/m^2 higher than a previous estimate of Balling *et al.* (1984). The main reason is new measurements showing higher values of thermal conductivity and also the recognition that the neutron log data cannot be interpreted in terms of intervals of real high porosity and water-filled pores resulting in reduced thermal conductivity. On the contrary, local intervals of apparent high porosity are generally observed as having low temperature gradients and thus increased thermal conductivity.

Nearby areas of continental crust in the Faroe–Shetland Basin south-east of the Faroe Islands have present-day heat flows between 45 and 65 mW/m^2 (Iliffe *et al.* 1999). In continental areas off the Norwegian coast, mean heat flow is between 50 and 65 mW/m^2 (Sundvor *et al.* 2000). A heat flow value of around 60 mW/m^2 is thus consistent with continental crust underlying the Faroe Islands. Heat flow from the mantle in Scandinavia is estimated to be around 25–35 mW/m^2 (Balling 1995). If similar values apply here, about 30 mW/m^2 must originate from heat produced by decay of radiogenic isotopes in the crust, which requires a crust of continental composition. Otherwise, a significant cooling component and/or significantly increased mantle heat flow must be assumed, for which there is no other evidence. However, this must be the case for areas of oceanic crust north of the Faroe Islands, where heat flow generally between 60 and 75 mW/m^2 is observed (Sundvor *et al.* 2000).

Summary and conclusions

The Lopra-1/1A borehole drilled to a depth of 3.5 km offers a unique opportunity of obtaining accurate information on the thermal structure to a great depth in the Faroe Islands. High-precision temperature logging was carried out to a depth of 2175 m almost 13 years after drilling. Temperatures in the upper 1200–1300 m are significantly disturbed by upward flow of ground water inside the borehole. For deeper levels, between 2175 m and total depth, only temperature logs from the commercial log-

ging runs measured a relatively short time (up to 53 hours) after drilling fluid circulation are available. These temperatures have been corrected for the estimated effect of disturbances. The deepest point of accurate temperature information is 3430 m with a measured temperature of 98.6°C and a corrected, estimated equilibrium temperature of 103.5°C.

Temperature gradients calculated for depth intervals greater than 500–1000 m show only small variations between 28 and 33°C/km. The least-squares mean gradient for the undisturbed part of the borehole (1400–3430 m) is 31.4°C/km. Levels of inflow of water to the upper part of the borehole are seen as major peaks on the 5 m mean interval temperature gradient. In addition, significant local temperature gradient variability is observed in the high-precision log between about 1250 m with minimum values down to 20–25°C/km and maximum values up to 45°C/km. The latter variations correlate closely with variations in other logging parameters and inferred lithological variations within the lava succession and cannot be explained by ground-water flow. Intervals of low temperature gradient generally match intervals of low density, high neutron porosity and increased borehole calliper and intervals of high temperature gradients match intervals of high density, low neutron porosity and decreased calliper.

The observed correlation with neutron porosity is surprising. In a conductive regime, the temperature gradient should increase in lithological units of high porosity and pores filled with free water of low thermal conductivity. Here, we observe that units of apparent high porosity have high gradients. This leads us to conclude that logged high neutron porosity does not represent real high porosity units with pores filled with free water. Instead, materials of relatively high thermal conductivity compared to normal basaltic material must be present in significant amounts.

The local temperature gradient variations are thus inferred to originate from variations in thermal conductivity. The latter variation is ascribed to secondary mineralisation and mineral alterations. This may produce both high conductivity minerals such as calcite, chlorite, quartz, epidote and haematite and low conductivity hydrous minerals such as clay and zeolite minerals.

Such inferred local variations in rock thermal properties are only partly reflected in our thermal conductivity measurements on core materials from the Lopra-1/1A borehole and samples from surface outcrops in the Lopra-1/1A area. These results, mostly on basalts and some on lapilli-tuff and tuff, show homogeneous conductivity with only small variations and mean values at about 1.8 (basalt) and 1.9 W/m °C (lapilli-tuff/tuff). Our measured lapilli-tuffs and tuffs generally show matrix (grain) conductivity about 20% higher than the basalts. The elevated conductivity of the former rocks may be explained by the abundance of secondary minerals with higher bulk conductivity than basalt. The increased conductivity in the originally porous part of flow units may be explained in a similar way by secondary mineralisation, as mentioned above. In some distinctly reddish intervals, haematite seems to contribute significantly to the increase in conductivity. However, further studies are needed in order to obtain a better understanding of the correlation between rock thermal properties and mineralogical alterations.

Because of the overall homogeneous mean temperature gradient structure, it is possible to obtain some information on palaeo-surface temperatures during the last glaciation by extrapolation of the temperature–depth function below 1200–1400 m to the ground surface. Extrapolating the depth interval 1400–2175 m, a surface intercept of –6.7°C is obtained. This is 13–14°C below present-day surface temperature. Although the extrapolation must be considered preliminary and approximate by nature, it suggests a temperature increase of the order of 12–16°C at the termination of the last glacial period.

From well-defined temperature gradients and information on mean characteristic thermal conductivity of the drilled basaltic sequences, we estimate a conductive heat flow at the Lopra-1/1A drill site of about 60 ± 5 mW/m^2. This is about 15 mW/m^2 higher than the previous estimate from the original borehole. The revised estimate is due mainly to new, higher thermal conductivity measurements and higher estimates of the conductivity of the porous parts of the basalt flows by taking secondary mineralisations into account. A heat flow value of about 60 mW/m^2 is consistent with the Faroe Islands being underlain by continental crust.

From our analysis we may conclude that the thermal regime and our reported temperatures, temperature gradients and heat-flow value from below a depth of 1200–1400 m represent conductive equilibrium conditions without significant disturbances from the effect of drilling, ground-water flow or palaeoclimatic surface temperature variations. Temperature structure, temperature gradients and heat flow may thus be taken as representative of a larger area around the drill site with similar basaltic lithology. With respect to heat flow, an assumption of similar lithology may not be necessary.

Acknowledgements

Valuable comments from two referees, Andrea Förster, GFZ, Potsdam and Torben Bidstrup, GEUS, Copenhagen are gratefully acknowledged. This study has been supported by funds from the Danish Natural Science Research Council.

References

Balling, N. 1995: Heat flow and thermal structure of the lithosphere across the Baltic Shield and northern Tornquist zone. Tectonophysics **244**, 13–50.

Balling, N., Kristiansen, J.I., Breiner, N., Poulsen, K.D., Rasmussen, R. & Saxov, S. 1981: Geothermal measurements and subsurface temperature modelling in Denmark. GeoSkrifter **16**, 172 pp. Århus, Denmark: University of Aarhus.

Balling, N., Kristiansen, J.I. & Saxov, S. 1984: Geothermal measurements from the Vestmanna-1 and Lopra-1 boreholes. In: Berthelsen, O., Noe-Nygaard, A. & Rasmussen, J. (eds): The deep drilling project 1980–1981 in the Faeroe Islands. Annales Societatis Scientiarum Faeroensis, Supplementum **IX**, 137–148. Tórshavn: Føroya Fróðskaparfelag.

Beck, A.E. 1988: Methods for determining thermal conductivity and thermal diffusivity. In: Haenel, R., Rybach, L. & Stegena, L. (eds): Handbook of terrestrial heat-flow density determinations, 87–124. Dordrecht: Kluwer Academic Publishers.

Beck, A.E. & Balling, N. 1988: Determination of virgin rock temperatures. In: Haenel, R., Rybach, L. & Stegena, L. (eds): Handbook of terrestrial heat-flow density determinations, 59–85. Dordrecht: Kluwer Academic Publishers.

Berthelsen, O., Noe-Nygaard, A. & Rasmussen, J. (eds) 1984: The deep drilling project 1980–81 in the Faeroe Islands. Annales Societas Scientiarum Færoensis, Supplementum **IX**, 159 pp. Tórshavn: Føroya Fróðskaparfelag.

Bott, M.H.P., Sunderland, J., Smith, P.J., Casten, U. & Saxov, S. 1974: Evidence for continental crust beneath the Faeroe Islands. Nature **248**, 202–204.

Chiozzi, P., Pasquale, V. & Verdoya, M. 2003: Heat from radioactive elements in young volcanics by γ-ray spectrometry. Journal of Volcanology and Geothermal Research **119**, 205–214.

Dahl-Jensen, D., Mosegaard, K., Gundestrup, N., Clow, G.D., Johnsen, S.J., Hansen, A.W. & Balling, N. 1998: Past temperatures directly from the Greenland Ice Sheet. Science **282**, 268–271.

Gariépy, C., Ludden, J. & Brooks, C. 1983: Isotopic and trace element constraints on the genesis of the Faeroe lava pile. Earth and Planetary Science Letters **63**, 257–272.

Hald, N. & Waagstein, R. 1983: Silicic basalts from the Faeroe Islands: evidence of crustal contamination. In: Bott, M.H.P. *et al.* (eds): Structure and development of the Greenland–Scotland Ridge, 343–349. New York: Plenum Press.

Hald, N. & Waagstein, R. 1984: Lithology and chemistry of a 2 km sequence of lower Tertiary tholeiitic lava drilled on Suðuroy, Faeroe Islands (Lopra-1). In: Berthelsen, O., Noe-Nygaard, A. & Rasmussen, J. (eds): The deep drilling project 1980–81 in the Faeroe Islands. Annales Societas Scientiarum Færoensis, Supplementum **IX**, 15–38. Tórshavn: Føroya Fróðskaparfelag.

Holm, P.M., Hald, N. & Waagstein, R. 2001: Geochemical and Pb-Sr-Nd isotopic evidence for separate hot depleted and Iceland plume mantle sources for the Palaeogene basalts of the Faroe Islands. Chemical Geology **178**, 95–125.

Horai, K. 1971: Thermal conductivity of rock-forming minerals. Journal of Geophysical Research **76**, 1278–1308.

Horai, K. 1991: Thermal conductivity of Hawaiian basalt: a new interpretation of Robertson and Peck's data. Journal of Geophysical Research **96**, 4125–4132.

Huang, S., Pollack, H.N. & Shen, P.-Y. 2000: Temperature trends over the last five centuries reconstructed from borehole temperatures. Nature **403**, 756–758.

Iliffe, J.E., Robertson, A.G., Ward, G.H.F., Wynn, C., Pead, S.D.M. & Cameron, N. 1999: The importance of fluid pressures and migration to the hydrocarbon prospectivity of the Faeroe–Shetland White Zone. In: Fleet, A.J. & Boldy, S.A.R. (eds): Petroleum geology of Northwest Europe: Proceedings of the 5th conference, 601–611. London: Geological Society.

Jørgensen, O. 1984: Zeolite zones in the basaltic lavas of the Faeroe Islands. In: Berthelsen, O., Noe-Nygaard, A. & Rasmussen, J. (eds): The deep drilling project 1980–81 in the Faeroe Islands. Annales Societas Scientiarum Færoensis, Supplementum **IX**, 71–91. Tórshavn: Føroya Fróðskaparfelag.

Jørgensen, O. 2006: The regional distribution of zeolites in the basalts of the Faroe Islands and the significance of zeolites as palaeotemperature indicators. Geological Survey of Denmark and Greenland Bulletin **9**, 123–156 (this volume).

Kappelmeyer, O. & Haenel, R. 1974: Geothermics with special reference to application. Geoexploration Monographs. Berlin: Gebrüder Borntraeger.

Kristiansen, J.I. 1991: NEPR: A FORTRAN-77 program for determining thermal conductivity and diffusivity by needle-probe inversion. Computers & Geosciences **17**, 351–390.

Kukkonen, I.T. & Joeleht, A. 2003: Weichselian temperatures from geothermal heat flow data. Journal of Geophysical Research **108**, http://dx.doi.org/10.1029/2001JB001579.

Larsen, L.M., Waagstein, R., Pedersen, A.K. & Storey, M. 1999: Trans-Atlantic correlation of the Palaeogene volcanic successions in the Faeroe Islands and East Greenland. Journal of the Geological Society (London) **156**, 1081–1095.

Oxburgh, E.R. & Agrell, S.O. 1982: Thermal conductivity and temperature structure of the Reydarfjordur borehole. Journal of Geophysical Research **87**, 6423–6428.

Rasmussen, J. & Noe-Nygaard, A. 1970: Geology of the Faeroe Islands. Danmarks Geologiske Undersøgelse 1. Række **25**, 142 pp.

Richardson, K., Smallwood, J.R., White, R.S., Snyder, D.B. & Maguire, P.K.H. 1998: Crustal structure beneath the Faroe Islands and the Faroe–Iceland Ridge. Tectonophysics **300**, 159–180.

Robertson, E. & Peck, D. 1974: Thermal conductivity of vesicular basalt from Hawaii. Journal of Geophysical Research **79**, 4875–4888.

Roy, S. & Rao, R.U.M. 1999: Geothermal investigations in the 1993 Latur earthquake area, Deccan Volcanic Province, India. Tectonophysics **306**, 237–252.

Skogseid, J., Planke, S., Faleide, J.I., Pedersen, T., Eldholm, O. & Neverdal, F. 2000: NE Atlantic continental rifting and volcanic margin formation. In: Nøttvedt, A. *et al.* (eds): Dynamics of the Norwegian Margin. Geological Society Special Publication (London) **167**, 295–326.

Sundvor, E., Eldholm, O., Gladczenko, T.P. & Planke, S. 2000: Norwegian–Greenland Sea thermal field. In: Nøttvedt, A. *et al.* (eds): Dynamics of the Norwegian margin. Geological Society Special Publication (London) **167**, 397–410.

Verdoya, M., Pasquale, V., Chiozzi, P. & Kukkonen, I.T. 1998: Radiogenic heat production in the Variscan crust: new determinations and distribution models in Corsica (northwest Mediterranean). Tectonophysics **291**, 63–75.

Waagstein, R. 1988: Structure, composition and age of the Faeroe basalt plateau. In: Morton, A.C. & Parson, L.M. (eds): Early Tertiary volcanism and the opening of the NE Atlantic. Geological Society Special Publication (London) **39**, 225–238.

Manuscipt received 4 May 2005; revision accepted 9 September 2005.

Mineralogical and thermodynamic constraints on Palaeogene palaeotemperature conditions during low-grade metamorphism of basaltic lavas recovered from the Lopra-1/1A deep hole, Faroe Islands

William E. Glassley

The sequene of secondary minerals that are reported for the Lopra-1/1A well records progressive zeolite facies to prehnite–pumpellyite-facies mineral progressions consistent with those of other well-studied hydrothermally altered rock sequences. Detailed comparison of the calc–silicate (zeolites and prehnite) mineral distributions of the Lopra-1/1A sequence with those from other regions indicates that this sequence exhibits consistently longer down-hole intervals for secondary mineral species than reported elsewhere. When compared to measured down-hole temperatures reported in other hydrothermally altered regions, the results suggest that the Lopra-1/1A mineral progression formed under conditions typical of low temperature hydrothermal systems that form shortly after eruption of thick basaltic piles. Maximum temperatures achieved at the 3500 m level of the well were at or below 200°C. The implied geothermal gradient was less than 50°C/km. An analysis of prehnite – fluid composition relationships was also conducted in order to determine if results compatible with the paragenetic sequence study could be obtained from thermodynamic constraints. In this case, the limiting temperature for prehnite formation in equilibrium with albite–quartz–calcite–laumontite (the mineral assemblage at the bottom of the hole) was determined for a range of fluid compositions. The resulting calculations suggest temperatures of formation of prehnite in the range of 140°C to 205°C, a conclusion which is broadly consistent with those reached from study of the paragenetic relationships. Comparison of these results with other studies of palaeogeothermal gradients of the North Atlantic margins suggests a consistent pattern in which relatively low geothermal gradients persisted in the Palaeogene rift basin.

Keywords: North Atlantic Volcanic Province, thermal history, geothermal gradients, low temperature metamorphism, fluid-rock interaction, reactive transport, zeolites, prehnite-pumpellyite

Lawrence Livermore National Laboratory, Livermore, California 94550, USA. E-mail: *glassley1@llnl.gov*

Minerals that crystallise from basaltic lavas are unstable with respect to a wide range of hydrous silicates and carbonates when subjected to low temperature conditions (< 300°C) in the presence of H_2O- and CO_2-bearing fluids. Recrystallisation of basaltic rocks under these physical and chemical conditions results in the development of minerals that characterise the zeolite, prehnite–pumpellyite and greenschist facies. It has been well-documented that the basalts of the East Greenland – Faroe Islands province record extensive development of minerals characteristic of the zeolite and lower prehnite–pumpellyite facies (Jørgensen 1984, 1997; Neuhoff *et al.* 1997; Larsen *et al.* 1999). What remains unclear is the temperature history recorded by these mineral assemblages.

Generally, under the lowest temperature conditions, clays, zeolites and hydrous Fe–Mg silicates form, giving way to less hydrated minerals at higher temperatures. Often this progression is recorded by the presence of a

complex sequence of zeolite minerals that have increasingly smaller amounts of molecular water bound in their structures (Bird *et al.* 1984; Neuhoff & Bird 2001). In principle, therefore, zeolitic and related minerals can be sensitive indicators of temperature conditions.

This temperature sensitivity is complicated by the equally important sensitivity of the zeolites to the composition of coexisting fluids. The thermodynamic properties of the zeolites are affected by substitution between the alkali metals, particularly Na, K and Ca, and Al–Si exchange (e.g. Neuhoff *et al.* 1997, 2002, 2003, 2004). The stability fields of the zeolites are also sensitive to the ratio of calcium activity to hydrogen ion activity (i.e. $[Ca^{++}]/[H^{+}]^2$) in the coexisting fluid phase (e.g. Surdam 1973; Bird *et al.* 1984). Hence, fluid chemistry has a strong influence on both the mineral compositions that develop and the specific mineral phases that form during low temperature recrystallisation.

The purpose of this paper is to define likely bounds for bottom-hole temperatures and the likely geothermal gradient active at the time of mineral development, based on paragenetic relationships and thermodynamic constraints, taking into account the effects of fluid chemistry. Detailed descriptions of the locations, mineralogies and geological settings for the Lopra-1/1A and Vestmanna-1 boreholes are presented in other chapters in this book and are only summarised here.

Geology

The basalts of the Faroe Islands were erupted subaerially onto continental crust during opening of the northern North Atlantic. The basalts have been divided informally into an upper, a middle and a lower formation. The lower basaltic sequence is more than 3000 m thick (established on the basis of field exposure and the Lopra-1/1A drilling programme), and ranges in age from *c.* 58.8 to 56.5 Ma (Waagstein *et al.* 2002). The overlying basalts and sediments (some of the sediments are coal-bearing) are more than 2000 m thick and were erupted between *c.* 56 and 55.5 Ma (Larsen *et al.* 1999). Recrystallisation of the lavas took place during subsequent burial, leading to the development of a wide range of zeolites and associated calc–silicate minerals (Jørgensen 1984, 1997). The argument that the secondary mineral development results from burial metamorphism, rather than significant tectonic stacking or folding, is based on the relatively flat-lying nature of the basaltic flows and the absence of any kinematic fabric.

Methods

Compiled published data

Published data from active hydrothermal systems where temperatures and mineral associations are recorded, provide the most direct evidence of the conditions under which specific mineral assemblages occur. For this reason, published data from a variety of drilled hydrothermal systems with depths less than 4000 m were analysed to identify temperature constraints that would apply to the mineral associations reported for samples from the Lopra-1/1A drilling programme (Jørgensen 1984, 1997). The reported Lopra-1/1A assemblages were confirmed by the author during independent examination of thin sections.

The best available data that correlate downhole temperatures, depth and mineral occurrences are from geothermal systems in Iceland (Kristmannsdóttir & Tomassón 1976), Japan (Seki *et al.* 1969; Boles 1981), Cerro Prieto (Bird *et al.* 1984), Wairakei (Steiner 1977) and Toa Baja (Cho 1991). The reports from Iceland and Japan discuss secondary mineral development related to alteration of basaltic rocks, which most closely correspond to the Lopra-1/1A sequence. The Cerro Prieto locality consists of sedimentary rocks (sandstones, siltstones and mudstones) that are predominately composed of quartz and feldspars. The Wairakei and Toa Baja localities consist of volcanic and volcanoclastic rocks and their associated clastic derivatives. The Wairakei rocks are primarily rhyolitic and the Toa Baja rocks primarily andesitic.

This suite of rock types spans the entire range from basalts through andesites to rhyolites, thus encompassing silica-poor to silica-rich compositions with varying abundances of alkali metals. On a whole-rock basis, then, the compositional range from these reported systems bounds that of the Faroe Island basalts considered here.

The different tectonic settings represented by these systems include both rift and convergent margin environments. Since these different settings evolved through different thermal histories, it is likely that the possible thermal conditions that may have affected the Faroe Island basalts, will be represented by at least some of the data recorded in the published studies.

The range of fluid compositions at the various sites is broad. The Cerro Prieto fluids were concentrated solutions with high total dissolved solids and salinities, while many of the solutions reported from the New Zealand region, particularly within the Broadlands-Ohaki (Hedenquist 1990) and Wairakei areas, included CO_2-rich and neutral-pH chloride waters and CO_2-poorer fluids occurred within the Iceland system. Thus, the published re-

ports examined include a range of solutions that are likely to encompass those that may have been present during alteration of the Faroe Island basalts.

Clear differences exist between sites with regard to the depth and extent of secondary mineral development, reflecting the effects of these combined intensive and extensive variables (i.e. T, bulk composition, fluid composition etc.). By considering this broad range of systems, it is possible to develop some insight into the extent to which differing geothermal and chemical conditions influenced the development of the mineral associations and how that influence is expressed at the Lopra-1/1A site. Comparison of the Lopra-1/1A suite with these reported mineral parageneses should provide a strong bound to the thermal gradient inferred from these data.

In this study, attention is focused on the calc–silicate mineral suite, which is comprised of the components $CaO–Na_2O–Al_2O_3–SiO_2–H_2O–CO_2$. Although potassium may play an important role in some of these mineral phases, particularly in zeolites where it may substitute for Na and Ca, it was not considered in this study because it is generally low in abundance in minerals that are characteristically part of the calc–silicate series in basaltic systems.

The minerals of interest in the calc–silicate system for the purposes of this study are the zeolites, prehnite, calcite and zoisite–clinozoisite (which are proxies in this study for epidote). This system was selected for detailed consideration because it is the most thoroughly characterised for low-grade mineral development. These minerals possess well-characterised structures and compositions. In addition, there has been a long history of research in the geochemical community to derive thermodynamic data for phases in this system (Liou 1971; Glassley 1974; Frey *et al.* 1991; Neuhoff *et al.* 1997, 2002; Fridriksson *et al.* 2001; Neuhoff & Bird 2001). Although of immense importance in determining relative conditions in shallow (< 3000 m), low temperature (< 150°C) systems, the clay minerals and chlorites exhibit such structural and compositional complexity that the thermodynamic data available for modelling their behaviour remain inadequate. For that reason, they are not considered further in this report, although work continues on them.

Consideration of the calc–silicate system also eliminates complexities that arise due to the effects of variable oxygen partial pressures, which can dramatically influence the stability of iron-bearing mineral phases. Hence, chlorites, smectites, Fe–oxy/hydroxides and related phases are not considered here. Two exceptions are considered in this paper. Pumpellyite, which is noted in several other studies and documented as a mineral phase of limited distribution at Lopra-1/1A, is considered here as part of the paragenetic assemblage, but does not play an important role in establishing the conclusions presented later. Prehnite is also considered here and does possess limited solid solution with an Fe^{3+} end member. Measured mole fractions in a limited suite of analysed prehnites (unpublished data 1999, R. Waagstein) average 0.08, with a range from 0.00 to 0.20 for 18 samples. Rose & Bird (1987) have shown that solid solution of as little as 10% of the Fe end member in Al-rich prehnite can significantly affect prehnite stability. Although the majority of prehnites analysed in the Lopra-1/1A rocks fall below this value, the impact of this effect must be borne in mind and is discussed later in this paper.

Although the stability fields of many of these minerals are reasonably well established for their ideal compositional end-members, each of these minerals belongs to a solid solution series. Generally, there are very little or no quantitative data available regarding the actual compositions of mineral phases in the low-grade rocks described in the referenced reports. In addition, thermodynamic mixing properties of the solid solutions are generally not available. Hence, when comparing stability relationships from one locality to another, it must be borne in mind that uncertainties of unknown magnitude are inherent in the comparison due to possible differences in the compositions of the minerals.

Thermodynamic calculations

Once mineral assemblages and distributions were compiled, the sensitivity of mineral development to thermal conditions and composition of coexisting fluids was modelled. This effort was undertaken because textural and compositional properties of these secondary minerals attest to the importance of mass transport involving carbonate–bicarbonate-bearing aqueous fluids. The thermodynamic properties of such solutions influence strongly the stability fields of the minerals and can thus be an additional means of placing limits on the physical conditions at the time of mineral growth.

The calculations employed the aqueous speciation/reaction progress software EQ3/6 (Wolery & Daveler 1992), using the .com database. The modelling was accomplished by performing speciation calculations over a range of temperatures and compiling the affinities of the possible solid phases that may develop in this system. Affinity here is defined as:

$$A = 2.303RT \log(Q/K)$$

where A is the affinity (in calories), R is the universal gas

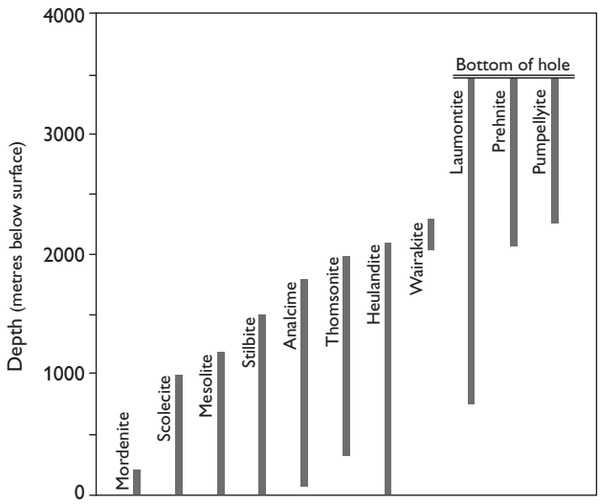

Fig. 1. Summary of depth distributions for minerals reported in the Lopra-1/1A samples (compiled from Jørgensen 1984, fig. 4; 1997, fig. 1). Zero depth corresponds to the ground surface at the drill site. The bottom of the well is indicated. Minerals are arranged along the horizontal axis in a sequence of increasing depth to the right. The depth intervals correspond to the reported occurrences where the individual minerals are most abundant. In some instances, spot occurrences of minerals occur outside the indicated intervals. Such occurrences can result from local variations in rock or fluid chemical conditions, or the consequences of locally controlled reaction kinetics, and are not plotted here.

constant (1987 calories/mole-degree Kelvin), T is temperature (Kelvin), Q is the activity product for the relevant species in the applicable hydrolysis reaction and K is the equilibrium constant for that same reaction. Affinities greater than zero identify mineral phases that are supersaturated in the water at the specified conditions and affinities less than zero identify mineral phases that are undersaturated for those same conditions. Positive affinities thus correlate with minerals that would be expected to precipitate from solution or form from mineral reactions in the rock, whereas negative affinities indicate that the respective mineral phase will dissolve, if present.

Particular attention was given to the development of prehnite since its compositional variability is less than that of the zeolites and its thermodynamic properties are better constrained. The affinities were calculated assuming in all cases that the system was saturated in quartz, laumontite and albite, since these phases coexist with prehnite (see below). These solids were used to constrain the activities of aqueous SiO_2, Al^{3+} and Na^{+}, respectively. The same simulations were repeated assuming that calcite was present as a control for Ca^{++} activity to determine the sensitivity of the results to this change in the system constraints. At the beginning of all of the simulations, it was assumed that the hydrogen ion activity was near neutral at the temperature considered. The initial fluid composition (a dilute, neutral-pH water at the temperature considered) was not in equilibrium with the constraining mineral phases but, for each simulation, was allowed to evolve toward equilibrium with the constraining mineral phases. The equilibrium fluid composition that evolved thus represented the composition of an aqueous fluid in equilibrium with the constraining phases and was the beginning point for further simulations that considered the effects of temperature and other compositional variables.

The sensitivity of the results to variations in total Cl^{-} and HCO_3^{-} was also considered. In this case, the simulations were conducted for Cl^{-} concentrations between 14 mg/l and 14.410 mg/l, and HCO_3^{-} concentrations between 10 mg/l and 1000 mg/l. This range of values was selected because it encompasses the vast majority of water compositions from hydrothermal systems around the world (see compilations and discussions in Roedder 1972; Ellis & Mahon 1977; Arnorsson *et al.* 1983; Fournier 1985).

Results

The depth intervals over which individual minerals occur at the Lopra-1/1A site are summarised in Fig. 1. Noteworthy in this compilation is that the progression with depth of the zeolite sequence is consistent with that from other localities (see summaries below under 'Compiled data'), and that epidote does not occur, even at the deepest levels. Also of significance is that most of the minerals persist over depth intervals that exceed significantly any other reported occurrence for that mineral.

Compiled data

The published temperature–depth data compiled from Iceland (Kristmannsdóttir & Tomassón 1976), Japan (Seki *et al.* 1969; Boles 1981), Cerro Prieto (Bird *et al.* 1984), Wairakei (Steiner 1977) and Toa Baja (Cho 1991) are shown in Figs 2–4. For each location, the depth interval over which a mineral occurs is indicated by connected symbols that link the high and low temperature and depth points that define the extent of the mineral phase.

Figures 2–4 also show the depth intervals over which mesolite, stilbite, heulandite, laumontite and prehnite occur in the Lopra-1/1A samples (Jørgensen 1984, 1997). The Lopra-1/1A depth–temperature relationships were constrained to be consistent with the following criteria:

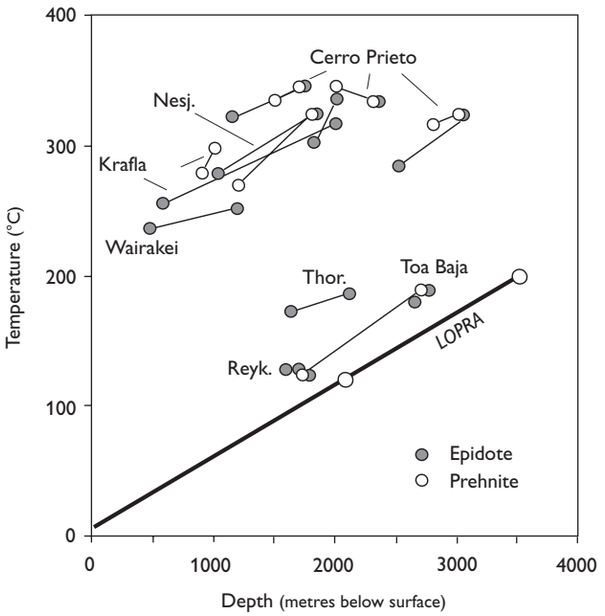

Fig. 2. Temperature–depth distributions reported from active thermal systems for the zeolites chabazite, scolecite–mesolite, mordenite, stilbite and heulandite. Lines between points indicate the temperature–depth intervals over which the minerals are reported to occur. Data sources are: Kristmannsdóttir & Tomassón 1976 for Iceland; Seki *et al.* 1969 and Boles 1981 for Japan; Bird *et al.* 1984 for Cerro Prieto, Baja California; Steiner 1977 for Wairakei, New Zealand; Cho 1991 for Toa Baja, Puerto Rico. The solid line labelled LOPRA is the geothermal gradient derived in Fig. 2, with the depth intervals for Lopra mesolite, stilbite and heulandite indicated. **Thor.**, Thorlakshofn, Iceland; **Reyk.**, Reykjavik, Iceland; **Nesj.**, Nesjavellir, Iceland.

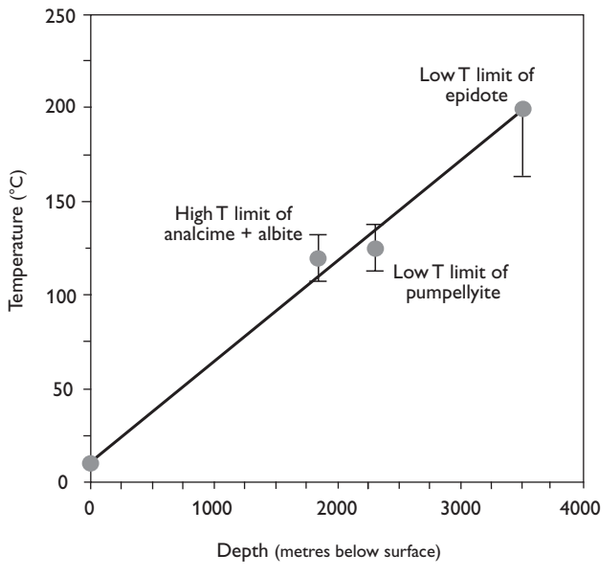

Fig. 3. Temperature–depth distribution for laumontite and prehnite. Laumontite occurrences are from Iceland, Japan and Toa Baja, and prehnite from Iceland, Toa Baja and Cerro Prieto (see Fig. 3 for references and abbreviations). Also shown for comparison is the inferred temperature–depth distribution for the same Lopra minerals along the derived geothermal gradient (Fig. 2).

1. Coexistence of analcime and albite is constrained by Cho (1991) to temperatures less than *c.* 120°C. Since albite is ubiquitous in the Lopra-1/1A volcanics, the maximum depth occurrence for analcime (*c.* 1850 m) is assumed to mark the *c.* 120°C isotherm.
2. Laumontite coexisting with prehnite is constrained to temperatures less than 160°C (Varna 1989). Since laumontite and prehnite occur together over a depth of more than 1000 m and extend to the bottom of the Lopra-1/1A hole, this constraint would place the base of the studied sequence at temperatures less than 160°C.
3. Epidote is considered to require minimum temperatures for development of 200°C (Bird *et al.* 1984). The exception to this would be systems rich in Fe^{3+} (Varna 1989), which the Lopra-1/1A basalts are not. Epidote is not reported within the Lopra-1/1A rocks, hence the bottom-hole temperature must be less than 200°C.
4. Pumpellyite requires temperatures in excess of 125°C for stable growth (Evarts & Schiffman 1983; Bevins *et al.* 1991). The first appearance of pumpellyite is at a depth of *c.* 2300 m, thus constraining the 125°C isotherm to be near this depth.

These observations were used to construct a palaeogeotherm (Fig. 3). In developing this palaeogeotherm, points 1 (the constraint on analcime and albite coexistence) and 4 (the minimum temperature for pumpellyite development) were accepted without qualification. It was also assumed that the mean annual surface temperature was 10°C and that the bottom-hole temperature was *c.* 200°C. The 200°C bottom-hole temperature, which exceeds the 160°C constraint inferred from coexistence of prehnite and laumontite (point 2), was used to assure a conservative estimate of maximum thermal conditions and represents a compromise between points 2 and 3. In other words, the temperature gradient developed by this approach will *overestimate* maximum likely thermal conditions.

The resulting geothermal gradient is linear. Least squares regression of the data points gives a correlation of fit of 0.9949 and a gradient of 0.05°C/m, or 50°C/km.

Using this geothermal gradient, the depth intervals for mesolite, stilbite and heulandite were plotted to be consistent with the permissible measured distance over which these minerals occur. Laumontite and prehnite were placed to be consistent with the implied thermal gradient and temperature constraints, as described above.

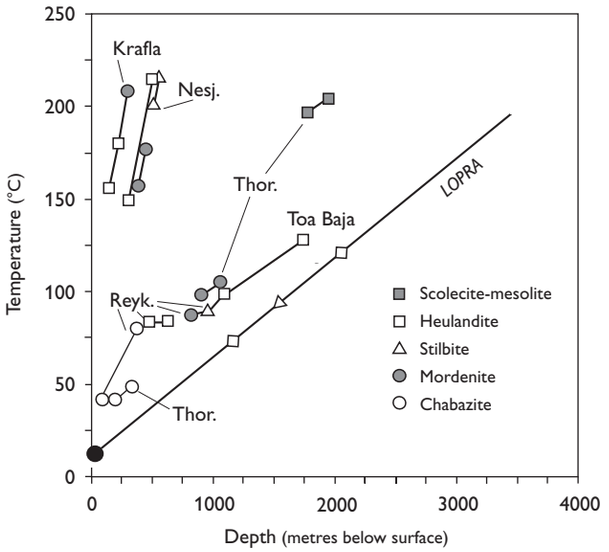

Fig. 4. Temperature–depth distribution for prehnite and epidote. Epidote occurrences are from Iceland, Cerro Prieto, Toa Baja and Wairakei (see Fig. 3 for references). Also shown is the inferred temperature–depth distribution for Lopra prehnite along the derived geothermal gradient (Fig. 2).

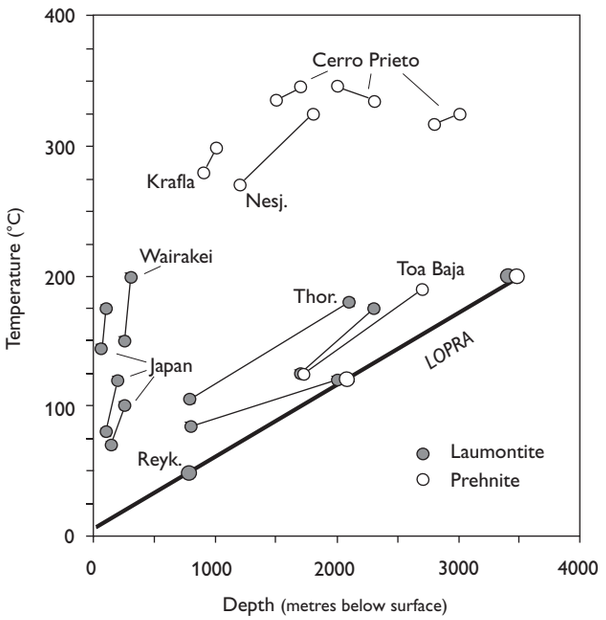

Fig. 5. Temperature constraints for the indicated mineral associations or occurrences. See text for sources and assumptions. The straight line is a least squares fit to the data points. The uncertainty bars for the analcime + albite 'out' and the pumpellyite 'in' data points span 25°C, and are presented only as an inferred, reasonable uncertainty envelope, in the absence of any available analytical data. The bar associated with the epidote lower T limit indicates the range of possible bottom hole metamorphic temperatures, based on the alternative constraint that the maximum temperature for laumontite coexisting with prehnite is 160°C. See text for further details.

This reconstruction provides a conservative estimate of the temperature gradient only if the extent of surface erosion since mineral development is small and if there has been minimal tectonic rotation of the volcanic sequence. The consequence of these points is elaborated on below. The following observations are significant for reconstructing conditions recorded in the Lopra-1/1A samples.

1. The zeolite group of minerals is stable at temperatures throughout the range 40°C to 210°C (Figs 2–4). The only reported occurrence of zeolites at higher temperatures is from the Wairakei, New Zealand, geothermal field, where wairakite is stable at temperatures of 240°C to 250°C, where it coexists with epidote. This is not an assemblage reported from Lopra-1/1A. The corresponding geothermal gradients for Wairakei range from a high of > 400°C/km to a low of *c.* 40°C/km. The highest temperature gradients require active volcanic/magma systems and are not typical of most environments. Nevertheless, the stability relationships for minerals from these systems provide useful information for defining thermal stability limits for the minerals being considered. It should be noted, too, that the higher temperature conditions likely reflect convective hydrothermal environments with highly non-linear geothermal gradients. Inevitably, lower geothermal gradients result in a particular mineral being observed over a much longer interval. This then implies that, for a given combination of rock- and fluid-compositional characteristics, the lower the temperature gradient, the greater will be the depth range of a borehole over which a particular mineral will occur.

2. Although local conditions (such as rock composition, coexisting fluid chemistry, local gas chemistry) at each site determine the exact zeolite sequence, the sequence of minerals generally follows one in which zeolites with high contents of molecular water (e.g. chabazite, scolecite, mesolite) are progressively replaced by zeolites with lower contents of molecular water (e.g. heulandite and laumontite) at higher temperatures.

3. In all cases considered, the assemblage prehnite–laumontite formed near the upper stability field of the zeolites and prior to the appearance of epidote. The temperature range for stable laumontite is in the range 70°C to 200°C. As noted by Surdam (1973) and Bird *et al.* (1984), prehnite–laumontite relationships are sensitive to the activity ratio $[Ca^{++}]/[H^{+}]^2$ in the fluid

phase. Variation in fluid chemistry is thus the likely cause for the broad temperature interval observed for laumontite stability.

4. In all cases, prehnite first forms at lower temperatures than epidote. However, both occur within the higher temperature range of the zeolites and are stable beyond the zeolite field (Fig. 4). Prehnite, for example, is reported to be stable in the temperature range 125°C to 340°C in the reports referenced in this study. This temperature interval is the same as reported for the stable presence of epidote, although the lower temperature occurrences of epidote are in systems that have high Ca^{++} and Fe^{3+} activity.

The mineral sequence recorded in the Lopra-1/1A well (Fig. 1) is typical of that reported in other geothermal systems. The zeolite sequence follows the pattern of generally decreasing molecular water content with increasing depth, reflecting the impact of elevated temperatures at deeper levels in the borehole. This observation is generally consistent with the view that the thermal history experienced by these basalts was relatively simple.

The highest temperature mineral assemblage that has developed is the prehnite–laumontite assemblage that is reported from the depth interval 2100 m to 3500 m. This assemblage clearly must extend beyond the bottom of the hole to an unknown depth. Nevertheless, the 1400 m length of this assemblage is one of the longest such intervals reported anywhere in the world. By comparison, the Toa Baja prehnite–laumontite zone, the longest interval reported for these minerals, has a total length of about 850 m, and a geothermal gradient of between 50°C/km and 70°C/km. The inferred temperature interval over which the prehnite–laumontite association formed at Lopra-1/1A is inferred to be approximately 120°C to 200°C.

Epidote does not occur in any of the samples from the Lopra-1/1A suite. Figure 4 shows that this would require the bottom hole temperature not to exceed *c.* 250°C to 350°C, which appears to be the temperature interval over which epidote is consistently observed, although lower temperature occurrences have been reported, for example at Thorlakshofn and Reykjavik in Iceland and at Toa Baja. As noted above, it is inferred that epidote will not form at temperatures less than *c.* 200°C under conditions of low to moderate Fe^{3+} and Ca^{++} activity. It is thus assumed that the Iceland and Toa Baja occurrences reflect chemical environments that satisfy these conditions.

The Vestmanna-1 hole, which was also part of the drilling programme (Jørgensen 1984, 1997) contains mineral assemblages typical of the shallowest levels of hydrothermal systems and overlap those of the Lopra-1/1A sequence. If these mineral assemblages developed simultaneously, the computed geothermal gradient for the Lopra-1/1A sequence would have to be considered a maximum. However, uncertainty exists regarding whether these mineral sequences for these two drill holes are coeval.

Thermodynamic calculations

A suite of thermodynamic calculations, using the code EQ3/6, was completed to determine the chemical conditions in the fluid phase that would constrain development of the mineral assemblage prehnite–laumontite–quartz–albite–calcite found in the wells. In these calculations, it was assumed that sodium, aluminium, calcium and silica aqueous concentrations are constrained by equilibrium with albite, laumontite, calcite and quartz, respectively. The calculated saturation state of the solution with respect to prehnite was monitored, as temperature and bicarbonate and chloride concentrations were changed. CO_2 partial pressure was allowed to evolve in response to the equilibrium conditions and monitored to assure that it remained within 'real world' bounds. By noting the temperature

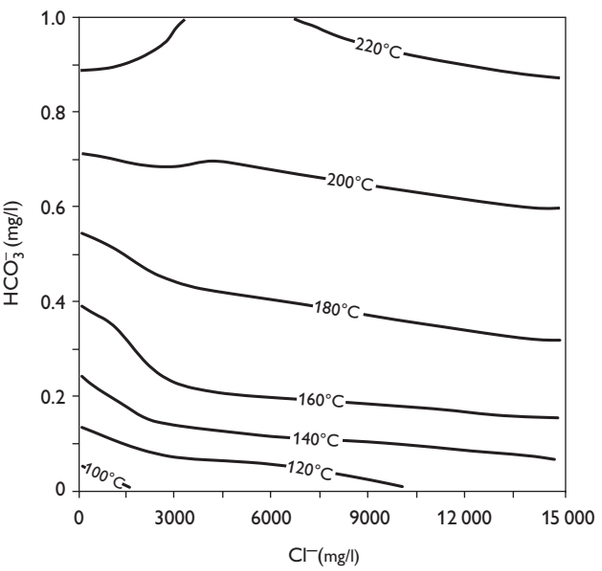

Fig. 6. Calculated lower thermal stability limit of prehnite coexisting with albite–calcite–quartz–laumontite, as a function of HCO_3^- and Cl^- concentrations in the coexisting aqueous phase. Contours on the stability limit surface are labelled in degrees centigrade. The mineral assemblage albite–calcite–quartz–laumontite was used in the calculations because it represents the highest temperature mineral assemblage observed in the bottom of the Lopra-1/1A hole.

and bicarbonate and chloride concentrations at which the solution became saturated in prehnite, it is possible to delineate those conditions that bound the stability field for the prehnite-bearing mineral assemblage.

The results of the calculations are presented in Fig. 6, which shows the contoured temperature surface for the stability of prehnite coexisting with a bicarbonate–chloride solution in equilibrium with laumontite–calcite–quartz–albite. The contours map the minimum temperature required for prehnite stability in this system. It must be emphasised that the exact location of these contours is somewhat imprecisely known, due to uncertainty in the thermodynamic data. The uncertainty in the bicarbonate values is approximately ± 50 mg/l, based on interpolations between simulations. These results show that prehnite stability is only slightly sensitive to the solution salinity (as indicated by the effect of variation in the chloride ion, Cl^-), but is very sensitive to the solution carbonate/bicarbonate concentration. This behaviour reflects the strong coupling between these variables and Ca speciation and pH. The more concentrated the solution in terms of carbonate/bicarbonate, the higher the temperature necessary to achieve prehnite stability. These calculations suggest that the wide range of prehnite thermal stability observed in natural systems (Figs 2, 5) is due, at least in part, to differences in fluid composition from one location to another. This probably is true for other minerals in this calc–silicate suite as well. As documented by Rose & Bird (1987), the redox state and iron content of the fluid will also be an important variable in controlling prehnite stability, due to the effect of Fe^{3+} substitution for Al in the prehnite structure.

Salinities determined from a preliminary fluid inclusion study of the Lopra-1/1A samples (Konnerup-Madsen 1998) gave Cl^- concentrations of between 0.167 and 1.49 equivalent weight per cent NaCl, which is approximately 1000 to 9000 mg/l Cl^-. The analytical bicarbonate ion concentrations with this salinity in natural solutions in hydrothermal systems and at these temperatures and pressures are usually in the range of 200 to 800 mg/l (see compilations and discussions in Roedder 1972; Ellis & Mahon 1977; Arnorsson *et al.* 1983; Fournier 1985) although the actual HCO_3^- concentrations in the reservoirs will be lower than this value and be controlled by CO_2 fugacity. This implies (Fig. 6) that the mineral association prehnite–laumontite–calcite–quartz formed at temperatures within the range of approximately 140°C to 205°C. This temperature interval is contained within the range of prehnite stability noted in other hydrothermal systems (see Figs 2, 5) and is thus consistent with natural occurrences of this assemblage. It is also broadly consistent with the inference from phase relationships described above, in which it is suggested that this assemblage spans the temperature interval of approximately 120°C to 200°C.

Discussion and conclusions

Secondary mineral assemblages documented for the basalts recovered from the Lopra-1/1A well are similar to those reported from other hydrothermal systems. Both the specific mineral occurrences and the relative sequence of mineral stabilities define a systematic distribution that records increasing temperature with depth. The absolute length of individual mineral zones, however, is greater than at other well-documented sites, and suggests that the geothermal gradient at the time of mineral development was low. The mineral associations, complemented by thermodynamic calculations of fluid-rock equilibrium relationships, suggest that the temperature at the bottom of the well did not exceed 200°C, implying a *maximum* thermal gradient of 50°C/km (assuming a surface temperature in the range of 10 to 25°C). This gradient was constructed based on the assumption that the mineral zones are approximately horizontal. There is currently no structural data available to suggest this assumption is far from accurate, but it remains to be established conclusively. Furthermore, it is also assumed that the total stratigraphic thickness at the time of mineral development did not greatly exceed that exposed and inferred today. This assumption is reasonable, based on the correlations established by Larsen *et al.* (1999) between the East Greenland volcanic complex and the Faroe Islands. The correlations indicate that the current thickness of basalts in the Faroe Islands is probably close to that which was originally erupted.

It has previously been suggested that mineral development may have occurred in several discrete episodes (Jørgensen 1984, 1997). Such an interpretation makes more complex the sequence and timing of mineral growth and may change the absolute depth intervals over which specific mineral associations formed within a given time period. This, in turn, would require reconsideration of the temperature history since such an observation could result only in shorter absolute depth intervals for each mineral development period. In this scenario, the currently observed distribution of minerals would represent the sum of the depth intervals over which an individual mineral formed at different time periods, assuming that no single episode of mineral development obliterated evidence of previous distributions of secondary mineral development. Nevertheless, the conclusion that the bottom hole tem-

perature did not exceed 200°C would still be valid, since that is based on the mineral association calcite–laumontite–prehnite–quartz, the temperature limit of which is constrained by laumontite and prehnite thermal stability and fluid composition effects.

Comparison of the derived geothermal gradient in the Faroes with those reported for the Atlantic margin region north of the United Kingdom and in East Greenland demonstrates a striking consistency that constrains evolution of the geothermal history in this region. Green *et al.* (1999) used fission track data from apatites as well as vitrinite reflectance data from a series of wells in the eastern North Atlantic Province to determine palaeogeothermal gradients. They reported geothermal gradients of between 35°C/km and 90°C/km, with the vast majority of the region falling within the lower portion of the range. Neuhoff *et al.* (1997) concluded that the zeolite facies metamorphism that affected East Greenland flood basalts during initial opening of the northern North Atlantic resulted from recrystallisation associated with a geothermal gradient of 40 ± 5°C/km. The regional heat flow they derived from this conclusion is consistent with that reported from a study of metamorphic recrystallisation (Manning *et al.* 1993). All of these values effectively bracket the inferred geothermal gradient in the Faroe Islands and argue for early development of relatively low geothermal gradients that persisted for some time in these regions. These results, and those of Larsen *et al.* (1999), provide conceptual constraints on models of the thermal evolution of this part of the northern North Atlantic province during early continental separation and basin development and argue for regions of low geothermal gradients that were not overprinted by later high heat-flow periods.

As a word of caution, it should be noted that these conclusions are based on the simplifying assumption that linear geothermal gradients existed during mineral growth in this region. There is substantial evidence in geothermal systems, however, that complex geothermal gradients commonly develop, such that temperature reversals or near isothermal conditions may develop in response to the local thermal–hydrological regime, particularly in environments dominated by convection-driven fluid flow. Although such features usually develop in regions of high heat flow and are not characteristic of environments such as the Faroe Islands region where heat flow is inferred to be low, evidence is currently inadequate to rule out this possibility conclusively. To evaluate the extent to which such behaviour occurred in the Faroe Islands volcanic province, a more detailed examination of mineral composition characteristics and distributions would be required, coupled with a more detailed modelling effort.

Acknowledgements

Regin Waagstein kindly provided timely access to thin sections, mineral composition data and mineral distribution data, as well as informative discussions. His assistance greatly aided this effort. Extensive comments from Dennis Bird and Bruce Christenson led to significant improvements in earlier versions of the manuscript, and are gratefully acknowledged. The editorial wisdom of James A. Chalmers significantly improved the presentation and style of this paper.

References

Arnorsson, S., Gunnlaugsson, E. & Svavarsson, H. 1983: The chemistry of geothermal waters in Iceland. II. Mineral equilibria and independent variables controlling water compositions. Geochimica et Cosmochimica Acta **47**, 547–566.

Bevins, R.E., Rowbotham, G. & Robinson D. 1991: Zeolite to prehnite–pumpellyite facies metamorphism of the late Proterozoic Zig-Zag Dal basalt formation, eastern North Greenland. Lithos **27**, 155–165.

Bird, D., Schiffman, P., Elders, W.A., Williams, A.E. & McDowell, S.D. 1984: Calc–silicate mineralization in active geothermal systems. Economic Geology **79**, 671–695.

Boles, J.R. 1981: Zeolites in low grade metamorphic rocks. In: Mumpton, F.A. (ed.): Mineralogy and geology of zeolites. Mineralogical Society of America Reviews in Mineralogy **4**, 103–135.

Cho, M. 1991: Zeolite to prehnite–pumpellyite facies metamorphism in the Toa Baja drill hole, Puerto Rico. Geophysical Research Letters **18**, 525–528.

Ellis, A.J. & Mahon, W.A.J. 1977: Chemistry and geothermal systems, 392 pp. New York: Academic Press.

Evarts, R.C. & Schiffman, P. 1983: Submarine hydrothermal metamorphism of the Del Puerto ophiolite, California. American Journal of Science **283**, 289–340.

Fournier, R.O. 1985: Continental scientific drilling to investigate brine evolution and fluid circulation in active hydrothermal systems. In: Raleigh, C.B. (ed.): Observation of the continental crust through drilling I, 98–122. Berlin: Springer-Verlag.

Frey, M., de Capitani, C. & Liou, J.G. 1991: A new petrogenetic grid for low-grade metabasites. Journal of Metamorphic Geology **9**, 497–509.

Fridriksson T., Neuhoof, P.S., Arnorsson, S. & Bird, D.K. 2001: Geological constraints on the thermodynamic properties of the stilbite–stellerite solid solution in low-grade metabasalts. Geochimica et Cosmochimica Acta **65**, 3993–4008.

Glassley, W. 1974: A model for phase equilibria in the prehnite–pumpellyite facies. Contributions to Mineralogy and Petrology **43**, 317–332.

Green, P.F., Duddy, I.R., Hegarty, K.A. & Bray, R.J. 1999: Early

Tertiary heat flow along the UK Atlantic margin and adjacent areas. In: Fleet, A.J. & Boldy, S.A.R. (eds): Petroleum geology of Northwest Europe, Proceedings of the 5th Conference, 349–357. London: Geological Society.

Hedenquist, J.W. 1990: The thermal and geochemical structure of the Broadlands–Ohaaki geothermal system, New Zealand. Geothermics **19**, 151–185.

Jørgensen, O. 1984: Zeolite zones in the basaltic lavas of the Faeroe Islands. In: Berthelsen, O., Noe-Nygaard, A. & Rasmussen, J. (eds): The Deep Drilling Project 1980–1981 in the Faeroe Islands. Annales Societatis Scientiarum Faroensis. Supplementum **9**, 71–91.

Jørgensen, O. 1997: Zeolites and other secondary minerals in cavities and veins, Lopra-1/1A well, Faroe Islands, 1996, 8 pp. + plates. Unpublished report, Technical studies prepared for Dansk Olie og Gasproduktion A/S, Copenhagen, Denmark (in archives of Geological Survey of Denmark and Greenland, GEUS Report File 26129).

Konnerup-Madsen, J. 1998: A preliminary examination of fluid inclusions in vug and fracture-filling quartz and calcite from Lopra-1/1a, Faroe Islands, 5 pp. Unpublished report, Geological Survey of Denmark and Greenland, Copenhagen.

Kristmannsdóttir, H. & Tomassón, J. 1976: Zeolite zones in geothermal areas in Iceland. In: Sand, L.B. & Mumpton, F.A. (eds): Natural zeolites; occurrence, properties, use, 277–284. Oxford: Pergamon Press.

Larsen, L.M., Waagstein, R., Pedersen, A.K. & Storey, M. 1999: Trans-Atlantic correlation of the Palaeogene volcanic successions in the Faeroe Islands and East Greenland. Journal of the Geological Society (London) **156**, 1081–1095.

Liou, J.G. 1971: Synthesis and stability relations of prehnite, $Ca_2Al_2Si_3O_{10}(OH)_2$. American Mineralogist **56**, 507–531.

Manning, C.E., Ingebritsen, S.E. & Bird, D.K. 1993: Missing mineral zones in contact metamorphosed basalts. American Journal of Science **293**, 894–938.

Neuhoff, P.S. & Bird, D.K. 2001: Partial dehydration of laumontite; thermodynamic constraints and petrogenetic implications. Mineralogical Magazine **65**, 59–70.

Neuhoff, P.S., Watt, W.S., Bird, D.K. & Pedersen, A.K. 1997: Timing and structural relations of regional zeolite zones in basalts of the East Greenland continental margin. Geology **25**, 803–806.

Neuhoff, P.S., Kroeker, S., Du, L.S., Fridriksson, T. & Stebbins, J.F. 2002: Order/disorder in natrolite group zeolites: a ^{29}Si and ^{27}Al MAS NMR study. American Mineralogist **87**, 1307–1320.

Neuhoff, P.S., Stebbins, J.F. & Bird, D.K. 2003: Si-Al disorder and solid solutions in analcime, chabazite, and wairakite. American Mineralogist **88**, 410–423.

Neuhoff, P.S., Hovis, G.L., Balassone, G. & Stebbins, J.F. 2004: Thermodynamic properties of analcime solid solutions. American Journal of Science **304**, 21–66.

Roedder, E. 1972: Composition of fluid inclusions. In: Data of geochemistry. U.S. Geological Survey Professional Paper **400-JJ**, 164 pp.

Rose, N.M. & Bird, D.K. 1987: Prehnite-epidote phase relations in the Nordre Aputiteq and Kruuse Fjord layered gabbros, East Greenland. Journal of Petrology **28**, 1193–1218.

Seki, Y., Onuki, H., Okumura, K. & Takashima, I. 1969: Zeolite distribution in the Katayama geothermal area of Japan. Japanese Journal of Geology and Geography **40**, 63–79.

Steiner, A. 1977: The Wairakei geothermal area, North Island, New Zealand: its subsurface geology and hydrothermal rock alteration. New Zealand Geological Survey Bulletin **90**, 136 pp.

Surdam, R.C. 1973: Low-grade metamorphism of tuffaceous rocks in the Karmutsen Group, Vancouver Island, British Columbia. Geological Society of America Bulletin **84**, 1911–1922.

Varna, C.L. 1989: Mineral reactions and controls on zeolite-facies alteration in sandstones of the Central Transantarctic Mountains, Antarctica. Journal of Sedimentary Petrology **59**, 688–703.

Waagstein, R., Guise, P. & Rex, D. 2002: K/Ar and 39Ar/40Ar whole-rock dating of zeolite facies metamorphosed flood basalts: the upper Paleocene basalts of the Faroe Islands. In: Jolley, D.W. & Bell, B.R. (eds): The North Atlantic Igneous Province: stratigraphy, tectonic, volcanic and magmatic processes. Geological Society Special Publication (London) **197**, 219–252.

Wolery, T.J. & Daveler, S.A. 1992: EQ6, A computer program for reaction path modeling of aqueous geochemical systems: theoretical manual, user's guide, and related documentation. Lawrence Livermore National Laboratory UCRL-MA-110662 Part IV, 338 pp.

Manuscipt received 22 December 1999; revision accepted 26 May 2005.

A reconnaissance study of fluid inclusions in fracture-filling quartz and calcite from the Lopra-1/1A well, Faroe Islands

Jens Konnerup-Madsen

Fracture-filling calcite and quartz from the Lopra-1/1A well (at 2380 m and 3543 m depth) contains both aqueous low-salinity fluid inclusions and hydrocarbon-dominated fluid inclusions. Microthermometry indicates that the aqueous fluids contain 0.2 to 1.4 equivalent weight% NaCl and occasionally contain traces of hydrocarbons. Homogenisation to liquid occurred between 90°C and 150°C. Modelling based on these fluid inclusion observations indicates that during burial the basaltic section was subjected to temperatures of 160°C and 170°C, occasional pressures of 600–700 bars and the simultaneous percolation of aqueous and hydrocarbon fluids. These fluid conditions may also be relevant to the formation of zeolite observed in the Lopra-1/1A well.

Keywords: Basalts, Faroe Islands, fluid inclusions, hydrocarbons, veins, zeolites

Geological Institute, University of Copenhagen, Øster Voldgade 10, DK-1350 Copenhagen K., Denmark.
E-mail: *jenskm@geol.ku.dk*

Fluid inclusions in cements or minerals filling vugs and fractures in buried sedimentary and volcanic rocks may provide important information on the chemical and physical nature and origin of mineral-precipitating fluids, on the potential interplay between migrating hydrocarbon and aqueous fluids, and on the temperatures and pressures of precipitation (e.g. Bodnar 1990; Jensenius & Burruss 1990). A reconnaissance study was undertaken of fluid inclusions in vug- and fracture-filling quartz and calcite from samples taken from the basalts penetrated by Lopra-1/1A. The two samples studied are from core 1 (2380 m) and sidewall core 1 (3543 m). The fluid inclusions were examined by ordinary microscopy, fluorescence microscopy and with a Chaixmeca heating and freezing stage.

Types and setting of fluid inclusions in selected samples

The samples were selected by examining about 40 thin sections taken between 2204 m and 3543 m depth in the Lopra-1/1A well. Only two samples, from 2380 m and 3543 m depth, were found to contain fracture-filling quartz and calcite with fluid inclusions suitable for further study.

Sample 2380 m (Lopra-1, core 1) is a sparsely plagioclase-glomerophyric olivine-clinopyroxene basalt with almost complete alteration of plagioclase and olivine. The quartz and calcite studied occur in mm-wide veins. The veins are rimmed by chlorite, calcite and quartz that appear to have been precipitated contemporaneously. According to Jørgensen (2006, this volume) the zeolites characterising this level in the core are laumontite, prehnite and pumpellyite.

Sample 3543 m (Lopra-1A, sidewall core 1) is a near-aphyric lapilli-tuff with extensively altered plagioclase, olivine and clinopyroxene phenocrysts in a cryptocrystalline groundmass. The irregular veins contain laumontite, prehnite, calcite and rare quartz. The veins are rimmed by chlorite. Again, calcite and quartz appear to have been precipitated contemporaneously, although quartz precipitation might have been slightly later.

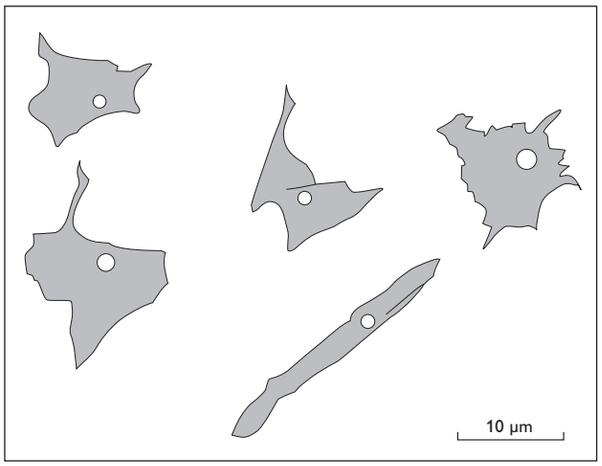

Fig. 1. Examples of typical morphologies of aqueous liquid-vapour fluid inclusions in quartz from core 1 (2380 m) from Lopra-1/1A.

Types of fluid inclusions in quartz and calcite

Two types of fluid inclusions were observed using fluorescence and ordinary light microscopy: (1) aqueous two-phase (liquid-vapour) inclusions with about 5 vol.% vapour at room temperature, and (2) one or two-phase hydrocarbon inclusions with fluorescence emission colours that vary from orange-yellow to green. With ordinary light microscopy it is difficult to distinguish between the two-phase liquid-vapour hydrocarbon and aqueous inclusions, although the latter seem to be characterised by a (perhaps) slightly lower vol.% vapour than the former. No clear relative chronology between the two fluid inclusion types could be established.

Examples of typical morphologies and phase proportions of fluid inclusions observed in quartz are shown in Fig. 1.

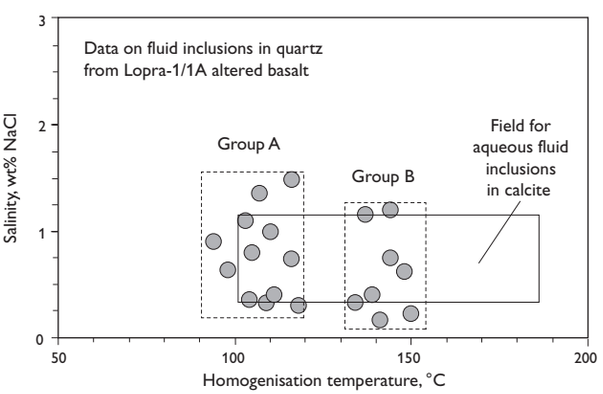

Fig. 2. Salinity versus liquid homogenisation temperatures of aqueous inclusions in quartz from Lopra-1/1A.

In general, the fluid inclusions are characterised by immature morphologies and occur in irregular groupings or in curved internal planar arrangements, suggesting periods for their entrapment which do not markedly postdate the growth of the host mineral. The liquid-vapour ratio in individual groupings varied slightly, most probably and mainly as a result of necking down of the inclusions after entrapment, because liquid-only inclusions could occasionally be observed together with the aqueous two-phase liquid-vapour inclusions. All inclusions indicative of having been influenced by necking down were avoided during the heating and freezing stage work.

Microthermometry results on aqueous fluid inclusions

The results of microthermometry of fluid inclusions in quartz and calcite are summarised in Fig. 2.

Fluid inclusions in quartz

Incipient melting of ice was observed at temperatures around –32°C, indicating the presence of additional ions such as Ca^{2+}, Mg^{2+} and/or Fe^{2+} in solution rather than chlorides of Na^{+} and/or K^{+} (Konnerup-Madsen 1979). Final melting temperatures were observed in the range –0.1°C to –0.9°C, corresponding to salinities from 0.167 to 1.49 equivalent weight% NaCl, respectively (average: 0.62 equivalent weight% NaCl) (Bodnar *et al.* 1989), but with no clear difference between the two samples. Temperatures of homogenisation occurred between 94°C and 150°C and bimodality in temperature is suggested from the data (see Fig. 2, groups A and B). Group A and group B inclusions gave average homogenisation temperatures of 108°C and 141°C, respectively.

Group B inclusions in quartz showed in three cases clear indications (ragged outline of meniscus between vapour and liquid) of the formation of a clathrate hydrate after initial ice melting, indicating the presence of trace amounts of volatiles such as hydrocarbons in the entrapped group B fluids. However, although no temperature of dissolution of the hydrate could be obtained and hence the identity of the volatile component could not be established, its formation suggests that the higher temperatures of homogenisation obtained for group B inclusions may reflect trace concentrations of hydrocarbons in the vapour phase of these inclusions.

Fluid inclusions in calcite

Only very few measurements were made on inclusions in calcite, as most inclusions occurred along well-defined healed fracture-planes so are secondary in origin. Final melting temperatures varied between –0.2°C and –0.7°C, corresponding to salinities of 0.33 to 1.16 equivalent weight% NaCl. Homogenisation temperatures varied from 101°C to 186°C (Fig. 2). However, the higher homogenisation temperatures might conceivably reflect partial decrepitation (stretching) of the inclusions during heating (e.g. Bodnar & Bethke 1984).

Two-phase (liquid-vapour) hydrocarbon inclusions were observed in fluorescence microscopy in both calcite and quartz. The abundance of hydrocarbon inclusions appears to be relatively higher in calcite and only very few were observed in quartz. The emission colours, from orange-yellow to green, may be interpreted roughly in terms of compositions corresponding to API gravities of 20–35 (Lang & Gelfand 1985). No successful heating and cooling runs were, however, obtained on the hydrocarbon inclusions in the two samples.

Interpretation of fluid inclusion data

An interpretation in terms of pressures and temperatures for entrapment of the fluid inclusions in quartz is shown in Fig. 3.

Isochores corresponding to group A and B inclusions (Brown 1989) in quartz are shown in Fig. 3, assuming them to be pure aqueous fluids with salinities as indicated by the final ice melting temperatures (Fig. 2). No indications of the entrapment of boiling aqueous fluids were observed during this study and the homogenisation temperatures for the fluid inclusions observed are thus considered to be minimum temperatures of fluid entrapment and host mineral formation. A comparison with geothermal gradients of 20°C/100 bars and 20°C/226 bars that are considered relevant for Lopra-1/1A and that reflect hydrostatic and lithostatic conditions, respectively, has been made in Fig. 3. If hydrostatic conditions prevailed, group A inclusions would indicate entrapment at around 140°C at pressures of around 600 bars.

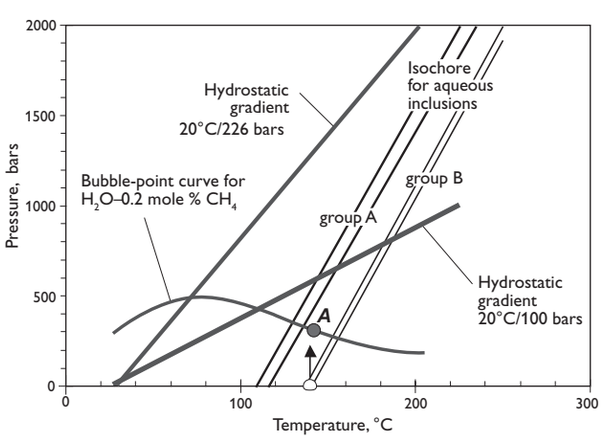

Fig. 3. Pressure-temperature diagram with isochores for groups A and B inclusions in quartz from Lopra-1/1A. The open and filled circles show pressure and temperature at homogenisation for pure aqueous and aqueous-0.2 mole%CH_4 fluids in group B inclusions, respectively. Bubble-point curve from Hanor (1980). See text for further comments.

Microthermometry indicated that Group B inclusions may contain traces of hydrocarbons and the isochores shown in Fig. 3 are therefore not strictly applicable because they assume an aqueous-only composition. As trace concentrations of hydrocarbons are present in group B inclusions, pressures at homogenisation will be considerably higher than indicated by the isochores drawn in Fig. 3. The presence of only a few parts per thousand methane in solution would shift homogenisation pressures to values of 400–600 bars at the observed temperatures of homogenisation (Hanor 1980). The actual isochoric path for group B inclusions should therefore be shifted to a setting essentially parallel to that shown but starting at the bubble-point curve for the actual aqueous-hydrocarbon system at around 400 bars (Fig. 3, point A). If this interpretation is valid, both groups of inclusions in quartz indicate minimum entrapment of fluids slightly different in composition at conditions of about 400 bars and 140°C. Assuming hydrostatic conditions, probable entrapment of both group A and B aqueous fluids low in salts (average 0.61 equivalent weight% NaCl) and containing occasional traces of hydrocarbons occurred at around 600–700 bars at temperatures of 160°C to 170°C. However, more data would be needed to substantiate this conclusion.

Concluding remarks

Although it is of a reconnaissance nature, the present study of fluid inclusions in fracture-filling quartz and calcite indicates that the basaltic sections represented by the samples examined were subjected to temperatures of 160°C to 170°C and pressures of 600–700 bars at stages during their burial. During these burial conditions, precipitation of quartz and calcite in fractures (and vugs?) occurred in the presence of low-salinity aqueous fluids containing occasional traces of hydrocarbons. Similar P–T-fluid-char-

acteristics may also be of relevance to the formation of e.g. zeolites in these rocks. Although no clear evidence for the simultaneous existence and migration of hydrocarbon and aqueous fluids was observed, such simultaneity is suggested by the occasional presence of hydrocarbons in the entrapped aqueous fluids and the hydrocarbon-dominated inclusions observed especially in calcite.

References

Bodnar, R.J. 1990: Petroleum migration in the Miocene Monterey Formation, California, USA: constraints from fluid-inclusion studies. Mineralogical Magazine **54**, 295–304.

Bodnar, R.J. & Bethke, P.M. 1984: Systematic stretching of fluid inclusions. Fluorite and sphalerite at one atmosphere confining pressure. Economic Geology **79**, 141–146.

Bodnar, R.J., Sterner, S.M. & Hall, D.L. 1989: SALTY: a FORTRAN program to calculate compositions of fluid inclusions in the system NaCl-KCl-H_2O. Computers & Geosciences **15**, 19–41.

Brown, P.E. 1989: FLINCOR: a microcomputer program for the reduction and investigation of fluid inclusion data. American Mineralogist **74**, 1390–1393.

Hanor, J.S. 1980: Dissolved methane in sedimentary brines: potential effect on the PVT properties of fluid inclusions. Economic Geology **75**, 603–617.

Jensenius, J. & Burruss, R.C. 1990: Hydrocarbon-water interactions during brine migration: Evidence from the composition of hydrocarbon inclusions in calcite from Danish North Sea oil fields. Geochemica Cosmochemica Acta **54**, 705–713.

Jørgensen, O. 2006: The regional distribution of zeolites in the basalts of the Faroe Islands and the significance of zeolites as palaeotemperature indicators. Geological Survey of Denmark and Greenland Bulletin **9**, 123–156 (this volume).

Konnerup-Madsen, J. 1979: Fluid inclusions in quartz from deep-seated granitic intrusions, south Norway. Lithos **12**, 13–23.

Lang, W.H. & Gelfand, J.C. 1985: The evaluation of shallow potential in a deep field wildcat. Log Analyst **26**, 13–22.

Manuscipt received 15 December 1999; revision accepted 29 June 2001.

The regional distribution of zeolites in the basalts of the Faroe Islands and the significance of zeolites as palaeo-temperature indicators

Ole Jørgensen

The first maps of the regional distribution of zeolites in the Palaeogene basalt plateau of the Faroe Islands are presented. The zeolite zones (thomsonite-chabazite, analcite, mesolite, stilbite-heulandite, laumontite) continue below sea level and reach a depth of 2200 m in the Lopra-1/1A well. Below this level, a high temperature zone occurs characterised by prehnite and pumpellyite. The stilbite-heulandite zone is the dominant mineral zone on the northern island, Vágar, the analcite and mesolite zones are the dominant ones on the southern islands of Sandoy and Suðuroy and the thomsonite-chabazite zone is dominant on the two northeastern islands of Viðoy and Borðoy. It is estimated that zeolitisation of the basalts took place at temperatures between about 40°C and 230°C. Palaeogeothermal gradients are estimated to have been 66 ± 9°C/km in the lower basalt formation of the Lopra area of Suðuroy, the southernmost island, 63 ± 8°C/km in the middle basalt formation on the northernmost island of Vágar and 56 ± 7°C/km in the upper basalt formation on the central island of Sandoy.

A linear extrapolation of the gradient from the Lopra area places the palaeosurface of the basalt plateau near to the top of the lower basalt formation. On Vágar, the palaeosurface was somewhere between 1700 m and 2020 m above the lower formation while the palaeosurface on Sandoy was between 1550 m and 1924 m above the base of the upper formation.

The overall distribution of zeolites reflects primarily variations in the maximum depth of burial of the basalt rather than differences in heat flow. The inferred thinning of the middle and upper basalt formation from the central to the southern part of the Faroes is in general agreement with a northerly source area for these basalts, centred around the rift between the Faroes and Greenland. The regional zeolite distribution pattern is affected by local perturbations of the mineral zone boundaries that reflect local differences in the temperature, perhaps related to the circulation of water in the underground. The zonal distribution pattern suggests that these temperature anomalies are in part related to NW–SE-trending eruption fissures or zones of weakness separating the present islands and are subparallel to transfer zones in the Faroe–Shetland Basin. Both the regional and the local distribution of zeolite assemblages are probably a reflection of the basic volcanic-tectonic pattern of the Faroe Islands.

Keywords: Faroe Islands, Palaeogene basalt plateau, zeolite zone, palaeotemperature indicators

O.J., *Scandinavian Asbestos & Mineral Analysis, Kildeskovsvej 62, DK-2820 Gentofte, Denmark.* E-mail: *Oj@oj-sama.dk*

The zeolites of the Faroe Islands have been known for more than 300 years (Debes 1673) although the islands remained nearly unknown to mineralogists until the end of the eighteenth century. Because of increasing interest in mineralogy in the nineteenth century, the Faroe Islands were visited by many naturalists. One of these was Brewster (1825), who proposed the name levyne for a new zeolite species he discovered at Dalsnípa on Sandoy. The first modern description of the distribution of Faroese minerals was published by Currie (1905), who visited the Faroe Islands and described the minerals at 120 localities. Five years later a new description of the Faroese zeolites was presented by Görgey (1910). Interest in the minerals of the Faroe Islands declined during the following 70 years until Betz (1981) visited the islands and reviewed the classic localities. The present author started a literature study to discover, if a system of zeolite zones exists on the Faroe Islands similar to that described by Walker (1960) in East Iceland, but concluded that published descriptions were based on minerals from the same set of localities that were known to be rich in mineral species and where large crystals could be collected. This sampling bias meant that it was not possible to decide if zeolite zones existed on the Faroe Islands, so in 1979 a systematic mapping of the zeolites in the Faroe Islands was initiated by the present author. During the following 20 years, more than 800 localities were visited and about 3000 rock samples were investigated in the field and in the laboratory. The work was extended by studying samples from the Vestmanna-1 and Lopra-1 boreholes drilled in 1980 and 1981, respectively (Jørgensen 1984; Waagstein *et al.* 1984). In 1996, the Lopra-1 borehole was deepened to a total of 3565 m (Lopra-1/1A) and the secondary minerals in the deepened part of the Lopra well were also described by the present author (Jørgensen 1997).

The aim of the present paper is to describe the secondary mineral distribution in the exposed parts of the Faroe Islands and in the Lopra-1/1A and Vestmanna-1 wells. The results of the mapping are used to estimate the palaeogeothermal gradients and the altitudes of the palaeosurfaces at various places in the Faroes basalt succession. The following topics will be discussed: (1) the general conditions for the use of zeolites as palaeotemperature indicators and the statistical distribution of zeolites in a vertical profile, (2) the original thickness of the three basalt formations and the volcanic evolution of the Faroese basalt complex, and (3) the regional distribution of the zeolite zones as a function of the thicknesses of the middle and the upper basalt formations.

Outline of the geology of the Faroe Islands

The Faroe Islands (62°N, 7°W) have a total area of 1400 km^2, an average height of 300 m above sea level and form part of the North Atlantic Brito-Arctic Cenozoic Igneous Province that extends from the British Isles to Greenland. The Faroe Islands consist almost exclusively of flood basalts that were erupted about 59–55 Ma (Waagstein 1988; Larsen *et al.* 1999).

The basalts on the exposed part of the Faroe Islands are divided into a *lower*, a *middle* and an *upper basalt formation*, separated by two horizons termed A and C in Fig. 1 (see also Fig. 4). According to Rasmussen & Noe-Nygaard (1969, 1970) the volcanic evolution of the Faroe Islands may be summarised as follows: Volcanic activity started west of the present islands with the eruption of the *lower basalt formation*. With time the production rate of lava slowed to a temporary standstill. During this quiet period, about 10 m of clay and coal bearing sediments were deposited (the *A-horizon*.). Volcanic activity restarted with an explosive phase, resulting in the deposition of coarse volcanic ash and agglomerates. An effusive phase followed during which the *middle basalt formation* was erupted from

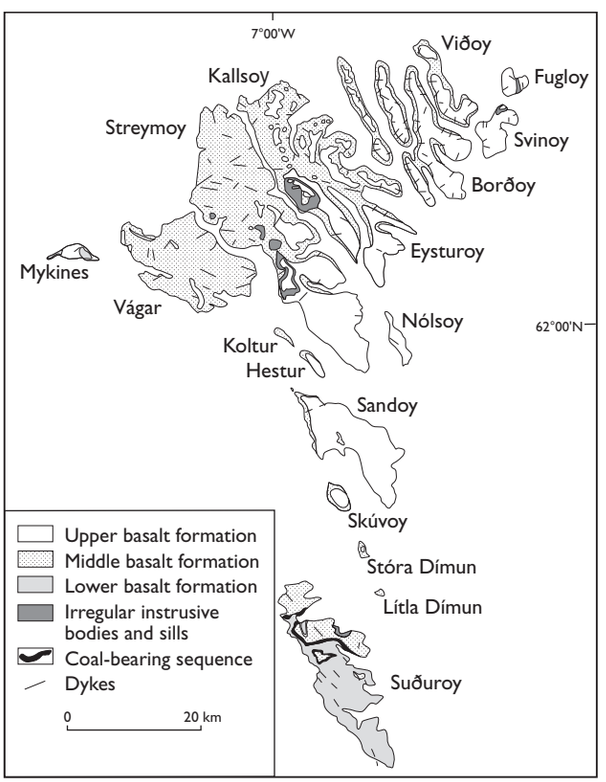

Fig. 1. Geological map of the Faroe Islands. From Rasmussen & Noe-Nygaard (1969).

several vents and small fissures within the present group of islands. Finally, volcanic activity moved farther east, away from the present islands, causing the lava flows of the *upper basalt formation* to transgress the middle basalt formation from the east. The discordant surface between the middle and upper basalt formations is named the *C-horizon*. After the upper basalt formation was formed, the basalt plateau was intruded by dykes and sills. Large sills were intruded near the boundary between middle and upper basalt formations in Streymoy and Eysturoy. Tectonic activity continued long after the volcanism ended until the Faroese basalt pile acquired its present gentle easterly dip.

Methodology

Sampling and mineral identification

Renewal of a large part of the road system of the Faroes just before initiation of the fieldwork made it possible to collect samples in fresh road cuts and new quarries along the roads. After most of the road sites had been examined, the mountains were traversed and samples collected along the old paths between the villages. In addition to the samples collected by the author, the present investigation is based on 500 specimens of Faroese zeolites collected privately by K. Jørgensen and on the collection of Faroese zeolites in the Geological Museum, Copenhagen.

The minerals were identified by their crystal morphology, optical properties, and X-Ray Diffraction (XRD) patterns or by chemical analysis carried out on a scanning electron microscope equipped with an energy dispersive analytical system. The XRD reference patterns were taken from Gottardi & Galli (1985).

Mapping of the mineral zones

Walker (1960, 1970) defined his zeolite zones by seven distinctive amygdale mineral assemblages. Each zone was

Table 1. Abbreviations used for mineral names

An: analcite	Le: levyne
Ap: apophyllite	Me: mesolite: solid
Ca: calcite	Me*: mesolite: hair-like
Ce: celadonite	Mo: mordenite
Ch: chabasite	Na: natrolite
Cl: chlorite	Ok: okemite
Cld: chalcedony	Op: opal
Ed: epidote	Ph: phillipsite
Ep: epistilbite	Pr: prehnite
Ga: garronite	Pu: pumpellyite
Gi: gismondine	Qz: quartz
Gy: gyrolite	Sc: scolecite
Ha: harmotom	Sm: smectites
He: heulandite	St*: stellerite
La: laumontite	

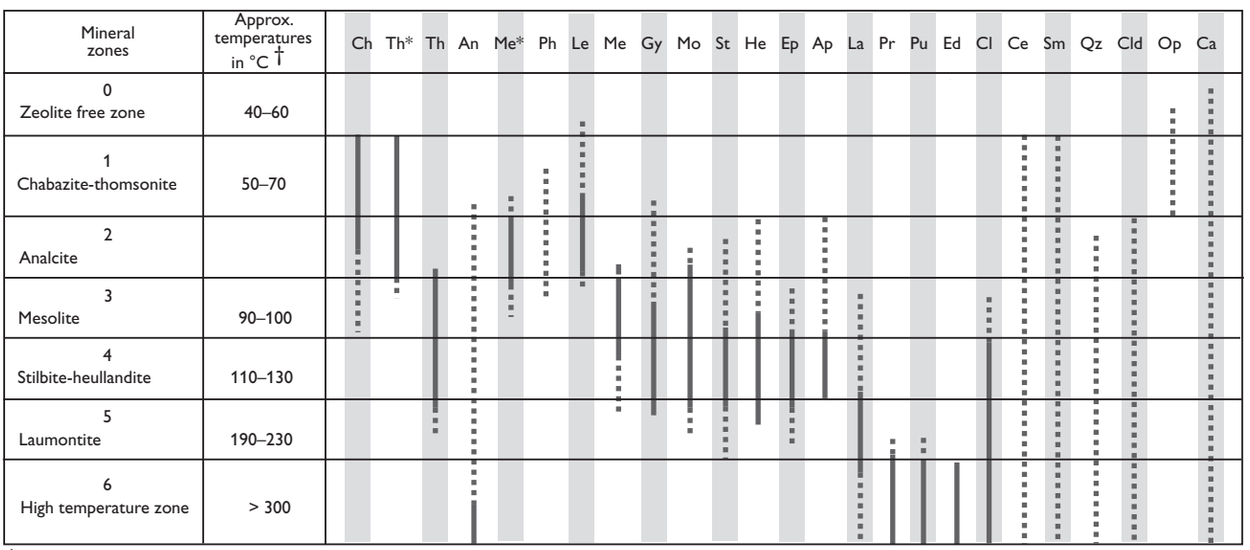

† Source: Kristmannsdóttir & Tómasson (1978), Kristmannsdóttir (1982) and Jakobsson & Moore (1986)

Fig. 2. Mineral temperature scale. The five zeolite zones are defined by the index minerals chabasite + thomsonite, analcite, mesolite, stilbite + heulandite and laumontite. The temperatures are shown at zone boundaries. Abbreviations used for the various minerals are shown in Table 1.

defined by the presence or dominance of certain mineral species, termed index minerals, whose names are used to designate the zones. In addition to the index minerals, other minerals may be present as indicated in Fig. 2. Walker's (1960) original zones are the carbonate, chabazite-thomsonite, analcite, mesolite, laumontite, prehnite and epidote zones. The original mesolite zone was later subdivided into a mesolite and a stilbite-heulandite zone. This extended zone definition was adopted in the present investigation (Fig. 2). The classification of the zeolite zones was normally based on the mineral assemblages of amygdales, and fracture fillings were used only in places without amygdales.

Classification of the mineral assemblages from samples from the Lopra-1/1A and Vestmanna-1 boreholes was originally based on the abundance of the individual index minerals expressed as the weight% of the total mass of index minerals (Jørgensen 1984). In the present investigation, which is based on about 3000 samples, quantitative analysis was carried out only on two selected mineral assemblages, one from the middle and one from the upper basalt formation. The assemblages from most localities consist of a large number of minerals which makes it difficult to estimate the relative abundance of the different minerals. Another complication was the fact that more than one index mineral often occurred at the same locality. The present investigation is therefore based on the *first formed index minerals in the amygdales,* i.e. the minerals that were deposited nearest to the host rock. Where more than one first formed index mineral was present at a locality, the index mineral assumed to have the highest temperature of formation was chosen to map the zones. The mineral zones mapped in this way thus reflect *the maximum temperature of mineralisation*. This method is different from a mapping based on abundance of the minerals, which shows the distribution of the zeolite zones as the result of the main mineralisation. Appendices A and B give the observed paragenesis in the 29 sections and two

Table 2. Relative frequency (in %) of amygdales and mineralised fractures in the exposed part of the Faroe Islands

Mineral	Average	Suðuroy	Sandoy	Vágar	Streymoy	Eysturoy	Borðoy	Viðoy
Zeolites:								
Analcite	*32*	**61**	*16*	*49*	*33*	*35*	*18*	*15*
Chabazite	**67**	**61**	**65**	**71**	**78**	**76**	**62**	**66**
Cowlesite	1	7	0	0	0	2	0	0
Epistilbite	<1	0	0	3	0	0	0	0
Garronite	4	8	0	6	8	8	0	0
Gismondine	4	0	10	0	5	8	3	0
Heulandite	*30*	*51*	**69**	**77**	**60**	**63**	*38*	*38*
Laumontite	11	5	*6*	*29*	*29*	3	5	0
Levyne	*17*	5	*16*	*23*	*20*	*26*	8	*20*
Mesolite	**61**	*56*	**65**	**86**	**63**	**60**	*48*	*50*
Mordenite	8	12	0	14	8	*19*	0	0
Natrolite	4	10	0	9	0	5	3	0
Scolecite	1	2	0	0	0	3	0	0
Stellerite	*45*	*24*	*55*	*26*	*20*	13	6	9
Stilbite	*37*	*37*	10	**74**	*38*	*39*	*33*	*26*
Phillipsite	8	*17*	6	*3*	3	11	10	15
Thomsonite	**64**	*59*	*45*	**60**	**60**	**75**	**73**	**79**
Other minerals:								
Apophyllite	*15*	*12*	13	*29*	*20*	*27*	3	*0*
Calcite	*36*	*37*	*39*	*34*	*43*	*32*	*32*	*32*
Celadonite	*19*	*15*	13	11	*38*	*27*	14	*15*
Chlorite	8	10	3	3	*23*	13	5	
CSH	2	5	0	3	0	8	0	*15*
Gyrolite	12	7	3	14	*28*	*29*	0	*21*
Smectites	*18*	7	3	*36*	*23*	*26*	*16*	
Silica minerals	*19*	*29*	6	14	20	*19*	*25*	41
Visited localities		160	85	148	302	235	52	41

Abundant minerals in ***bold face***, common minerals in *italics* and rare minerals in normal type face. CSH is calcium silicate hydrates. Silica minerals are opal, chalcedony etc.

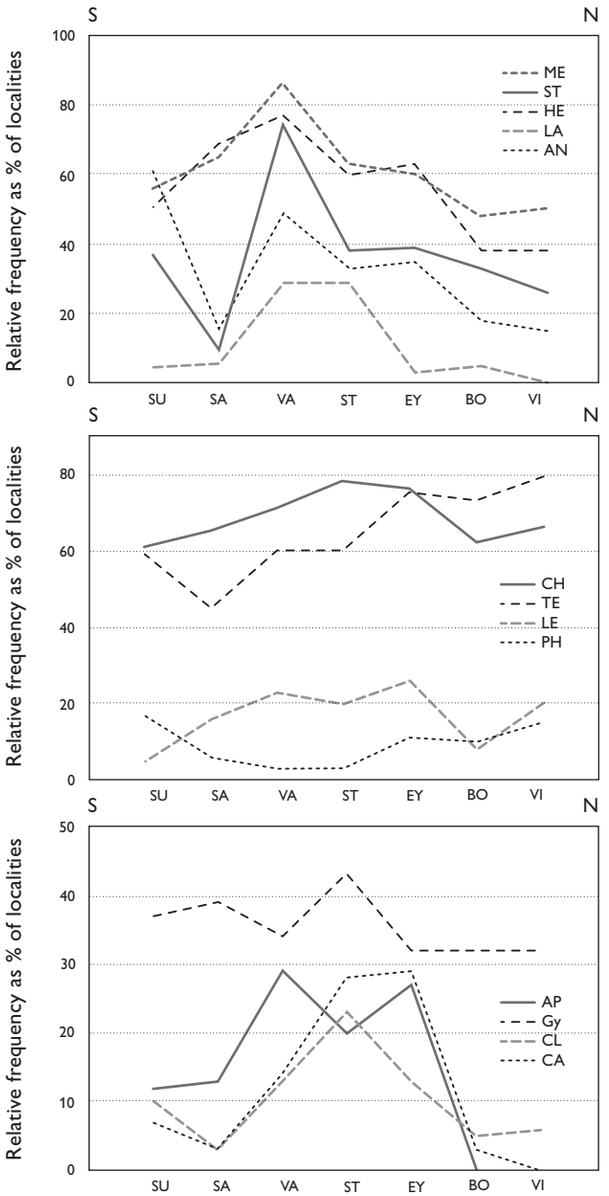

Fig. 3. Variation diagrams of the relative frequency of minerals on Suðuroy (SU), Sandoy (SA), Vágar (VÁ), Streymoy (ST), Eysturoy (EY), Borðoy (BO) and Viðoy (VI). Contractions for zeolite names are listed in Table 1.

wells mapped. The most probable temperature range of deposition of the zeolite zones is indicated in Fig. 2.

The rules of zone classification stated above could not be followed strictly everywhere. In the southern part of Suðuroy, mineralised vesicles are rare and, in this area, the mapping had to be based mainly on mineralised fractures. In the Lopra-1/1A borehole, the study was based on cuttings. They included fragments of amygdales and mineralised fractures, and the first formed index mineral could be determined only when part of the host rock adhered to the sample.

In order to establish a correlation between the zeolite zones and the temperature of formation of the minerals, the vertical distribution of index minerals and temperatures was examined in a number of boreholes in the geothermal areas of Iceland (Kristmannsdóttir & Tómasson 1978; Kristmannsdóttir 1982). The result was the mineral–temperature scale shown in Fig. 2. Examination showed that the temperatures at the boundaries of individual zeolite zones varied from place to place. This is probably caused by the fact that zeolites can be formed within a broad range of temperatures and that variations in the chemical composition of the rock and the hydrothermal solutions can affect the formation temperature of the zeolites (Barth-Wirsching & Höller 1989; Breck 1974). Another problem that makes it difficult to determine accurately the palaeotemperatures at the zone boundaries is the fact that zone boundaries are not well defined lines, a problem that will be discussed below. The temperatures at the boundaries of the zeolite zones are therefore indicated in Fig. 2 at the lowest and highest temperatures that occur at the Icelandic zone boundaries.

As mentioned above, the original classification of the mineral assemblages of the Lopra-1/1A and Vestmanna-1 drillholes was based on the most abundant index zeolite. It was therefore necessary to re-classify the mineral assemblages of the two drillholes according to the method used in the present investigation. This had a rather small effect on the zonation of the Lopra-1/1A drillhole. However, the first formed minerals from the Vestmanna-1 borehole are overgrown by abundant chabazite and thomsonite. Neglecting these later deposits, changes the zonation from a simple chabazite-thomsonite zone to an alternation between the mesolite and stilbite-heulandite zones.

The distribution of minerals, zones and temperatures

Frequency of occurrence of minerals

Table 2 shows the 17 zeolites and 8 associated minerals that were recorded in amygdales and mineralised fractures of the basalt in the islands of Suðuroy, Sandoy, Vágar, Streymoy, Eysturoy, Borðoy and Viðoy. In addition to the minerals listed, prehnite, pumpellyite, native copper and pyrite were found in the Lopra-1/1A borehole. All the zeolites listed in Table 2 have been reported previously from the Faroe Islands with the exception of garronite,

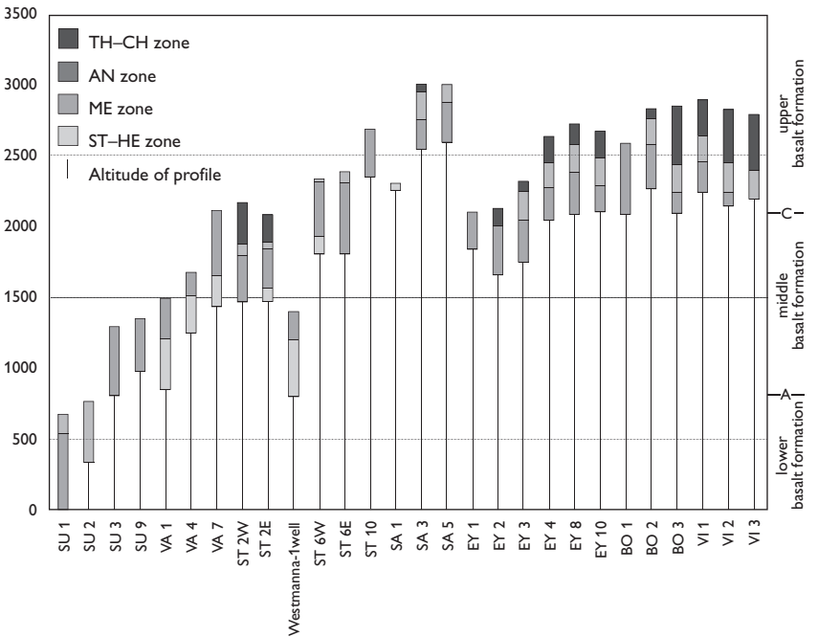

Fig. 4. Stratigraphic location of the zeolite zones in the 28 sections through the exposed part of the Faroe Islands. The data shown here are tabulated in Table 3.

which was found for the first time at several localities during the mapping reported here.

The minerals in Table 2 were divided into three classes: (1) very frequent minerals that occur at 60% or more of the localities; (2) common minerals that occur at between 15% and 60% of the localities; (3) rare minerals that occur at less than 15% of the localities. The frequency of occurrence is given as percentages of localities examined on each island.

From the column named *average* in Table 2, it is seen that chabazite, mesolite and thomsonite are the most frequent secondary minerals within the exposed part of the Faroe Islands, followed by stilbite, stellerite, heulandite, analcite and calcite. Epistilbite and scolecite are rare minerals in the exposed part of the Faroe Islands, but they are common in the Lopra-1/1A well.

Regional distribution of minerals and zones

Fig. 3 shows how the relative frequency of a number of index minerals and associated minerals varies from island to island. For most of the minerals, the relative frequency decreases from south to north and from west to east, but for the minerals of the analcite and the chabazite-thomsonite zone, the relative frequency increases in the direction of Viðoy (Fig. 1). The variation in relative frequency of minerals reflects the regional shift in the distribution of mineral zones. The analcite and mesolite zones are the dominant mineral zones on Suðuroy. From Sandoy to Vágar, the analcite zone is gradually replaced by a stilbite-heulandite zone that becomes widespread on Vágar. On Streymoy and Eysturoy the stilbite-heulandite zone has a less widespread distribution, so that the stilbite-heulandite and the mesolite zones are of equal importance. The areal extent of the mesolite and stilbite-heulandite zones is further reduced on Borðoy and Viðoy, so the chabazite-thomsonite zone becomes the major one on these two islands.

Description of mineral assemblages and zones

Figures 5–11 show the geographic distribution of the mineral zones on the islands Suðuroy, Sandoy, Vágar, Streymoy, Borðoy and Viðoy. In order to show the vertical distribution of the mineral zones, 28 local sections were constructed that are also shown on Figs 5–11. The sections have been arranged such that it is possible to follow the changes in the mineral zones both geographically and stratigraphically (Fig. 4). The data on which the sections are based are shown in Appendices A and B, and Table 3 gives the thickness of each zone.

In contrast to the profiles drilled by the Lopra-1/1A and Vestmanna-1 boreholes, the profiles from the exposed part of the Faroes have been constructed from observations along each section line, so the sections do not represent a single vertical profile through the lava pile.

Table 3. Stratigraphic position and thickness of mineral zones (see Fig. 4)

Section	Base level	ST-HE zone	ME zone†	AN zone	CH–TH zone
	Stratigraphic height in m*	Thickness in metres	Thickness in metres	Thickness in metres	Thickness in metres
SU1+LO	0	_	530†	180	_
SU2	330	_	–	430	_
SU5	798	_	480	_	_
SU9	970	_	373	_	_
VÁ1	842	350	300	_	_
VÁ4	1241	250	180	_	_
VÁ7	1424	219	463	_	_
ST2W	1461	_	325	82	293
ST2E	1461	100	272	50	200
Vestmanna-1	795	400	200	_	_
ST6W	1799	125	385	20	_
ST6E	1799	_	500	83	_
ST10	2344	_	340	_	_
SA1	2252	50	–	_	_
SA3	2545	_	200	200	46
SA5	2594	_	280	116	_
EY1	1831	166	270	_	_
EY2	1650	50	350	125	_
EY3	1745	_	300	195	75
EY4	2039	_	230	170	193
EY8	2080	_	300	190	149
EY10	2098	_	180	200	187
BO1	2084	_	503	_	_
BO2	2263	_	310	182	70
BO3	2091	_	150	190	415
VI1	2237	_	100	190	251
VI2	2140	_	_	208	375
VI3	2188	_		200	400

* Stratigraphic height within the exposed lava pile of the Faroe Islands.
† The mesolite zone is composed of the upper 330 m of the Lopra-1 mesolite zone plus the 200 m thick mesolite zone of section SU1.

Suðuroy (Fig. 5)

The distribution of the secondary minerals on Suðuroy is remarkably heterogeneous, a feature noted by Currie (1905). To the north of section SU2 that extends across the island from Fámjin to Holmssund, nearly all vesicles and fractures of the basalts are mineralised, but to the south of the section, amygdales and mineralised fractures are rare.

The boundary (section SU2) between the two parts of Suðuroy forms a transition zone in which the scattered vesicles are partly mineralised by an analcite assemblage composed of hair-like mesolite, thomsonite, analcite, chabazite, calcite, quartz and chalcedony. This mineral assemblage is found all along section SU2, which means that no relationship exists between the secondary minerals and their stratigraphic position within the lava pile.

To the north of section SU2, the number of mineral species and the degree of mineralisation increases gradually northwards and the area just north of Trongisvágsfjørður is in the mesolite zone. Despite apparent regularity, the northern part of Suðuroy is a mosaic of small areas in which the mineral assemblages vary from place to place. The largest area of this kind occurs around the summit of Gluggarnir (443 m). At this locality, nearly all minerals listed in Table 2 are present.

The southern part of the island is partly devoid of zeolites. The most abundant minerals are quartz, calcite and chalcedony, while mesolite, thomsonite, chabazite, analcite, heulandite and stilbite are less frequent. The mode of mineralisation is also different on the two parts of the island. On the northern part of Suðuroy, mineralised fractures and vesicles occur in equal numbers, whereas mineralised fractures are more common than amygdales on the southern part of the island, in spite of the fact that empty vesicles occur at many localities. Because of this, section SU1 is based mainly on mineralised fractures.

Despite the weak amount of mineralisation on south-

Fig. 5. Distribution of zeolite zones on Suðuroy and on sections SU1, SU2, SU5, SU9 and in the Lopra-1/1A borehole.

Fig. 6. Distribution of zeolite zones on Sandoy and on sections SA1, SA3 and SA5. The arrow indicates the apparent dip of the zeolite zones on section SA3.

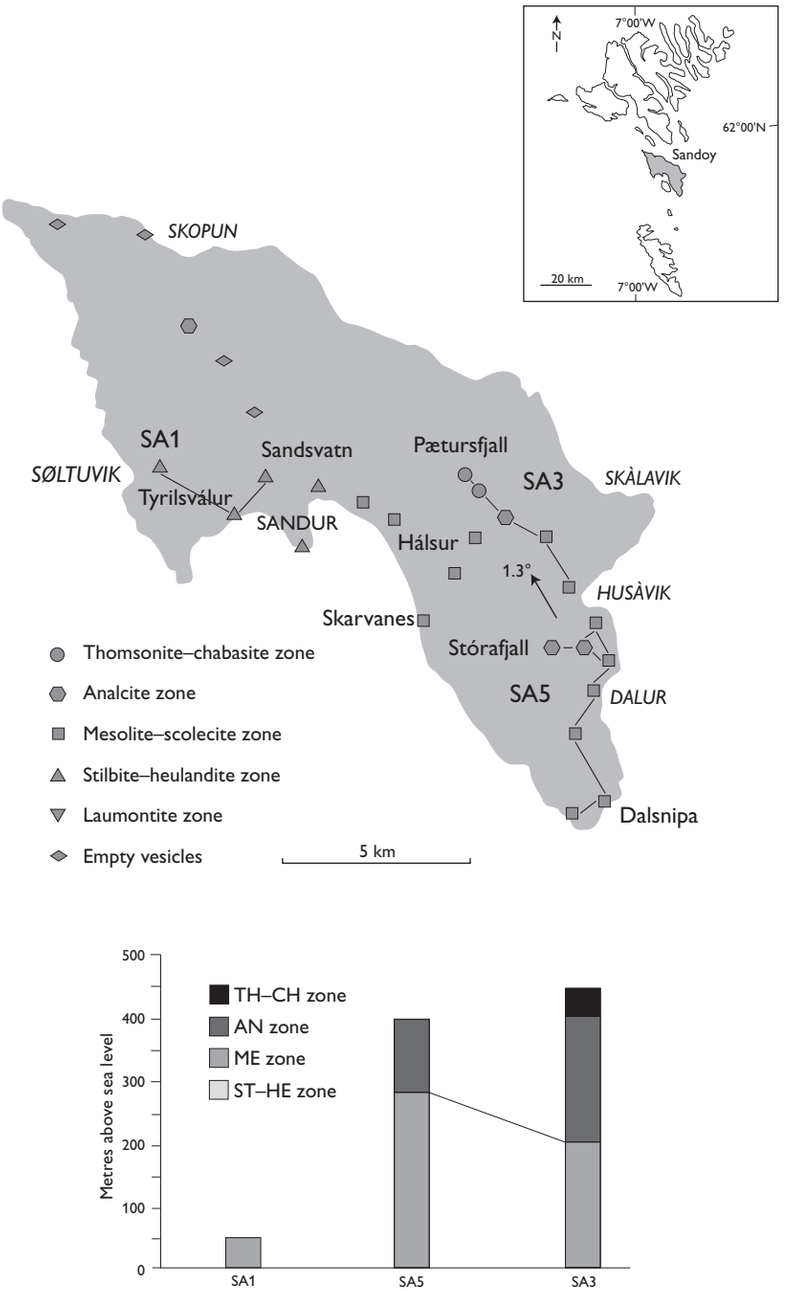

ern Suðuroy, a clear zonation can nevertheless be discerned along section SU1, where a 200 m mesolite zone is overlain by a 180 m analcite zone. The mesolite zone continues to a depth of 600 m below sea level in the Lopra-1/1A borehole (Fig. 5). The most abundant minerals there are mesolite, scolecite, stilbite, heulandite and mordenite. Chlorite, mesolite and scolecite were deposited first. Mesolite and scolecite are replaced by laumontite as the first formed mineral at a depth of –626 m, indicating the top of the stilbite-heulandite zone. At about –1200 m, epistilbite replaces stilbite as the first formed mineral so that the order of deposition becomes celadonite/chlorite-epistilbite-thomsonite-laumontite or celadonite/chlorite-epistilbite-laumontite-stilbite. Since an epistilbite zone has not yet been defined elsewhere, it was decided to include the total interval between –1200 m and –2200 m depth in the laumontite zone. A high temperature assemblage of laumonite, mordenite-prehnite, pumpellyite, chlorite, calcite and quartz is found from about –2200 m to the bottom of the Lopra-1A borehole at –3534 m.

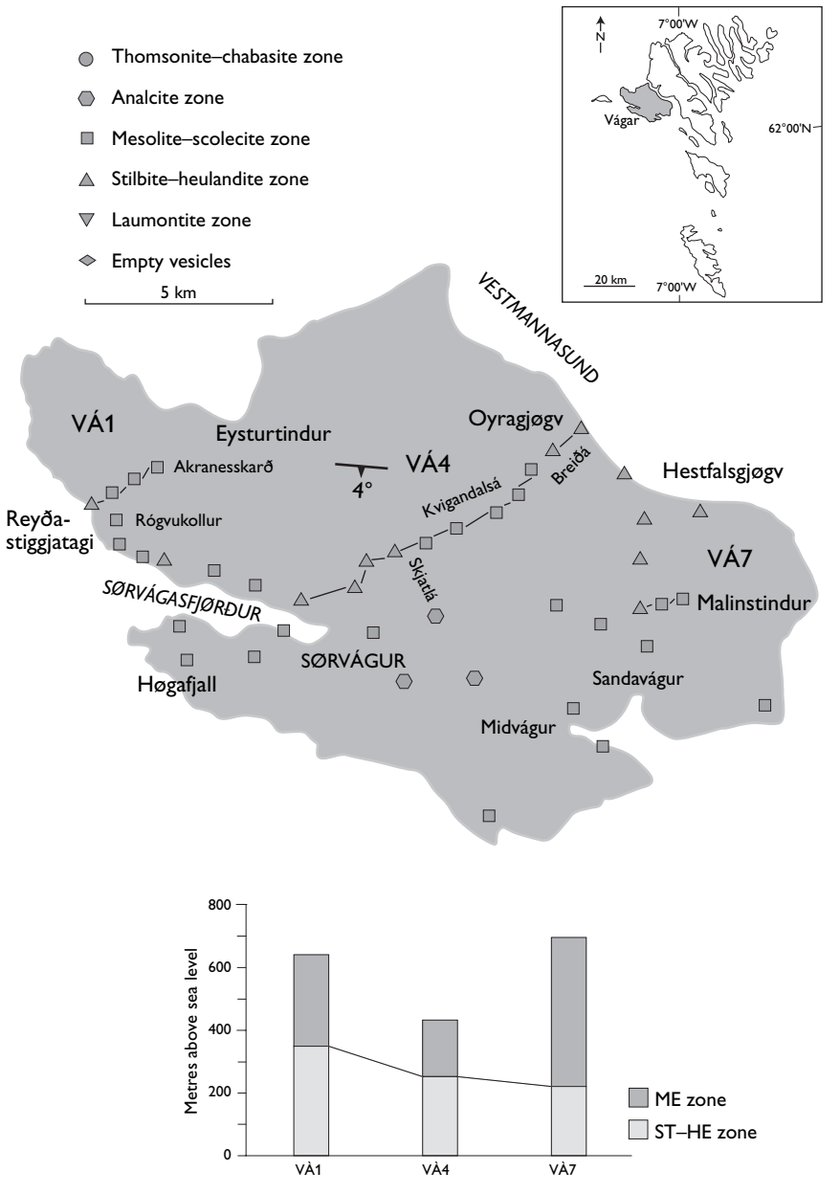

Fig. 7. Distribution of zeolite zones on Vágar and on sections VÁ1, VÁ4 and VÁ7. The dip and strike of the zeolite zones is indicated on the map.

The uppermost mineral zone preserved in the SU1 section is part of an analcite zone. In East Iceland, a chabazite-thomsonite zone (Walker 1960) and in East Greenland a zeolite free zone (Neuhoff *et al.* 1997) has been recorded in the uppermost parts of the basalt complexes whose total thicknesses are 700 m and 1400 m, respectively. If equivalent zones have ever existed on the southern part of Suðuroy, they must have been considerably thinner than those on Iceland and Greenland, because the palaeosurface of the lower basalt formation was about 300 m above the A-horizon (see below).

Sandoy (Fig. 6)

The southern part of Sandoy is strongly mineralised while the mineralisation in the northern part is weak. The area north of a line from Søltuvík to Skálavík is weakly mineralised by quartz, calcite, chalcedony, chabazite, hair-like mesolite, thomsonite and late formed stilbite or stellerite. Nearly all fractures and vesicles are totally mineralised to the south of the line. The most abundant zeolites are analcite, chabazite, heulandite, mesolite, stilbite and thomsonite. No distinct boundary has been observed between the northern and the southern part of the island.

Sections SA1, SA3 and SA5 (Fig. 6) show that four

zeolite zones exist on Sandoy. In the area between Sandur and Søltuvik, the uppermost 50 m of a stilbite-heulandite zone are exposed. The stilbite-heulandite assemblage consists of chlorite, heulandite, stilbite, mordenite and occasionally of laumontite and apophyllite. The latter two minerals occur mostly in fractures in the basalt.

However, the degree of mineralisation is low in the stilbite-heulandite zone and, by volume, only half of the vesicles are mineralised.

The southern and the eastern parts of Sandoy are dominated by a mesolite zone. The most abundant minerals are chabazite, heulandite, mesolite (solid or hair-like), stellerite, thomsonite and calcite together with minor gyrolite, gismondine and levyne. Heulandite and mesolite are the first deposited minerals. Dalsnípa at the south-east coast of Sandoy is the type locality of levyne (Brewster 1825). A detailed quantitative analysis of the mineral assemblage and the zeolite zones in section SA3 is given below.

Vágar (Fig. 7)

In contrast to Suðuroy and Sandoy, Vágar is totally mineralised and the island may be divided into two areas. North-east of a line from Sørvágur to Sandavágur, a stilbite-heulandite assemblage occurs at 40% of the localities that has not been observed farther south. South-east of the boundary line, the localities are dominated by a mesolite and analcite assemblage. Around Miðvágur hair-like mesolite with up to 100 mm long crystal needles can be found in larger fractures and cavities in the basalt.

The distribution pattern of the mineral assemblages on Vágar is controlled by the rise of the stilbite-heulandite zone towards the north-east. A calculation shows that the stilbite-heulandite zone dips from between 1–3°SSW to 0.6°ESE, while the basalt flows dip 3–4°ESE, i.e. the mineral zones are discordant to the lava stratification.

A quantitative analysis of the mineral assemblage and the zeolite zones on section VÁ1 is given below.

Streymoy (Fig. 8)

Streymoy can be divided into a northern, a central and a southern area. A stilbite-heulandite assemblage occurs along the coast from Tjørnuvík to Langasandur in the north. The observed minerals are stilbite, heulandite, thomsonite, compact mesolite, laumontite, gyrolite, okenite, tobermorite, apophyllite, celadonite and smectite. The mineral assemblage in the amygdales changes gradually towards the west. The hydrated calcium silicates, stilbite and laumontite, disappear from the amygdales although they still occur in fractures in the basalt. At Saksun near the north-west coast, the stilbite-heulandite assemblage is replaced by a mesolite assemblage, characterised by solid mesolite, thomsonite, heulandite, chabazite, calcite and montmorillionite. Gyrolite and stilbite are present, but only in fractures. The distribution pattern is reversed in the central part of Streymoy (between Langasandur, Vestmanna, Dalsnipa and Kollafjørður). There the stilbite-heulandite assemblage occurs along the west coast from Vestmanna to Dalsnipa, while a mesolite assemblage is found along the east coast between Langasandur and Kollafjørður.

Only the mesolite assemblage is found in the southern part of Streymoy. Because of the differences in mineral distribution, sections ST2 and ST6 have been divided into two columns, showing the eastern and the western parts of the sections, respectively (Fig. 8). The dip of the zeolite zones in the northern part of Streymoy is 2°SW and 2°NNE the central area.

The distribution of secondary minerals is rather complex at many localities in northern and central Streymoy and shows *repetitive zoning*, i.e. a regular repetition of two mineral zones. For example, on the path from Saksun to the summit of Borgin (643 m), a mesolite zone is first encountered, then a stilbite-heulandite zone, then, near the summit, a second mesolite zone. Repetitive zoning has also been observed at Loysingafjall (638 m), where the mesolite zone is overlain by a stilbite-heulandite zone, and along the main road between the villages of Vestmanna and Kvívík. Between Vestmanna and Kvívík, zones occur within which the vesicles and fractures of the basalt flows are mineralised, either by heulandite, stilbite, mordenite plus minor laumontite, or by compact mesolite, heulandite, stilbite, thomsonite and chabazite. The widths of the zones are from a few hundred metres to about 1 km.

Repetitive zoning also exists in the Vestmanna-1 borehole. The first classification of the Vestmanna-1 mineral assemblages was based on the mass concentration of major index minerals. Since chabazite and thomsonite are the most abundant minerals, the entire mineral assemblage was classified as a thomsonite-chabazite assemblage. During the reclassification based on the first formed minerals for the present work, it became apparent that the drilled lava succession contains a repetitive zoning of mesolite and stilbite-heulandite assemblages (Fig. 8).
It is unlikely that repetitive zoning is caused by vertical fluctuations of the geothermal gradient within such relatively short distances, but the repetitive zoning may reflect flows of water of different temperature that changed

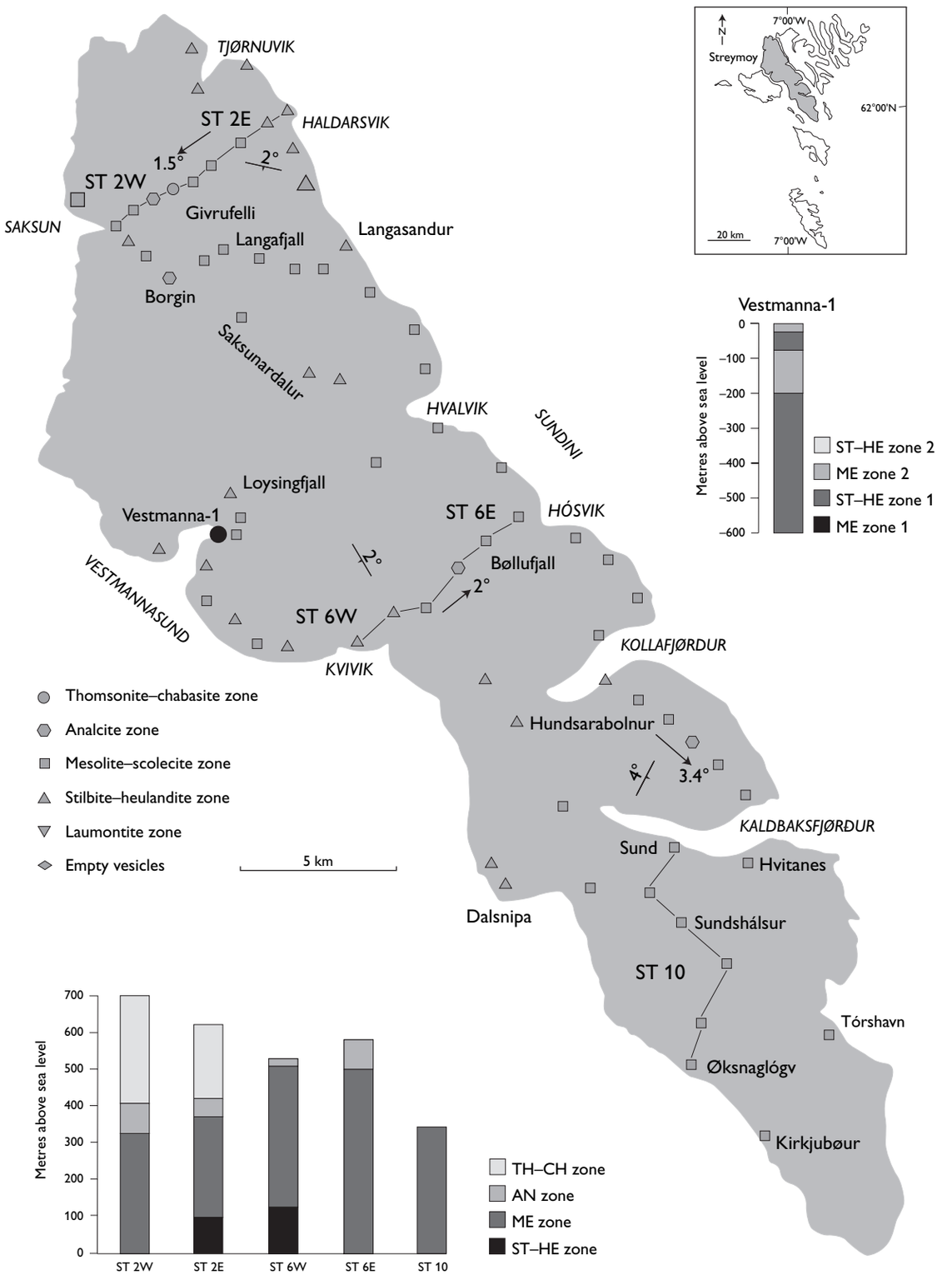

Fig. 8. Distribution of zeolite zones on Streymoy and on sections ST2E, ST2W, ST6E, ST6W, ST10 and in the Vestmanna-1 borehole. The dip and strike of the zeolite zones is indicated on the map. The arrows indicate the calculated strike of the zeolite zones between the sections.

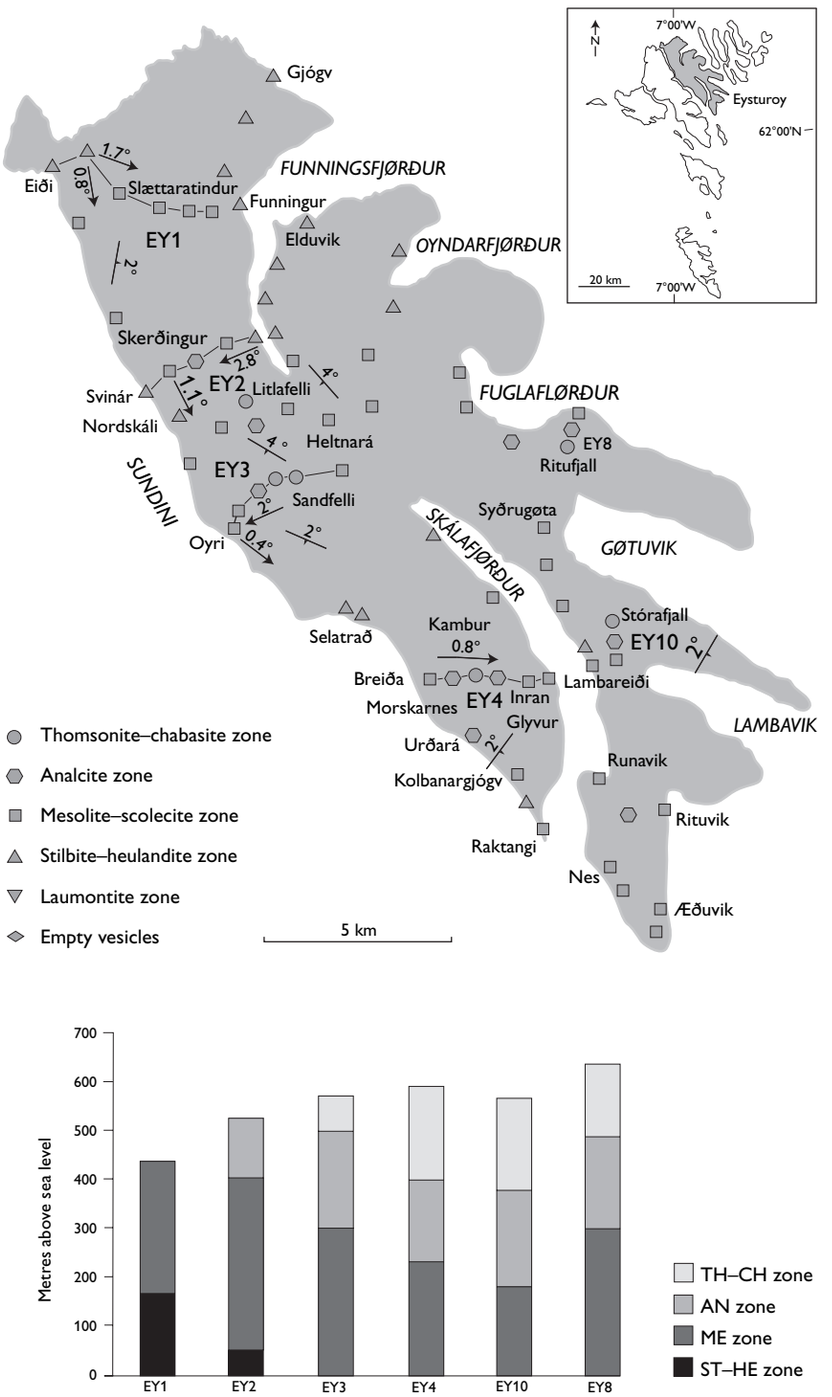

Fig. 9. Distribution of zeolite zones on Eysturoy and on sections EY1, EY2, EY3, EY8 and EY10. The dip and strike of the zeolite zones is indicated on the map. The arrows indicate the calculated dip of the zeolite zones between the sections.

locally the vertical distribution of temperature. Alternative explanations for repetitive zoning are: (1) local variations in the chemical composition of the basalt, or: (2) mineralisation in an open and closed system, caused by variations in the percolation speed of the geothermal water (Barth-Wirsching & Höller 1989; Gottardi 1989).

Eysturoy (Fig. 9)

Eysturoy may be divided into two for descriptive purposes. North of a line from Norðskáli to Fuglafjørður, the stilbite-heulandite assemblage occurs at 64% of localities. South of that line mineral assemblage occurs at only 12% of the localities (Fig. 9). The actual strike and dip of the

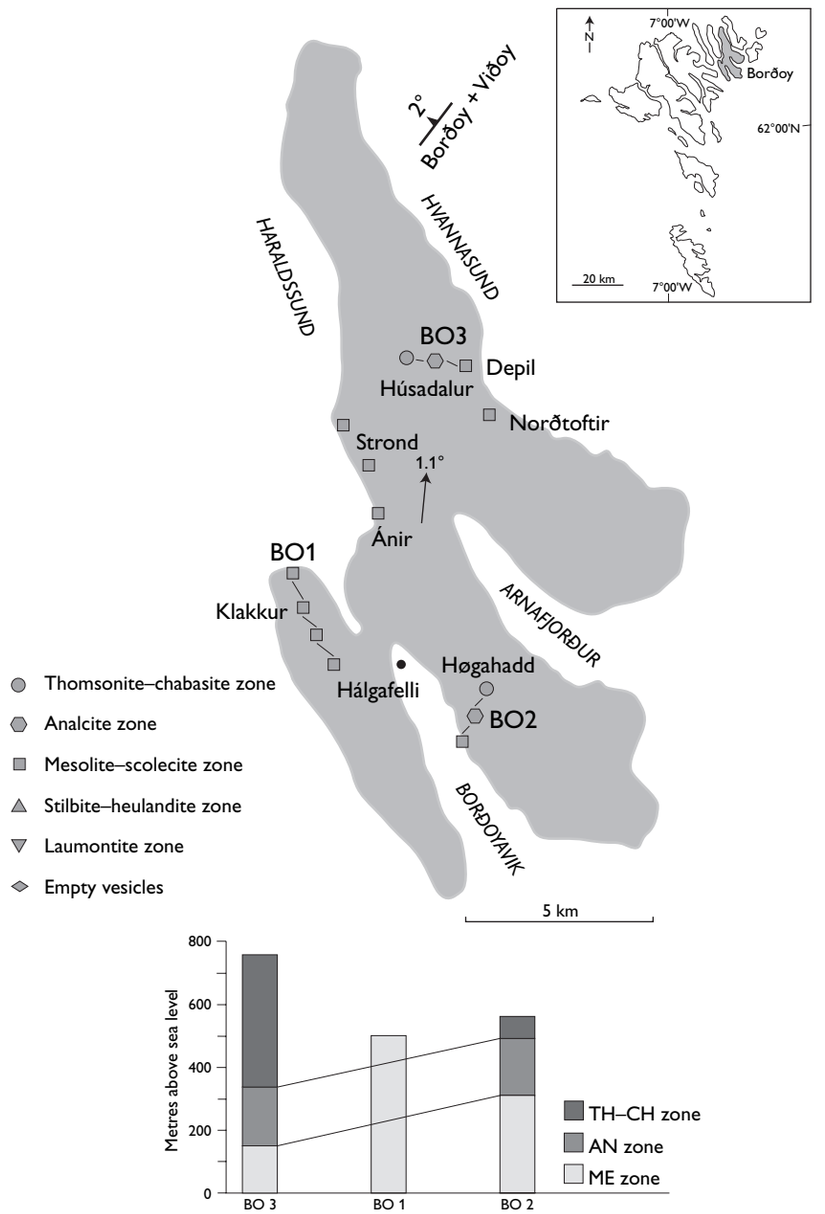

Fig. 10. Distribution of zeolite zones on Borðoy and on sections BO1, BO2 and BO3. The arrow shows the strike of the zeolite zones between BO2 and BO3. The common dip and strike of the zeolite zones on Borðoy and Viðoy is shown in the upper right corner.

zeolite zones can be determined by combining the dip of the zeolite zones along the sections with the dips between them. On Fig. 9 it can be seen that the strikes and dips change to follow the changes in mineralogy. North of a line from Svinár/Norðskáli to Fuglafjørður, the zeolite zones dip about 2° towards the east. To the south of the line, the dips of the zones shift gradually from 4° to the SW to 2° to the S. This means that the mineral zones are discordant to the lava bedding on the northern part of Eysturoy, but nearly concordant to it on the southern part of the island.

Borðoy (Fig. 10)

The mesolite, analcite and chabazite-thomsonite zones are the only ones exposed on Borðoy. At Klakkur (section BO1) the vesicles and fractures in the basalt are mineralised by heulandite, stilbite, mesolite (massive and hair-like), thomsonite (massive and hair-like), chabazite, levyne, phillipsite, montmorillionite and celadonite, but no clear relationship exists between the distribution of mineral and height in the lava pile. Since analcite and mesolite are the first deposited minerals in most vesicles, the mineral assemblage of section BO1 was classified as a mesolite zone assemblage. The poor zoning west of Borðoyavik suggests

Table 4. Quantitative analysis of section SA3, Sandoy. The table shows the number of observed and calculated amygdales containing the index mineral per 25 amygdales

Altitude metres	Me		Me*		Th		Th*		An		Ch	
	N_{obs}	N_{cal}	N_{obs}	N_{cal}	N_{obs}	N_{cal}	N_{obs}	N_{cal}	N_{obs}	N_{cal}	N_{obs}	N_{cal}
0	18	21.3	0	0.0	14	13.4	0	0.1	14	12.8	0	1.1
25	18	18.6	0	0.0	12	11.3	0	0.1	0	11.5	0	1.3
50	10	15.5	0	0.02	8	9.2	0	0.1	11	10.2	1	1.5
75	16	12.2	0	0.1	5	7.2	0	0.2	8	9.2	1	1.8
100	0	9.1	0	0.3	4	5.5	0	0.3	0	8.2	0	2.1
120	4	6.6	0	0.8	3	4.3	0	0.5	8	7.4	2	2.4
150	6	4.1	2	1.4	3	2.8	0	0.7	5	6.3	3	2.7
180	2	2.4	3	5.9	1	1.7	2	1.0	5	5.2	0	3.6
200	0	1.3	7	10.3	1	1.1	3	1.5	4	4.5	0	4.2
210	2	1.1	14	13.0	0	0.9	2	1.8	5	4.2	0	4.4
220	1	0.6	15	15.9	0	0.7	0	2.2	0	3.8	6	4.8
243	0	0.4	22	21.4	0	0.5	3	2.8	3	3.3	6	5.4
270	1	0.1	22	24.9	0	0.2	5	4.4	3	2.5	6	6.7
320	1	0.0	10	11.9	0	0.1	9	8.5	2	1.5	8	9.3
340	1	0.0	5	5.6	0	0.0	10	11.2	1	1.1	13	11.3
360	0	0.0	0	2.0	0	0.0	0	14.0	0	0.9	0	12.0
375	0	0.0	1	0.7	0	0.0	14	16.3	0	0.7	0	13.2
380	0	0.0	1	0.5	0	0.0	14	17.1	0	0.7	0	13.8
400	0	0.0	0	0.1	0	0.0	23	20.1	1	0.4	16	15.4
420	0	0.0	0	0.0	0	0.0	23	22.8	0	0.3	0	17.2
446	0	0.0	0	0.0	0	0.0	23	24.6	0	0.3	20	19.1
$R_{N,U}$†	–	0.988	–	0.996	–	0.875	–	0.991	–	0.982	–	0.952
S_H ‡	–	44	–	17	–	14	–	32	–	56	–	59

† $R_{N,U}$: Correlation coefficient of the regression line lnH versus U(N_{obs}). See equation (2).
‡ S_H: Standard deviation on Hcal. in m. See equation (3).

Table 5. Quantiative analysis of section VÁ1, Vágar. The table shows the number of observed and calculated amygdales containing the index mineral per 25 amygdales

Altitude metres	Ch		Th		Me		He		St	
	N_{obs}	N_{cal}	N_{obs}	N_{cal}	N_{obs}	N_{cal}	N_{obs}	N_{cal}	N_{obs}	N_{cal}
10	0	0.2	0	0.8	0	0.0	4	3.7	3	3.7
100	0	0.3	0	1.7	0	0.1	9	11.3	15	14.3
200	0	0.6	0	3.9	0	0.3	24	22.7	21	25.0
235	0	0.7	3	3.9	0	0.4	23	24.8	0	23.2
340	0	1.2	13	10.1	0	1.9	15	17.7	7	6.7
350	0	1.2	9	10.7	1	2.2	18	16.3	5	5.4
380	2	1.4	15	12.6	3	3.1	10	11.9	0	2.6
410	2	1.7	0	14.8	6	4.5	7	7.9	0	1.1
460	3	2.2	19	18.4	7	7.6	3	3.1	0	0.2
475	3	2.4	18	19.4	9	8.8	2	2.2	0	0.1
500	6	2.7	19	21.1	10	11.0	1	1.2	0	0.0
550	3	3.5	21	23.8	0	16.1	0	0.2	0	0.0
610	5	4.8	0	25.0	24	22.0	0	0.0	0	0.0
630	6	5.3	23	24.8	0	23.5	0	0.0	0	0.0
$R_{N,U}$†	_	0.987	_	0.972	_	0.851	_	0.837	_	0.871
S_H‡	_	58	_	27	_	25	_	26	_	97

† $R_{N:}$ Correlation coefficient of the regression line lnH versus U(N_{obs}). See equation (2).
‡ S_H: Standard deviation on Hcal. in m. See equation (3).

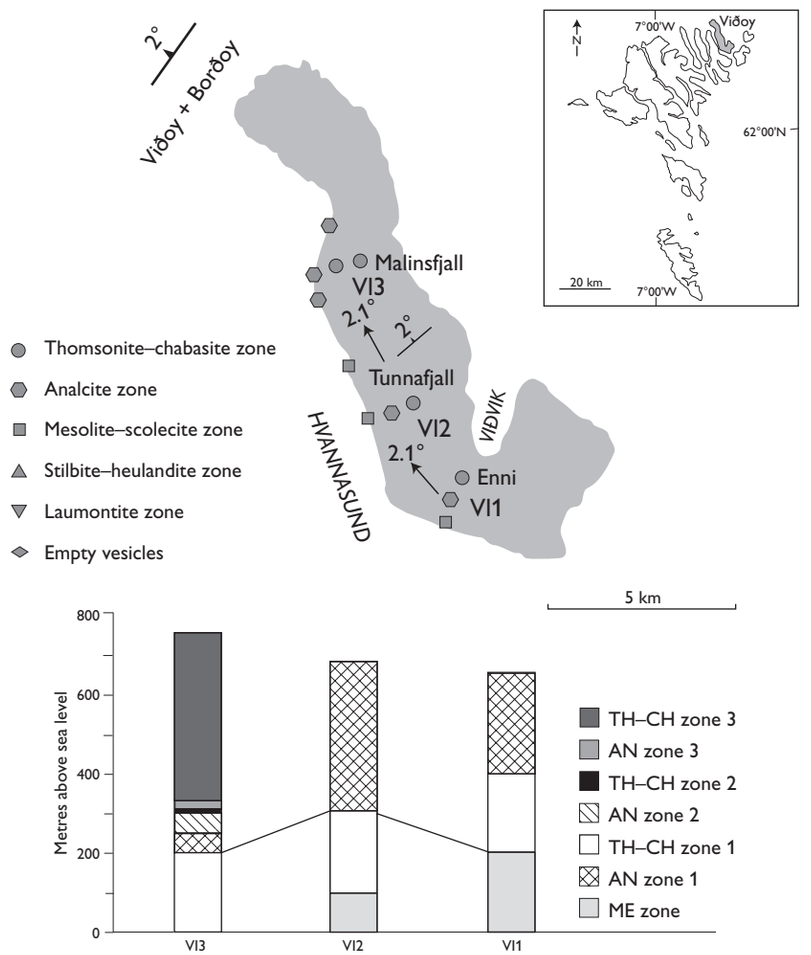

Fig. 11. Distribution of zeolite zones on Viðoy and on sections VI1, VI2 and VI3. The dip and strike of the zeolite zones is indicated on the map. The arrows indicate the strike of the zeolite zones in the profiles. The common dip and strike of the zeolite zones on Borðoy and Viðoy is shown in the upper left corner.

that the area has been affected by several generations of mineralisation.

The zoning becomes distinct farther eastwards on sections BO2 and BO3. The exposed part of the mesolite zone is 500 m on BO1, but 300 m on BO2 and 150 m on BO3 (Fig.10). The analcite and thomsonite-chabazite zones also appear at higher levels on sections BO2 and BO3. The mineral zones have apparent dips of about 1º towards the north and east. The analcite zone is about the same thickness on both BO2 and BO3, which suggests that the vertical displacement of the two zones reflects differences in altitude of the palaeosurface of the basalt plateau. The lava flows of Borðoy dip 1.6º to the SE, which means that the zeolite zones are discordant to the lava bedding.

Viðoy (Fig.11)

The distribution pattern of the secondary minerals on Viðoy is a continuation of that on Borðoy. The mineral zones are displaced downwards compared to those of Borðoy with the result that only between 100 m and 200 m of the mesolite zone is exposed on sections VI1 and VI2. On section VI3 a lower analcite zone about 200 m thick is exposed, which is separated from the thomsonite-chabazite zone by about 130 m of repetitive zoning. The chabazite-thomsonite zone is about 430 m thick, which is the maximum thickness recorded for that zone within the basalts exposed on the Faroe Islands.

Quantitative analysis of mineral distributions

Once the position and temperatures are known of the boundaries of the zeolite zones, the geothermal gradient

and the altitude of the palaeosurface of the basalt plateau can be estimated using least squares regression, assuming a linear palaeotemperature gradient. However, in order to make a reliable estimate, the regression must be based on three or more zone boundaries. This requirement is fulfilled only where the Lopra-1/1A and SU1 sections can be combined. Elsewhere, the number of exposed zone boundaries is too small to calculate a geothermal gradient. In order to overcome this limitation, an attempt has been made to estimate the position of unexposed mineral boundaries from a detailed analysis of the distribution of the exposed mineral zones.

Quantitative analyses carried out on the mineral assemblages of the Lopra-1/1A and Vestmanna-1 boreholes showed that the relative vertical frequency of the minerals followed a skewed distribution with one or more maxima (Jørgensen 1984). This observation has been used to extrapolate non exposed zone boundaries on section VÁ1 on Vágar and SA3 on Sandoy. The two sections were chosen because they are through the middle and the upper basalt formations respectively, the distribution of minerals in them is simple and nearly all rocks sampled contain a large number of well developed amygdales. In order to examine the relationship between the thickness of the zeolite zones and the distribution of index minerals, the number of amygdales containing a particular index mineral was recorded for 25 amygdales (see below). To ensure that the amygdales were selected randomly, all amygdales in the samples from each locality were numbered and the 25 amygdales for examination were selected by using a computerised random number generator. After the amygdales had been chosen, the first formed index mineral was determined and the total number of amygdales containing the same index mineral was recorded. These results are presented as columns N_{obs} in Tables 4 and 5.

Trials were carried out using different exponential distribution functions to find the best correlation between altitude and number of amygdales containing the same index minerals. The experiments showed that the best fit between the observed distribution and the calculated distribution was obtained by the log normal distribution function:

$$N_{i,cal} = N_0 \exp(-½[(\ln H - \ln H_0) / a]^2) \quad (1)$$

where:

$N_{i,cal}$ is the calculated number of amygdales containing index mineral i.

N_0 is the total number of amygdales investigated; in this case $N_0 = 25$.

H is the altitude of the sample above sea level.

H_0 is the altitude where the distribution function attains its maximum value.

a is a constant.

By transforming equation (1) to a linear form and replacing $N_{i,cal}$ by $N_{i,obs}$, we obtain:

$$\ln H = aU + \ln H_0, \text{ where } U = \pm [2 (\ln N_0 - \ln N_{i,obs})]^{½} \quad (2)$$

The constants a and H_0 can be determined by linear regression on U and lnH. The calculated number of amygdales ($N_{i,cal}$) containing index mineral i is shown in Tables 4 and 5. A t-test shows that U and lnH fit a straight line at the 1% confidence level.

The distribution curves in Figs 12 and 13 give only a best estimate for the height above sea level of the zone boundaries. To assess the degree of uncertainty of these estimates (see below) we calculate the standard deviation of the altitude (H) defined as:

$$S_H = [1/(n - 2)\ S\ (H - H_c)^2]^{½} \quad (3)$$

where:

n is number of pairs (H, N_i) along the distribution curve.

H is the altitude of the sample above sea level.

H_c is the calculated altitude of a point on the distribution curves corresponding to N_i amygdales that contain index mineral i.

In equation (3), n is reduced by 2 because of the loss of two degrees of freedom by the least squares estimation of a and H_0 in equation (1) (Miller & Freund 1977).

When N_i, H_0 and a are known, H_c can be calculated from equation (1). S_H for the distribution curves is shown in Tables 4 and 5 and a graphic representation of the calculated distributions of chabazite, thomsonite, mesolite, analcite, heulandite and stilbite on sections SA3 and VÁ1 is shown in Figs 12 and 13. The shape of the curves suggests that a temperature range existed around the altitude H_0 in which conditions were favourable for the formation of a particular zeolite. Where $H < H_0$, palaeotemperatures decreased away from H_0 to where they became too low for the zeolite to form. Where $H > H_0$, palaeotemperatures increased away from H_0. The zeolite that was most stable at H_0 would have been formed in some interval below H_0 but, at higher temperatures, formation of the first zeolite would gradually be inhibited and another one would have become stable. So a zeolite will most likely be found between the maximum slopes of its distribution curve versus height, which corresponds to a palaeotemperature interval.

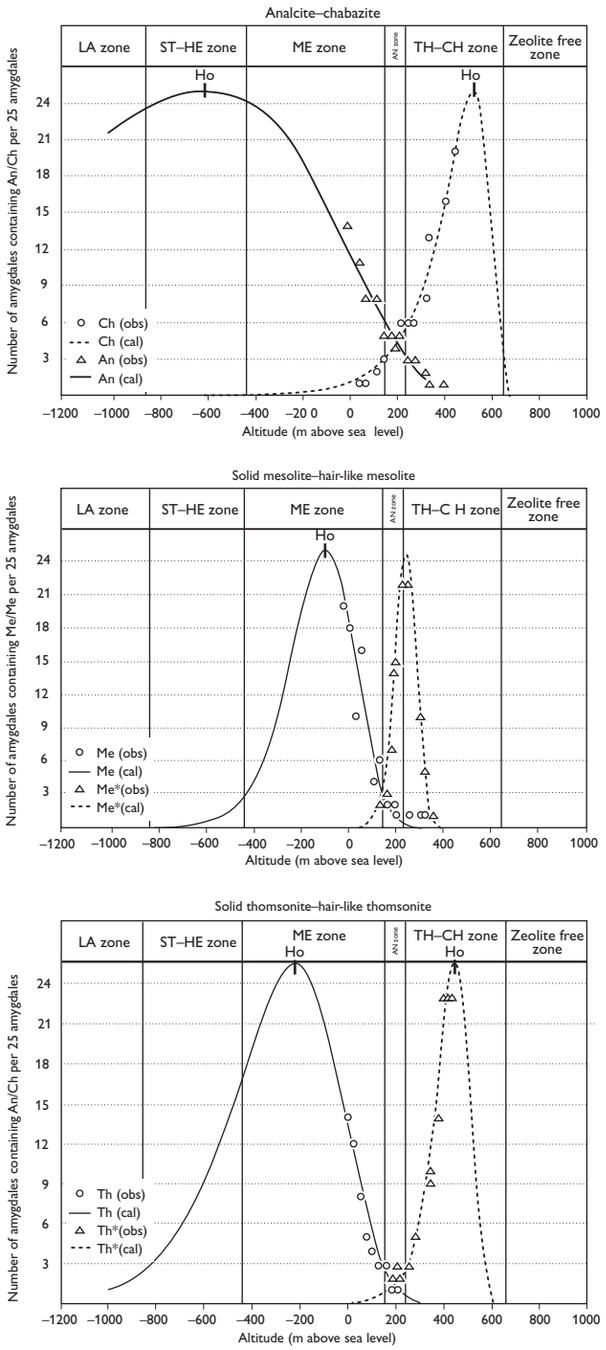

Fig. 12. The calculated distribution of chabazite, analcite, thomsonite (compact and hair-like) and mesolite (compact and hair-like) on section SA3, Sandoy.

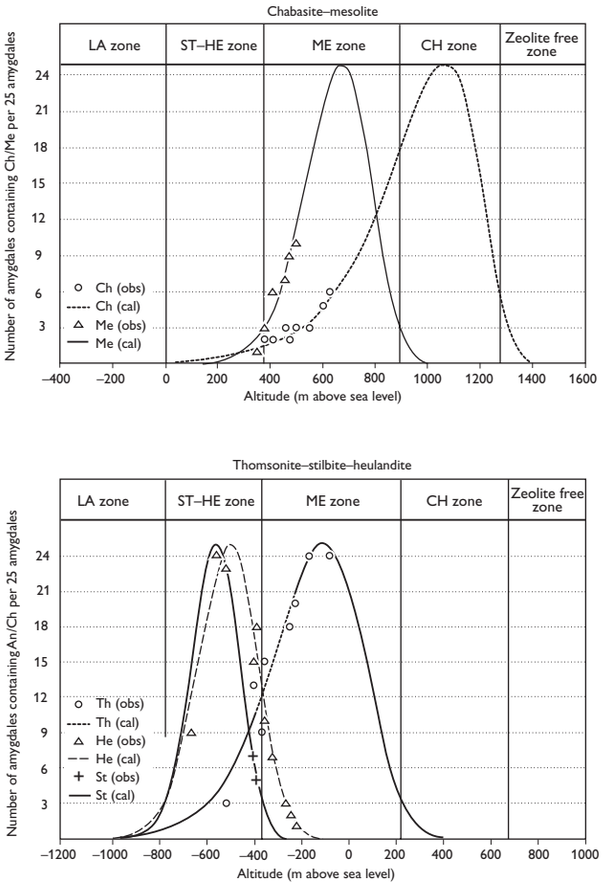

Fig. 13. The calculated distribution of chabazite, mesolite, thomsonite, stilbite and heulandite on section VÁ1, Váger.

The calculated distribution curves shown in Figs 12 and 13 show that the number of amygdales containing a particular zeolite decreases rapidly as $|H - H_0|$ increases. This has the practical consequence that it becomes harder to define a zone boundary by field mapping when sample numbers are small. A zone boundary is defined for mapping purposes to be reproducible with a probability of 95%. The probability (P) of discovering $N_{i,obs}$ objects (amygdales containing the new zeolite i) among N_0 objects (amygdales) can be calculated by means of the binomial distribution function (see e.g. Kreyszig 1975 or Miller & Freund 1977). It can be shown that when $N_0 = 25$ and P = 95%, then $N_{i,obs} = 3$. Fig. 12 shows that this reasoning can be applied to define the upper boundaries of the thomsonite-chabazite, analcite and mesolite zones at the heights where the upper end of the appropriate distribution curve intersects the line $N_i = 3$. However, this method cannot be used on the upper boundaries of the stilbite-heulandite and laumontite zones, because stilbite, heulandite and laumontite do not exist as first formed index minerals in section SA3. Fig. 12 shows that solid mesolite occurs most commonly in the mesolite zone and thomsonite occurs most commonly in the stilbite-heulandite plus the mesolite zone. If we assume that 95% of the two index minerals occurs within the zones in question, we can define the

Table 6. Estimated palaeothermal gradients and the altitude of the palaeosurfaces at Lopra-1/1A and sections SU1, VÁ1 and SA3

Zeolite zone	Zeolite free	Ch–Th	Me	St–He	La	Palaeothermal gradient	Altitude of palaeosurface	Correlation coefficient
Temperatures at the zone boundaries	40–60°C	50–70°C	90–100°C	110–130°C	190–220°C	°C/km	m above sea level	R
Altitude of zone boundaries (m above sea level):								
Lopra-1/1A + SU1	–	–	–590	–1200	–2200	66 ± 9	443–983	0.9547
VÁ1	1325	900	380	–	–	63 ± 8	1760–2080	0.9181
SA3	653	150	–425	–825	–	56 ± 7	1150–1524	0.8689

heights of the lower boundaries of the mesolite and the stilbite-heulandite zones where the lower end of the distribution curves interest the line $N_i = 3$. That 95% of an index mineral occurs within the interval in question can be verified by plotting the accumulated distribution of the index mineral in a probability diagram.

Analcite occurs only sporadically below 340 m on section VÁ1 (Fig. 13), so the analcite zone cannot be defined on this profile. The other zone boundaries were calculated as described above.

Estimation of palaeothermal gradients and altitudes of palaeosurfaces

If we assume that the palaeothermal gradient was constant with depth, it may be estimated by linear regression on the data from the combined Lopra-1/1A plus SU1 sections, the mineral zone boundaries obtained by calculation and shown in Figs 12 and 13 and the temperatures shown in Fig. 2. The resulting estimates are shown in Table 6. The new estimate from southern Suðuroy is considered more accurate than that in Jørgensen (1984), which was based on the mineral distribution in the Lopra-1 borehole only. From these palaeogeothermal gradients and assuming a surface temperature of 7°C, the altitudes of the palaeosurface of the basalts has been estimated (Table 6).

The altitude differences between the estimated palaeosurface and stratigraphic marker horizons A and C is different at the three localities (Table 7). On southern Suðuroy, the palaeosurface was about 0.7 km (± 0.3 km) above present day sea level, i.e. close to the extrapolated top of the lower basalt formation. On Vágar, the palaeosurface was 1.9 ± 0.2 km above the extrapolated top of the lower basalt formation (or 0.5 ± 0.2 km above the top of the middle formation), while on Sandoy, the palaeosurface was 1.7 ± 0.2 km above the top of the middle basalt formation. This suggests that the focus of volcanism shifted laterally with time as will be discussed below.

Table 7. Estimated thicknesses of the basalt formations along various sections across the Faroe Islands

Area	Section	Formation	Altitude of palaeo surface in m above sea level (Table 6)	Present stratigraphic thickness in m	Local altitude (m) of A- and C-horizons	Altitude of palaeosurface in m above A- or C-horizon
S. Suðuroy	Lopra-1/1A + SU1	L. Formation	443–983	> 3100[1]	A-horizon: 700	A-horizon: –257–283
W. Vágar	VÁ1	M. Formation	1760–2080	1410[2]	A-horizon: 60	A-horizon: 1700–2020
E. Sandoy	SA3	U. Formation	1150–1525	700–900[1,3]	C-horizon: –400	C-horizon: 1550–1924

Sources: [1)] Larsen *et al.* 1999, [2)] Waagstein & Hald 1984, [3)] Waagstein 1988.

Discussion

Palaeothermometry and zone boundaries

The use of zeolites as palaeotemperature indicators is based on the assumptions: (1) that the zeolite zones reflect univariant equilibrium with a high coefficient dP/dT of the Clausius-Clapeyron equation and: (2) that the formation temperature of the minerals is independent of the chemical composition of the hydrothermal solution.

Assumption (1) is fulfilled because the properties of condensed systems are nearly independent of pressure, if the pressure is not extremely high and the temperature is below the supercritical temperature (374ºC) of water. We can also estimate the error of the temperature determination when we ignore the external pressure of the system. The coefficient dP/dT is known only for a small number of systems that involve zeolites, but experimental studies of the systems stilbite-laumontite-H_2O and laumontite-wairakite-H_2O show that dP/dT is of the order of 25–33 bars/degree in the range P_{fluid} = 0–2000 bars (Liou 1971; Jové & Hacker 1997). Consequently, if the external pressure is equal to the fluid pressure and the original thickness of the lava pile is 2 km, the likely maximum error of the temperature determination is 8°C, disregarding the depth between the boundary of the zeolite zone and the unknown altitude of the palaeosurface.

In contrast to the effect of pressure, the chemical composition of the rock and the hydrothermal fluids has a much larger effect on the formation temperature of the minerals. Barth-Wirsching & Höller (1989) studied the formation of zeolites in glasses of different chemical compositions. They found that replacing rhyolitic glass by basaltic glass caused the formation temperature of different zeolites to increase by between 50°C and 100°C. This demonstrates the importance of choosing a reference area for the thermometry that consists of rocks with a chemical composition similar to that of the rocks in the area studied.

Other factors may also affect the formation of zeolites such as the texture of the rock, the content of glass and the porosity of the rock (Gottardi 1989).

The geothermal areas on Iceland were used as a reference for the thermometry in the present study. The basalts from the Faroe Islands are all tholeiites, but show large compositional variations that range from picritic to ferrobasaltic (Waagstein 1988). Most of the Icelandic basalts are also tholeiites, but minor amounts of acid rocks (rhyolites, andesites, granophyres, acid tuff) are found, mainly associated with volcanic centres (Sigurdsson 1967). This compositional variation of the Icelandic rocks may partly explain the large variation in temperature at the boundaries of the zeolite zones mentioned above (Fig. 2).

From the description of the sections shown in Figs 12 and 13 (and listed in Appendix A), it can be seen that the distribution of index minerals varies gradually between successive zeolite zones. An index mineral that defines a zone may thus overlap the boundaries of neighbouring zones which makes it difficult to define the exact boundaries between mineral zones. The problem was solved by statistical analysis on sections SA3 and VÁ1 from which the boundaries of the zeolite zones could be defined as the locations where 3 out of 25 amygdales contain the appropriate index mineral.

The overlap problem occurs in all the sections described in Appendix A and, because of the lack of quantitative mineral data, the distributions in SA3 and VÁ1 were the only ones that could be described by a simple distribution model. On all other sections, the zone division was based on a crude estimate of the abundance of the index minerals around the zone boundaries. Figs 12 and 13 show that the overlap between the zeolite zones varies from 100 m to 300 m. which means that, in the worst case, the zone boundaries could be determined with an accuracy of only ± 150 m when the zone boundary localities are based on a subjective estimate of the abundance of index minerals.

Volcanic and tectonic evolution

The average of the three calculated palaeogeothermal gradients is about 60°C/km and there may be a small decrease in the gradient from the lower to the upper basalt formation. If real, this decrease could reflect either a reduction in heat flow with time or a variation in heat flow with locality.

Rasmussen & Noe-Nygaard's (1969, 1970) summary of the volcanic evolution of the Faroe Islands that volcanic activity started in the west and moved eastwards with the times, must be modified, because evidence from the Lopra-1 drillhole indicates that the lavas of the lower formation were erupted from local centres (Waagstein 1988) and not from centres situated west of the present islands. This change might explain the change in the palaeogeothermal gradients shown in Table 6. The eruption centres of the lower and middle formations were located in the Faroe Islands and the geothermal gradient was high. Movement away to the east during eruption of the upper formation led to a decrease in the gradient.

Regional distribution of the zeolite zones

At the time when the Faroe lava pile was first mineralised, the thermal gradient seems to have been fairly constant, at least regionally and for some time. This is suggested by the rough equality of the calculated palaeogeothermal gradients from the southern, western and central part of the Faroes that represent different stratigraphic levels (Table 6). The overall regional distribution of zeolites is thus considered to reflect primarily variations in the maximum depth of burial of the basalt rather than differences in heat flow. The inferred palaeosurface on southern Suðuroy is close to the extrapolated top of the lower formation (Table 7), indicating that the total thickness of middle and upper formation lavas must have been small in this area. In contrast, in eastern Sandoy about 50 km farther north where the exposed thickness of the upper formation is of the order of 1 km, the estimated palaeosurface is >1.5 km above the base of the upper formation or stratigraphically approximately 3 km above the lower–middle formation boundary. If we use the palaeogeothermal gradient calculated on Sandoy, then the palaeosurface of the upper formation on Viðoy may have been at about 1.3 km ± 0.2 km above sea level. These results suggest that the upper formation had a similar or only slightly smaller thickness in the north-eastern part of the Faroes compared with the central part of the islands. On the other hand, the upper formation seems to have been much thinner or non existent in both the western and southern parts of the Faroes (Table 7) and the middle formation must also have been thin in the south.

The inferred thinning of the middle and upper formations from the central to southern part of the Faroes is consistent with a northerly source area for these basalts, centred on the rift between the Faroes and Greenland (Waagstein 1988; Hald & Waagstein 1991; Larsen *et al.* 1999). The thinning of the upper formation towards the west is consistent with Rasmussen & Noe-Nygaard's (1969, 1970) interpretation of an easterly source for this part of lava pile and may suggest a shift in the focus of volcanism.

The first order regional zeolite distribution pattern is affected by local perturbations of the mineral zone boundaries (Fig. 4). These perturbations show up as shifts in the dip of the zone boundaries within and between neighbouring islands as well as shifts in the degree of mineralisation. The latter effect is clearly seen towards the south. Southern Sandoy and northern Suðuroy are heavily mineralised, although at different temperatures, whereas the vesicles of the basalt in the adjoining areas of northern Sandoy and southern Suðuroy usually contain no zeolites.

On the northern and western islands, the zone distribution shows a tendency to symmetry around the narrow NW–SE-trending sounds that separate the islands (Figs 7–9). The distributions on the neighbouring north-eastern islands of Borðoy and Viðoy similarly seem to be mirror imaged, a distribution difficult to explain by variations in depth of burial. It is more likely that the distributions reflect local differences in palaeotemperature, perhaps related to the circulation of water underground with high temperatures in areas of up welling and low temperatures in areas of down welling. The symmetry of the zonal distribution patterns suggests that these temperature anomalies are in part related to NW–SE-trending eruption fissures or zones of weakness separating the present islands (Noe-Nygaard 1968; Rasmussen & Noe-Nygaard 1969, 1970). They are subparallel to the transfer zones in the Faroe–Shetland Basin described by Rumph *et al.* (1993) and later authors, and may indicate the presence of similar deep seated features. Both the regional and the local distribution of zeolite assemblages probably reflect the basic volcanic-tectonic systems that led to the development of the Faroe Islands.

Acknowledgements

I want to express my gratitude to the late Arne Noe-Nygaard and Jóannes Rasmussen for discussions and support during the first phase of this project. I also want to express my thanks to the Geological Survey of Denmark and Greenland for financial support to the present project, to curator Ole V. Petersen, Geological Museum, Copenhagen for permission to study the collection of zeolites from the Faroes and to Mrs. Kitty Jørgensen, Næstved, who kindly made her collection of zeolites from the Faroes available for my study. Finally, I want to thank Regin Waagstein, James Chalmers and Kjeld Alstrup for discussions and constructive criticism of the various versions of the manuscript. The comments of two anonymous reviewers are likewise greatly acknowledged.

References

Barth-Wirsching, U. & Höller, H. 1989: Experimental studies on zeolite formation conditions. The European Journal of Mineralogy **1**, 498–506.

Betz, V. 1981: Zeolites from Iceland and the Faroes. Mineralogical Record **12**, 5–26.

Breck, D.W. 1974: Zeolite Molecular Sieves: Structure, Chemistry and Use. New York: John Wiley.

Brewster D. 1825: A description of Levyne, a new mineral species. Edinburgh Journal of Science **2**, 322–334.

Currie, J. 1905: The minerals of the Faroes, arranged topographically. Transactions of the Edinburgh Geological Society (session 1905–1906) **9**, 1–68.

Debes, L.J. 1673: Færoæ et Færoa Reserata. Hafniæ: Suptibus Daniels Paaulli Reg. Bibl. (In Latin and Danish).

Görgey, R. 1910: Ein Beitrag zur topographischen Mineralogie der Färöer. Neues Jahrbuch der Mineralogie und Palaeontologie **XXIX**, 269–315.

Gottardi, G. 1989: The genesis of zeolites. European Journal of Mineralogy **1**, 479–487.

Gottardi, G. & Galli, E. 1985: Natural zeolites. In: Wyllie, P.J., Goresy, A.E., von Engelhard, W. & Hahn, T. (eds): Minerals and Rocks No. 18. Berlin: Springer Verlag.

Hald, N. & Waagstein, R. 1991: The dykes and sills of the early Tertiary Faroe Islands basalt plateau. Transactions of the Royal Society of Edinburgh: Earth Sciences **82**, 373–388.

Jørgensen, O. 1984: Zeolite zones in the basaltic lavas of the Faroe Islands. Annales Societatis Scientiarum Faroensis. Supplementum **9**, 71–91.

Jørgensen, O. 1997: Zeolites and other secondary minerals in cavities and veins, Lopra-1/1A well, Faroe Islands, 1996, 8 pp. + plates. Unpublished Report. Technical studies prepared for Dansk Olie og Gasproduktion A/S 1997 (in archives of the Geological Survey of Denmark and Greenland, GEUS Report file 26129).

Jove, C. & Hacker, B.R. 1997: Experimental investigation of laumontite ® wairakite + H_2O; a model diagenetic reaction. American Mineralogist **82**, 781–789.

Kreyszig, E. 1975: Advanced Engineering Mathematics, 707–709, 783–787. New York: John Wiley.

Kristmannsdóttir, H. 1982: Alteration in the IRDP drillhole compared with other drillholes in Iceland. Journal of Geophysical Research **87** (B8), 6525–6531.

Kristmannsdóttir, H. & Tómasson, J. 1978: Zeolite zones in geothermal areas in Iceland. In: Sand, L.B. & Mumpton, F.A. (eds): Natural zeolites, occurrence, properties and use, 277–284. Oxford: Pergamon Press.

Larsen, L.M., Waagstein, R., Pedersen, A.K. & Storey, M. 1999: Trans-Atlantic correlation of Palaeogene volcanic successions in the Faroe Islands and East Greenland. Journal of the Geological Society (London) **156,** 1081–1095.

Liou, J.G. 1971: Stilbite-laumontite equilibrium. Contribution to Mineralogy and Petrology **31**, 171–177.

Miller, I. & Freund, J.E. 1977: Probability and statistics for engineers, 50–63. Englewood, New Jersey: Prentice-Hall.

Neuhoff, P.S., Watt, W.S., Brid, D.K. & Petersen, A.K. 1997: Timing and structural relations of regional zeolite zones in basalts of the East Greenland continental margin. Geology **25**, 803–806.

Noe-Nygaard, A. 1968: On extrusion forms in plateau basalts; shield volcanoes of 'scutulum' type. Science in Iceland **1**,10–13.

Rasmussen, J. & Noe-Nygaard, A. 1969: Beskrivelse til geologisk kort over Færøerne i målestok 1:50 000. Danmarks Geologiske Undersøgelse I Række **24**, 370 pp. + map vol. (in Danish with summaries in Faroese and English).

Rasmussen, J. & Noe-Nygaard, A. 1970: Geology of the Faroe Islands (pre-Quaternary). Danmarks Geologiske Undersøgelse I Række **25**, 142 pp.

Rumph, B., Reaves, C.M., Orange, V.G. & Robinson, D.L. 1993: Structuring and transfer zones in the Faroe Basin in a regional tectonic context. In: Parker, J.R. (ed.): Petroleum Geology of Northwest Europe: Proceedings of the 4th Conference, 999–1009. London: Geological Society.

Sigurdsson, H. 1967: The Icelandic basalt plateau and the question of SIAL. In: Björnsson, S. (ed.): Iceland and mid-ocean ridges. Societas Scientiarium Islandica **XXXVIII**, 32–46.

Waagstein, R. 1988: Structure, composition and age of the Faroe basalt plateau. In: Morton, A.C. & Parson, L.M. (eds): Early Tertiary Volcanism and the Opening of the NE Atlantic. Geological Society (London) Special Publication **29**, 225–238.

Waagstein, R. & Hald, N. 1984: Structure and petrography of a 660 m lava sequence from the Vestmanna-1 drillhole. In: Berthelsen, O., Noe-Nygaard, A. & Rasmussen, J. (eds): The Deep Drilling Project 1980–1981 in the Faroe Islands. Føroya Fródskaparfelag, Tórshavn, 39–65.

Walker, G.P.L. 1960: Zeolite zones and dike distribution in relation to the structure of the basalts of Eastern Iceland. Journal of Geology **68**, 515–528.

Walker, G.P.L. 1970: The distribution of amygdale minerals in Mull and Morvern (Western Scotland). In: Murty, T.V.V.G.R.K. & Rao, S. (eds): Studies in Earth Sciences, West Commemoration Volume, 181–194. Faridibad, India: Today & Tomorrow's Publishers.

Manuscipt received 3 July 2001; revision accepted 7 December 2001.

Appendix A: Locations of sites along the sections discussed in the paper and minerals found in vesicles and fractures at each locality. The mineral zones are defined in Fig. 2

Profile	Locality	Altitude (m)	Vesicles	Fractures	Zone
SU1	Road exposure 0.5 km north of Lopranseiði	25	No vesicles.	He–Me. He–St–Ch. An–Ch. Ca. Qz.	2–3
SU1	The northern entrance of the Sumba tunnel	70	–	He–Me. He–Ch. Me–An. Ca. Ch–An.	2–3
SU1	Road exposure at the W slope of Siglidalur	200	–	Ch–An. Ca.	1–3
SU1	Road exposure at small stream on the W slope of Spinarnir	380	–	Ch–Th*. Op. Qz.	1–2
SU1		288	–	Ch–An. Op. Qz. Ca.	1–2
SU1	Road exposure at Stórá, 1km SE of Spinarnir	340	–	Th*–An. Op. Qz. Ca.	1–2
SU1	Lambaklettur	235	–	As above.	1–2
SU2	Road exposure 3 km E of Øravík	100	Empty vesicles.	Ca. Qz.	1–2
SU2	Road exposure 2.5 km E of Øravík	25	Ce–An. Ch–Me*–Th*.	An. Ca. St.	1–2
SU2	Exposure in Dalsá, 1.5 km W of Øravík	100	An, Me*. Ch. Ca. Cld.	Cld. Qz.	1–2
SU2	Road exposure just north of Høgiklovningur, 2.5 km S of Øravík	250	Ca–An. Ph–Th*.	Cld. Me*.	1–2
SU2	Øraskarð	278	Empty vesicles.	Ca.	1–2
SU2	NW slope of Nónfjall	360	Th*–An–Ch.	Th–Th*–An–Ch.	1–2
SU2	The summit of Nónfjall	427	An–Me* Ca. Qz.	An.	1–2
SU2	Road exposure 0.8 km S of the church in Fámjin	80	Ac. Ch.	Ch. An. Qz.	1–2
SU2	Road exposure 0.5 km S of the church in Fámjin	20	An–Th. Th*–Ch.	An. St. Me*.	1–2
SU5	Høvdatangi, Froðba	0–25	Empty vesicles.	Empty fractures.	–
SU5	Skarvatangi	60	Na–(Th, An). Me–Th. Ch.	Me–Me*. Me–St. Me–An. St–Ch. St*–St.	2–3
SU5	Exposure at the road Froðba–Nakkur	90	An–St. Me–St. Th–St. Th–Me.	Me*–Ch.	2–3
SU5	– do –	130	Na. Ch. Me–Sc. Me–Ch. Th–Ga–Ch.	Na–St*–St. An–Th. St–Ch.	2–3
SU5	– do –	140	An–Th*–Ch.	An–Me. St–Me–St. Me–La, Ch.	2–3
SU5	– do –	250	Me–Me*. Th–Me.	An. He–St. Op, Cld, Ca.	2–3
SU5	Summit of Kambur	483	Ce–He. Me in large acicular crystals like scolecite.	Ce–Me*, Ce–An. He.	2–3
SU9	Hamranes and the southern entrance of the tunnel Hvalba–Sandvík	0–100	He–St. He–Me–Ch. An–Me. Me–Me*–Gy. Me–Gy+Ap.	He–St–Ap. Me*–La. Th–Ch; He–(St, La). He–Ap. He–La. La–Ca. La–Gy.	2–3
SU9	The southern slope of Skálafjall	70	An–He. Me–Th. Cld.	As in the vesicles.	2–3
SU9	– do –	120	As above.		2–3
SU9	– do –	160	Scolecite-like Me. An–He. Me–He.	He–Me–Me*. Ca.	2–3
SU9	– do –	200	As above.		2–3
SU9	– do –	240	Me–St. He–St. He–Ch.	Ca–(Ch, Le).	2–3
SU9	– do –	260	Me–Me*–Ch. Th–Ch.		2–3

Profile	Locality	Altitude (m)	Vesicles	Fractures	Zone
SU9	The southern slope of Skálafjall	290	Th*–Ch. Me–Me*–Ch. Ca.		1–3
SU9	The summit of Skálafjall	374	As above.		1–3
SA1	Exposure at the cost line and at road cuttings in Søltuvík	0–50	Many empty vesicles. He. St. La. Ca.	La–St–Ca. Mo–He–St. Ca.	2–4
SA1	Road exposure at the road Sandur–Søltuvík, 1.5 km west of Sandur	60	He–St. He+Me–St. Th–St.	He+Me–St. Ca.	2–4
SA1	Large quarry at lake Sandvatn, 1 km north of Sandur	10	No vesicles.	St–La–Ca. He. St.	2–4
SA1	Sprutthol, Sandsvágur Bay	30	He–Me. Ch. Ca.	St. Ca.	2–4
SA3	Húsavíklið N of Húsavík	0–75	He–Me. Ce–Me. Th–Me.	St.	2–3
SA3	Road exposure 2 km W of Skálavík	78	Me–Ch. Gi. Cld.	He–St–Ca.	2–3
SA3	Road exposure at Hálsur, 3 km W of Skálavík	119	Me–Th. Me–Me*. He–Th.	St–St*. Ap.	2–3
SA3	Urðarklettar NW of Húsavík	120	Me–Th–Ch. An–Me–Th.		2–3
SA3	Húsavíklið N of Húsavík	150	Me–Th–Me. An. He. Ca.		2–3
SA3	Exposure at Gravaráin	140	Me–Th. He–St. He–Ch. An.	St. La.	2–3
SA3	Urðatklettar, NW of Húsavík	150	Ce–Me–Th–Me*, Me–Me*–Gy.	Me*.	2–3
SA3	– do –	180	Ca–Me–Me*. An–Me.		2–3
SA3	Húsavíklið, N of Húsavík	180–200	Me–Th*. An–Th–Me*.		2–3
SA3	Exposure at Gravaráin	210–220	Me–Ca–.Me*. An–Me*. An–Th*.	Ca–He–St. Ca–Ap.	1–2
SA3	Exposure at Stórá	243	Me–Me*. Me–Th*–Ca. Gi.	Ca–St.	1–2
SA3	Summit of Heiðafjall	266	He–Me*. An–Me*–An. Th*.		1–2
SA3	Exposure at Stórá	320–340	Me–An–Me*. Ch. Th*.		1–2
SA3	Skriðubakki	360–380	Th*–Ch. Me*–Ch.	Me*.	1–2
SA3	– do –	400–420	Ch–Th*. Th*–Ch. An. Many empty vesicles.		0–1
SA3	The summit of Pætursfjæll	447	Ch–Th*. Many empty vesicles.		0–1
SA5	Dalsnípa	150	Me–An. Me–Ap–St. Th–Ap. Ch–Ap. Th–Ch. An–Ch.	Le. He–St–Ap. Cld.	2–3
SA5	The S slope of Skúvoyafjall, 0.6 km NW of Dalsnipa	280	Me–St, Me–An, He.		2–3
SA5	The summit of Skúvoyafjall	354	Ce–Ch. Ce–Th–Th*.	St.	1–3
SA5	Road exposure at the end of the road Dalur–Skuvoyafjall	308	He–Me. Th–Me*. Ch–Th*.		1–3
SA5	Road exposure 2 km SW of Dalur	260	Th–Ap. St–Me–Le. Th–Le.	He–Me–La.	2–3
SA5	Dalur harbour	0–30	Ch. Ch–Le. An–Th–Th*. He–Me–St.	Ch. Le. Me–Ap–St. Me–Me*.	2–3
SA5	Road exposure at Kinnartangi	100	Ch. Ch–Th–Ch. St–Me–Gy. Gy–Me.		2–3
SA5	The SE slope of Stórafjall	160	Ch. An–Me–Me*. St–Th.	Ch. St. He. Gy.	2–3
SA5	– do –	220	Me–Me*–Ch. Th–Me.		2–3
SA5	– do –	260	As above.		2–3
SA5	– do –	300	Ph. Gi–Me*. Th*–Le. Me–Me*.		1–2
SA5	– do –	340	As above.	Ch–Le. He–Me–St–Ap.	1–2
SA5	– do –	360	As above.	He–Le.	1–2

Profile	Locality	Altitude (m)	Vesicles	Fractures	Zone
SA5	The summit of Stórafjall	396	Ch+Ph. Gi–Me*. Me*–Ch. Th–Ch.		1–2
SA5	The NE slope of Stórafjall	310	Ch. Me*–Ch. He.		1–2
SA5	Trigonometric station on the NE slope of Stórafjall	217	Ch. An. Me–Ch. He–St. He–Me–Gy.		2–3
SA5	Road exposure at Tjarnaheyggjur	60	As above.	Me–Ca.	2–3
VÁ1	Reyðastiggajatangi	0–10	He–St, An.	Cl–St–Ca–La.	3–4
VÁ1	Gásadalur, exposure along the path Gásadalur–Rógvukollur	100	He–St, St–La.	Cl–St–La.	3–4
VÁ1	– do –	200	He, St.	Me, La, An.	3–4
VÁ1	Gásadalur, exposure at the path Gásadalur–Rógvukollur	235	He–Th.	La, Ca.	3–4
VÁ1	Gásadalur. The pass between Knúkarnir–Neytaskarð	340	He, St, Th, An, Cl.		3–4
VÁ1	Grunnadalur, exposure at the branching of small streams	380	Cl–He–Th, Cl–He–St, Cl–St–Me.	St–La–St.	3–4
VÁ1	Rógvukollur , exposure at the W slope	380	He–Me, Me–Ch, Th–Ch–Th, Mo–He, Mo–Ch ± Cld.	Me, Ca.	2–3
VÁ1	Neytaskarð, exposure at the SE slope	400–420	As above.		2–3
VÁ1	The summit of Rógvukollur	464	He–Me, Me–He–Me, Th–Me, Th–Ch, Me–Ch.		2–3
VÁ1	Djúpidalur (the NW slope of Eysturtindur), exposure at stream	470–480	He–Me, He–Ch, Me–Ch, Th–Ch.		2–3
VÁ1		500	He, Me, Th, Ch.		2–3
VÁ1	Grunnadalur, exposure at the end of small streams	550	Th–Me*–Ch.	La, Ca.	2–3
VÁ1	Djúpidalur (the NW slope of Eysturtindur)	600–610	Ce–Th–Th, Ce–Ch.	St–Me–La, Ca.	2–3
VÁ1	The plateau between Eysturtindur and Akranesskarð	620–640	An, Th, Me, Sm.		2–3
VÁ4	Oyrargjógv ferry harbour and the path to Sørvágur	0–136	St–St*. Ep–St. La. Th. Ch.	St. La.	3–4
VÁ4	Large quarry 1 km W of Sørvágur	10	Cl–St–St*. St–La. Mo–He. Mo–Gy. An–Gy. Me–Me*–Ch. Me–Ap±Sm.	He–St–St*. Ep. La, Me.	3–4
VÁ4	Sjatlá, 1.5 km N of Sørvágsvatn	45–60	Cl–He–St. St–La. Ap.		2–4
VÁ4	Exposure at N end of small road from Sørvágur, just W of Sjatlá	114	Cl–St–Me. Cl–An. Cl–Ch±Sm.	St–La. Ap.	2–4
VÁ4	– do –, exposure at small tributary of Skjatlá	150	Cl–He–St. St–Ap. Cl–Me–Th. Cl–Me–Ch. Me–Ap. Me–Ch.	Me–Ap. An–Ap. He–Ch.	3–4
VÁ4	– do –	190	As above.		3–4
VÁ4	– do –	220	Cl–St–St*. Cl–He ± La. Th.	Mo–St.	3–4
VÁ4	End of Breiðá (Oyrargjógv)	250	Ce–Me. He–Me.		3–4
VÁ4	– do –	304	Ce–Me–Th. Ce–Th–Ch.	Gy–Me.	2–3
VÁ4	Kvígandalur, exposure at the SE tributary of Kvígandalsá	250	An. He–Le. Me–Le. An–Th–Ch.		2–3
VÁ4	Husadalur, exposure at the W? tributary of Kirjuá	275	An. Me. He.	Me–An.	2–3

Profile	Locality	Altitude (m)	Vesicles	Fractures	Zone
VÁ4	Kvígandalur, exposure at the SE tributary of Kvígandalsá	300–365	An. He. Le. Ch.		2–3
VÁ4	The cross between the path Oyrargjógv–Sørvágur and Sandavágur–Slættanes	436	Me. Th. St. Ch.		2–3
VÁ7	Road exposure 3 km north of Sandavágur	100–120	Ce–He–St. Ce–St–Me. Ce–He–Th. Ce–Mo–St. Ce–Me–St.	Ce–Mo–He. Ce–He–St. Ce–Me*–Ch. Ce–Ap.	2–4
VÁ7	The western slope of Malinstindur	219	As above.		2–4
VÁ7	– do –	235	Ce–He–Me. Ce–Me–Gy.	St–Ca.	2–3
VÁ7	– do –	280	Ce–Me–Ch.±Ca. ±Sm.		2–3
VÁ7	– do –	345	As above.		2–3
VÁ7	– do –	386	Empty vesicles.		–
VÁ7	– do –	410	Ce–He–Me. Th–Me. Th–An.	St. Ch.	2–3
VÁ7	– do –	500	As above.		2–3
VÁ7	– do –	538	He. An. Me. Th. Th*. Cld. Ca.	He–Me. Me*. Cld.	1–2
VÁ7	– do –	563	Me–Me*. Th*–Ph. Th*–Ch+Le.		1–2
VÁ7	The summit of Malinstindur	580	Ce–Me*.		1–2
VÁ7	– do –	620	He. Me. Ph. Ch. Th.	Ca. Cld.	1–2
VÁ7	– do –	683	Me–He. Me*–Ch. Ph–Ch.		1–2
VÁ7	– do –	690	He. Ch. Le. Th. Cld.		1–2
ST2W	The path Saksun–Haldarsvík: Kvíggjarhamar, Saksun	0–100	He. St. Th. Me. Ch.	St–Ca–St. Gy. Tb. Ok.	2–3
ST2W	The slope of the mountain between Skipá and Gellingará	150	He–Ch–Th. Me–St.		2–3
ST2W	– do –	200	Me. Ca.		2–3
ST2W	– do –	250	Th–Me. He–Me. Me–Ch.	St. La.	2–3
ST2W	– do –	310	As above.		2–3
ST2W	– do –	325	Me. Me*. Th*–Ch. He–Me.	Ok. Gy. Ca.	2–3
ST2W	– do –	355	Me–Me*. Th–Me*. Th*–Ch.		2–3
ST2W	– do –	360	Ce–Th*. He–Me*–Sm.		1–2
ST2W	– do –	380	An–Th*. Th*–Le.	Me*–Ca.	1–2
ST2W	– do –	407	Ce–Ph–Ch. Ce–Th*–Ch.		1–2
ST2W	– do –	430	Th*–Ch.		1–2
ST2W	– do –	460	Empty vesicles.		0–1
ST2W	– do –	555	Le–Ch. Th–Th*.		0–1
ST2W	Víkarskarð	600	Ce. Th. Ch. Cld.		0–1
ST2W	The NE slope of Gívrufelli	650	As above.		0–1
ST2W	The summit of Gívrufelli	701	As above.		0–1
ST2E	Víkarnes N of Haldarsvík	0–30	He–St. Ca.	Ca–La.	3–4
ST2E	The SE slope of Fjallið	100	As above + Th. Gy. Ok.	To–Gy. La.	3–4
ST2E	– do –	150	He. Me. Th.	To–St. Th–Gy–Ap.	2–3
ST2E	The summit of Fjallið	180	He–Me. He–Th*. Ca.		2–3

Profile	Locality	Altitude (m)	Vesicles	Fractures	Zone
ST2E	The path Haldarsvík–Saksun: exposure 0.5 km SW of Haldarsvík	148	He–St. Me.	Me–Th–Ch. Me–An. Ph–Le–Ch.	2–3
ST2E	– do –, exposure 1 km SW of Haldarsvík	200	He–St. He–Me.		2–3
ST2E	– do –, exposure at the Svínstiáir tributaries of Kluftá, 1 km SW of Haldarsvík	230	Me. Th. He.	St. Ca.	2–3
ST2E	– do –, exposure 1.2 km SW of Haldarsvík	250	He. Me. Mo.	He. St. Ap. Ca.	2–3
ST2E	– do –, exposure 1.5 km SW of Haldarsvík	280	Me–Th–Me–Gy–Sm.		2–3
ST2E	– do –, exposure 1.8 km SW of Haldarsvík	350	Me–Th.		2–3
ST2E	– do –, exposure 2 km SW of Haldarsvík	360	Me–Th. Me–Ph–Ch.		2–3
ST2E	– do –, exposure 2.3 km SW of Haldarsvík	370	Me–Th. An–Me–Me*.		2–3
ST2E	– do –, exposure 2.5 km SW of Haldarsvík	400	Th*–Ch. Me–Th*.	Ph–Ch. Ch + Le.	1–2
ST2E	– do –	410	Me–Me*. Ch–Le–Ch.		1–2
ST2E	The SE slope of Víkartindur	420	Me–Me*–Le. Ch–Ph–Sm.		1–2
ST2E	– do –	440	.Me*. Th–Th*–Ch.		1–2
ST2E	– do –	500	Th*. Ch. Cld.		0–1
ST2E	– do –	540	As above.		0–1
ST2E	– do –	620	As above.		0–1
ST6W	Road exposure at the main road Kvívík–Stykkið, 1.5 km E of Kvívík	50	He. St. La. Me. Th. Ap.	He. St. Ap. Me*. Th. Ch. An.	2–4
ST6W	Tunnel workplace at the village of Leynar	50	Me. St. La.		2–4
ST6W	Exposure at Leynarvatn along the old road Tórshavn-Vestmanna	60–125	He. St. Wa. La. Ce. Cld.	St. Ca. He. St. St*. La. Me*, Th, Le.	2–4
ST6W	The path Leynarvatn–Hósvík, exposure 0.3 km NE of Leynarvatn	150–190	Ce–He–St. Ce–Me–Gy. Cld.	Ph, Gy, Ap.	2–3
ST6W	– do –, 0.4 km NE of Leynarvatn	210	Ce–He–St. Ce–Me–Th. Ce–St–La.		2–3
ST6W	– do –, 0.5 km NE of Leynarvatn	260	Ce–Me–Th. Ce–He–Me. Ce–He–Th.	Me–Ca.	2–3
ST6W	The path Leynarvatn–Hósvík, exposure 0.5 km NE of Leynarvatn	300	As above.		2–3
ST6W	– do –, 0.6 km NE of Leynarvatn	340	As above.		2–3
ST6W	á Halsi, 1 km NE of Leynarvatn	380	As above.		2–3
ST6W	– do –, 1.5 km NE of Leynarvatn	463	Ce–He–Me–Me*. Ce–Th–Ch.		2–3
ST6W	– do –, 1.9 km NE of Leynarvatn	500	As above.		2–3
ST6W	– do –, 2 km NE of Leynarvatn	510	Me–He–Me*. Me–Me*. Th*–Ch.	He–Me.	2–3
ST6W	Hósvíksskarð	520–530	Th. Th*. Ph. Ch. Le. + Ce.		2–3
ST6W	The SW slope of Bøllufjall	550	As above.		1–2
ST6W	The summit of Bøllufjall	584	As above.		1–2
ST6W	The SW slope of Gívrufjall	530	As above.		1–2
ST6E	Road exps. between við Áir and Hosvík	15	He–St*. He–St–Ap. He–St–Ch. He–Th–Ch. Th–St. Th–Ch. Ga–Th. An–Ch. An–Ap. An–Th. An–Th–Ch±Ce.	He–Ch–St. Th–Gy+Ap. Ch–Th*–Ap.	2–3
ST6E	The path Hosvík–Leynar: Smørdalsá	160–203	He–Me. He–Ch–Th, Me–Gy. He–An–Th.		2–3

Profile	Locality	Altitude (m)	Vesicles	Fractures	Zone
ST6E	The path Hosvík–Leynar: Smørdalsá	240–260	Ce–Me–He. Ce–Th–Me. Cld.	Me–Th–Ap–Gy.	2–3
ST6E	– do –	360	As above.	Ca–La. Cld.	2–3
ST6E	The NE slope between Bøllufjall and Gívrufjall	436	Me–Th. He–Me–Ca. He–Th.		2–3
ST6E	– do –	480	He–Me–Me*. Th–Ch. Th–Th*.		2–3
ST6E	– do –	500	Th–Th*–Gy. Me*–Gy.		2–3
ST6E	The NE slope of Bøllufjall	530	Th–Th*. Th–Ph, Th*–Ch.		1–2
ST6E	The summit of Bøllufjall	584	As above.		1–2
ST10	Large quarry 0.5–1 km NW of Sund, Kalsbaksfjørður	15	Me. Me*. Th. An. Ph. Gi. Ap.		2–3
ST10	Exposure at Sundá, 1.2 km S of Sund	227	He. Me. Ca.		2–3
ST10	– do –, 1.6 km SW of Sund	265	Me. Th.	St–He.	2–3
ST10	Quarry 0.5 km SW of Lambafelli at the high road Tórshavn–Kollafjørður	340	Ce–He. Ce–Ch–Le. Ce–An. Ce–Ch.	Ce–He–Sm, Ce–He–Ch. Ce–He–Th–Ch.	2–3
ST10	Road exps. 1 km W of Sundshálsur along the high road Tórshavn–Kollafjørður	310	Ce–He–Me. Ce–Me–Ch. Ce–Th–Me.		2–3
ST10	Small quarry at end of road to the water reservoir of Havnardalur	170	He. Me. Th. Ch.		2–3
ST10	Road exposure at the road Tórshavn–Velbastaður, 0.5 km N of Velbastaður	160	Ce–Me. Ce–Th–Ch.		2–3
ST10	Exposure at the road Tórshavn–Velbastaður, just N of Velbasta ur	123	Me–Me*. Me–Ch. Me. Th–Ch. Th–Me–Me*.	Cld, Ca.	2–3
EY1	Road exposure at the road Eiði–Norðskáli, 0.4–0.5 km SE of Eiði	60–100	Ap–Gy–Me. Me–Ph. He–Gy–Me. He–Me–Ch. St–Aå–Sm. Th–Ap. Th–St–Ap. Th–Ch–Sm.	St–La–St*–Ca. He–St–Ch–Sm.	3–4
EY1	Localities on the road Eiði–Funningur: Quarry in Djúpidalur, 2 km east of Eiði	150	St–Gy. St–Th–Gy. Th–Ga–Th. Me–Th. Me–Ch.	St–La.	3–4
EY1	50 m long road cutting on W slope of Slættaratindur, 3.5 km east of Eiði	200–230	Me–Th*–Gy. Me–Th*–Ch. Me–He–Me. He–Me.	St–St*. La–Me*–Sm. He–Ap. St. Cld. Qz.	2–3
EY1	Road exposure 0.4–0.5 km E of Eiðisskarð just at the N slope of Vaðhorn	336–346	Ce–Me–Th*. Ce–Me–Ch.		2–3
EY1	The N slope of Vaðhorn	410	As above.	He–St–St*. Mo–St.	2–3
EY1	– do –	435	As above.		2–3
EY1	Small quarry at the road fork Eiði, Funningur, Gjógv, 1 km west of Funningur (165)	165	He. St. Me. Me*. Ch.		2–4
EY1	Exposure at the coast line at Funningur	5–10	Mo. He. St. Me. +Ce.	St. An. Me. Cld.	3–4
EY2	Exposure at the coast between Stóra and Marká	0–20	Mo. He. St.	St. Qz. Cld. Ca.	3–4
EY2	The path Svínár–Funningur	30–40	He–Me. He–St–Gy. He–Me–Gy.		3–4
EY2	– do –	100	Me–Th–Ch. Th–Gi. Th–Me*. An–Ch. An–Th–Ch.	Th–Gy–Ap. Me–Ap–St.	2–3
EY2	– do –	212	As above.		2–3
EY2	– do –	280	Me. Th. An. Ch.	An–Th*–Gy.	2–3
EY2	– do –	346	An. Me. Me*. Th. Th*. Th–Ch–Sm.		2–3
EY2	– do –	400	Ce–Th–Th*–Ch. Ce–Ch.	Th–Th*–Ch.	1–2
EY2	– do –	420	Ch–An. Ch. Gi–Th*. An–Ph–Ch.		1–2

Profile	Locality	Altitude (m)	Vesicles	Fractures	Zone
EY2	Kvígandalsskarð	460	Me*. Th*. Ch. Gy. Sm.		1–2
EY2	– do –	480	As above.		1–2
EY2	The E slope of Skerðingur	500	As above.		1–2
EY2	– do –	525	As above.		1–2
EY2	– do –	450	Ce–Th*. Ce–Me–Me*–Ch.		1–2
EY2	– do –	430	As above.		2–3
EY2	– do –	415	Ce–An. Ce–Qz. Cld.		2–3
EY2	– do –	380	Me.		2–3
EY2	Kvígandalur	363	He–Me. He–Th.		
EY2	Skipagjógv	180	Me–Th–Th*. Ch–Gi–Th.	An–Th–Ap–Gy–Sm. Cl. Ca.	2–3
EY2	– do –	80	He. Me. Th.	Ca.	2–3
EY2	– do –	50	Gy–He. Gy–Th–Me.		3–4
EY2	Skipagjósoyran	0–10	He. St. Th. La. Gy.	He. Me–La–St.	3–4
EY3	Large quarry 1 km S of Oyri	20–30	Me–Th–Sm. Me–Th–Ch–Sm. Me–Gy–Me*.	Cl–He–Th–Ap.	2–3
EY3	Oyrargjógv	100	Me–Th, Me–Gy.		2–3
EY3	– do –	210	No vesicles.	He. St. Me. Th. Gy.	2–3
EY3	The path Oyri–Skálafjørður	251	Me. Th. Ch.		2–3
EY3	– do –	300	He–Me. Th–Me. Th–Ch.		2–3
EY3	– do –	340	An. Me*–Ch.		1–2
EY3	– do –	350	Me*–Ch. Th–Th*.		1–2
EY3	– do –	400	Th–St–Gy. Ch. St.		1–2
EY3	– do –	426	An–Th*. An–Th*–Ca. Ch.		1–2
EY3	– do –	495	Th*–Ch+Le.		1–2
EY3	The SW slope of Sandfelli	527	Ce–Th*–Ch. Ce–Cld.	He. Me. Ca. Cld.	0–1
EY3	– do –	545	As above.	As above.	0–1
EY3	The summit of Sandfelli	572	As above.	As above.	0–1
EY3	The path on the S slope of Skálafjall	440	Me–Th. He–Me.		2–3
EY3	– do –	405	As above.		2–3
EY3	– do –, just at Öksnagjógv	200	As above.		2–3
EY4	Small quarry just N of Morskarnes, about 1 km N of Nesá	20	He–Th–Ch. Me–Th.	He–St. He–Ap. Ca.	2–3
EY4	The W slope of Neshagi, just E of the locality above	140	Cl–Me–Th. He–Th.		2–3
EY4	Exposure at Skotá	194	As above.		2–3
EY4	– do –	230	Me–Me*. Ch.		1–2
EY4	– do –	320	Th*. Me–Me*. Ch.	He–Me. He–St.	1–2
EY4	The SE slope of Kambur: exposure between the source of Skotá and Urðará	380	Me*. Ch, Le +Ce.		1–2

Profile	Locality	Altitude (m)	Vesicles	Fractures	Zone
EY4	The SE slope of Kambur: exposure between the source of Skotá and Urðará	400	As above.		1–2
EY4	– do –	430	Th*. Ch. Le. Ce.		0–1
EY4	– do –	462	Ch. Many empty vesicles.		0–1
EY4	The path Steffanstangi–Kambur	480	As above.		0–1
EY4	– do –	500	Th–Ch–Th*. Cld. Ca.		0–1
EY4	– do –	540	As above.		0–1
EY4	The summit of Kambur (trigonometric station)	593	As above.		0–1
EY4	The E slope of Heygshagi	440	Me*–Ch. Th*–Ch.		1–2
EY4	– do –	400	As above.		1–2
EY4	– do –	250	As above.		1–2
EY4	Markrá	250	Me–Me*. He–Th. He–Me*.		2–3
EY4	– do –	160	As above.		2–3
EY8	Road exposure at the old road Lervík–Fuglafjørður/Norðragøta, about 2 km NW of Lervík	80	Ce–Mo–He–Me. Ce–Ch.	He–Me–St.	2–3
EY8	Localities along Kálvadalsá in Kálvadalur	200	Mo–He–Me–Me*. An–Th–Ch. Le–Ch–Le.	He–Me–St–St*. An–Th.	2–3
EY8	– do –	270	As above.		2–3
EY8	– do –	300	He–Me*–Ch. An–Th*–Ch.		2–3
EY8	Mannsgjógv	400	An–Ph–Ch. An–Th–Ch, Me*–An.		1–2
EY8	The NE slope of Navirnar	300	He–Me–St*. He–Ch, He–Le. An–He.	He–St. He–Me.	2–3
EY8	The E slope of Ritafjall	440	He–Me*–Ch. An–Th*–Ch.		1–2
EY8	– do –	490	He–Th–Ch. Me*–St*.		1–2
EY8	– do –	520	Th–Ch. Me*–Ch.	He. St. Ca.	0–1
EY8	The summit of Ritafjall	560	Th. Ch. Le.		0–1
EY8	– do –	641	Th*. Nearly all vesicles are empty.		0–1
EY10	Large quarry just N of the road fork Skálafjørður–Runavík–Lambi	60–80	Me–St*. Th–St*. Th–Me–An. Th–Ch–St*. Co–Th. Ha.	He–St*. He–Th–Ca. Ph–Ch–Ph. Ha–Ca.	2–3
EY10	The SW slope of Ritafelli, NE of the locality above	180	No vesicles.	He–Me–Ch–Sm. Me*–Le–Ch–Sm. An–Me*–Sm.	2–3
EY10	– do –	200	Me–Me*. Ch. Th*. Ph.	An–Me*–Sm. Me*–Ph–Le. Ap–Sm.	1–2
EY10	– do –	230–240	As above.		1–2
EY10	– do –	270	He–Th–Ch. Th*–Ph. An–Th*, Ch–St. An–St. Ap–Th–Ph. Ca.	St–La. Me–Ap.	1–2
EY10	The edge of Ritafelli	350	St, Me*. Th*. Ph. Ch. Ce.		1–2
EY10	The SW slope of Stórafjall	380	Th*. Ch. Ph.		1–2
EY10	The W edge of Stórafjall	440	Th. Ph. Ch. An. Ce.	An. St. Ch. Ph. Sm.	0–1
EY10	– do –	490	Empty vesicles.	St, Th*. Ch. Ca. Cld. Sm.	0–1

Profile	Locality	Altitude (m)	Vesicles	Fractures	Zone
EY10	The W edge of Stórafjall	520	Th. Many empty vesicles.		0–1
EY10	The summit of Stórafjall	567	As above.		0–1
BO1	Large quarries at Klakkur	60	Me–Ch. He–Me. Cld.	Mo–St–La. Ca–St.	2–3
BO1	The NE slope of Klakkur	100	Mo–An. Mo–He. Me–Ch. Ca.		2–3
BO1	– do –	140	Me–Th*. Ga–Me. Ch–Gi–Th.	As in the vesicles.	2–3
BO1	The NE slope of Klakkur	160	Th–Me*–Ph. Ph–Ch.	He–St. Ca–St.	1–2
BO1	– do –	210	Mo–He–Ch. Ch–Th. Th–Ph. Le–Ch.	Ca–St.	1–2
BO1	– do –	260	Me–Th–La. An–St–La. An–Th–Ch.		2–3
BO1	The summit of Klakkur	414	Ch–Th. Th–Ph.		2–3
BO1	The S slope of Klakkur	380	As above.		2–3
BO1	– do –	300	Me–Th. Th*–Ch. Th–Ph–Ch.	He–St–La.	2–3
BO1	– do –	260	He–Me–Th. He–Th.		2–3
BO1	The NE slope of Hálgafelli	280	Ce–He–Me–St. Ce–Me–An.		2–3
BO1	– do –	300	As above.		2–3
BO1	– do –	360	As above.		2–3
BO1	– do –	380	Ce–Mo–He–Th. Ce–He–Me.		2–3
BO1	– do –	400	Ce–St–Ch.	He–Th–Me–St.	2–3
BO1	– do –	450	As above.		2–3
BO1	– do –	480	An–Me–Me*. Th–Ch.		2–3
BO1	The summit of Hálgafelli	503	Ce–He–Me.	St–La.	2–3
BO2	Exposure at stream 0.6 km SW of Norðoyri	20–80	He. Me. Ch. An. Ap.	St. Cld. Ca.	2–3
BO2	The W slope of Høgahædd	140	An. Me. Ch. Many empty vesicles.	As above.	1–3
BO2	– do –	220	He–St. He–Ch–St. Th–Ph.	St. Ca.	2–4
BO2	– do –	270	Empty vesicles.		–
BO2	– do –	310	He–Me–Me*. Me–An. Me–Ch.		2–3
BO2	– do –	320	Ch–Th*–Ch. He–Ch. Th*. An.		1–2
BO2	– do –	330	Me*. Th'. Ch. Ca.		1–2
BO2	– do –	360	As above.	Ch. Th*. Ca.	1–2
BO2	– do –	440	Th*. Ca. Op.	Cld.	1–2
BO2	– do –	474	Me. Me*. Th*. Ch.		1–2
BO2	– do –	510	Th–Th*. Ca. Cld. Many empty vesicles.		0–1
BO2	– do –	550	As above.		0–1
BO2	The summit of Høgahædd	563	As above.		0–1
BO3	Large quarry between Norðdepil and Depil	40–50	Ce–He–Th. Ce–He–Na–Th. Ce–Th–Ch.	Cl–He–St–Ap. Cl–Th–Ap. Cl–Ph.	2–4
BO3	Depilsá	150	Me–Me*–Ch–Le. Me–Me*–Ch. He–Me.		2–3
BO3	– do –	200	Me*–Ch, An–Ch.		1–2
BO3	– do –	300	He–Me*–Ch. He–Th*–Ch. An–Ph–Ch. +Ce.	He–St. He–Th–Ca.	1–2

Profile	Locality	Altitude (m)	Vesicles	Fractures	Zone
BO3	Depilsá	340	As above.		1–2
BO3	E slope of Lokki	375	Ch–Gi–Th'. Ch–An.		0–1
BO3	– do –	400	Ch–Th*–Ch. Ch–Le.		0–1
BO3	– do –	450	As above.		0–1
BO3	– do –	470	Th. Ch. Ca.	He–St–Th–Ca.	0–1
BO3	E slope of Lokkanøv	460	Ce–An–Ch. Ce–Th–Ch–Th*. Many empty vesicles.		0–1
BO3	– do –	580	As above.		0–1
BO3	– do –	700	As above.		0–1
BO3	The summit of Lokki (trigonometric station)	754	As above.		0–1
VI1	The starting point of the profile is the largest stream 0.5 km SE of Hvannasund	50	Ce–Me–St. Ce–An–Th–Me. Ce–Me–Ch. Ce–He–St–Me.	Ce–Cl–St. Ce–Cl–Me–Ca.	2–3
VI1	SW slope of Enni	120–132	Empty vesicles.		–
VI1	SW slope of Enni	180	Mo–An.		2–3
VI1	– do –	210	An. Ph–Ch. An–Th. Me–Me*. He–Me–Ch.	He–Me*–Ch. He–Ph–Ch. He–Th–Me.	2–3
VI1	– do –	225	As above.		1–2
VI1	– do –	240	Me*. Th*. An.		1–2
VI1	– do –	270	Ce–Th–Th*–Ch. Ce–Ch–Le. Ce–An–Ch. Ce–Ch–St. Ce–He. Ce–He–Cld.	He–St. Cld.	1–2
VI1	– do –	310	Ch–Gi–Th*. St–Ch. Ph–Ch. Th–Th*.		1–2
VI1	– do –	360	Ce–Ch. Ce–Ph–Ch. Ce–Th*. Ch.		1–2
VI1	– do –	380	Ch. Th. Le. Sm.	Cld.	1–2
VI1	– do –	420	Th*–Le–Ch–Sm.	Op. Sm.	0–1
VI1	– do –	550	As above. Many empty vesicles.		0–1
VI1	– do –	600	Ca and Siderite.		0–1
VI1	The summit of Enni	651	As above.		0–1
VI2	Small quarry at the road Hvannasund–Viðareiði, 2.6 km N of Hvannasund	40–80	Ce–He–Me. Ce–He–Th. Ce–He–Ch–Sm. Ce–Ch–Sm. Ce–Ph–Me*. Ce–Me–Me*.	He–Me–St.	2–3
VI2	W slope of Tunnafjall	80–100	He–Me–Me*. An–Th–Me. An–Th–Ch. An–Ph–Ch.	He–St. St–Me.	2–3
VI2	– do –	150	As above.		1–2
VI2	– do –	200	As above.		1–2
VI2	– do –	225	Me*. Th*. Ch. Ph. An.	He. St. Ca.	1–2
VI2	– do –	250	Me*. Th*. Ch.		1–2
VI2	– do –	300	Th*. Ch.		1–2
VI2	– do –	315	As above.		0–1
VI2	– do –	390	An. Th'. Ch. Ph.	Me*. Ph. St.	0–1
VI2	– do –	460	Th*. Ch. Le. Sm.	St. Sm.	0–1
VI2	– do –	520–550	Empty vesicles.	Qz. Cld. Ca.	0–1

Profile	Locality	Altitude (m)	Vesicles	Fractures	Zone
VI2	The summit of Tunnafjall	593	Th. Th*. Ch.		0–1
VI2	The S Slope of Myrnafjall	620	No vesicles.	Th. Th*.	0–1
VI2	The summit of Myrnafjall (trigonometric station)	688	Th. Th*. Only 20% of the vesicles are mineralised.		0–1
VI3	Small quarry at the road Viðareiði–Hvannasund, 2.5 km south of Viðareiði	80	He–Th*. Me–Me*–Ch–Se.	As in the vesicles.	1–2
VI3	The W and the SW slope of Malinsfjall	150	He–Th*. Me–Me*–Ch. An–Me*–Ph.		1–2
VI3	– do –	200–220	Th*. Ch. Le.	Me. Me*. Th. Th*. An. St.	0–1
VI3	– do –	255	Th*. Ph. An.	He–St.	1–2
VI3	The W and the SW slope of Malinsfjall	310	Th*–Ch.		0–1
VI3	– do –	300–330	Me–Th*. Gi–Ch.		0–2
VI3	– do –	440	Th*. Ch. About 50% of the vesicles are empty.	An–St.	0–1
VI3	– do –	540	As above.		0–1
VI3	– do –	605	Ch–Th–Le. Ca.	Ca–Th–Ca.	0–1
VI3	– do –	660	All vesicles are empty.		0–1
VI3	– do –	680	As above		0–1
VI3	– do –	710	Scattered mineralisations of Th and Ch.		0–1
VI3	The summit of Malinsfjall	750	As above.		0–1

Appendix B. Minerals found in vesicles within different depth intervals in the Lopra-1/1A and Vestmanna-1 boreholes

Max depth	Min depth	Vesicles	Zone
Lopra-1/1A			
–3543	–3400	**La**, Pr, Ca, Cl.	HT
–3400	–3200	**La, Mo**, Pr, Cl.	HT
–3200	–3000	**La, Mo**, Pr, Sm, Qz.	HT
–3000	–2800	**La**, Pu, Qz, Cl.	HT
–2800	–2600	(no data)	
–2600	–2400	**La**, Ca, Pr ,Cl.	HT
–2400	–2200	**La**, Pr, Pu.	HT
–2200	–2000	Th, Ep, He, **La**, Pr, Wa, Mo, Ca, Ce, Sm, Cl, Si.	5–6
–2000	–1800	Sc, Th, Ep, He, **La,** An, Ca, Ce, Cl, Si.	3–5
–1800	–1600	Sc, Th, **St**, Ep, **La**, An, Ca, Ce, Sm, Cl, Si.	3–5
–1600	–1400	Sc, Th, **St**, Ep, He, **La**, An, Ca, Ce, Sm, Si.	4–5
–1400	–1200	Me, Th, **St, Ep, He**, La, Ce, Sm, Cl, Si.	4–5
–1200	–1000	**Me, Sc, Th, E**p, He, La.	3–4
–1000	–800	**Me, Sc, Th, St, Ep**, He, La, An, Ca, Cl, Si.	3–4
–800	–600	Th, St, **Ep, He**, La, An, Cl.	3–4
–600	–400	Me, **Sc**, Th, Ep, He. An. Ca.	2–3
–400	–200	**Me, Sc**, Th, **Ep**, He, An, Ca, Cl, Si.	2–3
–200	0	**Me, Sc,** Th, **St, He**, An, Mo, Ca, Cl, Si.	2–3
Vestmanna-1			
–600	–575	He. He–Ch.	3–4
–575	–550	He. An. St–St*. Ch–Sm.	3–4
–550	–525	He–Ch. Ap. Th–Ap. Ch–Sm.	3–4
–525	–500	He. He–Ac. Th–Ch. St–Ch.	
–500	–475	An–Th–Mt. Th–Sm.	3–4
–475	–450	An–Th–Sm. Th–Sm.	3–4
–450	–425	Gy–Th–Sm. An. An–Th–Sm. Th. Sm.	3–4
–425	–400	An. He–La–Ch. Me–Ch. Th–Sm. Ch–Sm.	3–4
–400	–375	He–La–Ch. Me–Ap–Ch. Me–Ch+Le–Sm. Ch–Sm.	3–4
–375	–350	Me. Gy–Th–Sm. Th–Sm. Th*–Ch. Ch+Le.	2–4
–350	–325	Ap. Th–Ap. Gy–La. Gy–Th–St. Ph. Th*–Sm. Th*–Ch.	1–4
–325	–300	He. He–Me. He–La–Ch. Mo–He–Ch, Th*–Sm. Th*–Ch, Ch–Sm.	2–4
–300	–275	He. He–Ch. Me–He–St. Th–Ga–Ch. Th*–Ph–Ch. Th*–Ch. Ch–Sm.	2–4
–275	–250	Me. Me–Th–Ch. Me–Th–Ph–Ch.. La–Me. Ap. Th–Ch–Sm. Ch–Sm.	2–4
–250	–225	Th–Gy–Sm. Th–Th*–Ch. He–Th–Ap. Le–Sm.	2–4
–225	–200		
–200	–175	He. He–Ch–Ap–Sm. Me–Ch, Th–Th*–Ch. Th–Gy–Mt. Th–Ap. An. Ap. Le–Sm.	2–3
–175	–150	Me–He–Me*. Me–He–Ap. Me–Ap. Me–He–Th–Le. Me–Th–Ph–Ch. Th*–Ch –Le. Na–Ch. Ch–Sm.	2–3
–150	–125	Me. Me–Th–Ph–Ch. Ph–Sm. Me*–Ch An–Sm.	2–3
–125	–100		
–100	–75	Me. Me–Th–Ch–Sm. Me+Na–Ap–Sm. Me*–Ch. An–Ep–Ch. Mo–Ch. Th–Ch.	2–3
–75	–50	He. He–Th. Mo–He. Me–Th. Na–Ch. Th–Ch. Me*–Ch. Ch–Sm.	3–4
–50	–25	Ch–Sm. Ep–Ch.	3–4
–25	0	Me. Me*. Me–Ap. Me–Th. Me*–Ch. Mo–Ch.	2–3

Danmarks og Grønlands Geologiske Undersøgelse (GEUS)
Geological Survey of Denmark and Greenland
Øster Voldgade 10, DK-1350 Copenhagen K
Denmark

Geological Survey of Denmark and Greenland Bulletin is a new series started in 2003 to replace the two former bulletin series of the Survey, viz. *Geology of Greenland Survey Bulletin* and *Geology of Denmark Survey Bulletin*. The twenty-one volumes published since 1997 in those two series are listed below after the new bulletin series. The new series, together with *Geological Survey of Denmark and Greenland Map Series*, now form the peer-review scientific series of the Survey.

Geological Survey of Denmark and Greenland Bulletin (new series)

1	The Jurassic of Denmark and Greenland, 948 pp. (28 articles), 2003. *Edited by* J.R. Ineson & F. Surlyk.	500.00
2	Fish otoliths from the Paleocene of Denmark, 94 pp., 2003. *By* W. Schwarzhans.	100.00
3	Late Quaternary environmental changes recorded in the Danish marine molluscan faunas, 268 pp., 2004. *By* K.S. Petersen.	200.00
4	Review of Survey activities 2003, 100 pp. (24 articles), 2004. *Edited by* M. Sønderholm & A.K. Higgins.	180.00
5	The Jurassic of North-East Greenland, 112 pp. (7 articles), 2004. *Edited by* L. Stemmerik & S. Stouge.	160.00
6	East Greenland Caledonides: stratigraphy, structure and geochronology, 93 pp. (6 articles), 2004. *Edited by* A.K. Higgins and F. Kalsbeek.	160.00
7	Review of Survey activities 2004, 80 pp. (19 articles), 2005. *Edited by* M. Sønderholm & A.K. Higgins.	180.00
8	Structural analysis of the Rubjerg Knude Glaciotectonic Complex, Vendsyssel, northern Denmark, 192 pp., 2005. *By* S.A.S. Pedersen.	300.00
9	Scientific results from the deepened Lopra-1 borehole, Faroe Islands, 156 pp. (11 articles), 2006. *Edited by* J.A. Chalmers and R. Waagstein.	

Geological Survey of Denmark and Greenland Map Series (new series)

1	Explanatory notes to the Geological map of Greenland, 1:500 000, Humboldt Gletscher, Sheet 6, 48 pp. + map, 2004. *By* P.R. Dawes	280.00
2	Explanatory notes to the Geological map of Greenland, 1:500 000, Thule, Sheet 5 (1991), 97 pp. + map, 2006. *By* P.R. Dawes.	300.00

Geology of Greenland Survey Bulletin (discontinued)

173	Cambrian shelf stratigraphy of North Greenland, 120 pp., 1997. *By* J.R. Ineson & J.S. Peel.	250.00
174	The Proterozoic Thule Supergroup, Greenland and Canada: history, lithostratigraphy and development, 150 pp., 1997. *By* P.R. Dawes.	300.00
175	Stratigraphy of the Neill Klinter Group; a Lower – lower Middle Jurassic tidal embayment succession, Jameson Land, East Greenland, 80 pp., 1998. *By* G. Dam & F. Surlyk.	250.00

176	Review of Greenland activities 1996, 112 pp. (18 articles), 1997. *Edited by* A.K. Higgins & J.R. Ineson.	200.00
177	Accretion and evolution of an Archaean high-grade grey gneiss – amphibolite complex: the Fiskefjord area, southern West Greenland, 115 pp., 1997. *By* A.A. Garde.	200.00
178	Lithostratigraphy, sedimentary evolution and sequence stratigraphy of the Upper Proterozoic Lyell Land Group (Eleonore Bay Supergroup) of East and North-East Greenland, 60 pp., 1997. *By* H. Tirsgaard & M. Sønderholm.	200.00
179	The Citronen Fjord massive sulphide deposit, Peary Land, North Greenland: discovery, stratigraphy, mineralization and structural setting, 40 pp., 1998. *By* F.W. van der Stijl & G.Z. Mosher.	200.00
180	Review of Greenland activities 1997, 176 pp. (26 articles), 1998. *Edited by* A.K. Higgins & W.S. Watt.	200.00
181	Precambrian geology of the Disko Bugt region, West Greenland, 179 pp. (15 articles), 1999. *Edited by* F. Kalsbeek.	240.00
182	Vertebrate remains from Upper Silurian – Lower Devonian beds of Hall Land, North Greenland, 80 pp., 1999. *By* H. Blom.	120.00
183	Review of Greenland activities 1998, 81 pp. (10 articles), 1999. *Edited by* A.K. Higgins & W.S. Watt.	200.00
184	Collected research papers: palaeontology, geochronology, geochemistry, 62 pp. (6 articles), 1999.	150.00
185	Greenland from Archaean to Quaternary. Descriptive text to the Geological map of Greenland, 1:2 500 000, 93 pp., 2000. *By* N. Henriksen, A.K. Higgins, F. Kalsbeek & T.C.R. Pulvertaft.	225.00
186	Review of Greenland activities 1999, 105 pp. (13 articles), 2000. *Edited by* P.R. Dawes & A.K. Higgins.	225.00
187	Palynology and deposition in the Wandel Sea Basin, eastern North Greenland, 101 pp. (6 articles), 2000. *Edited by* L. Stemmerik.	160.00
188	The structure of the Cretaceous–Palaeogene sedimentary-volcanic area of Svartenhuk Halvø, central West Greenland, 40 pp., 2000. *By* J. Gutzon Larsen & T.C.R. Pulvertaft.	130.00
189	Review of Greenland activities 2000, 131 pp. (17 articles), 2001. *Edited by* A.K. Higgins & K. Secher.	160.00
190	The Ilímaussaq alkaline complex, South Greenland: status of mineralogical research with new results, 167 pp. (19 articles), 2001. *Edited by* H. Sørensen.	160.00
191	Review of Greenland activities 2001, 161 pp. (20 articles), 2002. *Edited by* A.K. Higgins, K. Secher & M. Sønderholm.	200.00

Geology of Denmark Survey Bulletin (discontinued)

36	Petroleum potential and depositional environments of Middle Jurassic coals and non-marine deposits, Danish Central Graben, with special reference to the Søgne Basin, 78 pp., 1998. *By* H.I. Petersen, J. Andsbjerg, J.A. Bojesen-Koefoed, H.P. Nytoft & P. Rosenberg.	250.00
37	The Selandian (Paleocene) mollusc fauna from Copenhagen, Denmark: the Poul Harder 1920 collection, 85 pp., 2001. *By* K.I. Schnetler.	150.00

Prices are in Danish kroner exclusive of local taxes, postage and handling

Note that information on the publications of the former Geological Survey of Denmark and the former Geological Survey of Greenland (amalgamated in 1995 to form the present Geological Survey of Denmark and Greenland) can be found on the Survey's website: *www.geus.dk*